

# **Integrated Optical Microring Resonator in SOI for Wide Range Refractive Index Sensing**

*A THESIS*

*submitted by*

**SUJITH C**

*for the award of the degree*

*of*

**DOCTOR OF PHILOSOPHY**



**DEPARTMENT OF ELECTRICAL ENGINEERING  
INDIAN INSTITUTE OF TECHNOLOGY MADRAS  
CHENNAI - 600036, INDIA**

**NOVEMBER 2016**

This is to certify that the thesis titled **Integrated Optical Microring Resonator in SOI for Wide Range Refractive Index Sensing**, submitted by **SUJITH C**, to the Indian Institute of Technology, Madras, for the award of the degree of **Doctor of Philosophy**, is a bonafide record of the research work done by him under my supervision. The contents of this thesis, in full or in parts, have not been submitted to any other Institute or University for the award of any degree or diploma.

**Dr. Bijoy Krishna Das**  
Research Guide  
Associate Professor  
Dept. of Electrical Engineering  
IIT-Madras, 600 036

Place: Chennai, India

Date: Thu 10<sup>th</sup> Nov, 2016

Dedicated to my **Family**  
for their eternal love and support

## **ACKNOWLEDGEMENTS**

My long journey towards the PhD study has been wonderful with experiences at various extends. At times I have had arguments, confusions and frustrations, all of which were outshone by the excitement and fulfillment along the way. I am grateful that I have worked with so many brilliant people and that I have learned so much from them, both in academic research and in personal life.

First, I wish to thank my supervisor, Dr. Bijoy Krishna Das, for his endless support and guidance throughout my PhD research. I always astonished to see the way he approaches the problems in academic research as well as in non-academic activities. I should admire his out of box thinking capability that has helped me at various obstacles that I have faced often in academic research. I am sure that all his students are molded to withstand adverse situations in academic and personal life through the way he is grooming his students. He introduced me towards the subject integrated optical circuits and has helped to understand very complicated research problems in terms of very simple fundamental aspects through long discussions in weekly group meetings.

I am highly indebted to Prof. Nandita DasGupta for her excellent lectures on VLSI Technology, which was the basis for my capability towards the development of a few technological aspects which resulted in a self-satisfying experimental research work.

I thank all my doctoral committee members, Prof. Nadita DasGupta, Dr. Balaji Srinivasan, Prof. Vijayan and Prof. Nilesh J. Vasa for their valuable comments and suggestions during the review meetings. I express my thanks to Mr. C. Rajendran, Jr. technical superintendent, Mr. J. Prakash, Jr. technician and Mr. T. Sridhar for their technical support in MEMS & Microelectronics lab. I admire there sincerity and dedication with the lab and all of them were a phone call away even if it is at late night or week end or vacation days.

My heartfelt thanks to Saktivel for teaching me the basic concepts of engineering

subjects which made me capable of getting admission in a premiere institute such as IIT Madras, without him it would have been only a dream for me to study in IIT.

I thank Rupesh, my senior student, for introducing me towards the microelectronic fabrication and characterization processes. I still and always remember the moment that he helped me in coupling light first time to the silicon waveguide which I had been struggling for days.

I thank Solomon, Naredran, John P. George, G. Sridhar, Krishna Karthik, Gaurang, Harish, Sidharth, Uppu Karthik and Sakthivel for creating such a wonderful work culture in IOLAB, where we used to discuss, argue and fight on various research problems as well as personal issues.

I thank Meenatchi Sundaram and Dr. A. Vijay Kumar for their most valuable friendship, care, motivation and support. I express my sincere thanks to Dr. Shantanu Pal, my senior, for his advices and guidance in academic and non-academic domains at various stages of my stay at IIT Madras.

My special thanks to Saket Kaushal for his silent jokes, Sidharth for his beautiful songs, Sumi for her motivating statements, Riddhi Nandi for her leadership in planning adventure trips which made later part of my stay at IITM eventful apart from their technical helps

I thank Ramesh K Gupta for his helping hands in fabrication and characterization whenever I wanted. I thank Srivatsa Kurudi for developing LabView programs to automate the experimental setups that made many of our experiments with less effort. I thank my fellow labmates Parimal Sah, Sooraj, Dadavaili, Chaithanya, Vivek, Seetha Lakshmi, V. Mani Teja, Usman, Amrutha, Katerina, Arijit Misra, Keerthana for their wishes and encouragements.

Word are limited to thank my parents and brother for their love and supports throughout my life. I am also indebted to my in-laws for taking care of my personal life. Finally, all credit goes to my wife Hridya, she solely has taken all the responsibilities herself to take care of our son Aarav and look after both of our families which allowed me to chase my dream. Without her love, support and motivation I could not have completed my PhD.

# ABSTRACT

**KEYWORDS:** Silicon Photonics, Silicon-on-Insulator, Ring Resonator, Refractive Index Sensor, Waveguides, Integrated Optics, 2D Taper, Spot-Size Converter, Shadow Masking, Surface Trimming.

Photonic wire waveguide based microring resonator is identified to be an important building block for CMOS optical interconnects in silicon-on-insulator (SOI) platform. It is also found to be an attractive integrated optical device for sensing biomolecules (Lab-on-Chip applications) as well as monitoring global warming and environmental issues by detecting various gas molecules in terms of their refractive index signatures. Over the years, many fascinating refractive index designs were demonstrated in laboratory level. However, many challenges still remain in system level integration, industrialization and commercialization. There are three important issues identified for a microring resonator based on-chip sensing.: (i) external fiber-chip-fiber light coupling, (ii) internal coupling between ring and bus waveguides, (iii) waveguide quality in term of losses, dispersion, evanescent field interaction with cladding analytes. They are studied systematically in this work.

We have developed CMOS compatible shadow mask etching process to fabricate a adiabatic 2D spot-size converters which can efficiently used for in-line fiber pigtailling of submicron silicon waveguides. The insertion loss of the 2D spot-size converter is measured to be 0.25 dB and it remains same for a broad wavelength range (1530 nm to 1565 nm). We have also fabricated grating assisted 1D spot-size converters (grating coupler) for out-of-plane fiber optic coupling. Though the insertion loss of the grating coupler is high (6 dB/facet), we found it is very useful to test devices quickly on wafer scale as it does not require any addition process for end-facet preparation.

After successful demonstration of low-loss 2D spot-size converters, we have studied a refractive index sensor which relies on the shift of critically coupled resonant

wavelength. It has been shown theoretically and experimentally that the dispersion in the transmission characteristics of a directional coupler based microring resonator with SOI waveguide in all-pass configuration can be enhanced significantly by just increasing the length of the directional coupler. This in turn helps to single-out highly extinct resonance(s) at and around the critically coupled wavelength. By tracking the critically coupled wavelength, it is possible to estimate cladding refractive index changes accurately. Microring resonators with various waveguide cross-section have been investigated theoretically as well as experimentally. A shallow etched waveguide (width  $\sim 560$  nm, rib height  $\sim 250$  nm and slab height  $\sim 150$  nm) on submicron (250 nm) SOI substrate has been preferred for the demonstration of wide range refractive index sensing though the theoretical sensitivity of the proposed device can be increased well above 500 nm/RIU for a short range of cladding refractive index with a cladding sensitive waveguide cross-section. Typical sensitivity of fabricated devices is measured to be 54 nm/RIU with an error limit of  $\sim 1.67 \times 10^{-2}$  RIU. By integrating an active element (e.g. microheater), the limit of detection can be improved significantly ( $\sim 10^{-4}$  RIU). The superiority of such a device lies in its simpler design, wider range and nearly accurate detection by electronic interrogation.

# TABLE OF CONTENTS

<b>ACKNOWLEDGEMENTS</b>	<b>iv</b>
<b>ABSTRACT</b>	<b>vi</b>
<b>LIST OF TABLES</b>	<b>xi</b>
<b>LIST OF FIGURES</b>	<b>xxi</b>
<b>ABBREVIATIONS</b>	<b>xxii</b>
<b>NOTATION</b>	<b>xxiv</b>
<b>1 Introduction</b>	<b>1</b>
1.1 Motivation and Literature Review . . . . .	1
1.2 Research Objective . . . . .	12
1.3 Thesis Organization . . . . .	14
<b>2 Microns to Submicron Waveguides: Design, Fabrication and Characterizations</b>	<b>16</b>
2.1 Waveguide Design . . . . .	17
2.1.1 Condition for Single-Mode Guidance . . . . .	18
2.1.2 Birefringence . . . . .	22
2.1.3 Dispersion . . . . .	23
2.1.4 Input/Output Coupling Loss . . . . .	25
2.1.5 Bend Induced Loss . . . . .	27
2.1.6 Fabrication Tolerance in Device Response . . . . .	27
2.2 Surface Trimmed Waveguides . . . . .	30
2.2.1 Oxide Growth and Removal . . . . .	32
2.2.2 Isotropic Dry Etching . . . . .	34
2.2.3 Modeling of Surface Trimmed Waveguides . . . . .	39



2.2.4	Single-mode Trimmed Waveguide . . . . .	41
2.2.5	Polarization Dependency . . . . .	46
2.3	Spot-Size Converters: Fabrication and Characterization . . . . .	49
2.3.1	2D Spot-Size Converters by Photolithography Definition . . . . .	49
2.3.2	2D Spot-Size Converters by Shadow Mask Etching . . . . .	54
2.3.3	Grating Assisted 1D Spot-Size Converter . . . . .	64
2.4	Summary . . . . .	73
<b>3</b>	<b>Ring Resonators: Microns to Submicron Technology</b>	<b>75</b>
3.1	Theory and Important Design Parameters . . . . .	75
3.1.1	Multimode Interference Coupler . . . . .	79
3.1.2	Directional Coupler . . . . .	85
3.1.3	Design of Ring Resonator Cavity . . . . .	95
3.2	Demonstration of Large Volume Ring Resonator . . . . .	98
3.3	Demonstration of Compact Microring Resonator . . . . .	102
3.3.1	Microring Resonator: Fabrication and Characterization . . . . .	102
3.3.2	Spectral Characteristics . . . . .	103
3.3.3	Propagation Loss Extraction . . . . .	106
3.3.4	Dispersion Characteristics . . . . .	106
3.4	Summary . . . . .	110
<b>4</b>	<b>Refractive Index Sensor: Design, Fabrication and Testing</b>	<b>112</b>
4.1	Device Design . . . . .	112
4.2	Experimental Demonstration . . . . .	122
4.3	Summary . . . . .	128
<b>5</b>	<b>Conclusions</b>	<b>130</b>
5.1	Research Summary . . . . .	130
5.2	Research Outlook . . . . .	133
<b>A</b>	<b>List of Publications Based on Thesis</b>	<b>145</b>
<b>B</b>	<b>Curriculum Vitae</b>	<b>147</b>



## LIST OF TABLES

2.1	Optimized spin coating parameters for HSQ (XR-1541) electron beam resist to achieve 100 nm thick uniform layer. . . . .	67
2.2	Optimized electron beam lithography parameters: measured beam current = 40 pA and developer - MF 319. . . . .	71
3.1	Optimized MMIC parameters (for TE polarization) on a 2 $\mu\text{m}$ and 0.25 $\mu\text{m}$ device layer SOI substrates. . . . .	83
3.2	Characterization summary of large volume MMICs based ring resonators (Untrimmed and trimmed) with 500 $\mu\text{m}$ ring radius. . . . .	100
4.1	Parameters used for studying dispersion characteristics of two types DCs designed with deeply-etched (DE) and shallow-etched (SE) waveguides. . . . .	116

## LIST OF FIGURES

1.1	Schematic representation of chip to chip communication using silicon photonics. Photographic/SEM images of important regions of optical interconnect are shown as inset [20]. . . . .	4
1.2	(a) Schematic top view of a microring resonator in add-drop configuration : $E_i$ , $E_p$ , $E_a$ and $E_d$ are the electric field amplitudes at input, pass, add and drop ports, respectively. $t_1$ and $t_2$ are the self coupling coefficients at the coupler 1 and 2, respectively. $k_1$ and $k_2$ are the cross-coupling coefficients at coupler 1 and 2, respectively. $n_{eff}$ - effective index of the guided mode, $L$ - ring perimeter, $m$ - order of resonance, $\lambda_m$ - resonant wavelength. (b) Typical transmission characteristics at the pass ( $T_p$ ) and drop ( $T_d$ ) ports of add-drop ring resonator: $ER_{p/d}$ - extinction ratio at pass/drop port, FSR - free spectral range and $FWHM_{p/d}$ - full width at half maxima at pass/drop port. . . . .	5
1.3	Schematic view of the measurement set-up for a ring resonator based biosensor [43]. . . . .	7
1.4	(a) Schematic top view of cascaded ring resonator sensor based on Vernier effect. Schematic spectral responses of (a) Ring# 1, (b) Ring# 2 and (c) cascaded combination of Ring# 1 and Ring# 2: blue and red lines represent the sensor response with and without analyte, respectively [57]. . . . .	8
1.5	Schematic view of a grating coupler used for coupling light between single mode fiber and photonic wire waveguide in SOI substrates [61].	10
1.6	(a) Schematic view of an inverse taper structure and (b) SEM image of inverse taper junction region showing polymer waveguide and silicon photonic wire waveguide [69]. . . . .	11
2.1	Schematic cross-sectional view of a typical optical waveguide geometry in SOI substrate: BOX - buried oxide, $W$ - waveguide width, $H$ - rib height and $h$ - slab height. . . . .	17
2.2	Calculated values slab height cut-off ( $h_c$ ) has been plotted as function $W$ for 5 $\mu\text{m}$ waveguide ( $H = 5 \mu\text{m}$ ). Area above blue and red lines represents the single mode regions for TM and TE polarization respectively. Bottom and top claddings are considered to be BOX and air, respectively. Calculation are carried out for $\lambda = 1550 \text{ nm}$ . . . . .	19

2.3	Calculated values slab height cut-off ( $h_c$ ) as function $W$ for 5 $\mu\text{m}$ device layer thickness ( $H = 5 \mu\text{m}$ ). Area above blue and red lines represents the single mode regions for TM and TE polarization respectively. Bottom and top claddings are considered to be BOX and air, respectively. Calculation are carried out for $\lambda = 1550 \text{ nm}$ . . . . .	20
2.4	Calculation of slab height cut-off ( $h_c$ ) values for single mode guiding of 2 $\mu\text{m}$ device layer thickness ( $H = 0.25 \mu\text{m}$ ) as a function of $W$ . Calculations are shown for TE polarization at $\lambda = 1550\text{nm}$ . . . . .	21
2.5	Structural birefringence comparison of various waveguide structures in SOI substrate. solid, dotted and dashed lines represent birefringence of LCRW( $W = 5 \mu\text{m}, H = 5 \mu\text{m}$ and $h = 4 \mu\text{m}$ ), RCRW ( $W = 1.5 \mu\text{m}, H = 2 \mu\text{m}$ and $h = 1 \mu\text{m}$ ) and PhWW ( $W = 0.5 \mu\text{m}, H = 0.25 \mu\text{m}$ and $h = 0 \mu\text{m}$ ) respectively. . . . .	23
2.6	Structural dispersion comparison of various waveguide structures in SOI substrate. Solid, dotted and dashed lines represent calculated group indices of 5 $\mu\text{m}$ waveguide ( $W = 5 \mu\text{m}, H = 5 \mu\text{m}$ and $h = 4 \mu\text{m}$ ), 2 $\mu\text{m}$ waveguide ( $W = 1.5 \mu\text{m}, H = 2 \mu\text{m}$ and $h = 1 \mu\text{m}$ ) and 0.25 $\mu\text{m}$ waveguide ( $W = 0.5 \mu\text{m}, H = 0.25 \mu\text{m}$ and $h = 0 \mu\text{m}$ ). The calculations are shown for TE polarized light. . . . .	24
2.7	Calculated waveguide coupling loss (modal overlap in dB scale) as a function waveguide width ( $W$ ) = height ( $H$ ), where the input light is taken as the direct output from standard single-mode fiber (SMF) with mode-field diameter of $\sim 9.5 \mu\text{m}$ (dashed line); and the focused lensed fiber (LF) output with spot-size diameter of 3.2 $\mu\text{m}$ (solid line), respectively. The calculations are carried out for TE-like waveguide mode excitation at $\lambda = 1550 \text{ nm}$ . Also the slab height is taken as ( $h$ ) = $0.7 \times H$ , ensuring single-mode guidance (checked up to $W = H = 30 \mu\text{m}$ ). . . . .	26
2.8	Calculated mode profiles for bend waveguides with (a) radius 10000 $\mu\text{m}$ for LCRW and (b) radius 500 $\mu\text{m}$ for RCRW. Both calculation has been carried out for TE polarization at $\lambda \sim 1550 \text{ nm}$ . Calculated values of bend induced loss for (c) LCRW and (d) RCRW. . . . .	28
2.9	(a) Change in 3 dB length ( $\Delta L_{3dB}$ ) of directional coupler and (b) resonant wavelength shift ( $\Delta \lambda_m$ ) of ring resonator as a function of width variation ( $\Delta W$ ) due to fabrication error on 5 $\mu\text{m}$ device layer ( $W = 5 \mu\text{m}, H = 5 \mu\text{m}$ and $h = 4 \mu\text{m}$ ), 2 $\mu\text{m}$ device layer ( $W = 1.5 \mu\text{m}, H = 2 \mu\text{m}$ and $h = 1 \mu\text{m}$ ) and 0.25 $\mu\text{m}$ device layer ( $W = 0.5 \mu\text{m}, H = 0.25 \mu\text{m}$ and $h = 0 \mu\text{m}$ ) respectively. . . . .	29
2.10	Processing flow for fabrication surface trimmed waveguides by repeated oxidation and removal. (a) photoresist pattern after photolithography, (b) after reactive ion etching, (c) oxidized waveguide structures and (d) after oxide removal. . . . .	32

2.11	(a) Microscopic images of surface trimmed waveguide after one oxidation and removal step, oxide has not been removed from the untrimmed section which reduces the oxidation rate for successive oxidation steps.	33
2.12	Fabrication process flow for naturally tapered surface trimmed waveguides. (a) Photolithographic definition of LCRWs, (b) LCRW definition by anisotropic RIE, (c) photolithography to protect input/output LCRW structures and (d) isotropic RIE process for surface trimming and SSC.	34
2.13	SEM images of the cross-sectional view fabricated LCRW (a) before and (b) after trimming using isotropic RIE process. (c) SEM image showing the integrated LCRW and RCRW on the same substrate by surface trimming technique and (b) magnified image of (a) showing the naturally 2D tapered LCRW-RCRW junction. . . . .	36
2.14	(a) Characterization set-up used for mode-profile measurement where PC - polarization controller, L - lens, P - polarizer, DUT - device under test, IRC - infrared camera. (b) Mode-size comparison of calculated and measured fundamental TE modes waveguides as function of waveguide width with $H = 2.2 \mu\text{m}$ , $h = 1.35 \mu\text{m}$ at $\lambda = 1550\text{nm}$ . (c) Measured guided mode profile of a typical LCRW coupler with $W_0 = 3 \mu\text{m}$ , $H_0 = 5 \mu\text{m}$ and $h_0 = 4 \mu\text{m}$ . (d) Typical guided mode profile for trimmed (RCRW) waveguide with $W_0 = 1.5 \mu\text{m}$ , $H_0 = 2.2 \mu\text{m}$ and $h_0 = 1.35 \mu\text{m}$ . . . . .	37
2.15	(a) Fiber butt-coupling setup used for measuring the efficiency of naturally tapered waveguides, red laser used for identifying the waveguides under characterization. (b) Comparison of throughput power of RCRW structures with/without LCRW couplers (note: reference waveguide # 3 is damaged). Characterization has been carried out at input power - $P_{in} = 6.5 \text{ mW}$ and wavelength $\sim 1550 \text{ nm}$ . . . . .	38
2.16	Schematic cross-sectional views of a $2 \mu\text{m}$ waveguide ( $W_0 = 2 \mu\text{m}$ , $H = 2 \mu\text{m}$ and $h = 1.5 \mu\text{m}$ ) at various instants trimming time ( $t$ ). . . . .	40
2.17	Color map shows the single mode region of the surface trimmed waveguide as a function of $W_0$ and $h_0$ for a rib height of $H_0 = 2 \mu\text{m}$ . Numerical values inside each cell correspond to the rib height reduction ( $\Delta H = H_0 - H$ ) in micrometer unit at which single mode waveguide mode transformed into multi-mode waveguides. The green cells represents initial waveguide dimension which remains single-mode throughout trimming ( $\Delta H \rightarrow H_0$ ). White cells represents the multi-mode region. The calculated values are shown on for TE-like modes and at an operating wavelength of $\lambda = 1550 \text{ nm}$ . . . . .	42
2.18	Color map shows the waveguide mode profile overlap of an RCRW ( $H_0 = 2 \mu\text{m}$ ) with lensed fiber mode with mode size $\sim 3.2 \mu\text{m} \times 3.2 \mu\text{m}$ . The calculated values are shown on for TE-like modes and at an operating wavelength of $\lambda = 1550 \text{ nm}$ . . . . .	43

2.19	Cross-sectional profiles of surface trimmed waveguides; contour lines represents crosssections of the waveguide at various instants of RIE, where $W_0 = 1.55 \mu\text{m}$ , $H_0 = 2 \mu\text{m}$ and $h_0 = 1.75 \mu\text{m}$ . . . . .	44
2.20	(a)- Intensity distribution of the guided mode of an untrimmed single-mode waveguide ( $W_0 = 1.55 \mu\text{m}$ , $H_0 = 2 \mu\text{m}$ , $h_0 = 1.75 \mu\text{m}$ ); (b), (c), (d), (e), (f), and (g)- intensity distributions of the guided modes for the trimmed single-mode waveguides with etching duration of upto 6 mins., in steps of 1 min.; (h) and (i)- the highest order guided mode intensity distributions for the trimmed waveguides (multi-mode) with etching duration of 7 mins. and 8 mins., respectively; (j)- intensity distribution of the guided mode for the further trimmed single-mode waveguide with an etching duration of 9 mins. White outline defines the device layer silicon profile. Simulation has been done for TE polarization at $\lambda = 1550 \text{ nm}$ . . . . .	45
2.21	Multi-mode region of surface trimmed waveguide as function of waveguide initial width ( $W_0$ ) and rib height reduction ( $\Delta H = H_0 - H$ ) for $H_0 = 2 \mu\text{m}$ ( $h_0 = 1.75 \mu\text{m}$ ). . . . .	46
2.22	(a) TE fraction of the fundamental guided mode (TE) of a $2 \mu\text{m}$ as function of trimming duration ( $t$ ). (b) Calculated polarization rotation parameter (R) for a single-mode waveguide with $W_0 = 1.55 \mu\text{m}$ and $h_0 = 1.75 \mu\text{m}$ for three different values of $H_0$ plotted as function trimming time $t$ (or surface etching of $\Delta H$ ) for TE polarization at $\lambda \sim 1550 \text{ nm}$ . . . . .	47
2.23	Calculated transverse electric field distribution of a waveguide ( $W_0 = 1.55 \mu\text{m}$ , $H_0 = 2 \mu\text{m}$ and $h_0 = 1.75 \mu\text{m}$ ) trimmed for 5 minutes ( $\Delta H = 1 \mu\text{m}$ ), (a) $E_x$ component and (c) $E_y$ components for TE polarization, (c) and (d) are $E_x$ and $E_y$ components for TM polarization. All the calculations are carried out for $\lambda = 1550 \text{ nm}$ . . . . .	48
2.24	SSC fabrication scheme: (a) 3D schematic view of LCRW along with photoresist mask for SSC, (b) 3D schematic view of an integrated LCRW, SSC and RCRW after second RIE, (c) photoresist mask showing tapering parameters $W_B$ , $W_T$ , $L$ , $L_{SSC}$ , and $L_H$ ; (d) plots showing calculated (solid lines) and measured (dots) values of $L_{SSC}$ and $L_H$ as a function of $L$ for a pre-defined values of $W_B = 7 \mu\text{m}$ and $W_T = 1 \mu\text{m}$ . . . . .	51
2.25	SEM images of fabricated spot-size converters, (a) LCRW and RCRW spot size converter along with reference RCRW waveguide and (b) Schematic top view of fabricated waveguide structures ( $l = 19 \text{ mm}$ ): W#T - waveguide with # SSC(s). . . . .	52
2.26	(a) Fiber butt coupling setup used for measuring the insertion losses and (b) extracted insertion loss of SSC as a function of taper length. . . . .	52
2.27	Confocal microscopic image of a SSC (color variation represents the relative height variation) with simulated mode profiles (shown as inset) at various parts of the SSC. . . . .	53

2.28	Schematic representation of the fabrication process flow for rib waveguide fabrication and follow-up surface trimming using a shadow mask: (a) definition of rib waveguide width by e-beam lithography using negative tone resist HSQ, (b) schematic view of initial rib waveguide (after first RIE and the removal of resist mask), (c) schematic view of adiabatically integrated trimmed waveguide (after second RIE using shadow mask with rectangular aperture), (d) spatial filtering scheme of reactive plasma using shadow mask (silicon substrate in this case) with a rectangular slit aperture, (e) cross-sectional view of the masking scheme during second RIE, and (f) lateral view of the masking scheme during second RIE. . . . .	55
2.29	Shadow masking steps for waveguide surface trimming using a RIE system (Oxford Plasmalab80Plus): (a) Waveguide sample is placed on the RIE chamber, (b) silicon substrate (thickness 500 $\mu\text{m}$ ) with a rectangular opening (aperture) is placed over the substrate and (c) two cleaved silicon substrates (rectangular shaped) are used as shadow mask to obtain finite length of trimmed waveguides. . . . .	57
2.30	Cross-sectional SEM image of waveguide fabricated to verify the fabrication process proposed, (a) before and (b) after trimming. . . . .	58
2.31	Photographic image of the fabricated sample. It shows two sets, each having 6 waveguides with 3 mm long trimmed sections. . . . .	58
2.32	(a) SEM image of an untrimmed rib waveguide region, (b) SEM image of a trimmed waveguide region, (c) confocal images of a SSC showing etch depth variation along the propagation length (magnified view of the confocal images is shown on the right side), (d) measured etch depth and (e) width variation of the SSC; etch depth was measured by confocal imaging, whereas width variation was estimated by taking SEM images at regular interval along the length. . . . .	59
2.33	(a) Characterization setup used for waveguide characterizations; Inset: photograph showing lensed fiber being aligned parallel to waveguide axis at the input side with the help of visible laser light ( $\lambda = 632 \text{ nm}$ ); (b) intensity distribution of the focussed spot-size of a lensed fiber at $\lambda = 1550 \text{ nm}$ ; (c) intensity distribution of the guided mode of an untrimmed waveguide measured at the output (near-field image). . . . .	61
2.34	(a) Fabry-Perot transmission characteristics of untrimmed 15 mm long reference waveguide (black line) and equally long waveguide with 7 mm long trimmed (red line) section for TE polarization; (b) Measured single-pass waveguide loss ( $\alpha_{SP}$ ) as function of wavelength over C band of optical communication spectrum, the values are extracted from Fabry-Perot resonance spectrum. . . . .	62



2.35	(a) Frequency domain discrete Fourier transformed data (corresponds to Fabry-Perot transmission characteristics for a wavelength range of $1550 \text{ nm} \leq \lambda \leq 1552 \text{ nm}$ ) plotted as a function of time-delay for the untrimmed reference waveguide (black line) and the waveguide having 7-mm-long trimmed section (red line). (b) Extracted group indices (ng) for untrimmed and trimmed waveguides a . . . . .	63
2.36	(a) 3D schematic view of grating coupler integrated with photonics wire waveguide to couple light from SMF and (b) lateral schematic view of the waveguide with grating coupler. . . . .	65
2.37	(a) Typical electron beam lithography mask layout consisting of ring resonators, straight waveguide and directional coupler with grating coupler at both the ends. Grating coupler and ring resonator regions are magnified and shown as inset. Dashed line in the layout represents the write field ( $100 \mu\text{m} \times 100 \mu\text{m}$ ) boundary. (b) SEM images of the PhW-SSC junction and (c) grating coupler section through which write field is passed. . . . .	68
2.38	(a) Schematic representation of the trace-retrace patterning strategy for waveguide. where arrows on the FBMS represents the patterning direction of FBMS. Design color represents the relative dose of the components.(b) Modified Mask layout for electron beam lithography. Magnified view of the grating coupler and ring resonator are shown in the inset. . . . .	69
2.39	SEM images of critical regions of the device: (a) junction region of the grating coupler attached to the waveguide section (b) grating coupler section where the write field boundary passes as shown in Figure 2.37(c), (c) DBR region of grating coupler and (d) directional coupler where the ring and bus waveguides are coupled. . . . .	72
2.40	(a) Grating coupler light coupling setup where input and output fibers angles are fixed $10^\circ$ normal to the waveguide axis and (b) response of grating coupler integrated with submicron straight waveguide ( $W = 560 \text{ nm}$ , $H = 250 \text{ nm}$ and $h = 150 \text{ nm}$ ). . . . .	73
3.1	(a) Schematic top view of a microring resonator: dashed outline represents coupler section with self coupling coefficient $t$ and cross-coupling coefficient $k$ , $E_{in}$ and $E_{out}$ are the input and output electric fields respectively. (b) Typical output characteristics of a photonics wire microring resonator with $L = 157 \mu\text{m}$ , $a = 0.91 \text{ dB/cm}$ , $n_{eff} = 2.76$ and $t = 0.96$ (for $\lambda \sim 1550 \text{ nm}$ ); where ER - extinction ratio, FSR - free spectral range and FWHM - full width at half maxima. . . . .	76
3.2	Schematic top views of ring resonator with (a) cascaded multi-mode interference coupler (MMIC) or asymmetric Mach-Zehnder interferometer (MZI) and (b) directional coupler (DC). The coupling strengths of (a) and (b) are controlled by the lengths $L_A$ and $L_{DC}$ , respectively. . . . .	78

3.3	Schematic view of a $2 \times 2$ MMIC . . . . .	80
3.4	(a) MMIC length ( $L_{mmi}$ ) optimization for surface trimmed MMIC by monitoring Bar/Cross port power as function of $L_{mmi}$ , black and red lines show the variation output power for Bar and Cross ports respectively. (b) Wavelength dependency of $2 \times 2$ trimmed MMIC designed on $2 \mu\text{m}$ SOI substrate. (c) Simulated top view of $2 \times 2$ (3 dB) MMIC with optimum waveguide parameters: $W_{mmi} = 24 \mu\text{m}$ , $L_{mmi} = 890 \mu\text{m}$ , $L_t = 200 \mu\text{m}$ , $W_{it} = 3 \mu\text{m}$ and $W_{ph} = 1.5 \mu\text{m}$ .(d) Schematic top views of (d) photo mask layout of MMIC on $5 \mu\text{m}$ device layer and (e) MMIC layout expected after surface trimming process. . . . .	82
3.5	(a) Schematic layout of a MMIC based power splitter for variable splitting ratio ( $r$ ): $L_A$ is the length of the asymmetric arm of width $W_a$ . (b) Output power variation of the coupler shown in (a) is plotted as a function of $L_A$ , where asymmetric waveguide cross-section is considered to be $H = 250 \text{ nm}$ , $W_1 = 500 \text{ nm}$ $W_2 = 450 \text{ nm}$ and $h = 0 \text{ nm}$ . (c) Wavelength dependent $r$ is shown for the coupler for $L_A = 3.65 \mu\text{m}$ : calculations are shown for the MMIC (on $0.25 \mu\text{m}$ device layer) parameters given in Table 3.1 for TE polarization. . . . .	85
3.6	Schematic top view of a $2 \times 2$ DC: $L_{DC}$ - length of DC, $G$ - coupled waveguide separation, $E_{in}$ , $E_{Bar}$ and $E_{Cross}$ are electric field amplitudes at Input, Bar and Cross ports. . . . .	86
3.7	Calculated electric field profiles for (a) symmetric and (b) anti-symmetric modes of a DC with $W = 560 \text{ nm}$ , $H = 250 \text{ nm}$ , $h = 150 \text{ nm}$ and $G = 150 \text{ nm}$ . Calculated (c) $\kappa$ and corresponding (d) $P_{Cross}$ for $L_{DC} = 10 \mu\text{m}$ plotted as a function of coupled waveguide separation ( $G$ ). . . . .	89
3.8	(a) Geometrical representation of DC region branching out the ring and the bus waveguides. (b) Cross coupled fraction of input power due to input and output bend regions of DC as a function of interaction length $z$ in the branching region for $R = 25 \mu\text{m}$ and $G = 150 \text{ nm}$ . . . . .	91
3.9	Dispersion characteristics of cross-coupling ( $k^2$ ) for shallow etched waveguide ( $W = 560 \text{ nm}$ , $H = 250 \text{ nm}$ and $h = 150 \text{ nm}$ ) at various lengths ( $2L_0, 4L_0, 6L_0$ and $8L_0$ ). $L_0$ represents the cross-coupling length of the DCs at a reference operating wavelength $\lambda_0 = 1550 \text{ nm}$ . . . . .	92
3.10	(a) Typical power distribution of bar and cross ports of an asymmetric DC as function of $L_{DC}$ : where, $W_{Bar} = 560 \text{ nm}$ for $W_{Cross} = 480 \text{ nm}$ . (b) Coupling induced delay and (c) corresponding effective group index of asymmetric DC is plotted as function of $L_{DC}$ for various values of cross port waveguide widths ( $W_{Cross}$ ) for a fixed bar port width ( $W_{Bar}$ ) of $560 \text{ nm}$ . All calculations are shown for $H = 250 \text{ nm}$ , $h = 150 \text{ nm}$ and $\lambda = 1550 \text{ nm}$ . . . . .	94
3.11	Bend induced loss of a shallow etched waveguide ( $W = 560 \text{ nm}$ , $H = 250 \text{ nm}$ and $h = 150 \text{ nm}$ ) as function of bend radius $R$ . . . . .	96

3.12	Calculated values of (a) ER and (b) Q-factor of shallow etched photonic wire ring resonator as function of $L_{DC}$ : where $L_0 = 13 \mu\text{m}$ . Calculations are done by including the bend induced coupling at the branching region of DC. Calculated output characteristics and corresponding $k^2$ (right axis) of ring resonator with (c) $L_{DC} = 18.5 \mu\text{m}$ and (d) $L_{DC} = 96 \mu\text{m}$ . Parameters used for calculation are : $\alpha = 5 \text{ dB/cm}$ , $W = 560 \text{ nm}$ , $H = 250 \text{ nm}$ , $h = 150 \text{ nm}$ , $G = 150 \text{ nm}$ and $R = 25 \mu\text{m}$ .	97
3.13	Optical microscopic images of polished end-facets for $5 \mu\text{m}$ waveguide (a) and trimmed $2 \mu\text{m}$ waveguide (b); and guided fundamental mode intensity distributions for $5 \mu\text{m}$ (c) and $2 \mu\text{m}$ (d), for TE polarized light at $\lambda = 1550 \text{ nm}$ .	99
3.14	(a) Optical microscopic image of MMIC based ring resonator (ring radius $\sim 500 \mu\text{m}$ ) with reference MMIC and straight waveguides. (b) SEM image of a surface trimmed MMIC. Measured transmission characteristics of ring resonators: (c) fabricated directly on $2 \mu\text{m}$ device layer and (d) fabricated on $5 \mu\text{m}$ device layer and surface trimming process is carried out to reduce waveguide cross-section.	101
3.15	(a) SEM image of the fabricated ring resonator with $L_{DC} = 10 \mu\text{m}$ and $R = 50 \mu\text{m}$ , where magnified view of the DC region is shown as the inset. (b) Measured transmission (normalized to straight waveguide) characteristics of the device shown in (a).	103
3.16	SEM images of fabricated race track ring resonators with (a) $R = 5 \mu\text{m}$ and (b) $R = 10 \mu\text{m}$ (b) $R = 25 \mu\text{m}$ (b) $R = 50 \mu\text{m}$ and their corresponding transmission characteristics are shown in (e), (f), (g), (h), (i) respectively. The waveguide parameters ( $W = 560 \text{ nm}$ , $H = 250 \text{ nm}$ , $h = 150 \text{ nm}$ and $G = 150 \mu\text{m}$ ) and $L_{DC} = 40 \mu\text{m}$ are same for all the devices.	104
3.17	(a) Measured and fitted transmission spectrum of a high Q-factor ring resonator with $R = 100 \mu\text{m}$ . (b) FSR (left axis) and resonant delay (right axis) variation are shown as a function $R$ for devices with $W = 560 \text{ nm}$ , $H = 250 \text{ nm}$ , $h = 150 \text{ nm}$ , $G = 150 \text{ nm}$ and $L_{DC} = 40 \mu\text{m}$ .	105
3.18	Measured transmission spectrum of ring resonators with (a) $L_{DC} = 40 \mu\text{m}$ and (b) $L_{DC} = 100 \mu\text{m}$ : $L_x$ is fixed to be $400 \mu\text{m}$ for the ring resonators.	107
3.19	Transmission spectrum of ring resonator with asymmetric DC ( $L_{DC} = 70 \mu\text{m}$ ) showing full cross-coupling at $\lambda \sim 1550 \text{ nm}$ . (b) Extracted values of waveguide group index $n_g^s$ and effective group index of the DC ( $n_g^{DC}$ ) at $\lambda \sim 1550 \text{ nm}$ are shown as a function of $L_{DC}$ .	108
3.20	Measured transmission characteristics of microring resonators with asymmetric DCs of (a) $L_{DC} = 49 \mu\text{m}$ and (b) $L_{DC} = 52 \mu\text{m}$ . Measured FSR for (a) and (b) are shown in (c) and (d), respectively.	109

4.1	(a) Schematic view of a ring resonator refractive index sensor in SOI substrate. Partially transparent material above the ring and DC represents the analyte with refractive index ( $n_c$ ). (b) Schematic cross-sectional view of the DC: $W$ - width of the waveguide, $H$ - rib height, $h$ - slab height and $G$ - separation between the coupled waveguides. . . . .	114
4.2	Dispersion characteristics of cross-coupling efficiency ( $k^2$ ) for DEDC (a) and SEDC (b) at various lengths ( $2L_0, 4L_0, 6L_0$ and $8L_0$ ). $L_0$ represents the cross-coupling length of the DCs at a reference operating wavelength $\lambda_0 = 1550$ nm. Calculations were carried out for TE-like guided mode . . . . .	116
4.3	Dispersion characteristics of cross-coupling efficiency of DCs for two different cladding indices ( $n_c = 1.30$ and $1.35$ ): (a) DEDC with $L_{DC} = 104 \mu\text{m}$ and (b) SEDC with $L_{DC} = 104 \mu\text{m}$ . . . . .	117
4.4	Calculated sensitivity ( $S$ ) is shown as function of $W$ and $h$ for (a) $G = 100$ nm and (b) $G = 150$ nm. . . . .	118
4.5	(a) Calculated sensitivity ( $S$ ) for a wide-range of cladding refractive index ( $1.2 \leq n_c \leq 2.0$ ) in steps of 0.1: black bars for DEDC and gray bars for SEDC, (b) Calculated $S$ as a function of $n_c$ for SEDCs with three different slab heights satisfying single-mode guidance in TE-polarization. . . . .	118
4.6	The cross-coupling strength ( $\kappa$ ) as function of operating temperature for the SEDC (red line) and DEDC (blue line) with DI water as cladding material. The corresponding slopes are $-1.6 \times 10^{-5}/\mu\text{m-K}$ and $-2.8 \times 10^{-5}/\mu\text{m-K}$ , respectively. . . . .	119
4.7	Transmitted V-shaped comb spectra of ring resonators with SE waveguides (see Table 4.1 for design parameters) for two different cladding indices ( $1.30$ and $1.35$ ): (a) $L_{DC}^{eff} = 4L_0$ , and (b) $L_{DC}^{eff} = 8L_0$ . The calculations were carried out assuming waveguide loss of $5$ dB/cm. . . . .	122
4.8	(a) SEM image of a fabricated ring resonator with $L_{DC} = 100 \mu\text{m}$ . Inset: Zoomed image of the DC region. (b) Photograph of the experimental setup highlighting devices under test (sample mounted on a vacuum chuck), drop of an analyte on top of a device (F-IMF-150), and the input/output fiber probes. Both input and output fibers are connected to a high resolution optical spectrum analyzer (OSA) with internal light source (Apex - AP2043B). . . . .	123
4.9	Measured transmission characteristics of fabricated ring resonators for $n_c = 1$ (air cladding): (a) $L_{DC} = 40 \mu\text{m}$ , and (b) $L_{DC} = 100 \mu\text{m}$ . . . . .	124
4.10	Comparisons of 30 dB envelope bandwidth ( $\Delta f_{env}$ ) and FSR for six ring resonator devices with increasing values of $L_{DC}$ . The critically coupled wavelengths extracted from the resonance envelopes are shown in the inset. . . . .	125

4.11	Transmission spectra of a dispersion enhanced ring resonator fabricated with SE waveguides ( $R = 25 \mu\text{m}$ , $L_x = 400 \mu\text{m}$ , $L_{DC} = 100 \mu\text{m}$ ) corresponding to the surface cladding of air (blue), DI water (red) and F-IMF-150 (black). . . . .	126
4.12	Measured transmission (normalized) characteristics of the sensor for air and various refractive index liquid claddings. (b) Critically coupled wavelength ( $\lambda_c$ ) as a function of $n_c$ for refractive index liquids shown in (a): error bar indicates maximum uncertainty ( $\pm \text{FSR}/2$ ) of locating $\lambda_c$ due to finite FSR value. . . . .	127
4.13	Measured transmission characteristics of the sensor for cladding refractive indices of 1.3 (red line) and 1.32 (blue line). (b) Transmission characteristics of the device for air cladding measured on March 2016 and November 2016 to test the spectral stability. . . . .	127
5.1	Schematic view of fabrication process flow for achieving DC based microring resonator sensor on submicron platform is integrated with large cross-section waveguide. (a) Photolithographically defined photoresist pattern of multiple input multiple output (MIMOW) platform, (b) MIMOW platform is transferred to silicon by RIE, (c) submicron device patterning using electron beam lithography and (d) final device on the submicron platform with microfluidic channel to supply analyte. . . . .	133
5.2	Schematic view of ring resonator refractive sensor with (a) heater for active phase tuning and (b) pin diode for electronic interrogation. . .	135

# ABBREVIATIONS

## Acronyms

<b>C-Band</b>	Conventional wavelength band ( $\lambda \sim 1527$ to $1567$ nm)
<b>L-Band</b>	Long wavelength band ( $\lambda \sim 1567$ to $1607$ nm)
<b>WDM</b>	Wavelength-division-multiplexing
<b>DWDM</b>	Dense wavelength-division-multiplexing
<b>BPM</b>	Beam Propagation Method
<b>CMOS</b>	Complementary Metal Oxide Semiconductor
<b>DI</b>	De-ionized (water)
<b>FEM</b>	Finite Element Method
<b>FSR</b>	Free Spectral Range
<b>ICP</b>	Inductively Coupled Plasma
<b>LCRW</b>	Large Cross-section Rib Waveguide
<b>MZI</b>	Mach Zehnder Interferometer
<b>PPR</b>	Positive Photo Resist
<b>LCRW</b>	Large Cross-section Rib Waveguide
<b>RCRW</b>	Reduced Cross-section Rib Waveguide
<b>PhW</b>	Photonic Wire Waveguide
<b>RIE</b>	Reactive Ion Etching
<b>SEM</b>	Scanning Electron Microscope
<b>SMF</b>	Single Mode Fiber
<b>SOI</b>	Silicon-On-Insulator
<b>TE</b>	Transverse Electric (polarization)
<b>TM</b>	Transverse Magnetic (polarization)
<b>EMI</b>	Electromagnetic interference
<b>UV</b>	Ultra-Violet

## Chemical Names

<b>Al</b>	Aluminum
<b>Ar</b>	Argon
<b>CHF<sub>3</sub></b>	Tri-fluoro Methane
<b>Cr</b>	Chromium
<b>HF</b>	Hydro Fluoric Acid
<b>HNO<sub>3</sub></b>	Nitric Acid
<b>H<sub>2</sub>O</b>	Water
<b>H<sub>2</sub>O<sub>2</sub></b>	Hydrogen Peroxide
<b>KOH</b>	Potassium Hydroxide
<b>NaOH</b>	Sodium Hydroxide
<b>SF<sub>6</sub></b>	Sulfur Hexafluoride
<b>Si</b>	Silicon
<b>SiO<sub>2</sub></b>	Silicon dioxide
<b>TCE</b>	Tri-chloro Ethylene

### *Units*

<b>dB</b>	Decibel
<b>dBm</b>	Decibel milli-Watts
<b>mW</b>	milli Watts
<b>μm</b>	Micrometer
<b>ps</b>	Pico Second
<b>μs</b>	Micro Second
<b>sccm</b>	standard cubic centimeter per minute
<b>mTorr</b>	milli-Torr (of pressure)
<b>mbar</b>	milli-Bar (of pressure)
<b>ml</b>	milli-liter (of fluid)

## NOTATION

$\mathbf{n}$	Refractive index
$\mathbf{n}_{eff}$	Effective refractive index
$\epsilon$	Permittivity
$\lambda$	Wavelength
$\beta$	Propagation constant
$\phi$	Phase of the EM wave
$\mathbf{R}$	Waveguide bending radius
$\mathbf{L}$	Length (refers to device length, component length)
$\kappa$	Coupling coefficient or strength of coupling
$\Gamma$	Overlap integral coefficient
$\alpha$	Loss per unit length
$\delta_{dB}$	Polarization extinction
$\omega_x$	Electric field distribution in horizontal direction (along x-axis)
$\omega_y$	Electric field distribution in vertical direction (along y-axis)



# CHAPTER 1

## Introduction

As concept and prospect of "silicon photonics" introduced comprehensively for the first time in 1985 [1], the development of integrated optoelectronic devices in silicon-on-insulator (SOI) platform has been taken very seriously and rightfully considered to be an excellent technological solution for ever increasing demand of high speed communication. Though, the advancement of silicon photonics is primarily focused to solve the interconnect bottleneck in electronic industry, it is also being explored for other important application areas such as spectroscopy, optical storage, specialized signal processing, medical diagnosis, sensing, etc. This thesis demonstrates an integrated optical microring resonator capable of sensing cladding analytes with wide range of refractive indices - which can be considered as a technological step forward for the fabrication of CMOS compatible and packageable Lab-on-Chip (LoC) for various sensing applications. The research motivation including literature review, set of objectives and thesis organization have been presented in this introductory chapter.

### 1.1 Motivation and Literature Review

The phenomenal progress of electronics industry in recent years is attributed to the development of silicon fabrication technology especially with CMOS process flow. As the transistor size is scaling down, its speed and integration density are following Moore's law [2]. However, the maximum speed achieved by the logic gates can not be utilized by the processors/memories due the interconnect bottleneck [3]. The interconnect delay is significantly higher when the metal interconnects from device to device or chip to chip are scaled down to submicron regime [4]. At higher operating frequencies, the down scaled metal lines exhibit higher resistance and capacitance which in turn increases the RC time delay; resulting into an over-all limitation in microprocessor speed. In addition to that the power dissipation is exponentially increased. However, it is identified that

the interconnect delay can be resolved by replacing the metal interconnects with optical interconnects. The basic requirements for a good optical interconnect are: (i) it should be compatible with the existing electronics fabrication technology, (ii) energy efficient and high speed optoelectronic conversion and (iii) higher integration density [5, 6]. These demands push towards a default solution to use silicon as a material platform for photonics circuits too. Fortunately, silicon material is transparent to the IR & MIR wavelengths ( $1.1 \mu\text{m} < \lambda < 6.7 \mu\text{m}$ ) which are used for optical communications. In addition to that, higher refractive index contrast between silicon (as core) and silicon dioxide (as cladding) offers compact optical devices which can be integrated with electronics in the same device layer using the same process flow as for CMOS electronics.

The first integrated silicon photonic circuit was demonstrated in 1985 with an epitaxially grown silicon core and a heavily doped silicon substrate as cladding [1]. The refractive index difference between core and cladding was about  $\sim 10^{-2}$  and hence the waveguide cross-section of this photonic circuit was relatively large  $\sim 10 \mu\text{m}$ . Moreover, the propagation loss for this first silicon waveguide was measured to be very high ( $\sim 15 \text{ dB/cm}$ ) due to heavily doped cladding layer. However, with the introduction of silicon-on-insulator (SOI) substrate in late 1990s and its commercial availability with desired device layer thickness, silicon waveguide cross-sections could be scaled down to submicron regimes [7]. Commercially available optical quality crystalline SOI substrate consists of a thick ( $\sim 500 \mu\text{m}$ ) silicon handle substrate, buried oxide (BOX) layer ( $\sim 1 - 3 \mu\text{m}$ ) and a thin ( $\sim 250 \text{ nm}$ ) device layer. The photonic structures are now defined on the high index ( $\sim 3.5$ ) silicon device layer with lower index ( $\sim 1.5$ ) BOX as bottom cladding. The higher refractive index difference ( $\sim 2$ ) between the core silicon layer and cladding BOX layer facilitates the fabrication of ultra-small integrated optical devices. However, as the integrated optical device dimensions are down scaled, the effect of fabrication induced error become significant. Especially, sidewall roughness by dry etching of silicon contributes to a higher propagation loss due to scattering as the electric field intensity at the sidewalls is relatively higher in smaller waveguides compared to large cross-section waveguides [8]. In order to reduce propagation loss due to sidewall surface roughness, various techniques such as oxidation of fabricated waveguide, anisotropic wet etching, waveguide definition by electron beam lithography, surface trimming etc. were introduced. It has been observed that surface roughness can

be effectively reduced by high temperature oxidation [9, 10, 11]. The problems associated with this solution for roughness reduction are that this oxidation process consumes extra silicon and it introduces stress [12], causing birefringence in the waveguide. The scattering loss can also be reduced by either surface encapsulation with SiN<sub>x</sub> [13], or high-temperature annealing with hydrogen ambiance [13, 14] in which the surface mobility of silicon atoms is enhanced so that those migrating atoms can smoothen out the surface roughness [13]. However, these methods involve harsh process conditions, like high temperature, and more importantly, they are not selective, which means that some other components that are not supposed to be processed at the same time on the same chip will be affected simultaneously, especially for chips with high density of integration. One novel solution is to use self-perfection by liquefaction (SPEL). A XeCl excimer laser with 308 nm wavelength and 20 ns pulse duration is applied to melt the surface layer of the waveguide selectively, which results in smooth sidewall upon resolidification [15]. Based on this method, reduction of roughness from 13 to 3 nm and roughness-induced propagation loss from 53 to 3 dB/cm have been reported. Another method introduced for low loss waveguide was the structural modification of the waveguide [16, 17]. Here the waveguide is relatively wider ( $\sim 2 \mu\text{m}$ ) and shallow etched (etch depth  $\sim 0.05 \mu\text{m}$ ). Thus the electric field intensity at the sidewalls are reduced significantly to achieve lower propagation loss. However, the shallow etched waveguides are not suitable for sharp bends, which is a key requirement for compact device design. In order to make compact bends the wider waveguide is adiabatically tapered to form deeply etched submicron wide waveguide. The minimum propagation loss achieved for this waveguide is  $\sim 0.026 \text{ dB/cm}$  [17] However, the major technological development to achieve low loss waveguides was the optimization of lithography and dry etching process [18, 19].

Low-loss single-mode silicon waveguides made a huge impact in silicon photonics by establishing energy efficient and high speed optical links between the electronic processor chips [20, 21, 22, 23]. Figure 1.1 shows the schematic representation of a chip-to-chip communication using optical interconnects with silicon photonic devices [20]. Photographic/SEM images of the critical parts of optical interconnect are shown in the inset. The electronic data stream from the microprocessor chip is encoded to four optical channels (wavelengths  $\lambda_1$  to  $\lambda_4$ ) by means of electro-optic modulators. Here,

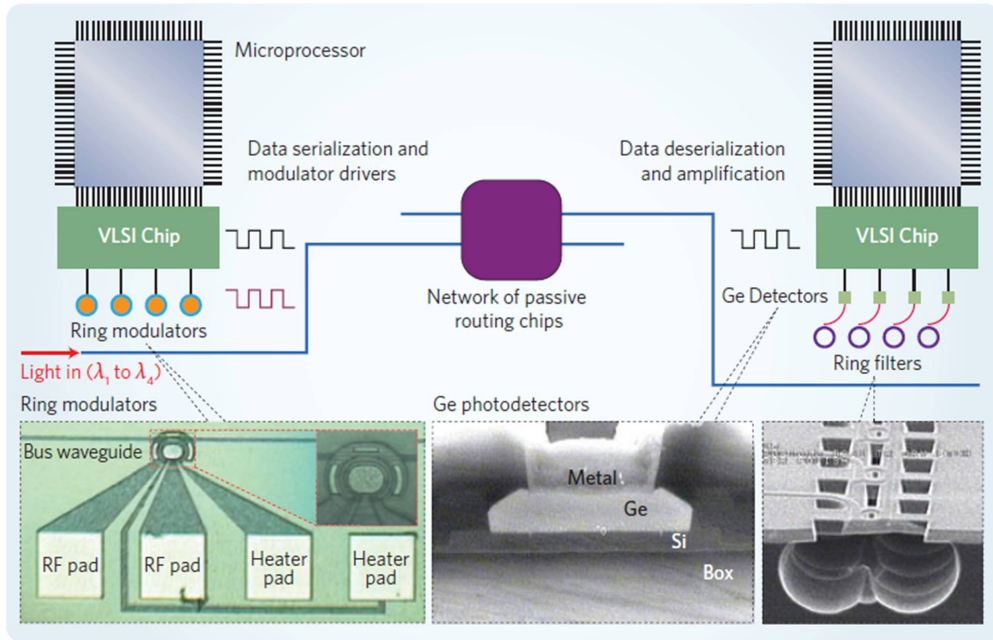


Figure 1.1: Schematic representation of chip to chip communication using silicon photonics. Photographic/SEM images of important regions of optical interconnect are shown as inset [20].

silicon ring resonators with an active p-n doped (across the waveguide) region are used as electro-optic modulators. These optical signals are multiplexed to a single optical waveguide and routed to the destination through passive optical network. At the receiver end, the optical signals are demultiplexed again using ring resonators. In this scheme, the microring resonators are utilized for electro-optic modulation as well as wavelength filtering. Both the properties have been nicely exploited for on-chip high-speed optical modulation/demodulation. The filtered optical signals are fed to the microprocessor at the receiver end after converting the signal back to electronic domain by means of Germanium photodetectors. An interesting point to be noticed here is the utility of a silicon microring resonator as modulators as well as wavelength filters - multiple functionalities using the same configuration/component. This extends the prospect of silicon photonics to wider domains such as switching networks [24, 25, 26], optical storage [27, 28, 29], electro-optic logic circuits [30, 31, 32], spectrometers [33, 34] sensors [35, 36, 37] etc.

The success of CMOS compatible silicon photonics technology has prompted researchers to explore integrated optical devices/circuits or Lab-on-Chip (LoC) in SOI for various types of sensing applications [38, 39, 40, 41, 42]. Since measurement of

refractive index of a given material/analyte is the key for most sensing applications, many functional devices/components have been demonstrated for the same purpose. Some examples are microring resonator [43, 44, 45], photonic crystal [46, 47], DBR [48], Mach-Zehnder interferometer [49, 50], Young's interferometer [51], etc. Each of these devices is characteristically unique in terms of their designs, footprints and working principles. The microring resonator based devices/circuits are found to be the most promising as they can be designed to be very sensitive to cladding refractive index change and to have longer interaction lengths but with smaller footprints.

Schematic top view of a typical microring resonator in add-drop configuration is shown in Figure 3.1(a), where,  $E_i$  and  $E_p$ ,  $E_a$  and  $E_d$  are the electric field amplitudes at input, pass, add and drop ports, respectively.  $t_1$  and  $t_2$  are the self coupling coefficients at coupler 1 and 2, respectively; similarly  $k_1$  and  $k_2$  are the the cross-coupling coefficients at coupler 1 and 2, respectively. The transmission at the pass ( $T_p$ ) and drop ( $T_d$ )

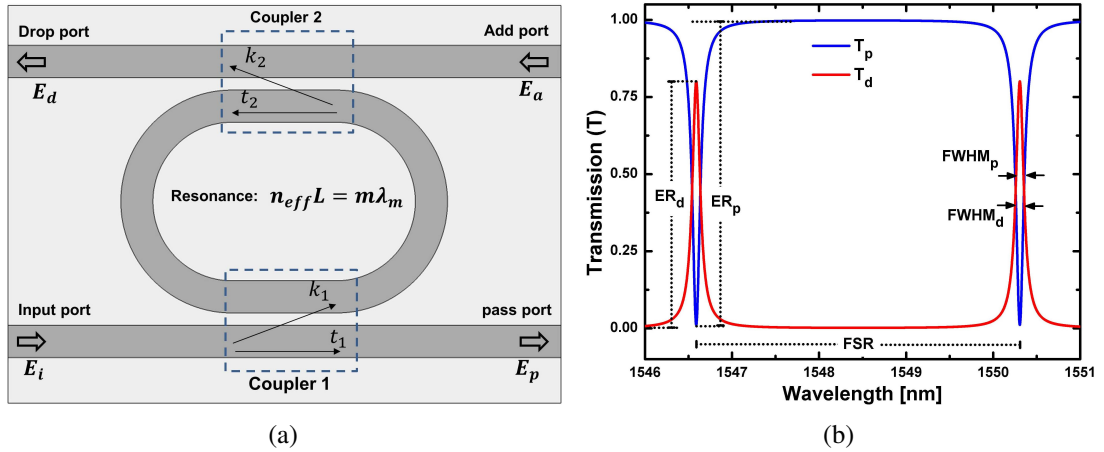


Figure 1.2: (a) Schematic top view of a microring resonator in add-drop configuration :  $E_i$ ,  $E_p$ ,  $E_a$  and  $E_d$  are the electric field amplitudes at input, pass, add and drop ports, respectively.  $t_1$  and  $t_2$  are the self coupling coefficients at the coupler 1 and 2, respectively.  $k_1$  and  $k_2$  are the cross-coupling coefficients at coupler 1 and 2, respectively.  $n_{eff}$  - effective index of the guided mode,  $L$  - ring perimeter,  $m$  - order of resonance,  $\lambda_m$  - resonant wavelength. (b) Typical transmission characteristics at the pass ( $T_p$ ) and drop ( $T_d$ ) ports of add-drop ring resonator:  $ER_{p/d}$  - extinction ratio at pass/drop port, FSR - free spectral range and  $FWHM_{p/d}$  - full width at half maxima at pass/drop port.

ports can be written as: [52]:

$$T_p = \frac{|E_p|^2}{|E_i|^2} = \frac{t_2^2 a^2 - 2t_1 t_2 a \cos(\theta) + t_1^2}{1 - 2t_1 t_2 a \cos(\theta) + (t_1 t_2 a)^2} \quad (1.1)$$

$$T_d = \frac{|E_d|^2}{|E_i|^2} = \frac{(1 - t_1^2)(1 - t_2^2)a}{1 - 2t_1 t_2 a \cos(\theta) + (t_1 t_2 a)^2} \quad (1.2)$$

where,  $a = e^{-\alpha L}$  is the round trip loss factor with a loss coefficient  $\alpha$ ,  $L$  is the perimeter of the ring,  $\theta = 2\pi n_{eff} L / \lambda$  is the round trip phase factor,  $n_{eff}$  is the effective index of the guided mode and  $\lambda$  is the wavelength of operation. The coupler sections are assumed to be loss-less ie,  $t_1^2 + k_1^2 = t_2^2 + k_2^2 = 1$ . Figure 3.1(b) shows typical transmission characteristics of a submicron photonic wire add-drop microring resonator plotted using Eqn. 1.1 and 1.2, where the ring parameters are considered to be  $L = 167 \mu\text{m}$ ,  $\alpha = 5 \text{ dB/cm}$ ,  $n_{eff} = 2.76$  and  $t_1 = t_2 = 0.96$  (for  $\lambda \sim 1550 \text{ nm}$ ). From the pass port transmission characteristics, it can be noticed that the output of certain wavelengths are much less than the input. The wavelengths with minimum  $T_p$  are said to be the resonant wavelength which satisfy the resonance condition  $n_{eff} L = m\lambda_m$  of the ring resonator, where  $m$  is integer number representing the order of resonance. From the transmission characteristics of drop port ( $T_d$ ), it is clear that the resonant wavelengths are dropped at the drop port using the coupler 2 (see Figure 3.1(b)). Similarly, the resonant wavelengths can be added to the pass port through coupler 1 and 2 when they are given to the add port, hence this ring resonator configuration is known as add-drop multiplexer. Since the resonant wavelengths are circulating inside the ring cavity multiple times by satisfying the constructive interference condition, the effective length of the resonator for the resonant wavelength can be very long. For example, in the case of a ring resonator sensor, in contrast to a simple straight waveguide, ring resonator interaction with the analyte is not estimated using the physical length of the resonator but with number of revolutions inside the ring and which would be indicated by the quality factor (Q-factor) of the resonator. The effective length ( $L_{eff}$ ) of a ring resonator can be related to its Q-factor as [42] :

$$L_{eff} = Q \frac{\lambda_m}{2\pi n_{eff}} \quad (1.3)$$

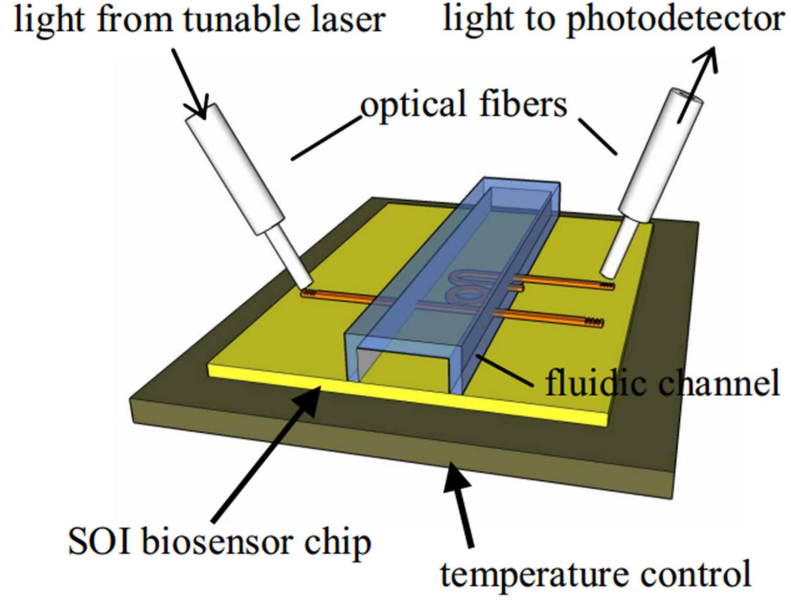


Figure 1.3: Schematic view of the measurement set-up for a ring resonator based biosensor [43].

where Q-factor is defined as:

$$\text{Q-factor} = \frac{\lambda_m}{FWHM} \quad (1.4)$$

Thus, silicon ring resonators of Q-factor  $\sim 10^6$  with a ring perimeter of length  $\sim 50 - 100 \mu\text{m}$  is equivalent to a straight waveguide of  $\sim 10 \text{ cm}$  long [53].

Figure 1.3 shows the schematic view of a compact microring biosensor which was one of the landmark research demonstrations of ring resonator based refractive index sensor in SOI substrate [43]. The ring resonator chip was fabricated with standard CMOS process and the optical chip is placed on a temperature controlled platform. A microfluidic channel is built over the sensing region to supply the analyte solution. The flow rate of the solution is controlled with the help of a peristaltic pump. Optical fibers are coupled to the sensor input and output with a pair of grating couplers. The sensitivity ( $S$ ) and resolution/limit of detection (LOD) of this configuration are measured to be  $66 \text{ nm/RIU}$  and  $10^{-5}$ , respectively. These parameters are considered to be the figure of merits which describe the quality of a sensor [54]. In ring resonator based sensors, the sensing is mainly performed by measuring the shift of a given order of resonance wavelength. Therefore,  $S$  is defined as the shift in resonance wavelength per refractive index unit (RIU) change in the cladding. The LOD is minimum detectable refractive

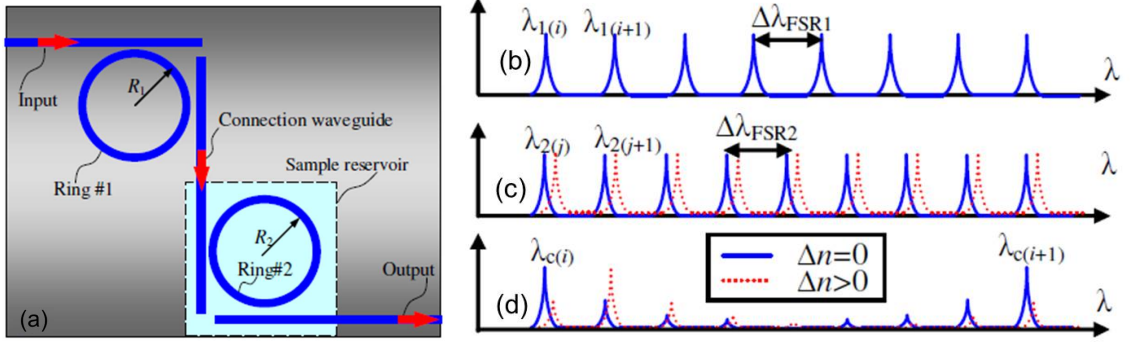


Figure 1.4: (a) Schematic top view of cascaded ring resonator sensor based on Vernier effect. Schematic spectral responses of (a) Ring# 1, (b) Ring# 2 and (c) cascaded combination of Ring# 1 and Ring# 2: blue and red lines represent the sensor response with and without analyte, respectively [57].

index change and is given by  $\lambda_m/(Q \times S)$  [55]. Since Q-factor can be increased by decreasing waveguide losses as well as by increasing the cavity volume; there will be scopes for ever to improve the value of LOD with the advancement of technology for low-loss waveguides. In general, the value of  $S$  is limited by the evanescent field overlap with the cladding material of a conventional waveguide ring resonator. Rodriguez et al. [56] could enhance the light matter interaction by fabricating the ring resonator with porous silicon waveguides and reported an improved value of  $S$  (380 nm/RIU), but higher waveguide losses results into a lower Q-value (10,000). It has been proposed that the value of  $S$  can be increased to a record level ( $\sim 3 \times 10^5$  nm/RIU) by using Vernier effect [57]. Figure 1.4(a) shows the schematic top view of the device with two cascaded ring resonators of slightly different radius. The difference in radius results in an unequal free spectral range (FSR) of the ring resonators. Figure 1.4(b)-(d) show the schematic spectral responses of the ring resonators: (a) for Ring# 1 with  $\text{FSR} = \Delta\lambda_{FSR1}$ , (b) for Ring # 2 with  $\text{FSR} = \Delta\lambda_{FSR2}$  and (c) for cascaded combination of Ring# 1 and Ring# 2 with  $\text{FSR} = (M - 1)\Delta\lambda_{FSR1}$ , where  $M$  is defined as:

$$M = \frac{\Delta\lambda_{FSR1}}{\Delta\lambda_{FSR1} - \Delta\lambda_{FSR2}} \quad (1.5)$$

Thus, a slight change in cladding refractive index ( $\Delta n > 0$ ), of Ring#2 shifts its resonance spectrum (in Figure 1.4(b)(c) red dotted line represent the shifted spectrum) which results in a large shift in the cascaded ring response (see the Figure 1.4(b)(d)).



So the  $S$  is improved by  $M$  times than that of Ring #1. In this device the minimum wavelength shift is discretized (shift is not continuous as a function of cladding refractive index) due to the inherent limitation of the Vernier effect (least count). This in fact limits the LOD of the sensor device. Nevertheless, with a slight modification in the ring resonator structure, the same principle has been utilized for the experimental demonstration of sensor with  $S > 2000$  nm/RIU and LOD of  $8.6 \times 10^{-6}$  [58]. However, fabrication requirement is observed to be very stringent as a slight difference in waveguide cross-sections of either of two cascaded ring resonators can change the response of the device to a large extent.

The slot waveguide based ring resonator was also found attractive because of direct interaction of analytes to the guided "air-mode" [59]. Very recently, a ring resonator designed with slot waveguides has been shown to be highly sensitive (1300 nm/RIU) to cladding index [55]. In slot waveguides, a major fraction of optical power associated with the guided mode lies outside the core region and it is highly dependent on the wavelength of operation. In this work, wavelength dependent loss is exploited to obtain V-shaped comb resonance spectrum centering at critically coupled wavelength (extinction ratio tends infinity). Since the loss factor is highly wavelength dependent, critically coupled wavelength stands out from the rest of the resonances at the transmission spectrum and which can be traced for refracting index sensing. However, this device could detect only a narrow range of refractive index, as the round-trip loss factor of ring degrades very fast (from 1 to 0) within a narrow range of cladding refractive index change ( $\Delta n_c \sim 0.2$ ). In this type of ring resonator design, smaller the FSR better is the LOD (unlike conventional ring resonator). However, the FSR can not be reduced by increasing the ring perimeter because of the inherent higher losses in slot waveguides. A vast variety of sensing techniques are proposed and demonstrated in SOI substrate over the years. Though most of them are unique in their design and performance, all these submicron waveguide devices suffer due to the poor input/output light coupling efficiency. Besides sensitivity and detection range of microring resonator based refractive index sensor, fiber-chip-fiber light couplings and/or integration of light source and photodetector is still treated as a major challenge as far as silicon photonics based Lab-on-chip is concerned.

There have been various approaches proposed and demonstrated for light coupling to the submicron silicon waveguides. Among them, widely accepted structures are grating couplers [60, 61, 62, 63] and inverse tapering [64, 65, 66, 67]. In grating coupler, the light from the fiber/waveguide is diffracted towards the waveguide/fiber with the help of a grating structure. In general, light from standard single mode fiber is positioned almost vertically  $\sim 80^\circ$  to the waveguide axis (see. Figure 1.5). The diffracted light from the grating region of  $10\ \mu\text{m}$  long and  $10\ \mu\text{m}$  wide with a grating periodicity  $\sim 600\ \text{nm}$  is collected by a laterally tapered (from the width of grating to the width of the submicron waveguide) 1D spot-size converter (SSC) of length  $\sim 100\ \mu\text{m}$  and fed light to silicon photonic wire waveguide. This structure is fabricated along with the waveguide using CMOS process and it does not require conventionally followed dicing and polishing which are often difficult. The higher alignment tolerance of the grating coupler makes it easy and impressive for optical characterizations on wafer (chip) level. Grating coupler can be used for characterizing optical circuit those are small or in between electronics circuits, as it can be probed similar to electronic devices. Also, it does not produce Fabry-Perot resonance that submerges the actual performance of the device due to high reflective end-facets as it is phase matched coupling. However,

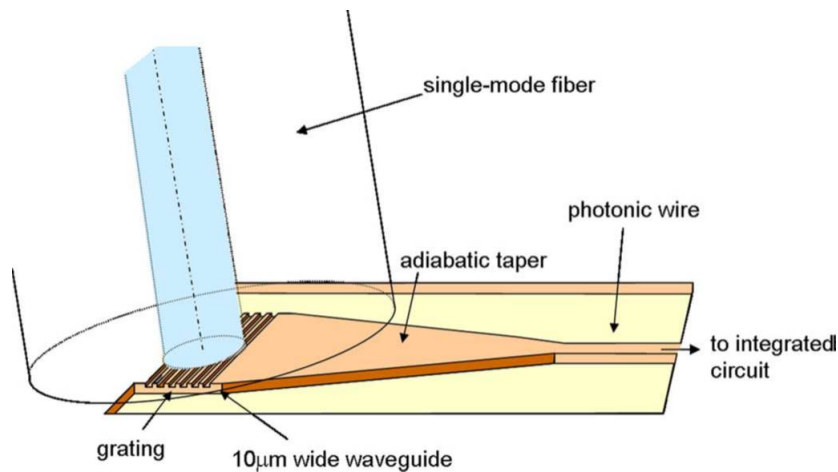


Figure 1.5: Schematic view of a grating coupler used for coupling light between single mode fiber and photonic wire waveguide in SOI substrates [61].

coupling loss, polarization dependency and bandwidth of operation are the drawbacks of grating coupler. Generally, grating coupler has been designed and fabricated for a particular polarization (TE or TM). As the fabrication tolerance of grating coupler is stringent, advanced lithographic techniques such as electron beam lithography or deep

UV lithography is used. Moreover the efficiency of grating coupler is directly proportional to the fabrication complexity. In order to improve the coupling efficiency of the grating coupler, one has to improve the overlap of scattered electric field to the mode profile of the single mode-fiber which is used to couple light in/out of the waveguide. To have better overlap, apodized gratings have to be fabricated. Again to avoid the substrate coupling (due other order of diffraction) metal coating has to be done at substrate layers, which adds to complication of the fabrication process of grating coupler [68].

An alternative structure used for light coupling from fiber to submicron waveguide is inverse tapering. The name inverse means that the waveguide mode field diameter (MFD) increases as the waveguide cross-section reduces due to lower mode confinement factor. This was introduced for silicon photonic waveguides by T Shoji et al in the year 2000 [64]. Figure 1.6(a) and (b) show the schematic and SEM image of a fabricated structure of inverse tapering respectively. In inversely tapered couplers, guided fundamental mode of submicron waveguide is adiabatically expanded by reducing the width of silicon waveguide and matches with the mode size of a larger waveguide (in this work polymer core) with a bulk refractive index which is nearly equal to silica waveguides. As the width of silicon waveguide reduces effective index contrast between core and cladding is reduced and hence the mode size is increased. When the mode size is comparable to the mode size of a larger waveguide with smaller refractive index, the taper section is terminated and the mode is evolved as the guided mode of the larger waveguide without additional transition loss. Generally, lensed fiber with MFD  $\sim 3 \mu\text{m}$  is used for coupling light in to inverse tapered structures. In comparison with grating couplers, the efficiency of the inverse taper structures is found to be better. The polarization dependency of inverse tapers is less and can be operated for wide range of wavelength. However, the fabrication of inverse taper structure is challenging as critical lithographic alignment is needed for defining second core with lower refractive index for an efficient mode matching. The alignment tolerance of the inverse tapered SSCs are found to be very stringent (1 dB tolerance  $< 500 \text{ nm}$ ). In addition to that, most of the reported inverse tapered waveguide structures are fabricated using polymer material and they are not thermally stable. Since, the fabrication of inverse taper structures are not compatible with CMOS process flow, these couplers are not yet included in multi project wafer program offered by IMEC or CEA-Leti foundries [70]. Though, the sili-

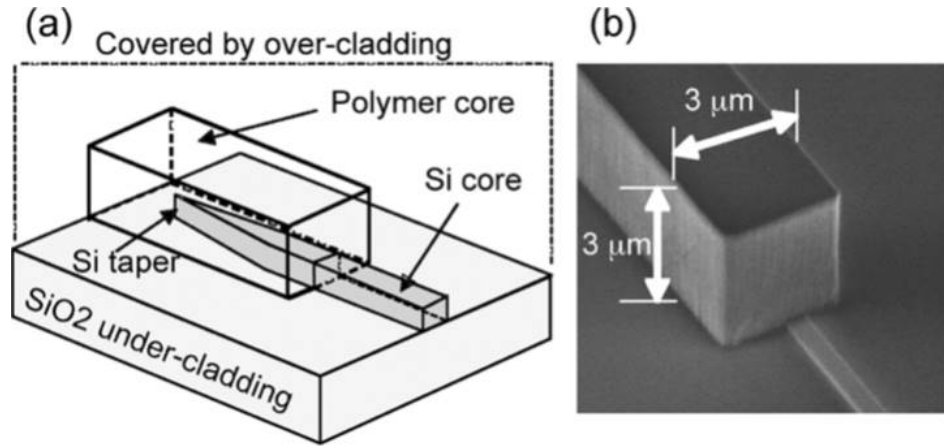


Figure 1.6: (a) Schematic view of an inverse taper structure and (b) SEM image of inverse taper junction region showing polymer waveguide and silicon photonic wire waveguide [69].

con photonics has grown to main stream photonic technology, the light coupling issue is still hindering the journey towards a packageable silicon photonics devices such as sensors.

Thus we understand from the above discussions that a microring resonator in SOI platform is an excellent candidate for sensor applications and its figures of merits can be improved by continued research. This thesis work was set to explore the critical design parameters of microring resonator and its on-chip integration process, leading to a simplified design for wide-range refractive index sensing of cladding materials. Finer details of research objectives are highlighted in the following section.

## 1.2 Research Objective

Over the years, numerous refractive index sensor designs based on microring resonators have been proposed and demonstrated in laboratory level. Many of the improved sensor performance (higher sensitivity and lower limit of detection) are achieved by design complexity and/or stringent fabrication requirements. However, all the silicon photonics based integrated optical sensors share common problems such as light coupling, spectral measurement based sensing, etc. Most of the microring resonator sensors are based on the shift of resonant wavelength in response to the analyte material. In this sensing scheme, high resolution spectrum analyzers are required for accurate sensing.

This in fact makes the detection very expensive as well as bulky as spectrum analyzer is externally connected. However, lately various research groups proposed and demonstrated sensing schemes with electronic interrogation where electric current or voltage is used as the detection probe. To make such devices commercially successful, a great deal of research and development have to be carried out further. The most challenging factor of silicon photonic devices is the fiber to chip light coupling and which is essential for device packaging. There were various approaches adapted to tackle this problem. Among those, grating coupler is one of the widely accepted methods as it complies with CMOS fabrication also it does not require any end facet preparation and it can be used for chip level testing of device at any part of the wafer. However, the problems associated with this component are the efficiency, polarization dependency and band limited operation. The best loss figure with linear grating structure is often  $\sim 5$  dB even with the cutting edge fabrication facilities at the foundry environment. Smart grating coupler structures are developed with loss figure  $< 1$  dB/facet but with apodized grating structures and metal coated mirror at the back surface. However, this requires additional stringent processing steps and which adds to the cost of device fabrication. The polarization dependency and bandwidth limitation of grating coupler still remain as challenges of this component. All these factors together keep the silicon photonic sensor devices far away from commercialization. To bridge the gap between the prototyping and commercialization, the sensing mechanism has to be simple, cheaper and reliable. Thus the research focus must be shifted towards achieving highly integrable ring resonator design for mass fabrication, cost-effective packaging solution, and energy efficient electronic interrogation for wide-range sensing of cladding analytes. This work was initiated with two-fold research objectives. Firstly, to investigate various waveguide design parameters to improve fiber-to-chip light coupling efficiency: both 2D spot-size converters for in-line fiber pigtailling and 1D spot-size converters for grating assisted out of plane fiber-optic coupling were taken into considerations. This part of the research is primarily aimed to achieve theoretical understanding and CMOS compatible fabrication technology development of micron to submicron waveguides and spot-size converters. Secondly, to demonstrate an integrated optical wide-range refractive index sensor using state-of-the-art fabrication and characterization facilities. This part is intended to verify theoretically and experimentally the performance of ring resonator in

terms of bus-ring coupling mechanism and choose a suitable coupling system such that the microring resonators can be used for the sensing of wide-range of cladding analytes with widely varying refractive indices.

### 1.3 Thesis Organization

The research work documented in this thesis is organized as follows:

In chapter 2, we have discussed the technology development from i-line (wavelength  $\sim 365$  nm) photolithography based micron sized waveguide cross-section to electron beam lithography based submicron waveguide cross-section. It starts with the theoretical analysis of waveguide cross-section dependent properties such as single mode guidance, dispersion, bend induced loss etc. In this section, we summarize the merits and demerits of silicon waveguides with micron and submicron sized waveguides. Then we discuss various fabrication techniques to achieve minimum feature size varying from micron to submicron regime. Finally, we discuss the interfacing (coupling) of various waveguides cross-sections in a single SOI substrate platform. In order to improve the coupling efficiency various techniques has been adopted and compared its performance.

In chapter 3, the design, fabrication and characterization of microring resonators with a fabrication friendly micron sized waveguides as well as fabrication stringent submicron sized waveguides are discussed. The chapter begins with the theory and working principle in general. Then we discuss the microring resonator design with micron sized and submicron sized silicon waveguides. This section also deals with the constrains introduced by the integration of spot-size converters (for efficient fiber to chip coupling) with the reduced cross-section waveguides. A solution to get rid of this constraints has also been discussed. At the end, merits and demerits of micro-ring resonator with micron as well as submicron sized cross-sections are compared for the realization of refractive index sensing. In chapter 4, we discuss the demonstration of a wide range refractive index sensor using dispersion enhanced critically coupled microring resonators. Initial part of the chapter gives a detailed theoretical analysis of the dispersion characteristics and cladding dependent properties of the directional coupler which is the key factor of sensor design. Then, we propose a novel microring resonator

design with a dispersive directional coupler for the demonstration of wide range refractive index sensor. We discuss the device fabrication and testing at the end with a detailed analysis of the experimental performance of the sensor. In chapter 5, we summarize the research carried out within the scope of this thesis and possible extensions of the work has been briefly outlined in the outlook of thesis.

## CHAPTER 2

# Microns to Submicron Waveguides: Design, Fabrication and Characterizations

Waveguide is the basic building block for integrated optics and hence for silicon photonics devices in SOI substrate. Various on-chip performances like improvement in light coupling efficiency, reduction in bending loss, control in evanescent field strength, polarization rotation/filtering, dispersion engineering, etc. are simply achieved by varying waveguide cross-sectional geometry and dimensions.

In this chapter, we discuss theoretical and technological aspects of SOI optical waveguides of cross-sections (and geometry) varying from microns to submicron scale and spot-size converters to improve the efficiency of light coupling to integrated optical submicron silicon waveguides. Section 2.1 gives a theoretical understanding of cross-section dependent waveguide properties such as single mode guidance, dispersion, birefringence, fabrication tolerance, bend induced loss etc. This study gives an insight to the choice of waveguide cross-sections depending on the application of interest. In section 2.2, we discuss various CMOS compatible fabrication approaches to achieve monolithic integration of various waveguide cross-sections and the modelling of the experimentally obtained waveguide structures. The proposed fabrication technique helps local modification of waveguide core by 2D physical trimming and thus facilitating to obtain submicron waveguide widths beyond the diffraction limit of photolithography process. We have discussed various technological approaches to develop adiabatic spot size converters for efficient light coupling from standard single mode fiber to submicron silicon waveguides in section 2.3. This section also includes the optimization (both design and fabrication parameters) of longer ( $\sim 5$  mm) silicon photonic wire waveguides in submicron device layer substrate using a stitching error-free electron beam patterning technique.



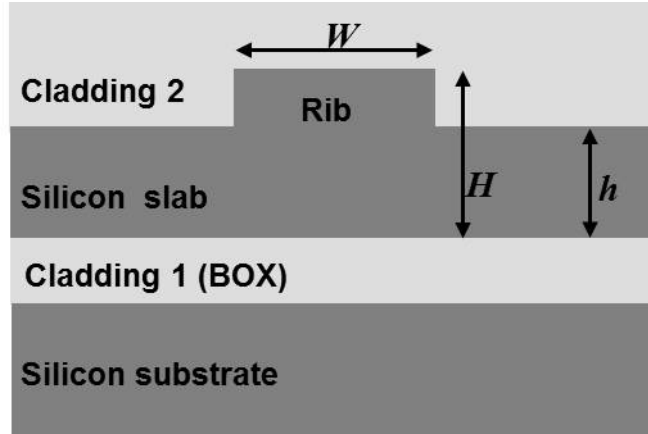


Figure 2.1: Schematic cross-sectional view of a typical optical waveguide geometry in SOI substrate: BOX - buried oxide,  $W$  - waveguide width,  $H$  - rib height and  $h$  - slab height.

## 2.1 Waveguide Design

A generic cross-section view of a silicon waveguide in SOI substrate is shown in Figure 2.1. Ideally, for an efficient integrated optic application, easier design criteria for single-mode guidance, birefringence free, non-dispersive, minimum bend induced loss, minimum propagation (scattering) loss and higher input/output light coupling efficiency with standard single-mode fibers (SMFs). However, achieving all these properties simultaneously is challenging or nearly impossible. For example, in order to achieve compact integrated optical devices with smaller bend radius; core-cladding index difference should be high enough such that the guided mode is tightly confined within the core. As the index contrast is high, the waveguide cross-section has to be small enough to make the waveguide single-mode at a given range of operating wavelengths. However, this results in the reduction of effective index of the guided mode which again controls the minimum bend radius achieved. Also, the smaller cross-section makes the waveguide highly wavelength dependent (dispersive) as well as lossy. The waveguide loss in a SOI waveguide operating at  $\lambda \sim 1550$  nm) is attributed to the interaction of guided mode with the side-wall roughness. In order to control the scattering loss, the waveguide aspect ratio ( $W/H$ ) can be varied, but this makes the waveguide birefringent. So, properly scaling the values of waveguide width ( $W$ ), rib height ( $H$ ) and slab height ( $h$ ) of silicon waveguide (2.1), one can design a single mode waveguide depending on the applications. Generally, large cross-section rib waveguides with  $W \sim 5$   $\mu\text{m}$ ,

$H \sim 5 \mu\text{m}$  and  $h \sim 4 \mu\text{m}$  are used for dispersion free and polarization independent photonic circuits [71, 72]. Even larger waveguide structures are used for efficient chip to fiber light coupling[73]. However, large cross section single-mode silicon waveguide structures cannot be used for the fabrication of compact devices such as ring resonator, DBR etc. Devices with  $\sim 2 \mu\text{m}$  waveguide width/height have been proposed for highly manufacturable photonics transceiver solutions [20]. They are moderately dispersion free and polarization independent. Commercially available lensed fiber with mode field diameter  $\sim 3 \mu\text{m}$  can be efficiently used for coupling light in to the micron sized waveguides. This  $2 \mu\text{m}$  waveguide also found to be useful for moderately compact bend (radius  $\sim 100 \mu\text{m}$ ) structures [20]. Silicon photonic wire waveguide with sub-micron cross-section ( $W \sim 0.5 \mu\text{m}$ ,  $H \sim 0.25 \mu\text{m}$  and  $h \sim 0 \mu\text{m}$ ) are invariably used for the demonstration of ultra compact (bend radius  $\sim 0.5 - 5 \mu\text{m}$ ) integrated optic devices [8, 74, 75, 76, 77]. However, the wavelength/polarization dependency of the waveguide are the major limitation of this cross-section. In addition to that light coupling to sub-micron photonic wire dimension is difficult as compared to large cross-section silicon waveguides. To study the cross-section dependent waveguide properties, we have categorized the large cross section rib waveguide (LCRW) for  $5 \mu\text{m}$  device layer thickness ( $H = 5 \mu\text{m}$ ), medium or reduced cross-section rib waveguide (RCRW) for  $2 \mu\text{m}$  device layer thickness ( $H = 2 \mu\text{m}$ ) and sub-micron photonic wire waveguide (PhWW) for  $0.25 \mu\text{m}$  device layer thickness ( $H = 0.25 \mu\text{m}$ ), respectively..

### 2.1.1 Condition for Single-Mode Guidance

Single-mode waveguides (assumed for operating wavelength  $\lambda \sim 1550 \text{ nm}$ ) are preferred to minimize loss and inter-modal dispersion. Though the typical length of waveguides used in integrated optics and/or on-chip optical interconnect devices is much much smaller than the optical fibers used for long-haul and/or short-haul communication systems, inter modal dispersion plays a vital role at high speed optical interconnect devices. Particularly in resonant structures such as ring resonators, Fabry-Perot cavities, the existence of higher order modes makes additional resonant peaks which is undesirable. Thus, single-mode guidance is a necessary condition for most of integrated optical functions. A waveguide with higher relative refractive index difference  $\Delta \equiv \frac{n_1^2 - n_2^2}{2n_1^2}$  between

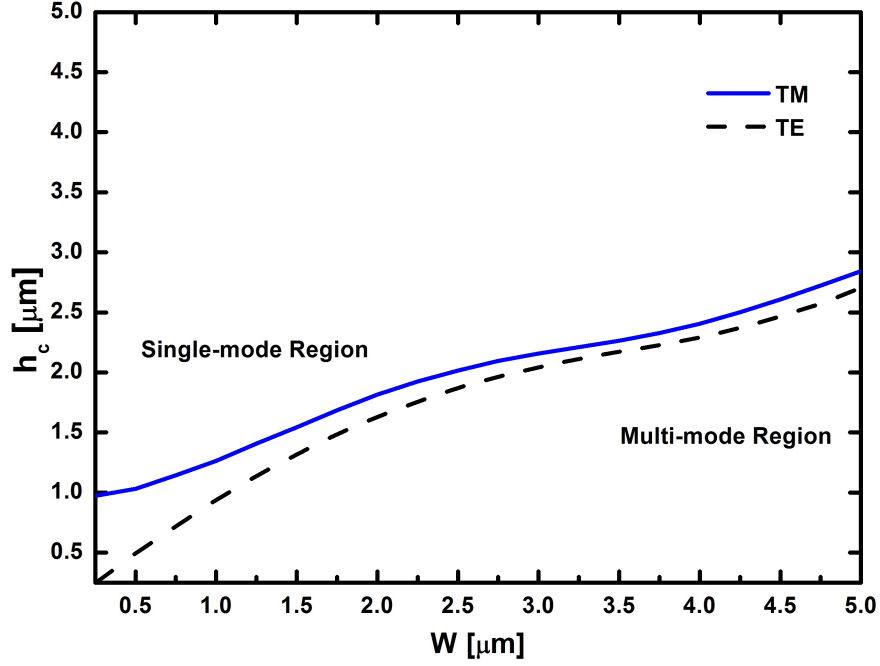


Figure 2.2: Calculated values slab height cut-off ( $h_c$ ) has been plotted as function  $W$  for  $5 \mu\text{m}$  waveguide ( $H = 5 \mu\text{m}$ ). Area above blue and red lines represents the single mode regions for TM and TE polarization respectively. Bottom and top claddings are considered to be BOX and air, respectively. Calculation are carried out for  $\lambda = 1550 \text{ nm}$ .

core (index  $n_1$ ) and cladding (index  $n_2$ ) limits the waveguide cross-section to be very small to satisfy single-mode guiding condition. Silicon waveguide with  $\Delta \sim 0.41$  (considering silicon dioxide as cladding) restricts the single-mode waveguide cross-section to be  $\sim 0.1 \mu\text{m}^2$ . However, it is possible to design single-mode guidance for LCRWs with  $W = 5 \mu\text{m}$  and  $H = 5 \mu\text{m}$  show single mode propagation. Here, the difference compared to sub-micron single-mode structure is that the lateral claddings are not silicon dioxide but silicon slab with height slightly less than the core height. So, the effective refractive index difference between core and lateral cladding is less ( $\Delta \sim 0.001$ ) which facilitates a larger cross-section for single-mode propagation though absolute refractive index of the core is high. The  $h$  of the waveguide is designed such that higher order modes excited in core region is leaked through the lateral cladding (silicon slabs) whereas slab remains forbidden region for fundamental mode. Consequently, the choice  $h$  of the waveguide is not only important for making structure single mode, but also for controlling waveguide properties such as propagation loss, bend induced loss, birefringence, etc. The value of  $h$  is especially very important in the case of  $5 \mu\text{m}$  and  $2 \mu\text{m}$  waveguides as the silicon slab regions decide the lateral confinement of the guided

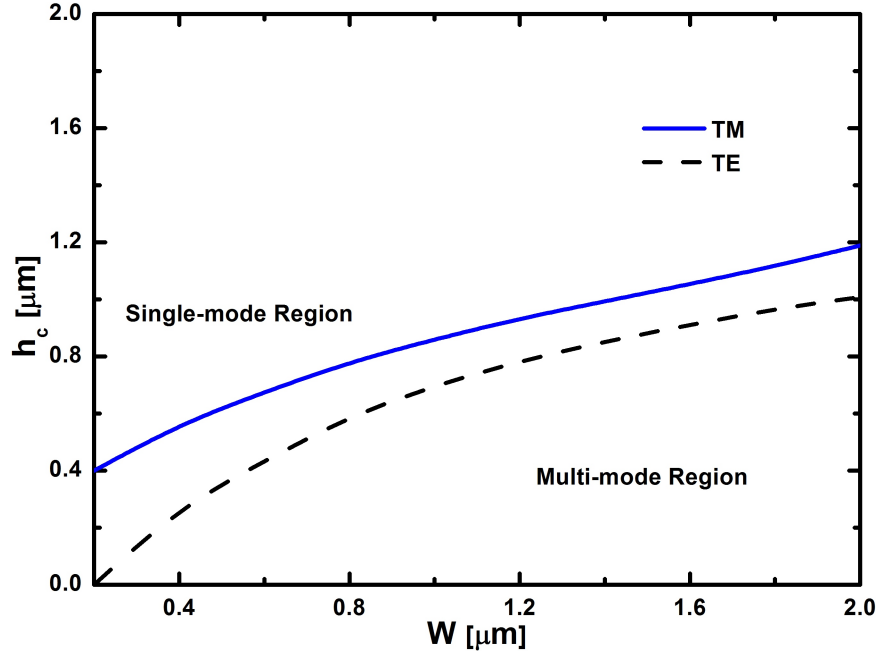


Figure 2.3: Calculated values slab height cut-off ( $h_c$ ) as function  $W$  for  $5 \mu\text{m}$  device layer thickness ( $H = 5 \mu\text{m}$ ). Area above blue and red lines represents the single mode regions for TM and TE polarization respectively. Bottom and top claddings are considered to be BOX and air, respectively. Calculation are carried out for  $\lambda = 1550 \text{ nm}$ .

mode. Figure 2.2 shows the slab height cut-off ( $h_c$ ) values as a function of  $W$  for single-mode propagation of  $5 \mu\text{m}$  device layer thickness. Bottom and top cladding are assumed to be BOX (refractive index  $\sim 1.44$ ) and air (refractive index  $\sim 1$  respectively). The  $h_c$  values have been calculated using Lumerical - MODE Solutions simulation tool. They are defined as the cut-off values of  $h$  at which the effective indices of the first order mode in the core (rib) region and the fundamental mode in the slab region are equal for the respective polarization. The calculations are shown for both TE-like and TM-like modes. In general, the TE-like guided modes have dominant electric field component parallel to the BOX layer interface, whereas, for TM/TM-like polarization, the major electric field component oriented perpendicular to the BOX-silicon interface. In Figure 2.2, blue line and black line represents the  $h_c$  values for TM and TE polarization respectively. Any value of  $h > h_c$  satisfy single-mode guidance condition for the respective polarization; however, the choice of  $h$  depends again the propagation loss, bend induced loss, overlap with input/output single-mode fiber profile, etc.

Similarly, Figure 2.3 shows the calculation of  $h_c$  as function  $W$  for  $2 \mu\text{m}$  waveguide. The region above blue line represents the single-mode domain for both polarization and

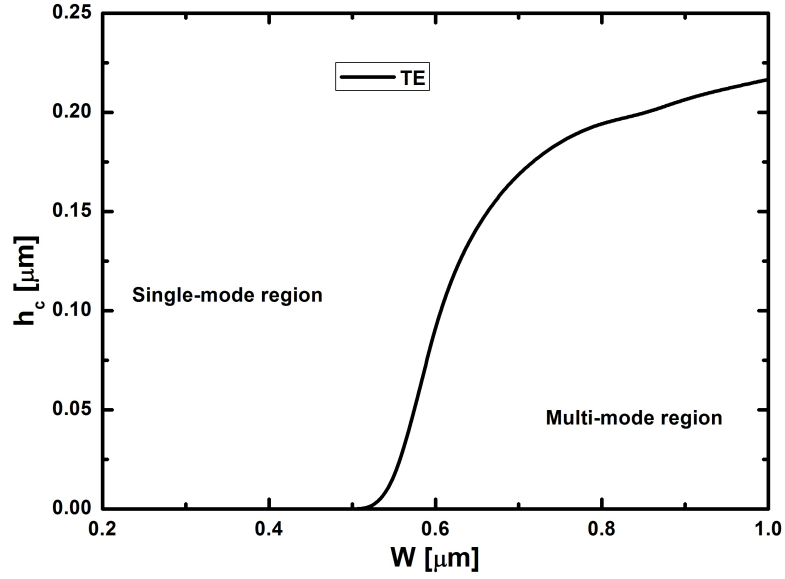


Figure 2.4: Calculation of slab height cut-off ( $h_c$ ) values for single mode guiding of  $2\ \mu\text{m}$  device layer thickness ( $H = 0.25\ \mu\text{m}$ ) as a function of  $W$ . Calculations are shown for TE polarization at  $\lambda = 1550\text{nm}$ .

the area between the blue and black line allows single-mode propagation only for TE polarization. The  $h_c$  values for  $2\ \mu\text{m}$  waveguide has been scaled down compared to  $5\ \mu\text{m}$  waveguides. This results in higher values of  $\Delta \sim 0.01$ , allowing more sharper waveguide bends.

Figure 2.4 shows the  $h_c$  calculation for  $0.25\ \mu\text{m}$  waveguide. In contrast to  $5\ \mu\text{m}$  and  $2\ \mu\text{m}$  waveguides, submicron waveguide modes are hybrid (quasi TE/TM) in nature. Since the aspect ratio ( $W/H$ ) of generally used submicron silicon waveguides are low, both  $E_x$  and  $E_y$  components of fundamental quasi TM mode are nearly equal. In such cases, fundamental TE mode is calculated to be the lowest order guided mode with highest effective index and both components of electric fields are confined inside the waveguide. However, it may happen that, for shallow etched waveguides  $E_x$  component of quasi TM mode is leaked out due to the fact that the effective index of the fundamental quasi TM mode is less than the effective index of the fundamental TE in the slab region. As a result, it is very difficult to represent the single-mode guiding condition as a function of  $W$  quasi TM mode in submicron waveguides. Though, sub-micron silicon waveguide does not require slab region to achieve single-mode guidance, it is still preferred for some special applications (especially to integrate active elements). In active photonic devices, the slab region is used for diffusion doping of n-type/p-type impuri-

ties [78]. In passive sub-micron photonic structures slab region is used for achieving lower propagation loss [16].

### 2.1.2 Birefringence

Birefringence ( $n_{eff}^{TE} - n_{eff}^{TM}$ ) of a waveguide is defined as the effective index difference between TE-like and TM-like guided modes. The source of birefringence can be either material or because of waveguide geometry or due to the combination of both. The material birefringence originates from the molecular structure of material and geometrical/structural birefringence is mostly due the asymmetric structure of the waveguide and often it can be due photoelastic effect [79]. Since silicon is a centro-symmetric material, material birefringence can be discarded. Waveguide structural birefringence can be significant if the waveguide structure is not symmetric in terms of geometry or cladding. Even for a waveguide core with equal width and height (square cross-sectional geometry), the geometrical birefringence can still be present if the cladding material (and/or stress) is not same all-around. Moreover, higher bulk refractive index of silicon core makes it extremely challenging to design a polarization independent (or birefringence free) waveguide. Especially, in sub-micron silicon waveguides birefringence is very large due the asymmetric geometry of the waveguide. However, photoelastic effect has been utilized to control the polarization sensitivity up to some extent in  $1 - 2 \mu\text{m}$  waveguides [80, 81, 82]. The effective way to control polarization independent silicon waveguides is to modify the waveguide cross-section [72, 83] Figure 2.5 shows the wavelength dependent birefringence comparison of various waveguide cross-sections in SOI substrate. We have used Salzberg and Villa model [84] for wavelength dependent refractive index of silicon. Bottom and top claddings of the waveguide are considered to be BOX ( $n_{sio2} = 1.4777$ ) and air ( $n_{air} = 1$ ), respectively. Solid line represents the birefringence of  $5 \mu\text{m}$  waveguide with a single-mode cross-section dimension,  $W = 5 \mu\text{m}$ ,  $H = 5 \mu\text{m}$  and  $h = 4 \mu\text{m}$ . Birefringence has been found to be as minimum as  $\sim 10^{-4}$ . dotted line represents the birefringence of  $2 \mu\text{m}$  waveguide with single-mode cross-section,  $W = 1.5 \mu\text{m}$ ,  $H = 2 \mu\text{m}$  and  $h = 1 \mu\text{m}$ . The birefringence value of  $2 \mu\text{m}$  is found to be  $\sim 10^{-3}$ . dashed line represents the birefringence of  $0.25 \mu\text{m}$  waveguide with single-mode cross-section,  $W = 0.5 \mu\text{m}$ ,  $H = 0.25 \mu\text{m}$  and

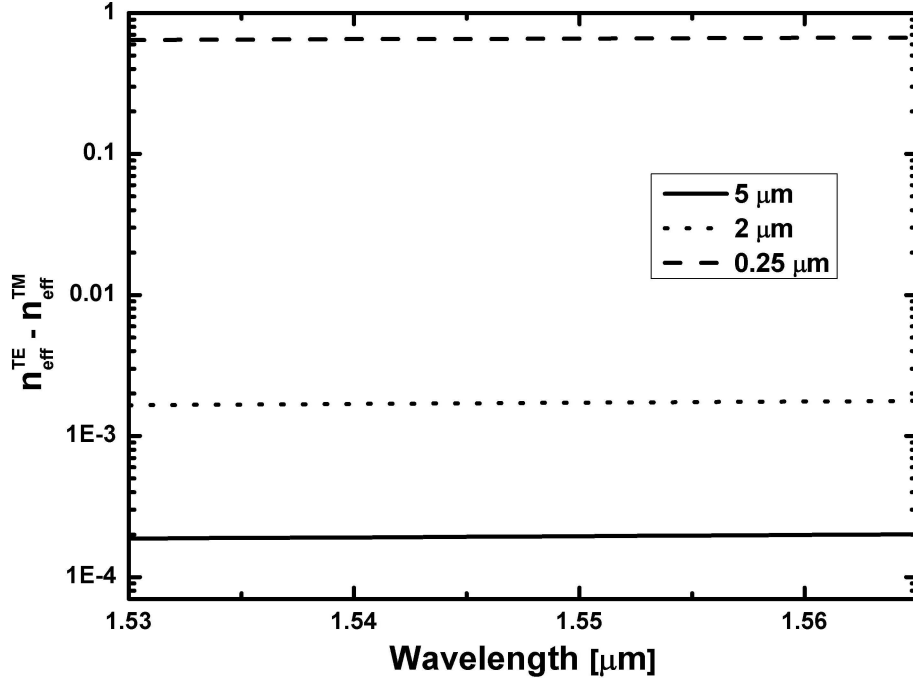


Figure 2.5: Structural birefringence comparison of various waveguide structures in SOI substrate. solid, dotted and dashed lines represent birefringence of LCRW ( $W = 5 \mu\text{m}$ ,  $H = 5 \mu\text{m}$  and  $h = 4 \mu\text{m}$ ), RCRW ( $W = 1.5 \mu\text{m}$ ,  $H = 2 \mu\text{m}$  and  $h = 1 \mu\text{m}$ ) and PhWW ( $W = 0.5 \mu\text{m}$ ,  $H = 0.25 \mu\text{m}$  and  $h = 0 \mu\text{m}$ ) respectively.

$h = 0 \mu\text{m}$ . The birefringence of the PhWW structure is found to be as high as  $\sim 1$ . This clearly shows that for the fabrication of a polarization independent waveguides, one should choose larger waveguide cross-section. However, structural birefringence of sub-micron waveguides can be reduced by modifying the waveguide cross-section to square geometry and with a symmetric cladding (silicon core is surrounded by silicon dioxide cladding). In such cases, though the waveguide behave as birefringence free ( $n_{eff}^{TM} = n_{eff}^{TE}$ ), coupled waveguide structures such as directional coupler shows polarization depend splitting ratio, because of boundary conditions of the waveguide [85].

### 2.1.3 Dispersion

Waveguide dispersion is observed due to wavelength dependent phase velocity/effective index of the guided modes of the waveguide. This can be classified in to either inter-modal dispersion or intra-modal dispersion. The inter-modal dispersion is due to phase

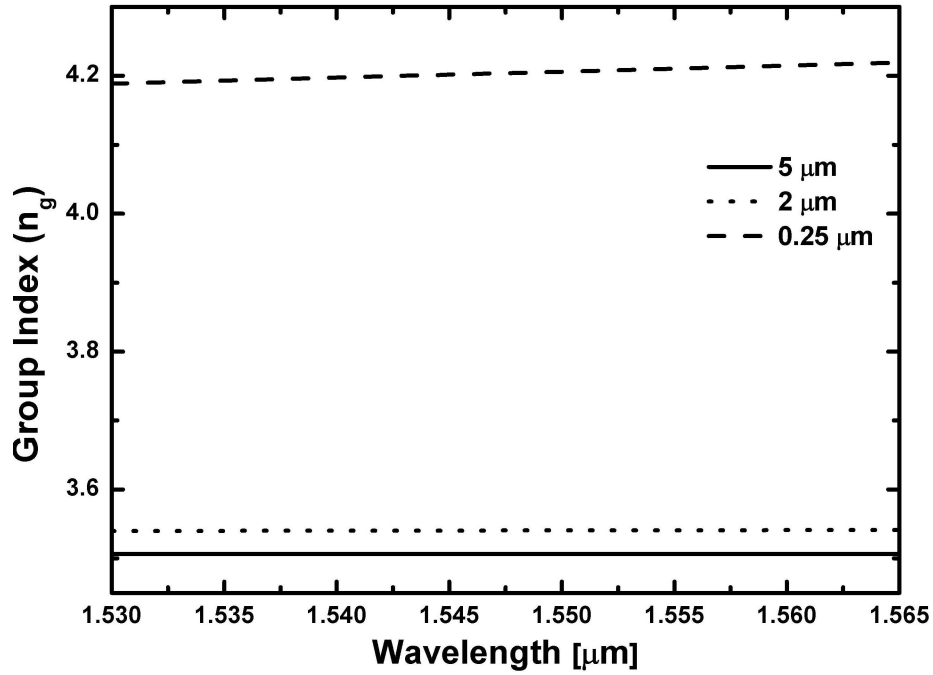


Figure 2.6: Structural dispersion comparison of various waveguide structures in SOI substrate. Solid, dotted and dashed lines represent calculated group indices of 5  $\mu\text{m}$  waveguide ( $W = 5 \mu\text{m}$ ,  $H = 5 \mu\text{m}$  and  $h = 4 \mu\text{m}$ ), 2  $\mu\text{m}$  waveguide ( $W = 1.5 \mu\text{m}$ ,  $H = 2 \mu\text{m}$  and  $h = 1 \mu\text{m}$ ) and 0.25  $\mu\text{m}$  waveguide ( $W = 0.5 \mu\text{m}$ ,  $H = 0.25 \mu\text{m}$  and  $h = 0 \mu\text{m}$ ). The calculations are shown for TE polarized light.

velocity difference between the guided modes. However, this can be completely suppressed by designing a single mode waveguide. The intra-modal dispersion can be either due to material dispersion where the refractive index of the material changes as a function of wavelength or due to the structural dispersion where the effective index of the guided mode changes as a function cross-sectional geometry though the bulk index remains constant. It is known from Salzberg and Villa refractive index model for silicon [84] that the material dispersion is not dominant as far as silicon waveguides are concerned. However, structural dispersion plays an important roll in silicon waveguide especially in sub-micron dimensions. Figure 2.11 shows the comparison of group index of various waveguide cross-sections generally used in silicon photonics. The cross-section dimensions of the waveguides were same as the birefringence calculation. Solid line represents the group index calculated for 5  $\mu\text{m}$  waveguide over C band of optical communication. Group index of this large cross-section waveguide is found to be minimum and approximately equal to the bulk refractive index of silicon. Also it remains constant through out the C+L band of optical communication. Dotted



line represents the group index of 2  $\mu\text{m}$  waveguide. Though, the group index of 2  $\mu\text{m}$  structure is slightly higher than 5  $\mu\text{m}$  structures, it remains constant through out larger wavelength range. In contrast, the group index (dashed line) of sub-micron structures are high ( $\sim 4.35$ ) and are highly dependent on the wavelength of operation. Therefore, large cross-section waveguides are preferred for silicon photonic devices which is meant to operate a broader wavelength range [72]

#### 2.1.4 Input/Output Coupling Loss

Silicon photonics research advancement is very rapid compared to any other photonics material platform. Such a high rapid impact of silicon photonics is due to the matured fabrication technology used silicon electronics. So the only delay appears to be in transferring the technology to photonics domain as well innovative ideas and designs. However, one of major concerns of silicon photonics which persists even today is input/output interfacing of integrated photonic circuits to standard single mode fiber (SMF) which is widely used for optical communication. High index contrast of sub-micron silicon waveguides with ultra high modal confinement enables the construction of very compact circuits. However, the high index contrast between the silicon core and silica claddings requires the use of a very small mode size to achieve a single-mode condition, and it makes difficult to efficiently couple light from a single-mode optical fiber. Various approaches such as grating coupler [60, 61], inverse tapering [64, 66], adiabatic taper [86], rib to strip converters [87], double stage taper [88], 2D taper [89, 90], etc. were proposed and demonstrated to address fiber to chip light coupling issue. Though, grating couplers and inverse tapers have been attractive for chip level testing of sub-micron photonic circuits in research labs, the commercial viability of most of the proposed techniques are still questionable due fabrication complexity and/or coupling efficiency. Consequently, the industry prefers micron scale waveguides for highly manufacturable photonic circuits [20]. Figure 2.7 show the mode mismatch loss of a silicon rib waveguide with standard single-mode fiber (SMF) and lensed fiber (LF) as function of  $W$ . The MFD of SMF and LF is assumed  $\sim 9.5 \mu\text{m}$  and  $3.2 \mu\text{m}$ , respectively. Fresnel reflection loss has not been considered for the calculation of mode mismatch loss as it can be minimized with a proper anti-reflection coating. In order to

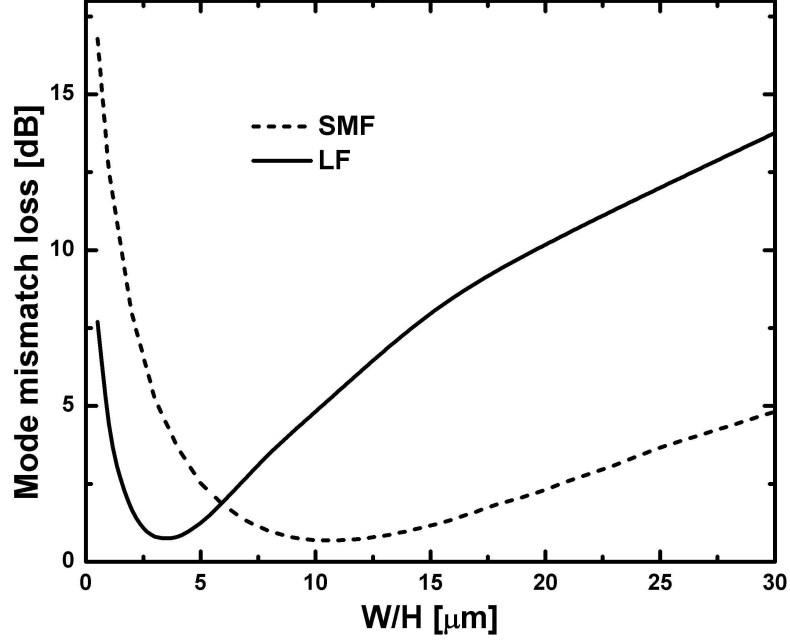


Figure 2.7: Calculated waveguide coupling loss (modal overlap in dB scale) as a function waveguide width ( $W$ ) = height ( $H$ ), where the input light is taken as the direct output from standard single-mode fiber (SMF) with mode-field diameter of  $\sim 9.5 \mu\text{m}$  (dashed line); and the focused lensed fiber (LF) output with spot-size diameter of  $3.2 \mu\text{m}$  (solid line), respectively. The calculations are carried out for TE-like waveguide mode excitation at  $\lambda = 1550 \text{ nm}$ . Also the slab height is taken as ( $h$ ) =  $0.7 \times H$ , ensuring single-mode guidance (checked up to  $W = H = 30 \mu\text{m}$ ).

maintain the waveguide to be single-mode throughout the width from  $1 \mu\text{m}$  to  $30 \mu\text{m}$ ,  $H$  is kept to be equal to  $W$  and  $h = 0.7 \times H$ . Though, MFD of the SMF is  $\sim 9.5 \mu\text{m}$ , the optimum mode matching happens at  $W = 20 \mu\text{m}$ ,  $H = 20 \mu\text{m}$  and  $h = 14 \mu\text{m}$ . Whereas, for LF with MFD of  $3.2 \mu\text{m}$ , the optimum coupling is obtained at  $W \sim 7 \mu\text{m}$ . This is due to the asymmetric rib waveguide mode profile relative to the fiber mode profile. In order to achieve perfect mode-matching (0-dB loss), both the waveguide and fiber mode profiles should be identical. Since, the fiber mode profile is circular, it is nearly impossible to have perfect mode-matching within the single mode regime, however, it can be optimized by modifying the waveguide cross-section. The mode mismatch loss between SMF (LF) and a waveguide of  $W = 0.5 \mu\text{m}$  is calculated to be  $\sim 17 \text{ dB}$  ( $\sim 8 \text{ dB}$ ). This ensures that the the LCRWs are the better choice for efficient light coupling from SMF to silicon waveguide.

### 2.1.5 Bend Induced Loss

We have seen that LCRWs are good for polarization independent, dispersion free and input/output light coupling. However, bend induced loss in the LCRW relative to RCRW/PhW is very high. The reason for the high loss is the small effective index difference between the core and lateral slab regions (cladding). This results in weak mode confinement and hence higher bend induced loss. However, one can enhance the mode confinement of LCRW by increasing the etch depth, but this results in higher propagation loss due to higher interaction of light with sidewall roughness. Also, higher etch depth may push the waveguide in to the multi-mode regime as we can see from figure 2.2. Figure 2.8 shows the comparison of mode profile of bend regions of LCRW ( $W = 5 \mu\text{m}$ ,  $H = 5 \mu\text{m}$  and  $h = 4 \mu\text{m}$ ) and RCRW ( $W = 1.5 \mu\text{m}$ ,  $H = 2 \mu\text{m}$  and  $h = 0.85 \mu\text{m}$ ).

The bend induced waveguide loss is simulated using Lumerical ModeSolution solver by mapping the index of the waveguide to cylindrical coordinate system. The radius considered for LCRW (2.8(a)) is  $20000 \mu\text{m}$  and for RCRW (2.8(b)) it is  $500 \mu\text{m}$ . The loss of LCRW with  $R = 20000$  is calculated to be  $\sim 50 \text{ dB/cm}$ , where as the loss of RCRW with  $R = 500 \mu$  is found to be  $\sim 9 \text{ dB/cm}$ . Figures 2.8(c) and 2.8(d) show the bend induced loss calculation as function of  $R$  for LCRW and RCRW respectively. Though the bend radius of RCRW is 40 times smaller than that of LCRW, the mode has been confined within the waveguide and the bend induced loss is significantly smaller than LCRW. PhWWs with core-cladding index contrast  $> 1$  are found to be suitable for compact integrated optical circuits. The bend loss for a PhWW ( $W = 0.5 \mu\text{m}$ ,  $H = 0.25 \mu\text{m}$  and  $h = 0 \mu\text{m}$ ) with bend radius  $\sim 1.5 \mu\text{m}$  is calculated to be  $< 0.5 \text{ dB/cm}$ .

### 2.1.6 Fabrication Tolerance in Device Response

One of the important requirements for waveguide devices with tightly confined guided modes is its tolerance to fabrication related uncertainties [91]. One of widely used compact integrated optics component is ring resonator using sub-micron waveguide cross-section on SOI substrate. For a ring resonator, the uncertainty/inhomogeneities in ring waveguide dimensions results into a shift in resonance wavelengths. Similarly, the un-

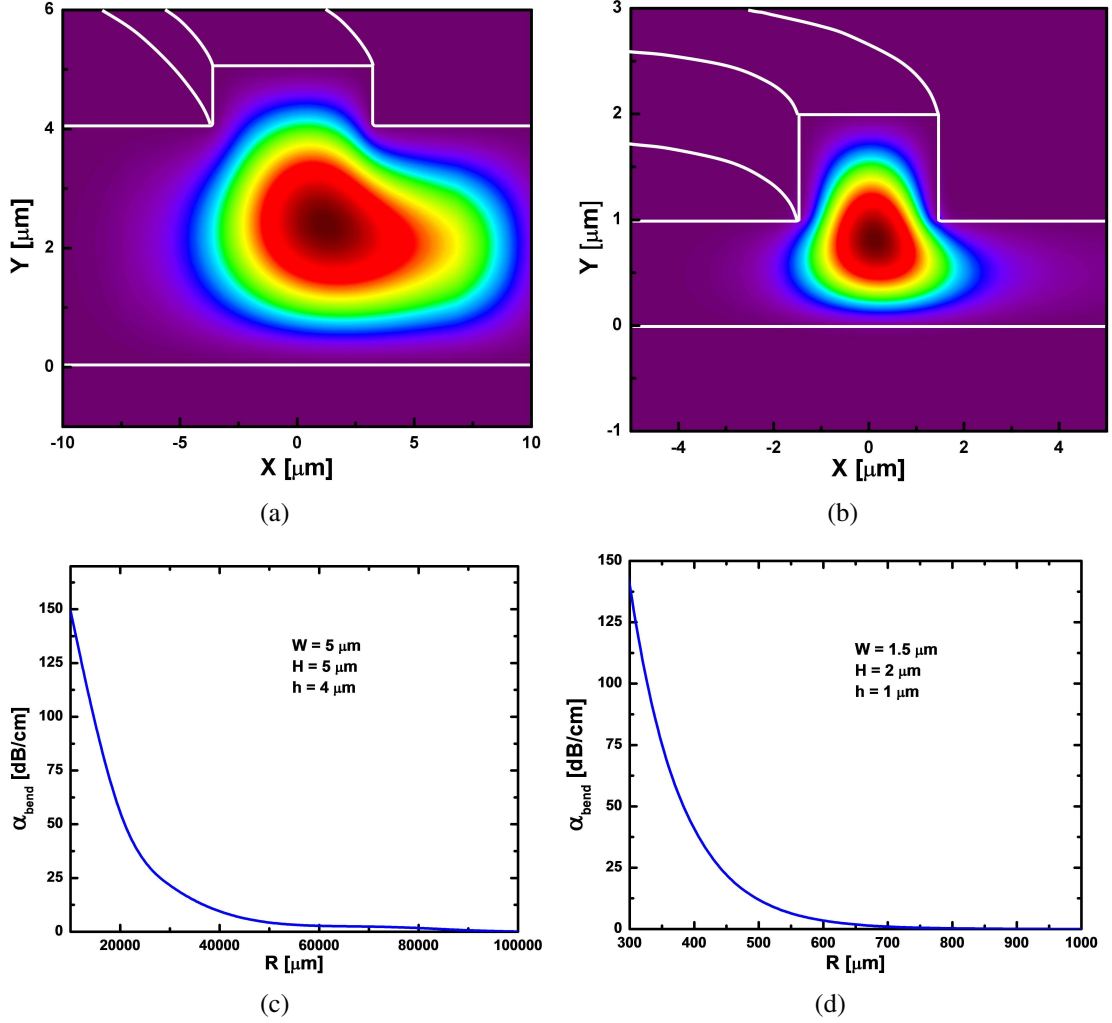


Figure 2.8: Calculated mode profiles for bend waveguides with (a) radius 10000  $\mu\text{m}$  for LCRW and (b) radius 500  $\mu\text{m}$  for RCRW. Both calculation has been carried out for TE polarization at  $\lambda \sim 1550$  nm . Calculated values of bend induced loss for (c) LCRW and (d) RCRW.

certainty/inhomogeneities in ring-bus coupled waveguides (directional coupler) results into a deviation in coupling strength (and hence Q-value), etc. Commonly, DCs are used for coupling light from bus waveguide to the ring resonator cavity [74, 75, 76, 77]. Conventionally, sub-micron waveguide structures are defined using either by deep UV photolithography or electron beam lithography on a photo/electron sensitive material coated on the SOI substrate. As a result, width ( $W$ ) is the waveguide parameter which more prone to fabrication error. In the case of DC, fabrication error is predominant due to diffraction limit or proximity effect as the coupled waveguides are defined very closely (separation  $\sim 100$  nm). In the coupler section, if the waveguide width is reduced/increased by  $\Delta W$ , the separation between the waveguides is increased/reduced

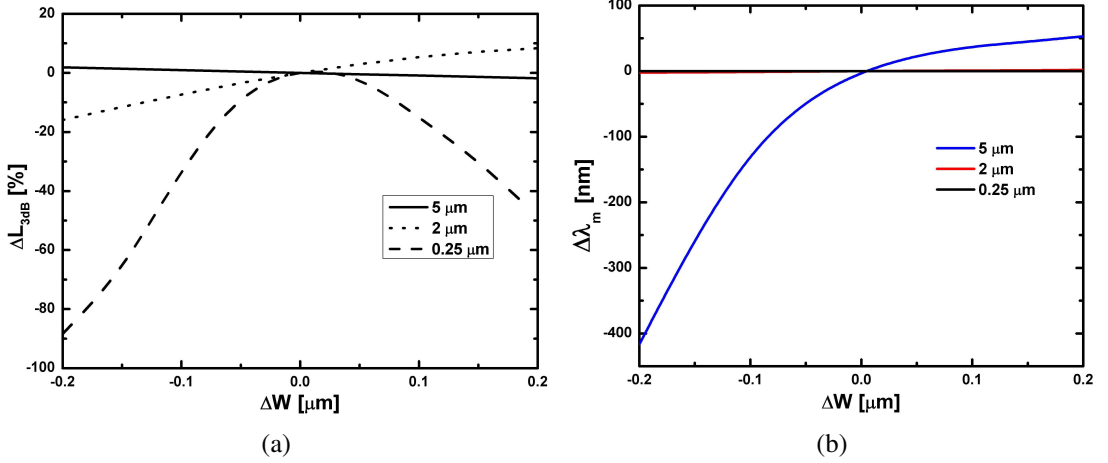


Figure 2.9: (a) Change in 3 dB length ( $\Delta L_{3dB}$ ) of directional coupler and (b) resonant wavelength shift ( $\Delta \lambda_m$ ) of ring resonator as a function of width variation ( $\Delta W$ ) due to fabrication error on 5  $\mu\text{m}$  device layer ( $W = 5 \mu\text{m}$ ,  $H = 5 \mu\text{m}$  and  $h = 4 \mu\text{m}$ ), 2  $\mu\text{m}$  device layer ( $W = 1.5 \mu\text{m}$ ,  $H = 2 \mu\text{m}$  and  $h = 1 \mu\text{m}$ ) and 0.25  $\mu\text{m}$  device layer ( $W = 0.5 \mu\text{m}$ ,  $H = 0.25 \mu\text{m}$  and  $h = 0 \mu\text{m}$ ) respectively.

by same amount  $\Delta W$ . This leads to a change in coupling efficiency of the DC. Figure 2.9(a) shows the 3 dB length variation ( $\Delta L_{3dB}$ ) of DC as a function of fabrication error for 5  $\mu\text{m}$ , 2  $\mu\text{m}$  and 0.25  $\mu\text{m}$  waveguide structures on SOI substrate. Where waveguide separation between the coupled waveguides are set to be 2  $\mu\text{m}$ , 1  $\mu\text{m}$  and 0.2  $\mu\text{m}$  for waveguides with  $H \sim 5 \mu\text{m}$ , 2  $\mu\text{m}$  and 0.25  $\mu\text{m}$  respectively. Horizontal axis of Figure 2.9(a) shows the variation ( $\Delta W$ ) from designed  $W$ . The designed waveguide cross-sections for 5  $\mu\text{m}$ , 2  $\mu\text{m}$ , and 0.25  $\mu\text{m}$  waveguides are same as the values used for birefringence calculation. Vertical axis shows the percentage of variation of 3 dB length relative to the designed value of the directional coupler. The variation in 3 dB length is defined as:

$$\Delta L_{3dB}[\%] = \frac{L_{3dB}^{cal.} - L_{3dB}^{des.}}{L_{3dB}^{des.}} \times 100 \quad (2.1)$$

Where  $L_{3dB}^{cal.}$  is the calculated 3dB length with corresponding fabrication error and  $L_{3dB}^{des.}$  is the 3 dB length for a designed directional coupler. The variation for LCRW directional coupler is found to be maximum variation  $\sim 1.8 \%$ ; for RCRW, maximum difference is found to be  $\sim -15 \%$ ; and for PhW the highest variation is calculated to be  $\sim 90 \%$  from the designed value. This calculation shows that the submicron PhWs are highly fabrication error sensitive compared to larger cross-section waveguides. Experimental investigation fabrication related uncertainties of submicron directional coupler

is discussed in detail in the next chapter.

Similarly, Figure 2.9(b) shows the resonant wavelength shift ( $\Delta\lambda_m$ ) of ring resonator as a function of  $\Delta W$  due to fabrication error, where  $\Delta\lambda_m$  is calculated by the following expression:

$$\Delta\lambda_m = \frac{\lambda_m}{n_g} \frac{dn_{eff}}{dW} \Delta W \quad (2.2)$$

where,  $n_{eff}$  and  $n_g$  are the effective index and group index of the waveguide, respectively. In the Figure, Black, red and blue lines represent  $\Delta\lambda_m$  of ring resonators on device layers 5  $\mu\text{m}$ , 2  $\mu\text{m}$  and 0.25  $\mu\text{m}$ , respectively. As it is clear from the Figure that, for device layers 5  $\mu\text{m}$  and 2  $\mu\text{m}$ ,  $\Delta\lambda_m$  is almost equal and remains constant as a function of  $\Delta W$ . Whereas, for 0.25  $\mu\text{m}$  device layer thickness,  $\Delta\lambda_m$  is highly dependent on  $\Delta W$  and which challenges the fabrication reproducibility of microring resonator in sub-micron device layer. The above discussions (based on numerical calculations) clearly depicts the need for different waveguide cross-sections for various applications. In the following section, we are going to discuss a novel method to integrate various waveguide cross-sections monolithically in a single SOI substrate. This technique found to be useful for the compensation of fabrication error as well as dispersion engineering.

## 2.2 Surface Trimmed Waveguides

The previous section gives an overview of cross-section dependent waveguide properties and it is observed that the optimum waveguide cross-section should be an application oriented choice. Larger waveguide cross-sections are preferred for low birefringence, low dispersion, higher light coupling efficiency etc., whereas smaller waveguide cross-section (with higher refractive contrast between core and cladding) offers higher light matter interaction and device compactness. As a result, monolithic integration of diverse waveguide cross-sections provides the options to have various functional applications on a single substrate. In this section, we discuss various approaches for fabricating waveguides with multiple waveguide cross-sections on same substrate. Though our primary focus is to use larger waveguides for efficient light coupling between standard single-mode fiber to chip and smaller cross-section for compact device footprint,

these CMOS compatible fabrication techniques can be used for applications such as post fabrication phase error correction (as discussed in the previous section), dispersion engineering etc.

The characteristics of an integrated optical silicon waveguide is decided by the properties such as width ( $W$ ), rib height/device layer height ( $H$ ) and slab height ( $h$ ). So, multiple waveguide cross-section on same substrate demands for multiple device layer on same substrate. This can be achieved in various techniques. We follow the simplest approach where larger waveguides are defined initially on an SOI substrate and trim (reduce) the waveguide cross-section along with the substrate device layer to form reduced/submicron waveguide cross-sections. Surface trimming is a technique generally used in integrated optics for the modification the waveguide properties such as waveguide cross-section, refractive index of core/cladding in the post fabrication step. The application of this technique involves the compensation of fabrication error/tolerance the optical circuit [92, 93, 94, 95], reconfigure/fine tune [93, 94, 95], athermalization of device characteristics [96] etc. There were various approaches for waveguide trimming, for example: (1) Deposition of photo/electron sensitive cladding- where the cladding properties such as refractive index or geometry (compaction of cladding induced strain in the core region) is changed upon the exposure of light/electron beam. This changes the refractive index of core region which results in the modification of circuit/device characteristics. (2) Fabrication of waveguide core with UV sensitive a-Si:H silicon- where the refractive index of the core changes as it is exposed to the UV light hence the modification/reconfiguration of device characteristics. This techniques are selective as well as extremely useful, However, the maximum tunability of effective refractive index of the core is  $\sim 10^{-1}$ . In this section, an alternative approach is introduced for the modification of effective index of the waveguide up to a value which is 10 times higher than the previously mentioned techniques. In addition to that this technique can be employed to form various waveguide cross-sections at same substrate.

## 2.2.1 Oxide Growth and Removal

Oxidation of a silicon substrate is a well known semiconductor fabrication process where the silicon atom reacts with oxide molecules and forms silicon dioxide at the interface of silicon substrate. Though, the silicon dioxide is derived from the silicon substrate, the properties of silicon and silicon dioxide are entirely different. As a result, these materials can be treated separately in terms of chemical reactions. We have exploited this property to derive smaller waveguide cross-section from a larger waveguide by a repeated oxidation and removal process. Figure 2.10 shows the schematic view of fabrication steps for surface trimmed waveguides using repeated oxidation and removal. Initially, LCRW structures are patterned on positive photoresist (S1813) coated on a

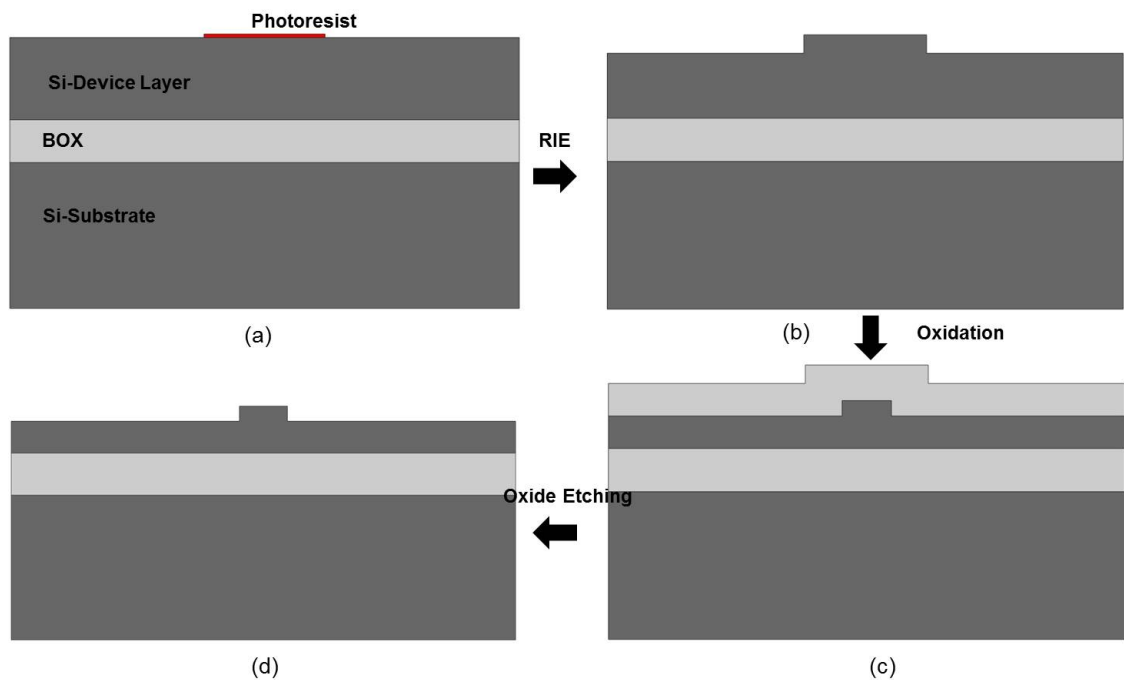


Figure 2.10: Processing flow for fabrication surface trimmed waveguides by repeated oxidation and removal. (a) photoresist pattern after photolithography, (b) after reactive ion etching, (c) oxidized waveguide structures and (d) after oxide removal.

SOI substrate (handle wafer thickness  $\sim 500 \mu\text{m}$ , BOX thickness  $\sim 1 \mu\text{m}$  and device layer thickness  $\sim 5 \mu\text{m}$ ) with an i-line (wavelength  $\sim 365 \text{ nm}$ ) photolithography system (SUSS MicroTec MA6/BA6). SOI substrate with photoresist pattern is then taken for a reactive ion etching (RIE) process (gas flow rate -  $\text{SF}_6$  : Ar :: 20 sccm : 20 sccm, cham-



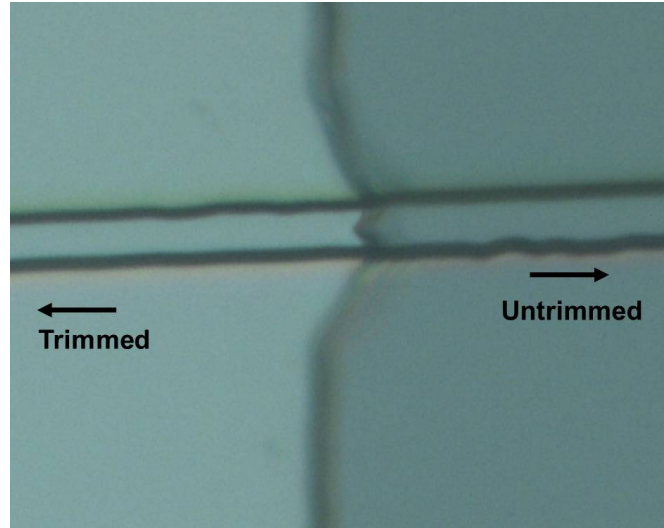


Figure 2.11: (a) Microscopic images of surface trimmed waveguide after one oxidation and removal step, oxide has not been removed from the untrimmed section which reduces the oxidation rate for successive oxidation steps.

ber pressure - 200 mT, substrate temperature - 20 °C, RF Power - 150 W) to define initial LCRW structures (see Figure 2.10(b)). After the removal (using acetone) of photoresist mask and thorough cleaning, the sample has taken for an oxidation process (see. Figure 2.10(c)). The sequence for oxidation was dry-wet-dry and this ensures good quality thick oxide on the device layer. First dry oxidation ( $\sim 1$  hour) for defect free oxide surface, wet oxidation (5 hours) gives higher oxidation rate and final dry oxidation ( $\sim 1$  hour) reduce interfacial defects in the oxide. Total thickness of the oxide formed is measured (using ellipsometer) to be  $\sim 1 \mu\text{m}$  after 7 hours of oxidation process. After oxidation, a photolithography step has been carried out to protect input/output sections during oxide removal using buffered hydrofluoric (BHF) acid solution. As a result, in the next oxidation step, the oxidation rate at input/output regions is slowed down (as previously grown oxide present) compared to the trimmed region where fresh silicon is exposed after oxide removal. This ensures a slight modification in the untrimmed section and higher cross-section reduction in the trimmed region depending on the number of oxidation steps. Figure 2.10(d) shows the the reduced (trimmed) waveguide cross-section upon removal of the thermally grown oxide. Each oxidation step forms  $\sim 1 \mu\text{m}$  thick oxide which consumes  $\sim 0.44 \mu\text{m}$  (44 % of oxide thickness) of device layer silicon. Figure 2.11 shows the top view image of the waveguide after one oxidation and removal step. In each oxidation step, an oxide of thickness  $\sim 1 \mu\text{m}$  is grown and

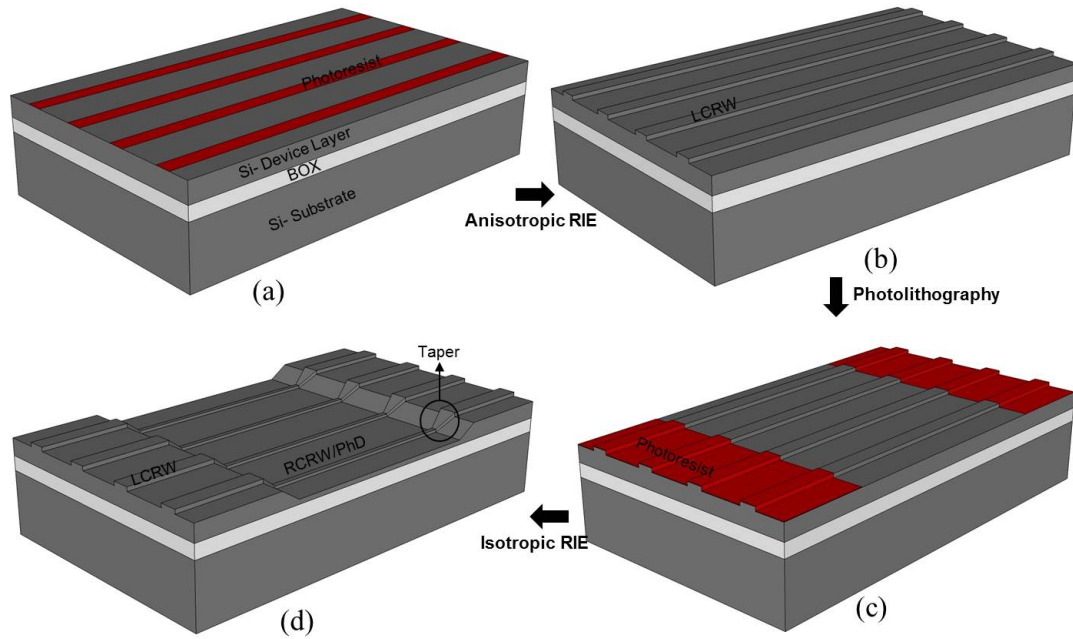


Figure 2.12: Fabrication process flow for naturally tapered surface trimmed waveguides. (a) Photolithographic definition of LCRWs, (b) LCRW definition by anisotropic RIE, (c) photolithography to protect input/output LCRW structures and (d) isotropic RIE process for surface trimming and SSC.

etched with BHF solution, the width and height reduction of the waveguide is measured to be  $1\ \mu\text{m}$  and  $0.5\ \mu\text{m}$  respectively as each oxidation consumes almost 50% of silicon. Though, repeated oxidation and oxidation removal process can be used for waveguide trimming, it is observed to a slow process. Considering 7 hours of oxidation produces  $\sim 1\ \mu\text{m}$  thick silicon dioxide which consumes  $0.44\ \mu\text{m}$  device layer silicon, it takes approximately 9 oxidation steps to make  $5\ \mu\text{m}$  high LCRW to submicron PhWW which is really slow and cumbersome to make a simple submicron waveguide.

### 2.2.2 Isotropic Dry Etching

We have seen that the surface trimming technique by repeated oxidation and removal could be a potential method for fabricating multiple waveguide cross-sections on same substrate. However, the process is too slow and required multiple lithography steps to protect LCRW region during oxide removal. In view of this, we have modified the fabrication process flow based on an isotropic dry etching for the realization of surface trimmed waveguides. 3D schematic view of dry etching based surface trimming is

shown figure 2.12. First two steps, photolithographic definition (figure 2.12(a)) and RIE (figure 2.12(b)) for LCRWs are similar to the previously mentioned fabrication process. In the third step, a photolithography step is carried out to protect input/output sections of LCRW structures and middle device layer region is exposed for surface trimming (see figure 2.12(c)). This helps in protecting the input and output waveguide regions during the subsequent RIE process. Finally, a second RIE is carried out to trim the waveguides in the middle region. Second RIE recipe (gas flow rate - SF<sub>6</sub>:Ar :: 25 sccm:25 sccm, chamber pressure - 250 mT, RF power - 150 W and temperature - 20 °C) provides isotropic etching profile to trim waveguide height and width simultaneously. In contrast to the first RIE chemistry, we have modified the gas flow rate and chamber pressure in the second RIE process. This in fact reduces the acceleration of reactive plasma as a consequence of reduced DC bias of the recipe and provides an isotropic etching profile as well as smooth trimmed surfaces. Figure 2.13(a) and 2.13(b) show the cross-sectional SEM images of polished end-facets of LCRW ( $W = 5 \mu\text{m}$ ,  $H = 5 \mu\text{m}$  and  $h = 4 \mu\text{m}$ ) before and after isotropic RIE respectively. It can be clearly observed from the Figure 2.13(b) that surface roughness of the trimmed waveguide is almost negligible.

In addition to the waveguide size reduction, second RIE provides naturally tapered section at the transition region from LCRW (untrimmed) to trimmed waveguide. This taper section is formed as a result of under etching through the photoresist pattern during trimming process. Figure 2.12(d) shows the schematic view of trimmed waveguide integrated with LCRWs through naturally tapered section at input and output regions. The length of the taper section depends on the duration of surface trimming RIE process. The SEM image of a RCRW along with its LCRW coupler has been shown in Figure 2.13(c). Magnified image of the LCRW-RCRW junction (see figure 2.13(d)) reveals that the natural tapering is along both vertical and horizontal directions. In order to check the efficiency of trimmed waveguide and naturally tapered waveguides, two samples were prepared on optical grade SOI substrate (device layer thickness = 5  $\mu\text{m}$ , BOX = 1  $\mu\text{m}$  and handle wafer thickness = 500  $\mu\text{m}$ ) by two step RIE process. The mask used for first RIE defines 5 sets of LCRW structures - each set consists of 7 waveguides of varying widths (2, 2.5,...5  $\mu\text{m}$ ). In sample # 1, size of single-mode LCRW structures were reduced to single-mode RCRW structures uniformly whereas,

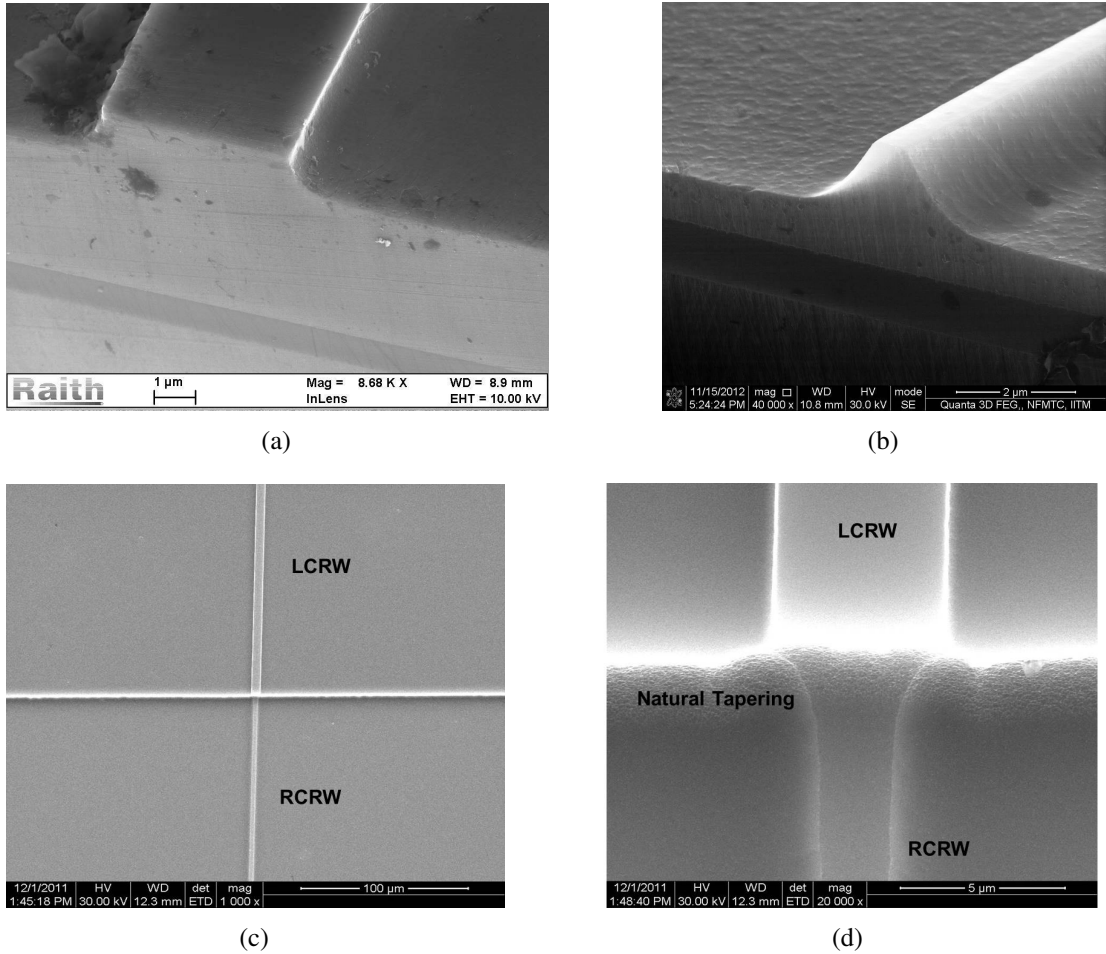


Figure 2.13: SEM images of the cross-sectional view fabricated LCRW (a) before and (b) after trimming using isotropic RIE process. (c) SEM image showing the integrated LCRW and RCRW on the same substrate by surface trimming technique and (b) magnified image of (a) showing the naturally 2D tapered LCRW-RCRW junction.

in sample # 2, input/output LCRWs were protected using planar photoresist masks (except 1 set for reference) during second RIE. Figure 2.14(a) shows the schematic view of the characterization setup used for the mode-profile measurements. A fiber coupled infrared laser light ( $\lambda \sim 1550$  nm) is aligned to a particular polarization (TE/TM) using a polarization controller (PC). The linearly polarized light is then collimated using a lens ( $L_1$ ) and passed through a polarizer to ensure it is aligned to the desired polarization (TE/TM). Then it is focused to the end facet of the waveguide device under test (DUT) with another objective lens ( $L_2$ ). The output is collected using a lens ( $L_3$ ) and collimated to the computer controlled infrared camera (IRC) through the analyzer ( $P_2$ ). Figure 2.14(b) shows the lateral (along the direction of waveguide width)

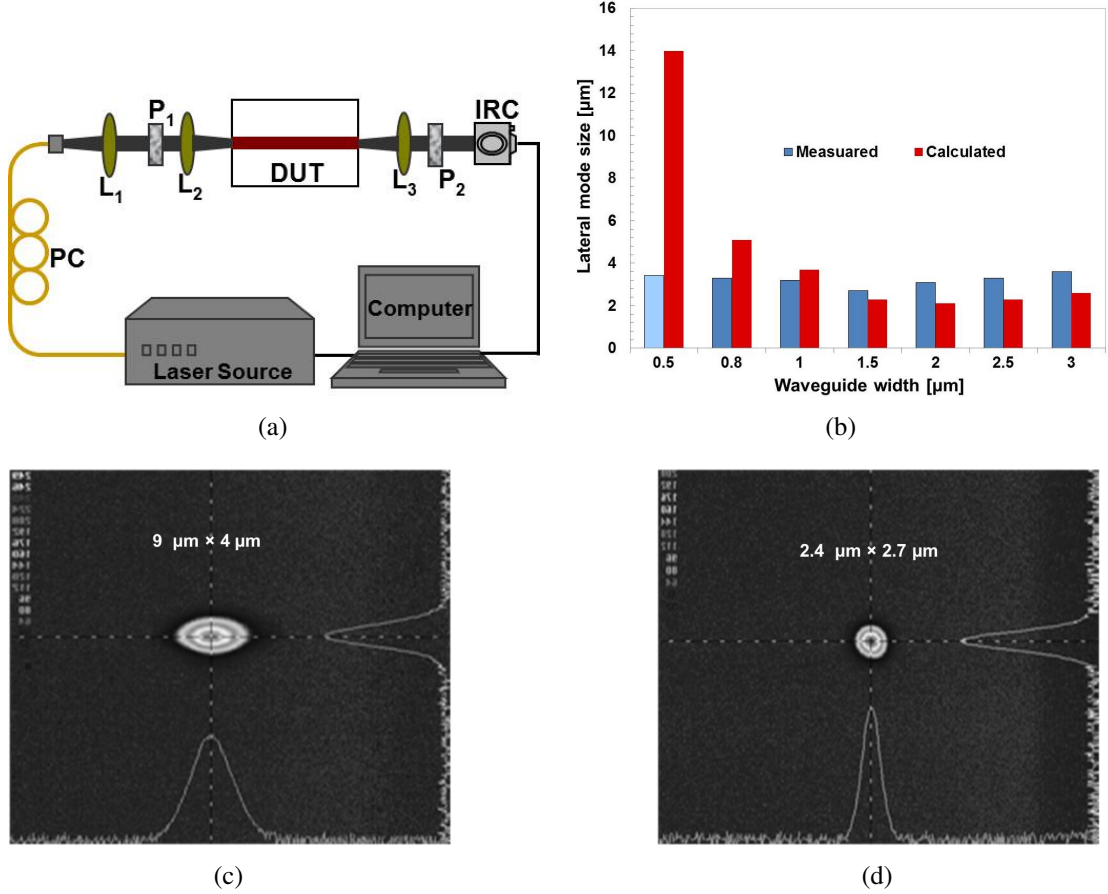


Figure 2.14: (a) Characterization set-up used for mode-profile measurement where PC - polarization controller, L - lens, P - polarizer, DUT - device under test, IRC - infrared camera. (b) Mode-size comparison of calculated and measured fundamental TE modes waveguides as function of waveguide width with  $H = 2.2 \mu\text{m}$ ,  $h = 1.35 \mu\text{m}$  at  $\lambda = 1550\text{nm}$ . (c) Measured guided mode profile of a typical LCRW coupler with  $W_0 = 3 \mu\text{m}$ ,  $H_0 = 5 \mu\text{m}$  and  $h_0 = 4 \mu\text{m}$ . (d) Typical guided mode profile for trimmed (RCRW) waveguide with  $W_0 = 1.5 \mu\text{m}$ ,  $H_0 = 2.2 \mu\text{m}$  and  $h_0 = 1.35 \mu\text{m}$

mode-size comparison of calculated and measured fundamental mode profiles (TE polarization) of a trimmed waveguide as function of width ( $W$ ) with  $H = 2.2 \mu\text{m}$  and  $h = 1.35 \mu\text{m}$  (sample # 1) at  $\lambda = 1550 \text{ nm}$ . For mode-size calculations we have considered the waveguide cross-section as rectangular which is somewhat different from experimentally obtained waveguide cross-section (see Figure 2.13(b)). This leads to a slight difference between the calculated and measured mode profiles. Typical measured profiles (TE -fundamental mode) of untrimmed LCRW ( $W = 3 \mu\text{m}$ ,  $H = 5 \mu\text{m}$  and  $h = 4 \mu\text{m}$ ) and RCRW ( $W = 1.5 \mu\text{m}$ ,  $H = 2.2 \mu\text{m}$  and  $h = 1.5 \mu\text{m}$ ) are shown in Figure 2.14(c) and 2.14(d) respectively. After the successful testing of sample # 1, we have

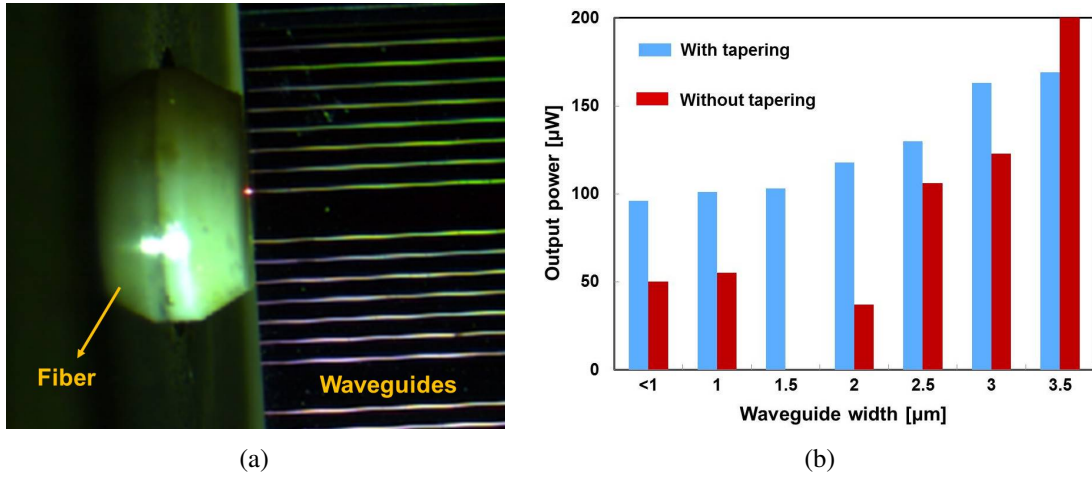


Figure 2.15: (a) Fiber butt-coupling setup used for measuring the efficiency of naturally tapered waveguides, red laser used for identifying the waveguides under characterization. (b) Comparison of throughput power of RCRW structures with/without LCRW couplers (note: reference waveguide # 3 is damaged). Characterization has been carried out at input power -  $P_{in} = 6.5$  mW and wavelength  $\sim 1550$  nm.

used the values of width reduction rate ( $\alpha = 0.39\mu\text{m}$ ) and height rate ( $\beta = 0.36\mu\text{m}$ ) during the surface trimming process (second RIE) of sample # 1 to estimate the duration of second RIE for sample # 2. After second RIE for a duration of 4 min., each set of single-mode LCRWs in sample # 2 is converted in to RCRWs with varying widths ( $\sim 0.5, 1, \dots, 3.5 \mu\text{m}$  corresponds to waveguide # 1, 2, ..., 7 in each set),  $H = 3.5 \mu\text{m}$  and  $h = 2.5 \mu\text{m}$ . All the RCRWs (with and without LCRW couplers) have been characterized by measuring the transmitted output power when input laser light ( $P_{in} = 6.5$  mW and  $\lambda = 1550$  nm) was launched through butt-coupled standard single-mode fiber. Figure 2.15(a) shows the photograph of fiber butt-coupling to the sample where red laser is used for identifying the waveguide under test. It is evident from Figure 2.15(b) that the average throughput of RCRWs with LCRW couplers are higher (up to  $\sim 3$  dB) than those of RCRWs. This ensures that the spot size converters (SSC) made out of natural tapering of the waveguide during surface trimming process is advantageous when the trimmed waveguide cross-section is extremely smaller. However, the insertion loss of this non-adiabatic taper section is higher and which requires a detailed investigation. In addition to that, the discrepancy between calculated and measured profiles (see. Figure 2.14(b)) clearly suggests the modeling of trimmed waveguide is necessary for the complete analysis of trimmed waveguides. So we will discuss modeling of the trimmed

waveguide and its analysis in the following sections.

### 2.2.3 Modeling of Surface Trimmed Waveguides

We have seen from the experimental results that smaller waveguide cross-sections are prone to coupling loss when they are interfaced with the fibers. Whereas smaller cross-section waveguides integrated with larger waveguides are found to be better in terms of coupling loss though the transition region (SSC) is not well optimized. It is clear that if the length SSC is increased the efficiency of the coupling can be improved. However, it is observed that the characteristics of trimmed waveguide are different from the conventionally defined rectangular waveguide structure. So, it is very important to model the trimmed waveguide cross-sections for the theoretical analysis of various aspects which can affect the coupling efficiency of SSC. Primary factor which decides the coupling efficiency is the mode profile overlap between the fiber and the silicon waveguide. Since the input/output regions are protected during the trimming process, overlap calculation is required only for the untrimmed waveguide. However, two important properties of trimmed waveguide which can significantly influence the SSC performance are: (i) higher order mode excitation in the transition region and (ii) polarization rotation. In trimmed waveguides, polarization rotation is expected due to the slanted side walls (see Figure 2.13(b)). In the proposed surface trimming process, the geometry of the reduced waveguide is decided by initial waveguide dimension, duration of second RIE process and the recipe (etching profile) of RIE. Though, the cross-section of larger waveguide defined in the the first step can be assumed as rectangular in shape (due to first anisotropic RIE), reduced waveguide cross-section is modified to be trapezoidal or triangular depending on the duration and nature of second RIE. As a result, structural modeling of the waveguide is extremely important to study exact nature of the trimmed/reduced cross-section. We have modeled the reduced waveguide cross-section based on the lateral and vertical etch rates of the second RIE. This model has been used for the simulation of reduced waveguide cross-sections. Since single-mode guiding conditions are more stringent at smaller waveguide cross-sections, our analysis is confine to a starting SOI device layer thickness to 2  $\mu\text{m}$  and trim it down to submicron ( $\sim 200$  nm) dimension. In addition to that the guided mode-size of an untrimmed

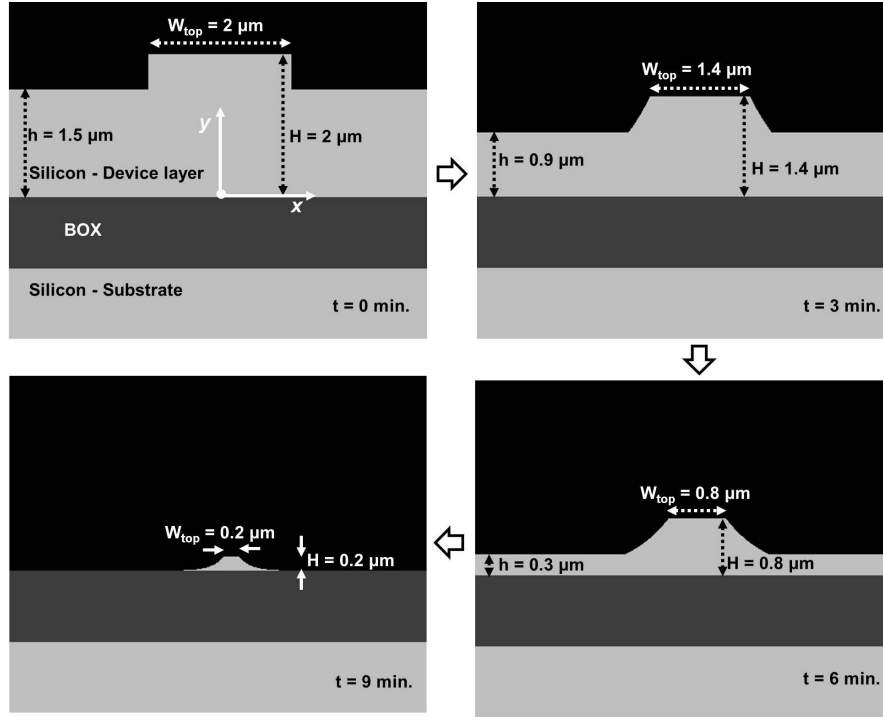


Figure 2.16: Schematic cross-sectional views of a 2  $\mu\text{m}$  waveguide ( $W_0 = 2 \mu\text{m}$ ,  $H = 2 \mu\text{m}$  and  $h = 1.5 \mu\text{m}$ ) at various instants trimming time ( $t$ ).

2  $\mu\text{m}$  waveguide is found to be matching with the mode-size of commercially available lensed fiber which enhances the coupling efficiency between the fiber and the silicon waveguides. However, the same analysis can be extended to evaluate the characteristics of trimmed waveguide derived from a larger ( $\sim 5 \mu\text{m}$ ) initial device layer height of SOI. Figure 2.16 shows the schematic cross-section views of a typical 2  $\mu\text{m}$  waveguide ( $W_0 = 2 \mu\text{m}$ ,  $H_0 = 2 \mu\text{m}$  and  $h_0 = 1.75 \mu\text{m}$ ) at various instants of surface trimming time ( $t$ ). Based on the model, the waveguide parameters are modified as [97]:

$$W_{top} = W_0 - \alpha t_{etch} \quad (2.3)$$

$$H = H_0 - \beta t_{etch} \quad (2.4)$$

$$h = h_0 - \beta t_{etch} \quad (2.5)$$

Here,  $W_{top}$ ,  $H$  and  $h$  are the waveguide top width, rib height and slab height respectively at any instant of time  $t$ .  $\alpha$  and  $\beta$  are the width and height reduction rates respectively, and  $t_{etch}$  is the duration of second RIE process. We have considered the uniform reduction of waveguide width and height so as values of  $\alpha = \beta = 0.2 \mu\text{m}/\text{min}$ . By studying



the dynamics of second RIE process which is in fact isotropic in nature, we observed an exponential height profile variation of the reduced waveguide structure and it can be expressed as:

$$H_T(x) = \begin{cases} H & \text{for } -W_{top}/2 \leq x \leq W_{top}/2 \\ H \exp[-a(x - W_{top}/2)] & \text{for } W_{top}/2 \leq |x| \leq W_0/2 \\ h & \text{for } |x| \geq W_0/2 \end{cases} \quad (2.6)$$

$$a = 2 \frac{\ln(H/h)}{W_0 - W_{top}} \quad (2.7)$$

It is worth mentioning here that the above equation 2.6 is valid only for  $\beta t \geq H - h$  and  $\alpha t \leq W_0$ . In this model, we have considered the values of  $\alpha$  and  $\beta$  are same, however which can be modified depending on the second RIE chemistry. The side wall angle of the waveguide is decided by the ratio of  $\alpha$  and  $\beta$ . Since the cross-sectional geometry of the trimmed waveguide is entirely different from a waveguide with rectangular geometry, its single-mode guiding characteristics have to be analyzed separately. In addition to that the sidewalls of the trimmed waveguides are slanted which will definitely affect polarization dependency of the waveguides. So, in the subsequent sections, we will discuss the important properties of the trimmed waveguide using the proposed model.

## 2.2.4 Single-mode Trimmed Waveguide

In this section, we analyze the single-mode characteristics of a trimmed waveguide on SOI substrate using Lumerical ModeSolutions simulation tool. In this analysis, single-mode cut-off region is calculated by comparing the effective indices of first order mode in the waveguide rib region and fundamental mode in the slab region for the respective polarization. If the waveguide first order mode effective index is higher than the slab region fundamental mode, then the waveguide is said to be multi-mode waveguide as the first order mode is well confined in the rib region. Figure 2.17 shows the single-mode region of 2  $\mu\text{m}$  waveguide ( $H_0 = 2 \mu\text{m}$ ) for TE polarization at  $\lambda = 1550 \text{ nm}$  during surface trimming. Colored region shows the single-mode region at trimming time  $t = 0$  minute. Numerical values inside each cell corresponds to the rib height reduction

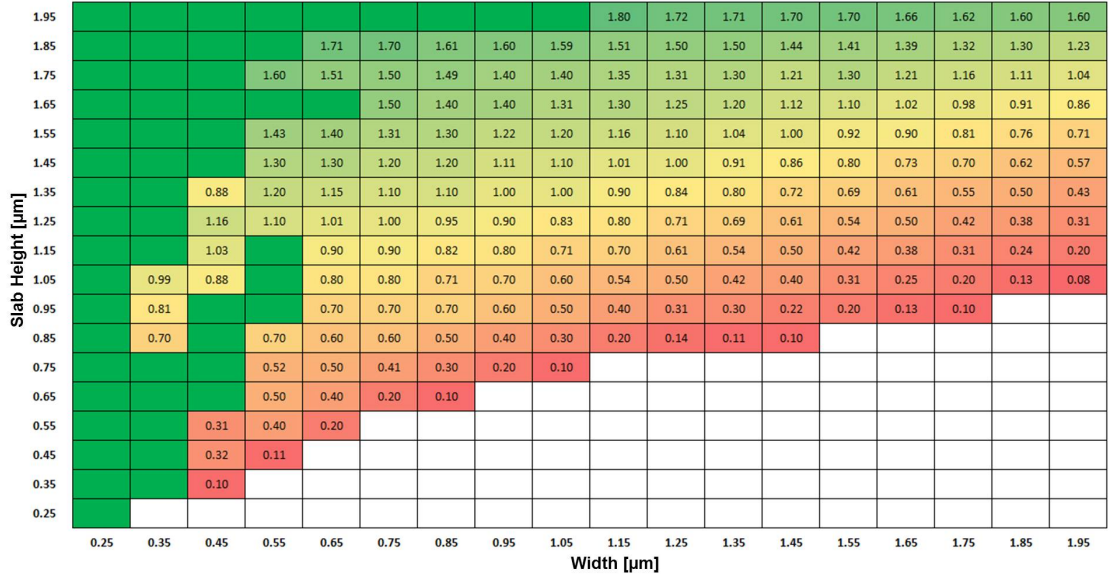


Figure 2.17: Color map shows the single mode region of the surface trimmed waveguide as a function of  $W_0$  and  $h_0$  for a rib height of  $H_0 = 2 \mu\text{m}$ . Numerical values inside each cell correspond to the rib height reduction ( $\Delta H = H_0 - H$ ) in micrometer unit at which single mode waveguide mode transformed into multi-mode waveguides. The green cells represents initial waveguide dimension which remains single-mode throughout trimming ( $\Delta H \rightarrow H_0$ ). White cells represents the multi-mode region. The calculated values are shown on for TE-like modes and at an operating wavelength of  $\lambda = 1550 \text{ nm}$ .

( $\Delta H = H_0 - H$ ) in micrometer unit at which single-mode waveguide is transformed into multi-mode waveguide. The green cells represents the initial waveguide dimension which remains single-mode throughout trimming. Though all the colored cells represent initial single-mode region, the choice of initial dimension depends on mainly two aspects: (1) size/width of desired single-mode trimmed/reduced cross-section at the end of the process (2) power coupling efficiency between the waveguide and input/output fiber. From Figure 2.17, it is obvious that green cells are the better choice in terms of single-mode condition as it remains single-mode throughout. However, one should also consider mode overlap of those waveguides with input/output fiber. It is observed that the coupling efficiency of  $2 \mu\text{m}$  with SMF (mode field diameter  $\sim 9.5 \mu\text{m}$ ) is very poor. So, we have used a lensed fiber with mode field diameter  $\sim 3.2 \mu\text{m}$  for calculation of power coupling efficiency. Figure 2.18 shows the waveguide fundamental mode overlap with a typical lensed fiber with mode size  $\sim 3.2 \mu\text{m} \times 3.2 \mu\text{m}$  for TE polarization. Colored region represents single-mode region of RCRW with  $H_0 = 2 \mu\text{m}$

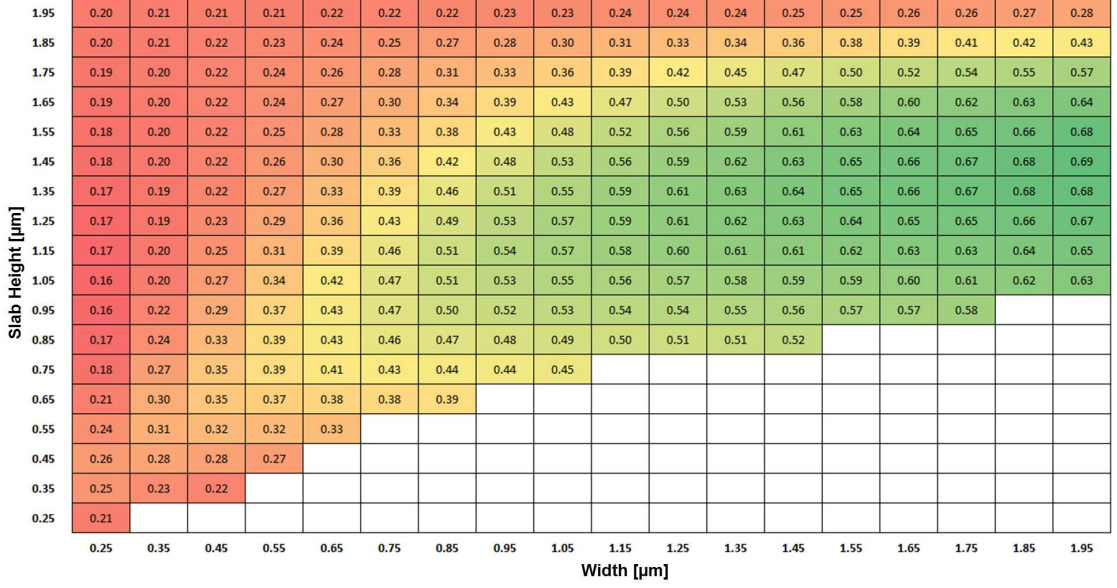


Figure 2.18: Color map shows the waveguide mode profile overlap of an RCRW ( $H_0 = 2 \mu\text{m}$ ) with lensed fiber mode with mode size  $\sim 3.2 \mu\text{m} \times 3.2 \mu\text{m}$ . The calculated values are shown on for TE-like modes and at an operating wavelength of  $\lambda = 1550 \text{ nm}$

and the numerical values inside the cell represents the value overlap integral between the fundamental modes of the waveguide and lensed fiber. As the value of overlap increases the coupling efficiency of light from fiber to chip is increased. The maximum overlap of an RCRW with  $H_0 = 2 \mu\text{m}$  is found to be 69 % for waveguide with  $W_0 = 1.95 \mu\text{m}$  and  $h_0 = 1.35 \mu\text{m}$ . However, from figure 2.17 we can see that the waveguide with higher mode overlap can trim down  $\Delta H$  only to  $0.43 \mu\text{m}$  which corresponds to  $H = 1.57 \mu\text{m}$ . If the waveguide is trimmed more i.e,  $H < 1.57 \mu\text{m}$ , the waveguide supports higher order modes, which is not desirable. As a result, though the waveguide mode overlap is high with a lensed fiber, this waveguide cross-section cannot be used for deriving submicron waveguide geometry. In this regard, there has to be trade-off between the light coupling efficiency and the minimum single-mode waveguide dimension which can be achieved. However one can find out the product of overlap and the maximum trimming depth which will give a figure of merit. The highest figure of merit is obtained for a waveguide dimension  $W_0 = 1.55 \mu\text{m}$ ,  $H_0 = 2 \mu\text{m}$  and  $h_0 = 1.75 \mu\text{m}$ . This waveguide can be trimmed down to  $W = 0.25 \mu\text{m}$ ,  $H = 0.7 \mu\text{m}$  and  $h = 0.45 \mu\text{m}$  which is sufficient to obtain compact waveguide bends. The mode overlap with lensed fiber mode is calculated to be 50 %. The equations 2.6 - 2.7 has been used to model the trimmed submicron waveguide cross-sections at various instances of etching duration -

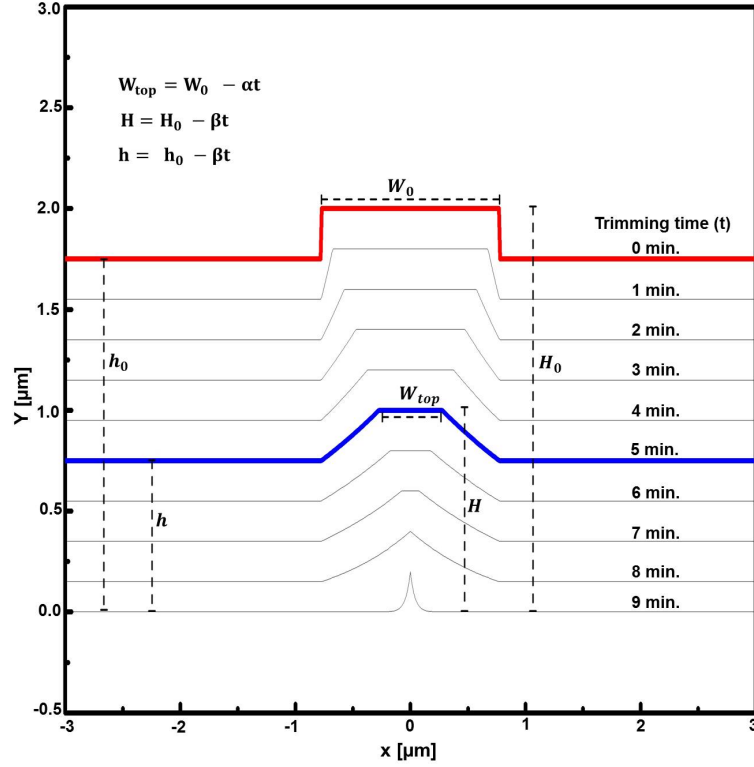


Figure 2.19: Cross-sectional profiles of surface trimmed waveguides; contour lines represents crosssections of the waveguide at various instants of RIE, where  $W_0 = 1.55 \mu\text{m}$ ,  $H_0 = 2 \mu\text{m}$  and  $h_0 = 1.75 \mu\text{m}$ .

the simulated results are presented in figure 2.19. The contour plot at  $t = 0$  minutes corresponds to the cross-sectional view of initial waveguide parameters of  $W_0 = 1.55 \mu\text{m}$ ,  $H_0 = 2 \mu\text{m}$  and  $h_0 = 1.75 \mu\text{m}$  (waveguide with highest figure of merit). It must be noted that, the width reduction rate ( $\alpha$ ) and height reduction rate ( $\beta$ ) have been assumed to be the same ( $0.2 \mu\text{m}/\text{min.}$ ) and the bottom width of the waveguide remains as  $W_0$  until the slab region is fully etched. Once the slab is completely exhausted the cross-section of the triangular shaped waveguide geometry reduces further with base and height reduction rate at  $\alpha$  and  $\beta$  respectively. Though the surface trimming has been shown to be effective in core-size reduction up to a sufficiently low dimension, one need to ensure single-mode guiding condition to be retained. We have carried out numerical simulations (using full vectorial MODE Solutions solution) to determine highest order confined mode for each of the waveguide geometries shown in Figure 2.19 The corresponding intensity distributions for the highest order confined modes (TE like,  $\lambda = 1550 \text{ nm}$ ) have been shown in Figure 2.20. It is evident that the single-mode condition is maintained upto submicron waveguide heights ( $< 1 \mu\text{m}$ ) and becomes multi-moded

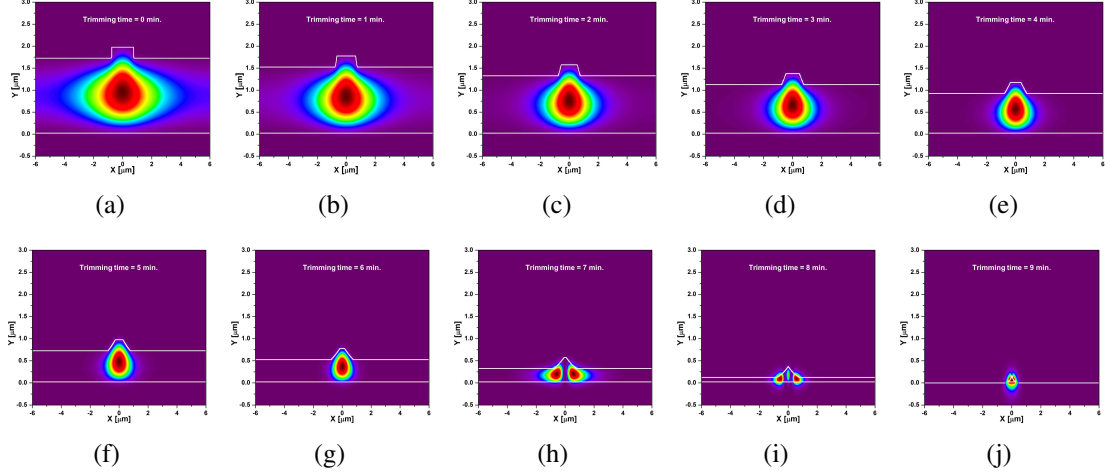


Figure 2.20: (a)- Intensity distribution of the guided mode of an untrimmed single-mode waveguide ( $W_0 = 1.55 \mu\text{m}$ ,  $H_0 = 2 \mu\text{m}$ ,  $h_0 = 1.75 \mu\text{m}$ ); (b), (c), (d), (e), (f), and (g)- intensity distributions of the guided modes for the trimmed single-mode waveguides with etching duration of upto 6 mins., in steps of 1 min.; (h) and (i)- the highest order guided mode intensity distributions for the trimmed waveguides (multi-mode) with etching duration of 7 mins. and 8 mins., respectively; (j)- intensity distribution of the guided mode for the further trimmed single-mode waveguide with an etching duration of 9 mins. White outline defines the device layer silicon profile. Simulation has been done for TE polarization at  $\lambda = 1550 \text{ nm}$ .

for a certain duration of surface trimming time (approximately for  $6.5 \text{ min} < t < 8.5 \text{ min}$ ). However, for a surface etching duration of  $t = 9 \text{ min}$ , the resulting triangular shaped waveguide cross-section becomes single-mode. It is obvious from the calculated intensity distribution profiles that the guided mode size can be gradually reduced from an untrimmed single-mode waveguide (Figure 2.20(a)) to a uniformly trimmed single-mode waveguide (Figure 2.20(f)), if the maximum etching duration is limited to about 6 minutes. Typically, any initial single-mode waveguide can be trimmed down to a reduced waveguide height and cross-section; but one need to take into account that a multimode regime may appear for a specific band of etching duration. Figure 2.21 shows the multimode/single mode (TE-like) cut-off for the given  $\Delta H$  values as a function of  $W_0$  for the initial  $H_0 = 2 \mu\text{m}$  and  $h_0 = 1.75 \mu\text{m}$ . It is obvious from the plot that during surface trimming, single-mode waveguide is modified into multi-mode waveguide and again transformed back to singlemode waveguide as we have seen earlier in Figure 2.20. The first transition is due to the higher effective index value of first order mode in the rib region compared to the fundamental mode of the slab. The second tran-

sition for the single-mode guidance again is because of the lower effective index value of the first order mode in the rib compared to the bulk index of lower cladding (BOX).

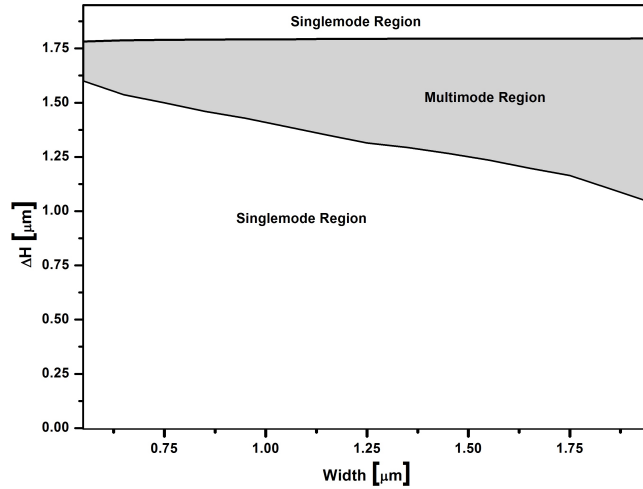


Figure 2.21: Multi-mode region of surface trimmed waveguide as function of waveguide initial width ( $W_0$ ) and rib height reduction ( $\Delta H = H_0 - H$ ) for  $H_0 = 2 \mu\text{m}$  ( $h_0 = 1.75 \mu\text{m}$ ).

## 2.2.5 Polarization Dependency

We have seen from section 2.5 that submicron waveguides are highly dependent on polarization of operation. As the surface trimming technique is used for waveguide size reduction up to submicron regime, it is important to study the polarization dependency of the waveguide as function of surface trimming. Silicon is a centro-symmetric material, as a result, material birefringence is absent. The only possibility of waveguide polarization dependency is the structural birefringence. Fabrication of square waveguide with symmetric claddings (cladding material is same for all four sides) are capable of eliminating the structural birefringences. However, this poses fabrication difficulty such as deep dry etching of waveguide with vertical side walls. Vertical side walls can be achieved with the cost of increased surface roughness. This in turn increases the propagation loss of the waveguide. In silicon photonics generally shallow etched or low aspect ratio ( $H_0/W_0$ ) waveguides are preferred to reduce waveguide loss. In addition to that, the waveguides are designed to operate at one polarization, generally TE polarization. So we prefer here shallow etched waveguide which is meant to operate at TE

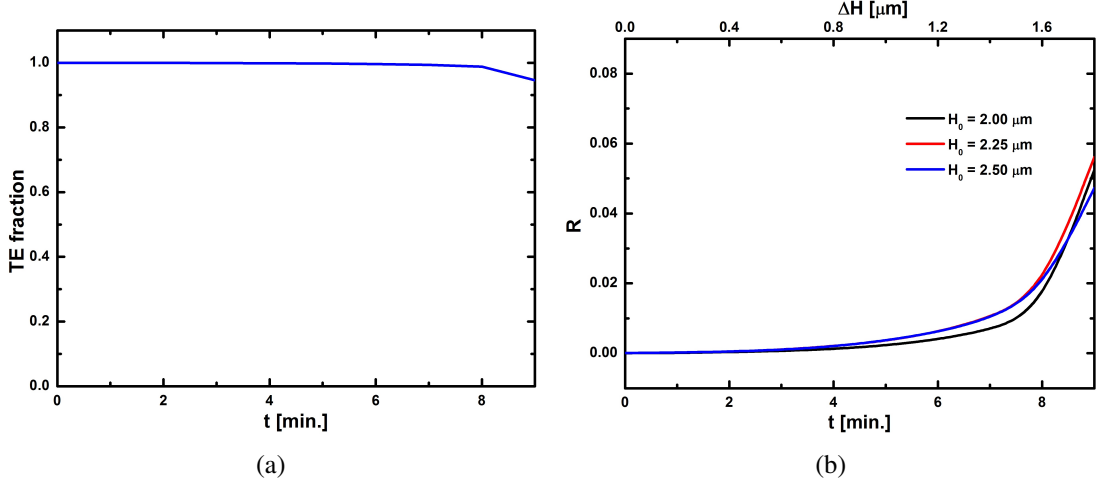


Figure 2.22: (a) TE fraction of the fundamental guided mode (TE) of a 2  $\mu\text{m}$  as function of trimming duration ( $t$ ). (b) Calculated polarization rotation parameter ( $R$ ) for a single-mode waveguide with  $W_0 = 1.55 \mu\text{m}$  and  $h_0 = 1.75 \mu\text{m}$  for three different values of  $H_0$  plotted as function trimming time  $t$  (or surface etching of  $\Delta H$ ) for TE polarization at  $\lambda \sim 1550 \text{ nm}$ .

polarized light. The choice of shallow waveguide is due to the fact that it can remain as single-mode waveguide for a longer trimming duration. As we have mentioned earlier, surface trimming modifies the vertical waveguide sidewalls to angled. Though the tilted waveguide side walls tend to rotate polarization when a fabrication error/perturbation is occurred [98], we found that, for a shallow etched 2  $\mu\text{m}$  waveguide, initial proportions of field components of TE-like fundamental mode remain nearly unchanged upto sub-micron trimmed waveguides of trapezoidal/triangular cross-sectional geometries. Figure 2.22 shows the TE fraction of the fundamental guided mode of a 2  $\mu\text{m}$  waveguide as function of  $t$ . Here the TE fraction indicates the major component of electric field. For  $z$  propagating mode, it is equal to the integrated  $E_x$  electric field intensity divided by the integrated transverse electric field intensity (Lumerical MODE Solutions). Figure 2.22(b) shows the polarization rotation parameter  $R$  as a function  $t$  for various values of  $H_0$  (top axis shows  $\Delta H$  corresponds to  $t$ ). The value of  $R$  is computed by a qualitative expression [99]:

$$R = \frac{\int \int n^2(x, y) E_y^2(x, y) dx dy}{\int \int n^2(x, y) E_x^2(x, y) dx dy} \quad (2.8)$$

where  $n(x, y)$  is the transverse refractive index profile,  $E_y(x, y)$  and  $E_x(x, y)$  are  $y$  and  $x$  component of transverse electric field for TE polarization respectively. The value  $R \sim 0.1$  corresponds to the eigen state principally polarized along  $x$  direction resulting no

polarization rotation even for a longer trimming duration of 9 minutes ( $\Delta H = 1.8 \mu\text{m}$ ). In addition to that the variation of  $H_0$  hardly affect the value of  $R$ , allowing tolerance

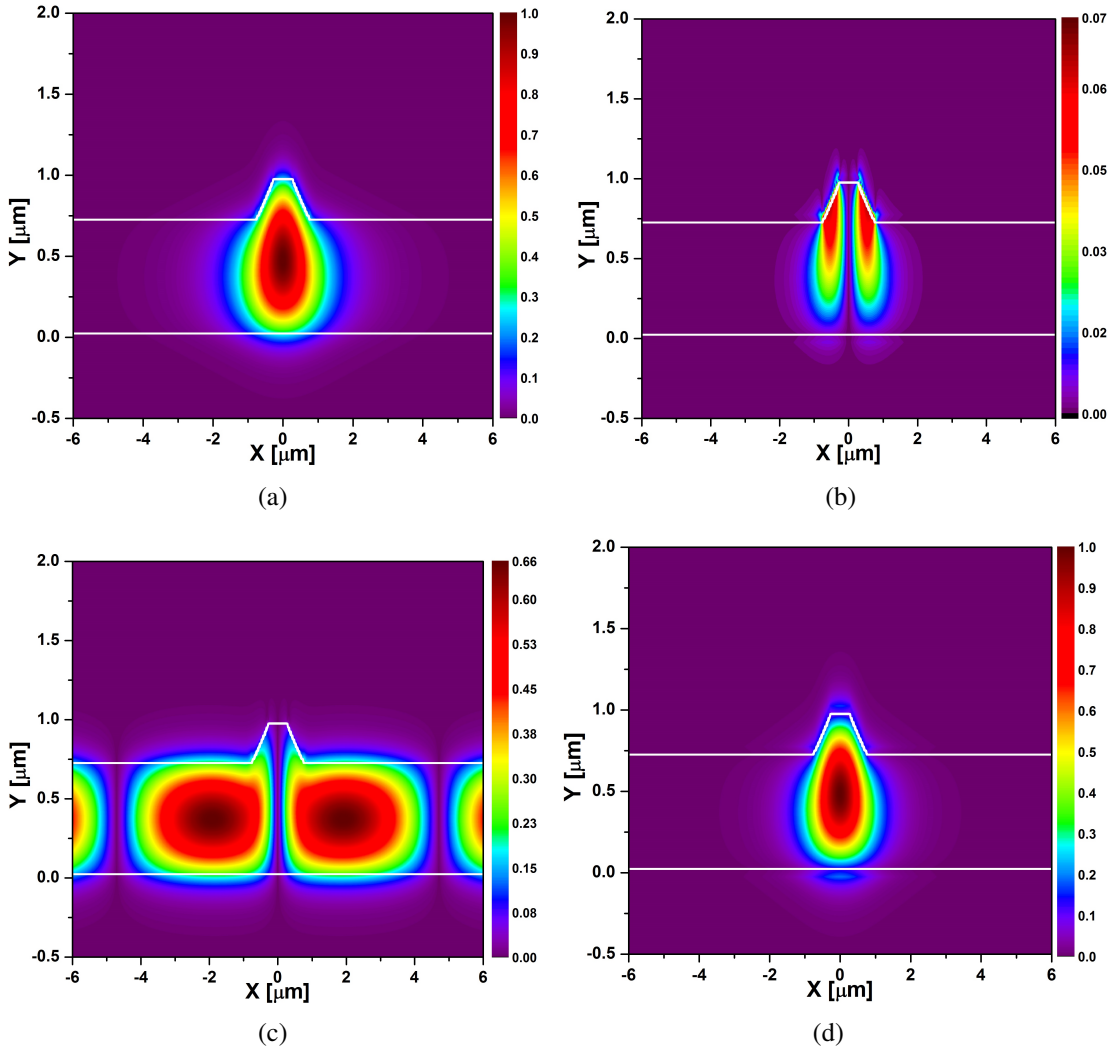


Figure 2.23: Calculated transverse electric field distribution of a waveguide ( $W_0 = 1.55 \mu\text{m}$ ,  $H_0 = 2 \mu\text{m}$  and  $h_0 = 1.75 \mu\text{m}$ ) trimmed for 5 minutes ( $\Delta H = 1 \mu\text{m}$ ), (a)  $E_x$  component and (c)  $E_y$  components for TE polarization, (c) and (d) are  $E_x$  and  $E_y$  components for TM polarization. All the calculations are carried out for  $\lambda = 1550 \text{ nm}$

in the variation of device layer thickness. Moreover, one can optimize the input/output waveguide parameters ( $W_0$ ,  $H_0$  and  $h_0$ ) such that any small amount of excited TM-like mode dissipates to the slab region of the waveguide. Figure 2.23 shows the distributions of electric field components ( $E_x$  and  $E_y$ ) for confined TE-like mode and leaky TM-like mode of a trimmed waveguide (for a trimming duration of 5 minutes). Thus the design ensures a nearly adiabatic transition of TE-like mode from micron-sized waveguide to sub-micron-sized surface trimmed waveguide, if fabricated monolithically using the



techniques discussed in the following sections.

## **2.3 Spot-Size Converters: Fabrication and Characterization**

A variety of spot-size converters (SSCs)/Mode size converters (MSCs) have been designed and demonstrated mainly to minimize the impedance/mode-size mismatch between standard single-mode fiber and lower dimension SOI waveguides. The most attractive design is the inversely tapered SSC, where the waveguide width reduces from 400-500 nm (typical width of a PhWW) to about 50-100 nm. Though the design of such SSCs is relatively compact (a few tens of micrometer in length), their fabrication is challenging as the small features at the tip of the tapered waveguide is extremely critical in terms of lithographic definition. Moreover, materials like silicon dioxide, silicon nitride or polymers are deposited over the tapered region to define waveguide with larger cross-sections and lower refractive indices comparable to standard single-mode fiber. In this section, we discuss various approaches to fabricate 2D SSCs utilizing the surface trimming technique.

### **2.3.1 2D Spot-Size Converters by Photolithography Definition**

We have seen in section 2.2.2 that during surface trimming process, a naturally tapered spot-size converter (SSC) is formed between the trimmed and untrimmed waveguide as a result of protecting input/output regions with photoresist mask. It is also observed that naturally formed SSCs are useful as trimmed waveguide cross-section is smaller. However, the insertion loss such 2D taper structures were relatively high ( $>5$  dB) because of the shorter taper length ( $<10$   $\mu\text{m}$ ). Here, we present a new design concept of 2D tapered SSC such that its length and tapering slope can be controlled by standard lithographic definition and subsequent surface trimming process. Initially, the width ( $\sim 5$   $\mu\text{m}$ ) of LCRW was defined photolithographically and then first RIE was carried out to achieve a slab height of  $\sim 4$   $\mu\text{m}$ . A photoresist mask was then used to protect input/output portions of LCRWs and to define the length of spot-size converter (see Figure 2.24(a) and

2.24(b)) while carrying out second RIE process for a controlled surface trimming. As shown in the scheme (Figure 2.24(a) and 2.24(b)), the photoresist mask terminates with horizontally tapered section along the waveguides ( $L \sim 100 \mu\text{m}$ ,  $W_B = 7 \mu\text{m}$ ,  $W_T = 1 \mu\text{m}$ ). The expected values of  $L_{SSC}$  (length of lateral tapering) and  $L_H$  (length of vertical tapering) can be calculated from the following slope equations:

$$L_{SSC} = \frac{W_0 - W_T}{W_B - W_T} L \quad (2.9)$$

$$L_H = \frac{\alpha t - W_T}{W_B - W_T} L \quad (2.10)$$

Here,  $L_{SSC}$  is controlled mainly by the photoresist mask and  $L_H$  is controlled by photoresist mask as well as the isotropic nature of second RIE. To study the length dependent insertion loss of the taper structure, the tapering mask lengths were varied from  $60 \mu\text{m}$  to  $240 \mu\text{m}$  with a step of  $20 \mu\text{m}$  for fixed values of  $W_B = 7 \mu\text{m}$  and  $W_T = 1 \mu\text{m}$ . The value of  $W_B$  was intentionally kept higher than the width of LCRW to avoid rounding corners at the junction; whereas,  $W_T$  was kept lower than the width of RCRW for a smooth vertical as well as horizontal tapering of SSC after second RIE. The duration of second RIE was 7 min. 20 sec. so that the effective length of SSCs ( $L_{SSC}$ ) is expected to be varying from  $40 \mu\text{m}$  to  $160 \mu\text{m}$ . The overall waveguide height is also expected to be reduced from  $5 \mu\text{m}$  to about  $2 \mu\text{m}$  over a length ( $L_H$ ) ranging from  $20 \mu\text{m}$  to  $80 \mu\text{m}$ . Calculated and experimental values (measured from confocal microscopic images) of  $L_{SSC}$  and  $L_H$  as a function of  $L$  are plotted in Figure 2.24(d). The deviation in measured values is mainly due to misalignment during the lithography process. SEM image of a fabricated SSC which was originally designed with  $L = 60 \mu\text{m}$ ,  $L_{SSC} = 40 \mu\text{m}$  and  $L_H = 20 \mu\text{m}$  has been shown in figure 2.25(a) along with a neighboring reference RCRW. After the fabrication, effective lengths of  $L_{SSC}$  and  $L_H$  as estimated by confocal microscopy are  $42 \mu\text{m}$  and  $18 \mu\text{m}$ , respectively. This deviation is again attributed to the slight misalignment during photolithographic definition of SSCs which is clearly evident in the SEM image shown in figure 2.25(a). Six different types of device structures were monolithically integrated to study overall performances of SSCs with ten different lengths. They include reference waveguides (LCRW and RCRW/PhWW), waveguide with one taper (W1T), waveguide with two tapers (W2T), waveguide with four tapers (W4T) and waveguide with six tapers (W6T). Schematic layout of a set of fabricated

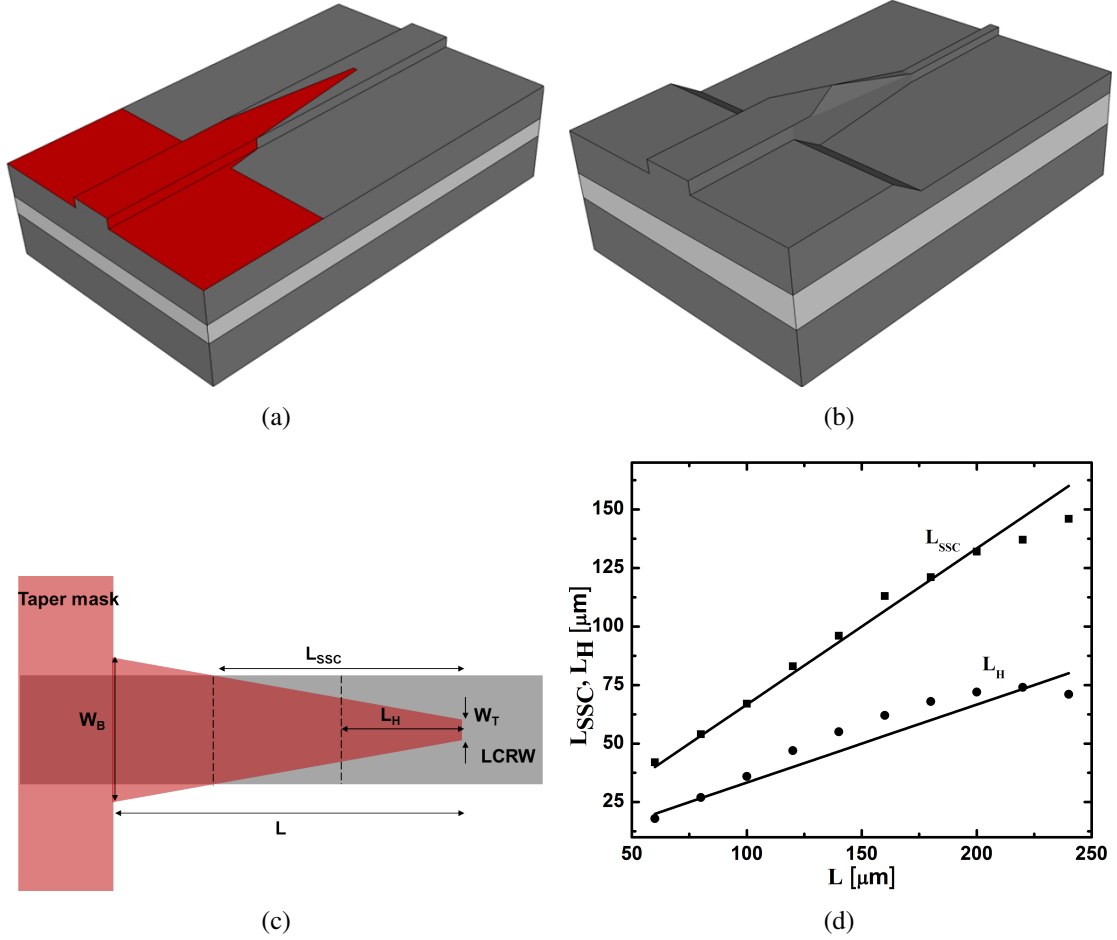


Figure 2.24: SSC fabrication scheme: (a) 3D schematic view of LCRW along with photoresist mask for SSC, (b) 3D schematic view of an integrated LCRW, SSC and RCRW after second RIE, (c) photoresist mask showing tapering parameters  $W_B$ ,  $W_T$ ,  $L$ ,  $L_{SSC}$ , and  $L_H$ ; (d) plots showing calculated (solid lines) and measured (dots) values of  $L_{SSC}$  and  $L_H$  as a function of  $L$  for a pre-defined values of  $W_B = 7 \mu\text{m}$  and  $W_T = 1 \mu\text{m}$ .

devices is shown in Figure 2.25(b). In order to obtain insertion/coupling losses, the devices were butt-coupled with standard single mode fibers (Corning SMF-28e) at both input and output waveguide end-facets (see figure 2.26(a)). Typical insertion loss for an LCRW, a W2T ( $L_{SSC} = 145 \mu\text{m}$ ) and an RCRW were measured to be  $\sim 8$  dB,  $\sim 13$  dB, and  $\sim 17$  dB, respectively. Comparing the insertion losses between LCRW and W2T, one can estimate the insertion loss of 2.5 dB for a 145- $\mu\text{m}$ -long SSC (assuming same waveguide losses for LCRW and RCRW). Similarly, comparing the insertion losses between W2T and RCRW, we could estimate improvement in fiber-to-chip coupling efficiency by a margin of 2 dB (fiber-LCRW-SSC-RCRW vs fiber-RCRW). To minimize errors in fiber-waveguide misalignment, we replaced the output side fiber coupler with

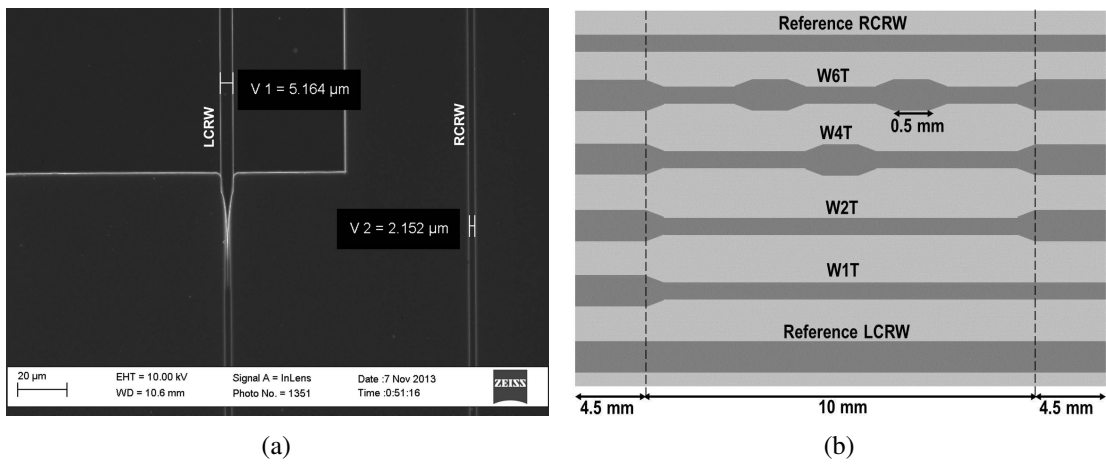


Figure 2.25: SEM images of fabricated spot-size converters, (a) LCRW to RCRW spot size converter along with reference RCRW waveguide and (b) Schematic top view of fabricated waveguide structures ( $l = 19$  mm): W#T - waveguide with # SSC(s).

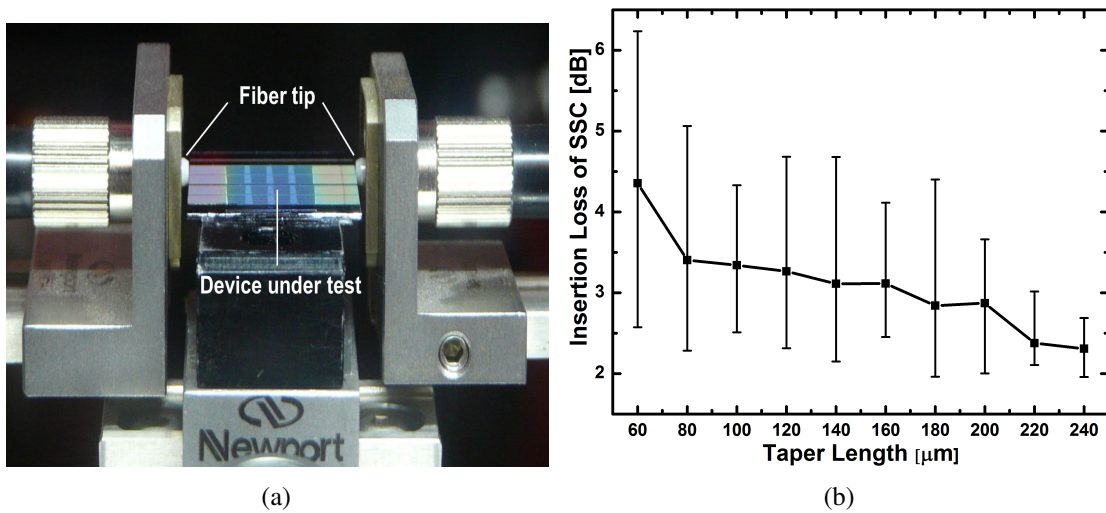


Figure 2.26: (a) Fiber butt coupling setup used for measuring the insertion losses and (b) extracted insertion loss of SSC as a function of taper length.

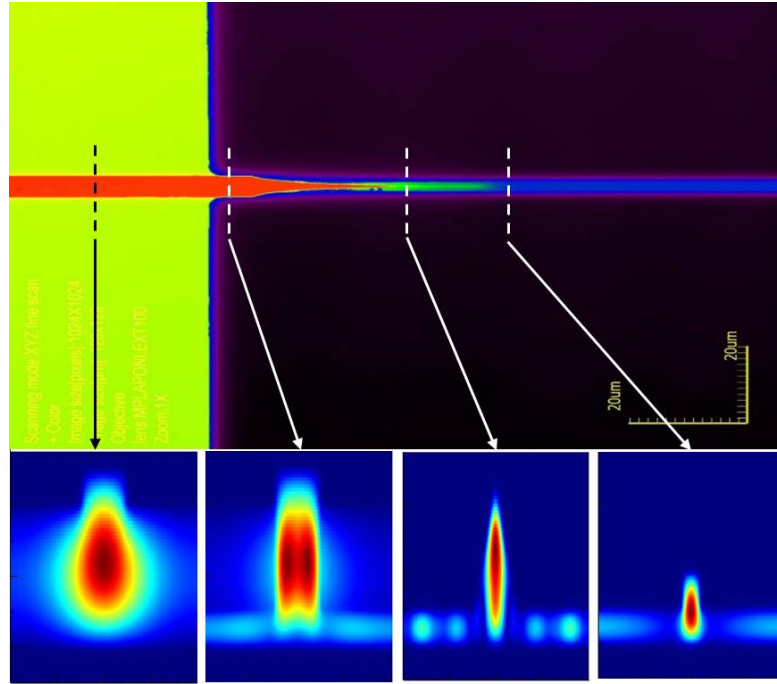


Figure 2.27: Confocal microscopic image of a SSC (color variation represents the relative height variation) with simulated mode profiles (shown as inset) at various parts of the SSC.

a free-space lens coupling arrangement to measure throughput power. The insertion losses for SSCs were extracted from experimental results and their average values are plotted as a function of  $L$  in Figure 2.26(b). Average insertion loss of  $\sim 2.3$  dB has been noted for 145  $\mu\text{m}$ -long SSCs (slightly lower than the earlier measurement). Better alignment during the photolithographic definition of SSCs can ensure further improvements in insertion loss and fiber-to-chip coupling efficiency. It is interesting to notice from Figure 2.26(b) that the average insertion loss of the SSC reduces as  $L$  increases. However, fluctuation of the insertion loss from device to device is in fact very high. This hints that the possible excitation of higher order modes in transition region (SSC). In order to confirm this, we have used the Lumerical Eigen Mode Expansion (EME) solver for simulating SSC structure. Figure 2.27 shows the confocal microscopic image of a SSC with the simulated mode profiles at various parts of the SSC (shown as inset). From the confocal image, it is clear that the height of the rib varies slowly (color gradually varies from red to blue). However the slab height variation is not gradual indicated by an abrupt change of yellow color to black at the beginning the shoulder of SSC. This leads to a deeply etched rib region which supports many modes as it is obvious from the simulated mode profiles in the inset. This suggests that an energy efficient spot size

conversion demands adiabatic variation of all geometrical parameters of the waveguide ( $W$ ,  $H$  and  $h$ ).

### 2.3.2 2D Spot-Size Converters by Shadow Mask Etching

In this section, we present a novel fabrication technique to achieve adiabatic SSC for efficient interconnection of micron to submicron waveguides. In contrast to the photolithographically defined SSC (discussed in the previous section), this technique enables adiabatic transition of all the geometric parameters of the waveguide ( $W$ ,  $H$  and  $h$ ) with the help of a shadow mask etching process such that the higher order mode excitation is suppressed. The schematic view of the entire fabrication process flow has been described in Figure 2.28. Initially, larger waveguides are defined using a photolithography and subsequent RIE (Figure 2.28(a) and (b)). In the next step, surface trimming RIE process is carried out with a shadow mask to obtain reduced cross-section/submicron waveguides integrated with adiabatic SSC (Figure 2.28(c)). A detailed schematic representation of shadow masking is shown in Figure 2.28(d), (e) and (f). In this fabrication process, the shadow mask (plasma mask) is kept above the sample with a separation of about  $500\ \mu\text{m}$  (thickness of silicon substrate) from the sample surface where the waveguides are patterned (see Figure 2.28(d)). Consequently, the plasma is penetrated through the opening (rectangular aperture) made for uniform surface trimming to reduce the waveguide cross-section. However, the plasma penetration through the edges of the aperture is not uniform (Figure 2.28(e) and (f)) and which creates graded plasma distribution along the waveguide. This is in fact responsible for the adiabatic tapering of the waveguides to form an efficient SSC. In this section, we are going to discuss the demonstration of SSC on  $2\ \mu\text{m}$  device layer SOI by obeying the design criteria made in section 2.2.3 as we found that the mode-size of commercially available lensed fiber is matching with the untrimmed waveguide on  $2\ \mu\text{m}$  SOI substrate.

Initially, the singlemode rib waveguides of length ( $L_{tot}$ )  $\sim 15\ \text{mm}$  were fabricated in SOI substrate having handle wafer thickness of  $500\ \mu\text{m}$ , device layer thickness ( $H_0$ ) of  $2.2\ \mu\text{m}$  (vendor specification  $2 \pm 0.5\ \mu\text{m}$ ) and BOX layer thickness of  $1\ \mu\text{m}$ . The width ( $W_0 = 1.7\ \mu\text{m}$ ) of the waveguides were defined by e-beam lithography using neg-

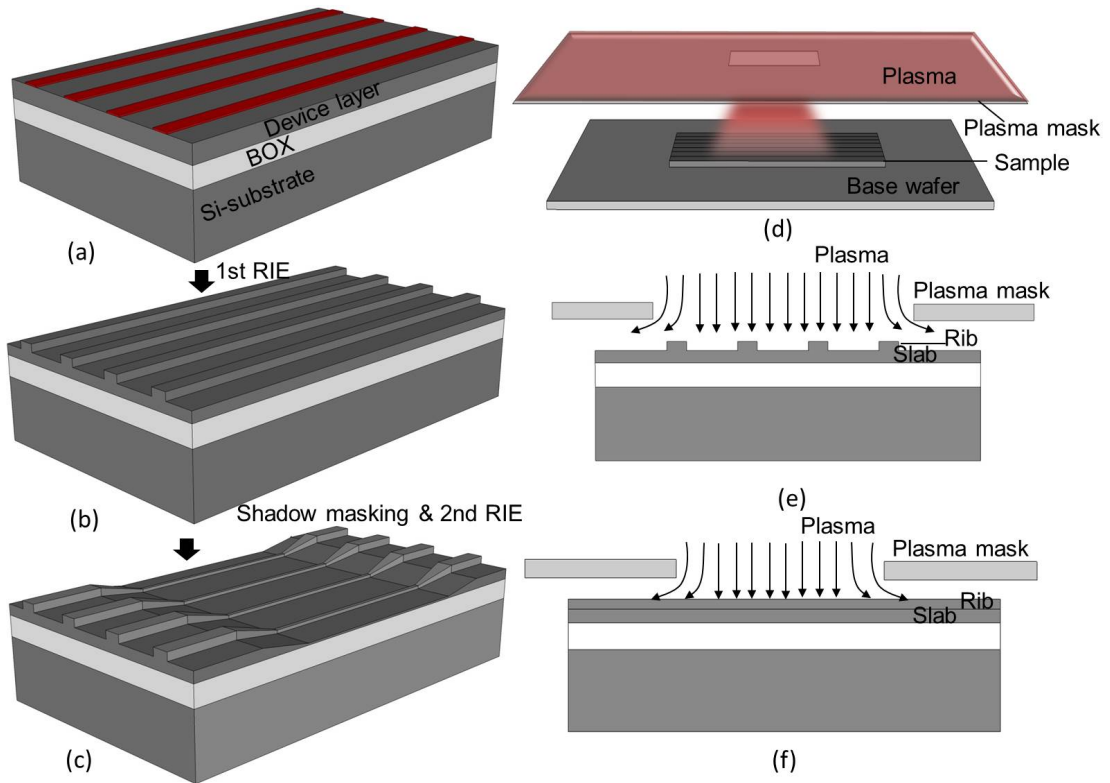


Figure 2.28: Schematic representation of the fabrication process flow for rib waveguide fabrication and follow-up surface trimming using a shadow mask: (a) definition of rib waveguide width by e-beam lithography using negative tone resist HSQ, (b) schematic view of initial rib waveguide (after first RIE and the removal of resist mask), (c) schematic view of adiabatically integrated trimmed waveguide (after second RIE using shadow mask with rectangular aperture), (d) spatial filtering scheme of reactive plasma using shadow mask (silicon substrate in this case) with a rectangular slit aperture, (e) cross-sectional view of the masking scheme during second RIE, and (f) lateral view of the masking scheme during second RIE.

ative tone resist HSQ (Hydrogen Silsesquiane) of thickness  $\sim 100$  nm. Subsequently, a standardized RIE process (gas flow rate = SF<sub>6</sub>:Ar::20:20 sccm, chamber pressure = 200 mT, RF power = 150 W) was carried out to obtain slab height  $h_0$  (etch depth  $H_0-h_0$ ) of  $1.6 \pm 0.5$   $\mu\text{m}$  ( $0.4$   $\mu\text{m}$ ). The etch depth was carefully chosen so that single-mode guidance is not violated even for a device layer thickness variation of  $\pm 0.5$   $\mu\text{m}$ . A second RIE chemistry was used for a localized surface trimming (defined by shadow mask with rectangular shaped slit/aperture) which eventually offers the waveguide height reduction rate ( $\beta$ ) of  $\sim 0.28$   $\mu\text{m}/\text{min}$  and top width reduction rate ( $\alpha$ ) of  $\sim 0.23$   $\mu\text{m}/\text{min}$ . Notice that the difference in the values of  $\alpha$  and  $\beta$  comparing to the values we measured in section 2.2.2 is attributed to the loading effect of dry etching. Figure 2.29 shows the photograph of shadow mask arrangement inside a reactive ion etching system (Oxford Plasmalab80Plus). First, the sample (with pre-defined single-mode waveguides) is placed inside the RIE chamber (see Figure 2.29(a)). Then, a silicon substrate of about 500  $\mu\text{m}$  thickness with a rectangular aperture/opening (fabricated by deep RIE process) is placed on the sample such that waveguides are exposed through the opening (see Figure 2.29(b)). In order to make shadow masking for waveguide surface trimming of finite length, two more cleaved silicon substrates (rectangular shaped) are used (see Figure 2.29(c) and 2.29(d)). Through this arrangement, we could spatially filter a uniform plasma flux on the sample surface of area defined by shadow mask plates (placed about 500  $\mu\text{m}$  above the waveguide surface) and a penetrating graded plasma flux at the boundaries. The penetrated graded plasma flux beneath the shadow mask boundaries helps to form adiabatic SSCs at both ends of trimmed waveguides and ensures efficient light coupling from untrimmed waveguide to the trimmed section.

Prior to final device fabrication, test waveguide samples were fabricated and partly trimmed using the shadow mask technique as discussed. Figure 2.30(a) represent the cross-section of untrimmed waveguide (after first RIE) and Figure 2.32(b) shows the cross-section of trimmed section (after second RIE) for a trimming duration of 2 min. 30 seconds. After ensuring the etching dynamics of surface trimming on 2  $\mu\text{m}$  device layer, we fabricated uniformly trimmed waveguides with a height (width) reduction of 1.1  $\mu\text{m}$  (0.85  $\mu\text{m}$ ) of three different lengths (3 mm, 5 mm, and 7 mm) terminating with adiabatic SSCs of lengths  $\sim 1$  mm at both ends. Figure 2.31 shows microscopic image of two sets of waveguides with 3 mm long trimmed section. The SEM images of



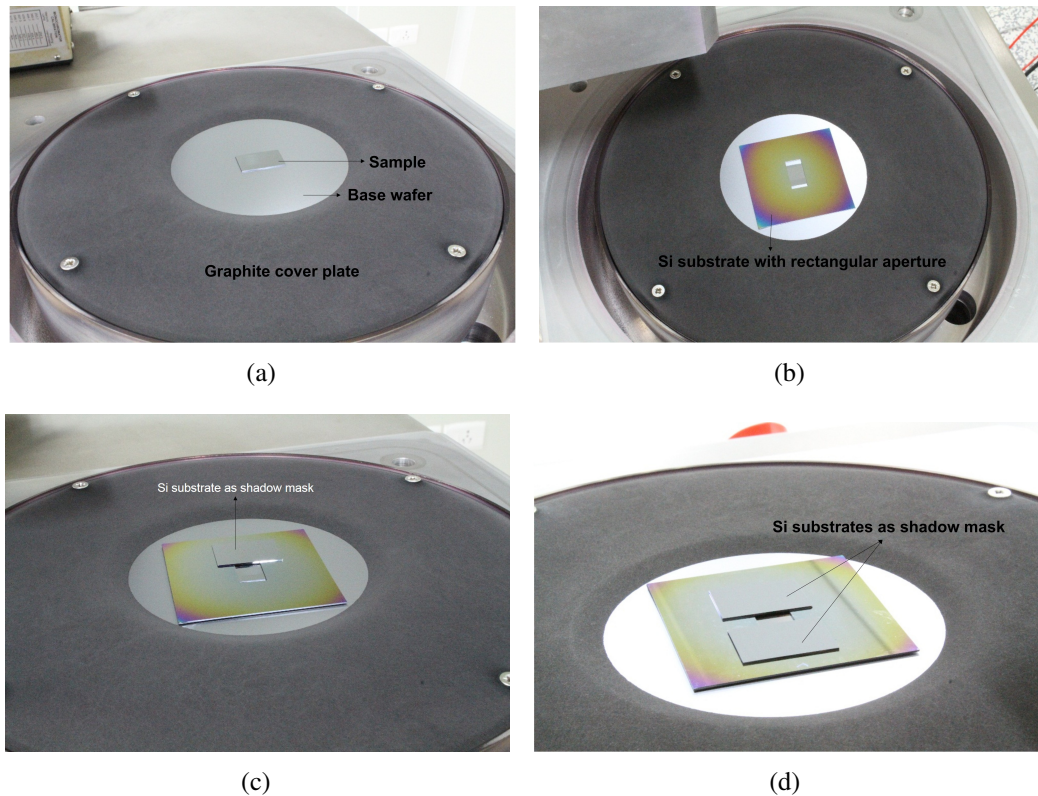


Figure 2.29: Shadow masking steps for waveguide surface trimming using a RIE system (Oxford Plasmalab80Plus): (a) Waveguide sample is placed on the RIE chamber, (b) silicon substrate (thickness  $500\ \mu\text{m}$ ) with a rectangular opening (aperture) is placed over the substrate and (c) two cleaved silicon substrates (rectangular shaped) are used as shadow mask to obtain finite length of trimmed waveguides.

untrimmed and trimmed sections of a waveguide have been shown in figures 2.32(a) and 2.32(b), respectively. It is evident that a rib waveguide of width  $\sim 1.7\ \mu\text{m}$  has been trimmed down to a submicron waveguide of width  $\sim 0.85\ \mu\text{m}$ . The confocal image of a tapered SSCs formed between untrimmed and trimmed waveguides has been shown in figure 2.32(c). It is in fact reveals that the SSCs have three distinct height reduction features (see figures.2.32(d)): the first feature has a measured height reduction of  $50\ \text{nm}$  for a propagating length of  $\sim 430\ \mu\text{m}$ , the second feature has a height reduction of  $\sim 600\ \text{nm}$  for a propagating length of  $\sim 50\ \mu\text{m}$ , and the third feature has a height reduction of  $\sim 500\ \text{nm}$  for a propagating length of  $\sim 550\ \mu\text{m}$ . However, the width reduction has two distinct features (see Figure 2.32(e)): the first feature has Gaussian type width reduction of  $400\ \text{nm}$  for a propagation length of  $70\ \mu\text{m}$ , and the second feature has an exponential type width reduction of  $450\ \text{nm}$  over a propagation length of  $\sim 1\ \text{mm}$ . All these fine tapering

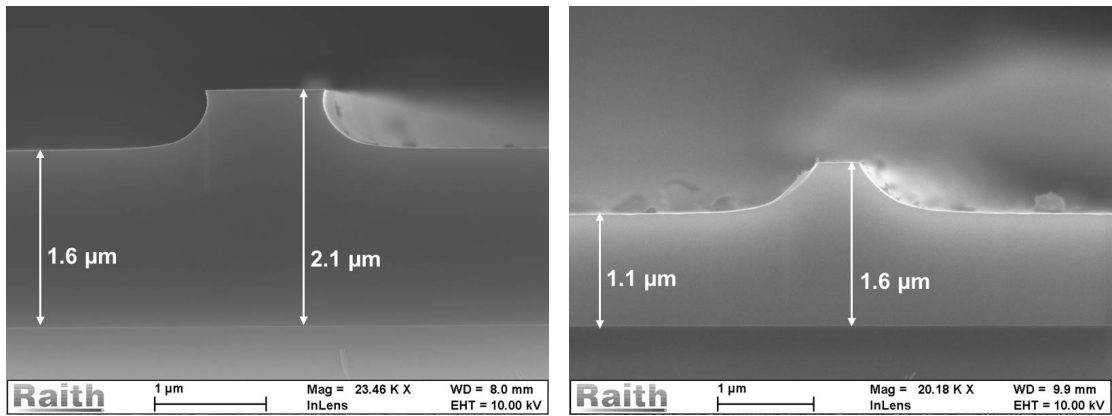


Figure 2.30: Cross-sectional SEM image of waveguide fabricated to verify the fabrication process proposed, (a) before and (b) after trimming.

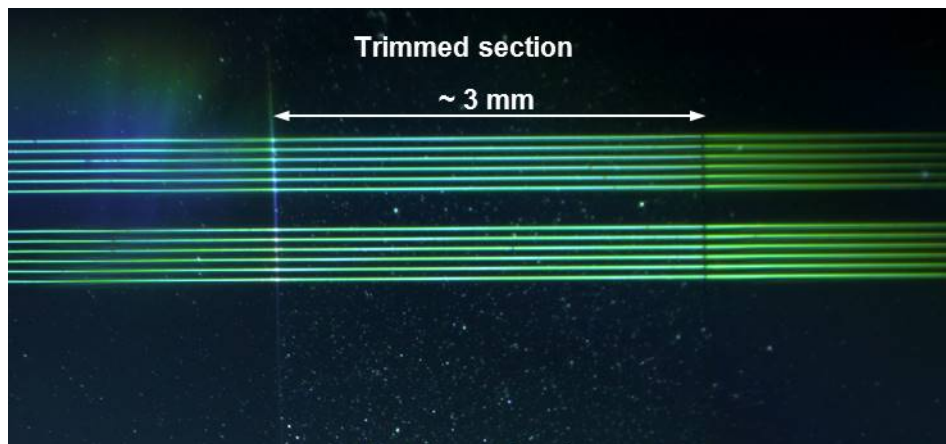
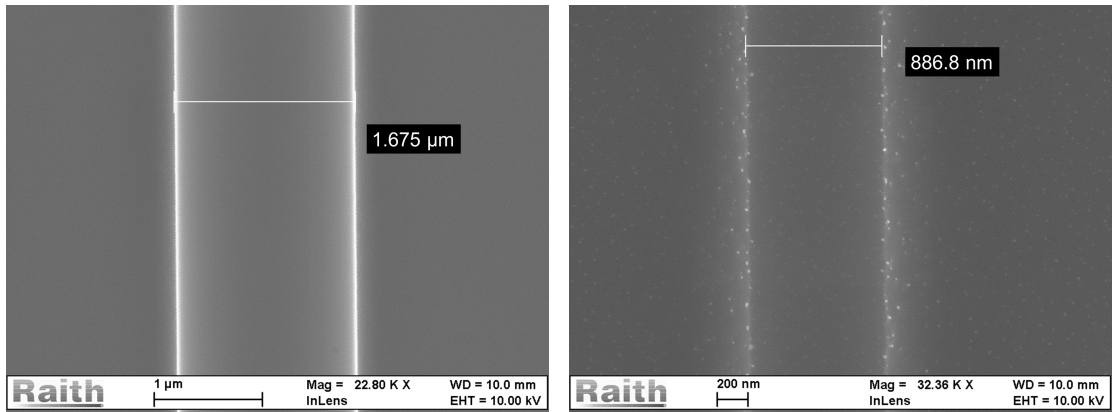
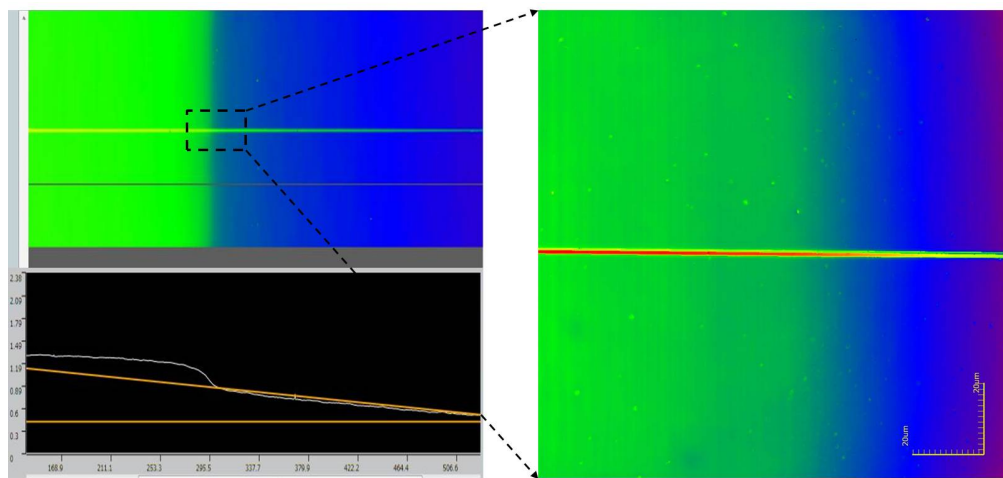


Figure 2.31: Photographic image of the fabricated sample. It shows two sets, each having 6 waveguides with 3 mm long trimmed sections.

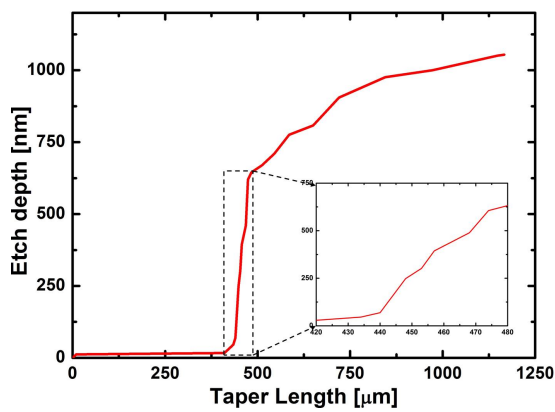


(a)

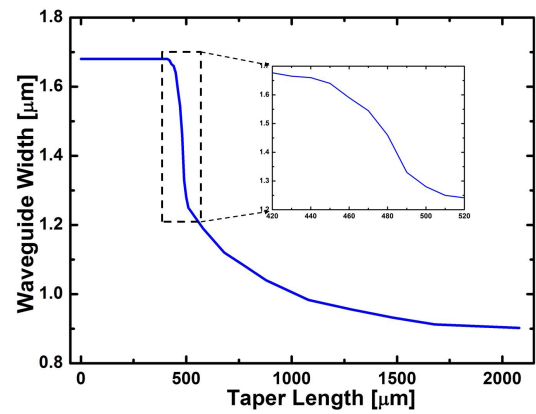
(b)



(c)



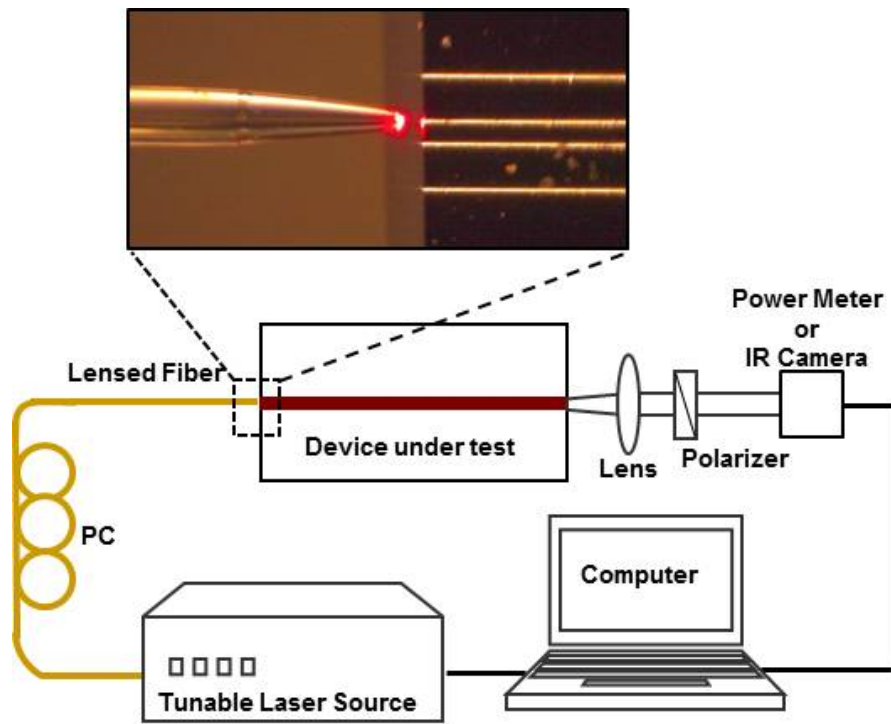
(d)



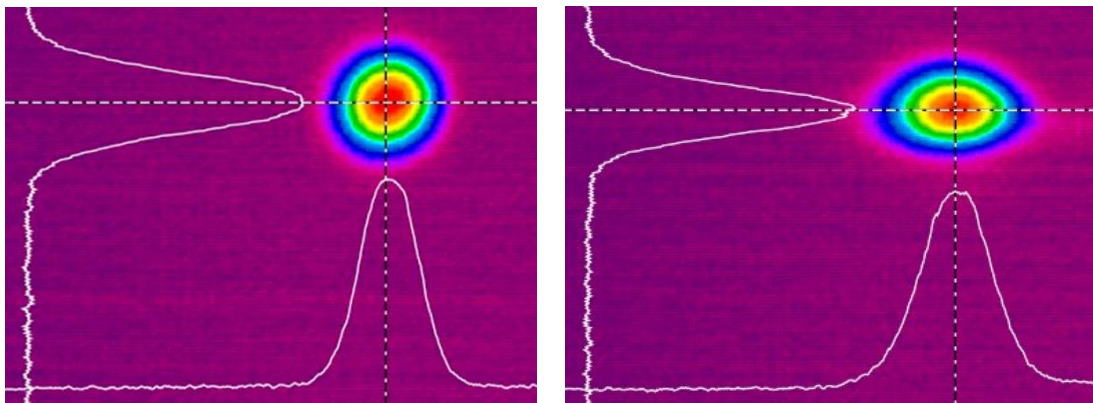
(e)

Figure 2.32: (a) SEM image of an untrimmed rib waveguide region, (b) SEM image of a trimmed waveguide region, (c) confocal images of a SSC showing etch depth variation along the propagation length (magnified view of the confocal images is shown on the right side), (d) measured etch depth and (e) width variation of the SSC; etch depth was measured by confocal imaging, whereas width variation was estimated by taking SEM images at regular interval along the length.

features may be attributed to a nonuniform distribution of plasma flux near the edges of the shadow mask (cleaved silicon wafer). Further, it is also confirmed that the slab height surrounding the SSC reduces at the same rate as the rib height. This in fact results into a single-mode guidance (at  $\lambda \sim 1550$  nm) throughout. The insertion loss and group index ( $n_g$ ) of the above mentioned locally defined submicron trimmed waveguides have been extracted by Fabry- Perot resonance technique; cavity is formed by careful polishing of input/output waveguide end-facets. Fabry-Perot transmission characteristics as a function of wavelength were obtained using the end-fire light coupling setup (see Figure 2.33(a)). Light from a tunable laser source is launched at the input waveguide (untrimmed) with the help of a lensed fiber (supplied by OZ Optics Ltd.) having focussed spot-size of  $\sim 3.3 \mu\text{m} \times 3.3 \mu\text{m}$  ( $1/e^2$  intensity distribution) at a distance of  $\sim 30 \mu\text{m}$  from the fiber tip. The inset of Figure 2.33(a) shows the microscopic image of lensed fiber kept at  $\sim 30 \mu\text{m}$  away from the input waveguide end-facet. Initially, a visible laser light ( $\lambda \sim 632$  nm) was used for aligning the input beam parallel to waveguide axis. At the output side, a  $60\times$  objective lens has been used to collect the transmitted light from waveguide and collimated to IR camera (for mode profile measurements) or power meter (for wavelength dependent transmission characteristics) after a polarization filter (TE-like or TM-like). Figures. 2.33(b) and 2.33(c) show the measured intensity distribution (for TE-polarization at  $\lambda = 1550$  nm) at the focal plane of lensed fiber and the guided mode intensity distribution (near-field) of an untrimmed waveguide, respectively. The guided mode-size of the untrimmed waveguide is measured to be  $\sim 4.5 \mu\text{m} \times 2.7 \mu\text{m}$ . Thus we could ensure an overlap of  $\sim 86\%$  between focussed spot-size of the lensed fiber and the guided mode of the untrimmed waveguide at the input. The completely untrimmed reference waveguide and three different waveguides with trimmed section (integrated in the middle) of lengths 3 mm, 5 mm, and 7 mm, respectively, were fabricated on the same SOI substrate and all are of 15 mm in total length; the reference waveguides and input/output region of the trimmed waveguides were protected by the shadow mask during second RIE (for surface trimming). The Fabry-Perot transmission characteristics (for TE-polarization) of a completely untrimmed reference waveguide and a partly trimmed waveguide (7-mm-long trimmed section in the middle) have been shown in Figure 2.34(a). The transmission characteristics of a waveguide with longer trimmed section helps to minimize errors in estimating the differential



(a)



(b)

(c)

Figure 2.33: (a) Characterization setup used for waveguide characterizations; Inset: photograph showing lensed fiber being aligned parallel to waveguide axis at the input side with the help of visible laser light ( $\lambda = 632$  nm); (b) intensity distribution of the focussed spot-size of a lensed fiber at  $\lambda = 1550$  nm; (c) intensity distribution of the guided mode of an untrimmed waveguide measured at the output (near-field image).

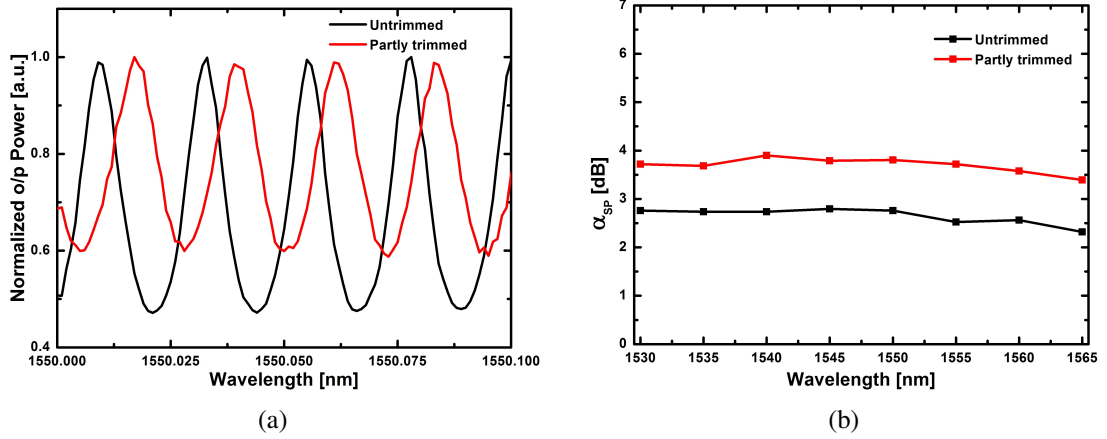


Figure 2.34: (a) Fabry-Perot transmission characteristics of untrimmed 15 mm long reference waveguide (black line) and equally long waveguide with 7 mm long trimmed (red line) section for TE polarization; (b) Measured single-pass waveguide loss ( $\alpha_{SP}$ ) as function of wavelength over C band of optical communication spectrum, the values are extracted from Fabry-Perot resonance spectrum.

change in group index and propagation losses, etc. It should be noted that the Fabry-Perot transmission characteristics of the waveguides integrated with trimmed section do not exhibit any additional signature (of a possible cavity formed between SSCs), which in fact ensures a smooth and adiabatic spot-size conversion. By noting down the contrast of Fabry-Perot transmission characteristics, we have calculated single-pass propagation loss of  $\sim 2.7$  dB (equivalent to the waveguide loss of  $\sim 0.18$  dB/mm) for untrimmed reference waveguides, whereas that for the waveguides with 7-mm-long trimmed section is  $\sim 3.9$  dB. Similarly, the single-pass propagation loss for waveguides with 5-mm-long and 3-mm-long trimmed sections have been estimated to be  $\sim 3.6$  dB and  $\sim 3.2$  dB, respectively. These single-pass propagation losses were estimated by assuming the end-facet reflectivity equal to  $R_F = [(n_{eff} - n_{air}) / (n_{eff} + n_{air})]^2 = 0.31$ ; where,  $n_{eff}$  is the calculated effective index of the guided fundamental mode of an untrimmed reference waveguide. However, the actual end-facet reflectivity  $R$  will be always lower than the value of  $R_F$  because of imperfections in end-facet preparation. Thus the actual single-pass losses must be much lower than the above mentioned calculated values. Therefore, it is reasonable to conclude that the insertion loss of a typical SSC should not exceed  $[(3.2 \text{ dB} - 2.7 \text{ dB}) / 2] = 0.25$  dB; and the trimmed waveguide loss can be approximated to be  $[3.9 \text{ dB} - 0.25 \text{ dB} \times 2 - 6 \text{ mm} \times 0.18 \text{ dB/mm}] / 7 \text{ mm} = 0.33$  dB/mm. Figure 2.34(b) shows the wavelength dependent single pass loss ( $\alpha_{SP}$ )

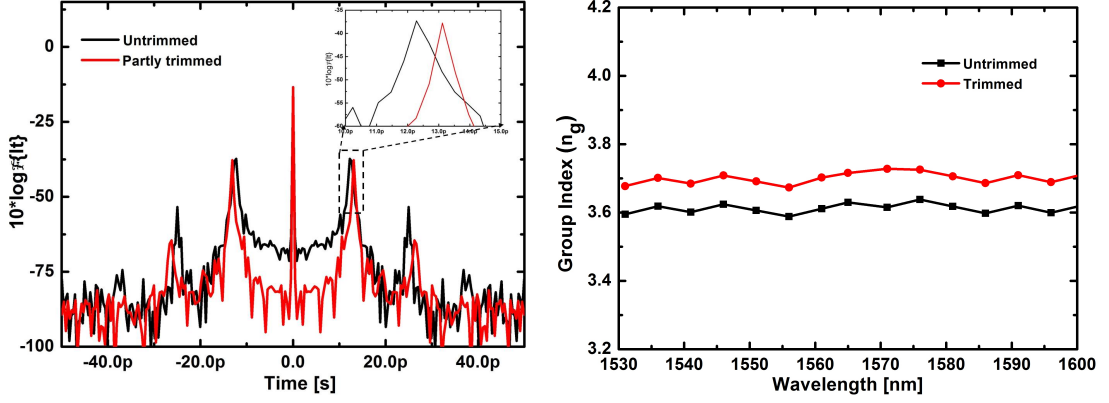


Figure 2.35: (a) Frequency domain discrete Fourier transformed data (corresponds to Fabry-Perot transmission characteristics for a wavelength range of  $1550 \text{ nm} \leq \lambda \leq 1552 \text{ nm}$ ) plotted as a function of time-delay for the untrimmed reference waveguide (black line) and the waveguide having 7-mm-long trimmed section (red line). (b) Extracted group indices ( $n_g$ ) for untrimmed and trimmed waveguides a

for both untrimmed and partly trimmed waveguides for TE polarization. The values have been extracted from the Fabry-Perot resonance spectrum. The plots show that the fabricated trimmed waveguide are nearly wavelength independent. Though the upper limit of various loss parameters could be extracted directly from the measured Fabry-Perot transmission characteristics as a function of wavelength, the differential change in group index in trimmed waveguide sections could not be extracted as the free spectral range ( $\text{FSR} = \lambda^2 / 2n_g L$ ) could not be resolved below 1 pm (limited by wavelength tunability of the laser source used in the experiment). To overcome this, we recorded Fabry-Perot transmission spectrum as a function of wavelength for a span of 2 nm (in steps of 1 pm) around a given operating wavelength. Subsequently, converting wavelengths into angular frequency ( $\omega = 2\pi c / \lambda$ ), we carried out discrete Fourier transform (DFT) of the transmitted spectrum to obtain round-trip group delay of the Fabry-Perot cavity (and hence the group index  $n_g$ ) by estimating the distance between two successive peaks. The DFT spectra of a reference waveguide and a test waveguide (with 7-mm-long trimmed section in the middle) have been presented in figure 2.35(a) for  $1550 \text{ nm} \leq \lambda \leq 1552 \text{ nm}$ . The difference in round-trip group delay could be resolved ( $\sim 0.8 \text{ ps}$ ) between the two waveguides by noting down the peak positions (see the inset of figure 2.35(a)).

The absolute group indices for the untrimmed and trimmed waveguides have been

evaluated and shown in figure 2.35(b) as a function of wavelength for TE-polarization. The group index of the integrated trimmed waveguide was calculated using the following relation:

$$n_g^T = \frac{n_g^C \times L_{tot} - n_g^{UT} \times L_{UT}}{L_T} \quad (2.11)$$

Here,  $n_g^T$ ,  $n_g^{UT}$  and  $n_g^C$  are the group indices of trimmed, untrimmed and combined waveguide structures respectively.  $L_{UT}$  and  $L_T$  are the lengths of untrimmed and trimmed sections respectively.  $L_{tot}$  is the total length of the combined structure, in this case 15 mm. As expected the group index of trimmed waveguide is reduced by a margin of  $\Delta n_g \sim 0.1$ , which is slightly higher than the theoretical prediction.

### 2.3.3 Grating Assisted 1D Spot-Size Converter

Apart from integrating multiple waveguide cross-sections on a single substrate platform, we found that the proposed waveguide trimming is also useful for dispersion engineering as well as fabrication error correction or local modification of waveguide cross-section in the post-fabrication steps. Though the proposed trimming technique is useful for various applications, it is not desirable to define structures such as directional couplers, DBR, etc. in submicron regime. In the proposed trimming technique, structures are defined in larger cross-section and trimmed down to reduce waveguide cross-section. Consequently, separation between the waveguides/features, in case of directional coupler/DBR region is increased. This severely affects the performance of the directional coupler/DBR. So the solution to this problem would be fabricating these components directly on a submicron device layer ( $\sim 250$  nm) SOI.

But the main challenge with this devices fabricated directly on submicron SOI substrate is that the light coupling from standard single-mode fiber (SMF). There were various approaches (as discussed in Chapter 1) that has been adopted for coupling light from SMF to submicron waveguides. Among that grating coupler is found to be most feasible CMOS compatible approach in the fact that this can be fabricated along with waveguide without additional process steps and no end-facet preparation is required as in the case of inverse or forward SSC. In addition to that light can be coupled in and out anywhere on the chip is being tested. In grating assisted SSC converter, light from SMF



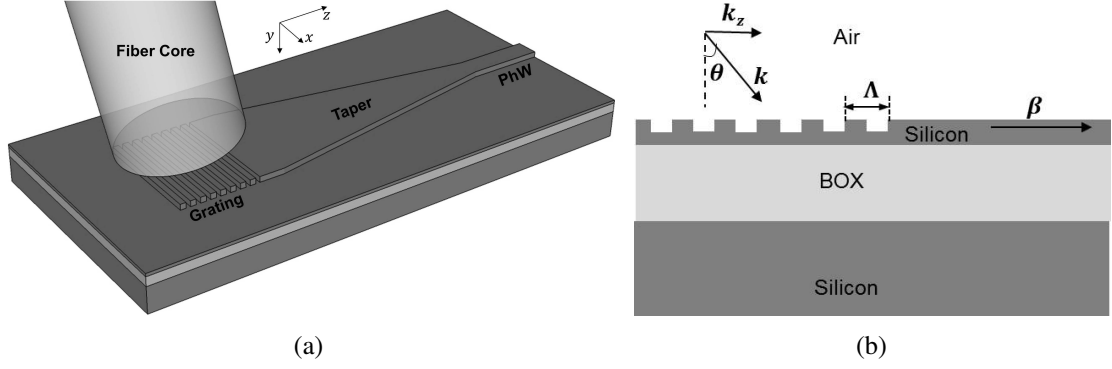


Figure 2.36: (a) 3D schematic view of grating coupler integrated with photonics wire waveguide to couple light from SMF and (b) lateral schematic view of the waveguide with grating coupler.

is coupled to the waveguide with the help of grating structures formed on the waveguide. Figure 2.36(a) shows the 3D schematic view of a grating assisted SMF to PhWW light coupling setup. Lateral schematic view of the grating coupler along waveguide direction is shown in Figure 2.36(b). Here the light from the SMF is falling on the grating region with a wavevector  $\mathbf{k}$  and diffracted towards the taper section. This diffracted light can be coupled to the guided mode of the waveguide by a phase matching condition:

$$\beta - k_z = \frac{2\pi}{\Lambda} \quad (2.12)$$

where,  $k_z = \mathbf{k} \sin \theta = 2\pi \sin \theta / \lambda_0$  is the  $z$  component of the wavevector  $\mathbf{k}$ ,  $\beta = 2\pi n_{eff} / \lambda_0$  is the propagation constant fundamental mode with effective index  $n_{eff}$  of the waveguide and  $\Lambda$  is the grating period. Using eq. 2.12 the value of  $\Lambda$  for a waveguide fabricated on 250 SOI substrate can be calculated to be  $\sim 600$  nm. As a result, the minimum feature size is estimated to be  $\sim 300$  nm for grating with a 50 % duty cycle. Lithographic definition of this submicron feature size is not possible with i-line (365 nm) photolithography. So, the remaining part of this section discusses the fabrication optimization of submicron waveguide structure using electron beam lithography system (Raith 250 TWO) and characterization of submicron waveguide integrated with grating coupler SSC.

Fabrication optimization for submicron waveguide structures using electron beam lithography include the right choice of system parameters such as aperture, acceleration voltage, working distance along with the process parameters such as spin coating of

electron beam resist, electron beam dose, developing time and dry etching. The size of patterning aperture decides the electron beam current and energy spread of the electron beam. Smaller aperture is better for constant electron beam energy and higher depth of focus. However, the electron current for a small aperture is low which in turn increases the patterning time. As a result, aperture size should be selected optimally considering the patterning time also. Acceleration voltage decides the energy of the electron beam which in turn decides the spread due to forward or backward scattering. At lower acceleration voltage forward scattering is dominated and which results in the proximity effects (unwanted electron beam exposure) of closely spaced structure. At higher acceleration voltage, backward scattering is dominated, however, for an electron beam resist with thickness  $< 200$  nm, backscattering does not create much problem as the beam is penetrated deep in to the substrate. The challenge at higher acceleration voltage is surface imaging or beam correction as the higher energy electron hardly produces secondary electrons at the surface of the resist. As a result, the acceleration voltage should be selected by considering the proximity effects as well as easiness of imaging or beam correction. Working distance (distance between the column and sample surface) decides the magnification and depth of focus. At smaller working distance the magnification can be increased and thus better resolution of electron beam patterning. However, the depth of focus of the electron beam deteriorates at smaller working distance and thus poor quality of writing over a large area exposure. Thus the working distance has to be chosen by considering the required magnification (resolution) and area of patterning (uniformity).

As a first step of process optimization, we have chosen Hydrogen silsesquioxane (HSQ) as electron beam resist. Since HSQ (XR-1541) is a negative tone resist, patterning time can be minimized as it needs to expose only on the waveguide regions. In addition to that an uniformly coated HSQ can be used as etch mask during pattern transfer to silicon using dry etching process. The optimum HSQ spin coating parameters for an uniform thickness of  $\sim 100$  nm is found to be: speed - 3000 rpm, acceleration - 1500 rpm/sec. and time - 40 sec. We have used MF-319 (Microposit <sup>®</sup>) solution as developer for HSQ. Optimized HSQ coating parameters are summarized in Table 2.1. Spread step is used to spread the resist over sample surface and Coat step is used for getting an uniform resist layer of 100 nm. For electron beam patterning, Raith 150

Process step	Speed [rpm]	Acceleration [rpm/sec.]	Time [sec.]
Spread	100	100	10
Coat	3000	1500	40

Table 2.1: Optimized spin coating parameters for HSQ (XR-1541) electron beam resist to achieve 100 nm thick uniform layer.

TWO electron beam lithography system provides two different patterning techniques - (1) conventional patterning (CP) and (2) fixed beam moving stage (FBMS). In CP, the entire patterning area is divided as small write fields and each write field is written sequentially. While patterning on each write field, the stage (which holds the sample) position is fixed such that the electron gun is at the middle of the write field and electron beam is deflected throughout the write field to pattern the design. Then the stage is moved to the next write field and continues the patterning in similar fashion. This patterning may create stitching error between the write fields if the stage is not exactly positioned and practically there can always be a positioning error of  $\sim \pm 100$  nm. This poses a difficulty of patterning longer (5 -10 mm) waveguide structures using CP technique. In FBMS patterning technique, as its name suggests the beam is fixed and the stage is continuously moving according to the design. This enables stitch free writing of longer patterns. However, FBMS is not capable of patterning any arbitrary shape but it facilitates the patterning of a line with predefined width to write any shape. The width of FBMS line can be varied from a single pixel to several microns between the design components but not in a single component. In photonic waveguide design, waveguide is defined using the FBMS patterning as the width of the waveguide remains same throughout. However, the width of 1D taper section associated with the grating coupler region changes along the propagation direction (see Figure 2.36(a)), this demands the patterning of this region using CP technique. Then the difficulty is to align the patterns written using two different patterning strategies (CP and FBMS) as practically there would be stage positioning error. In order to overcome this problem, we have written the waveguide and the boundary of grating coupler as a single unit using FBMS technique, and the inside portion of grating coupler is filled by CP. Since we have kept an overlapping region between FBMS and conventional writing, misalignment patterning can be ruled out. Figure 2.37(a) shows a typical mask layout consisting

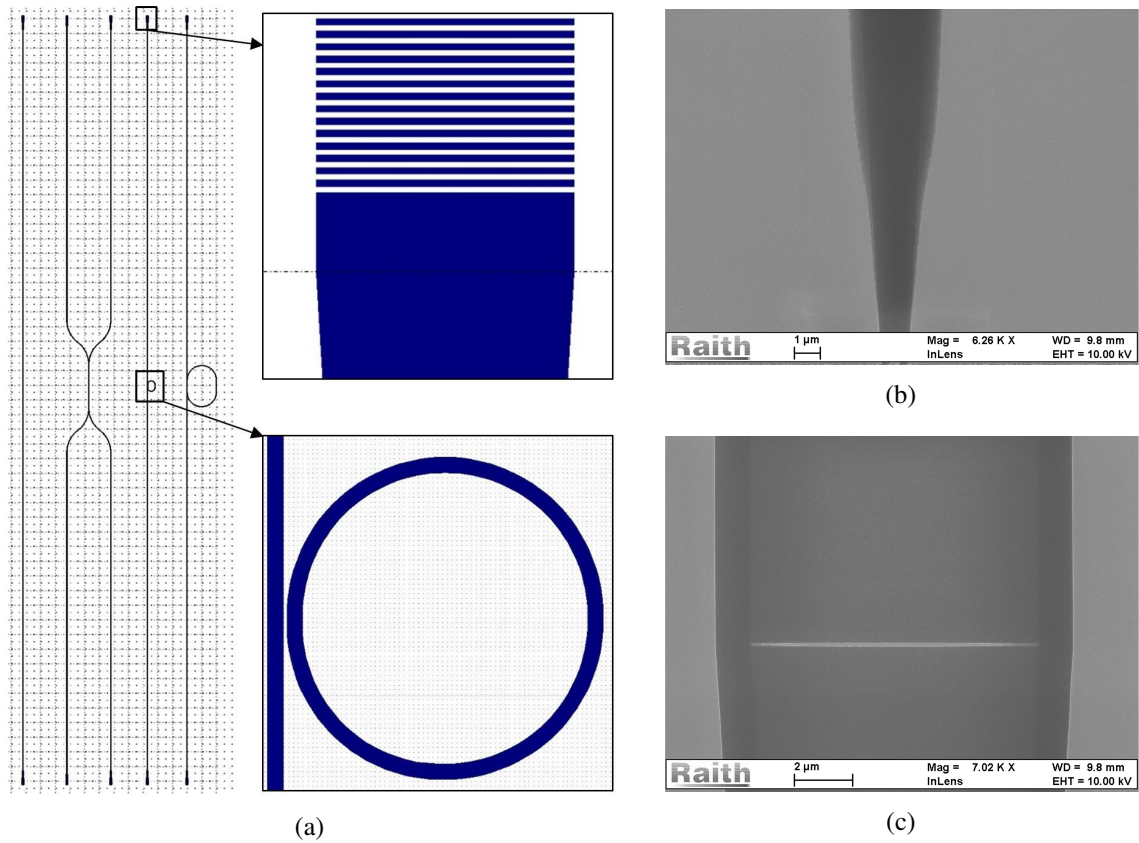


Figure 2.37: (a) Typical electron beam lithography mask layout consisting of ring resonators, straight waveguide and directional coupler with grating coupler at both the ends. Grating coupler and ring resonator regions are magnified and shown as inset. Dashed line in the layout represents the write field ( $100 \mu\text{m} \times 100 \mu\text{m}$ ) boundary. (b) SEM images of the PhW-SSC junction and (c) grating coupler section through which write field is passed.

of ring resonators, directional couplers and straight waveguides with grating coupler at both ends. Critical regions of the design are shown as inset. The write field size for the patterning is set to be an optimum value of  $100 \mu\text{m} \times 100 \mu\text{m}$  for better resolution as well as to keep the stitch fields minimum as possible for the CP. The dashed line in Figure 2.37(a) represents the write field boundary. During initial optimization process, we have observed that the designed FBMS line width and the patterned line widths are not equal and the patterned line width is  $\sim 100 \text{ nm}$  less than the design at optimum dose. So, we estimated that to have a  $550 \text{ nm}$  wide waveguide, the FBMS line width in the design should be  $650 \text{ nm}$ . This would ensure an overlap of  $325 \text{ nm}$  between the FBMS and CP elements in the grating coupler region. As a result, the design can accommodate a shift (misalignment) up to  $325 \text{ nm}$  between the conventional and FBMS structures. Since a single FBMS line covering the longer waveguide region and the

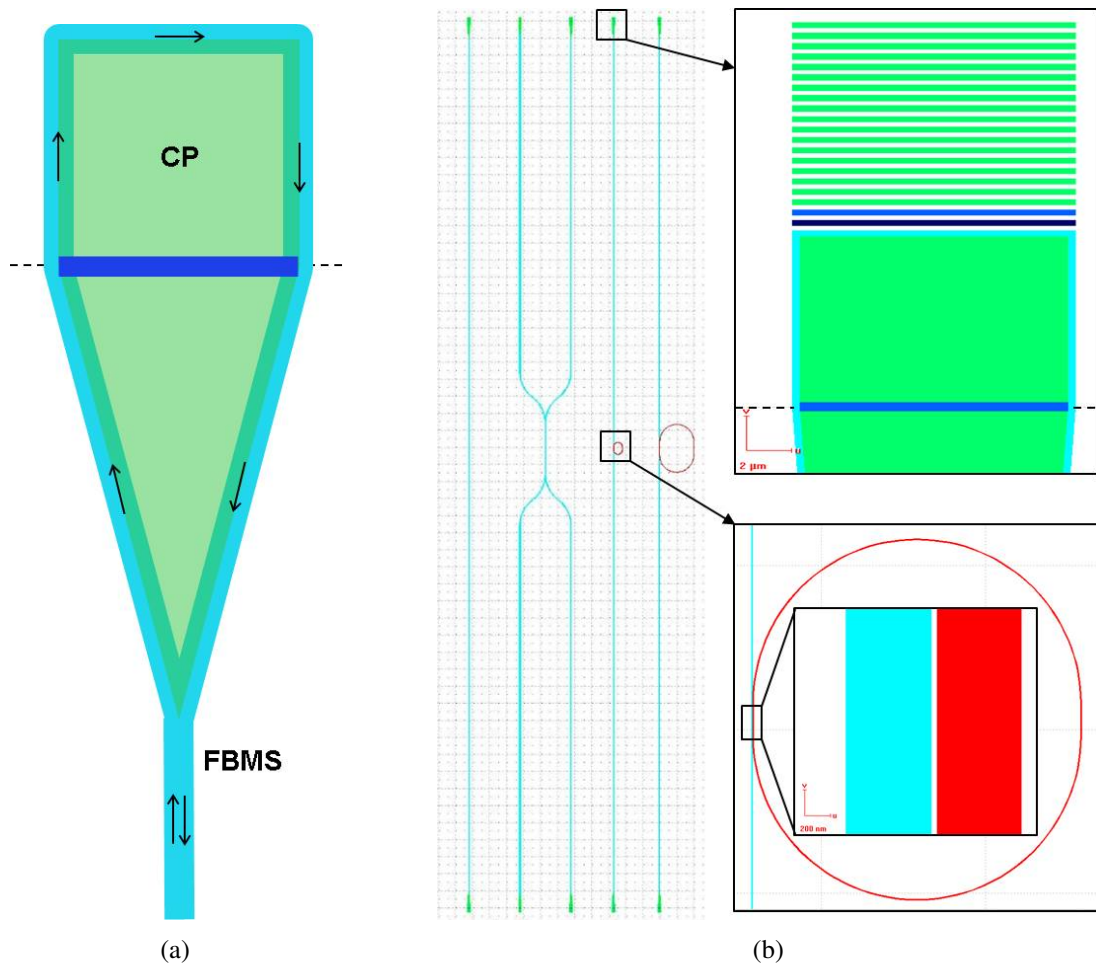


Figure 2.38: (a) Schematic representation of the trace-retrace patterning strategy for waveguide. where arrows on the FBMS represents the patterning direction of FBMS. Design color represents the relative dose of the components.(b) Modified Mask layout for electron beam lithography. Magnified view of the grating coupler and ring resonator are shown in the inset.

outline (boundary) of grating coupler, FBMS dose along the path is same. This creates another problem that when the FBMS dose is optimum for the waveguide region, the grating coupler boundary and the grating coupler-waveguide junction are widened due to over dose at optimum CP dose. Figure 2.37(b) shows the grating coupler-waveguide junction when the optimum dose for both the waveguides (FBMS) and grating coupler taper region (CP). Due to the proximity effects between conventional and FBMS patterning, the junction region has not been defined clearly. In order to circumvent this problem, we have slightly reduced the conventional pattern dose so that proximity effects are reduced at the grating coupler boundary. The reduction of CP dose has in fact eliminated the proximity effects at the grating coupler boundary and junction regions, however, stitch field error at the write field boundary has become more prominent (see Figure 2.37(c)). In addition to that the HSQ layer thickness in the grating coupler taper region is reduced to a large extent as the dose is reduced and it can be clearly observed from Figure 2.37(c).

Considering all the above mentioned problems during the electron beam patterning, we decided to use trace-retrace patterning technique to write FBMS lines for waveguides. Figure 2.38(a) shows the schematic view of the trace-retrace patterning, where the arrows are representing the direction of FBMS patterning. In this process, PhW regions are patterned twice (once in forward and other in reverse direction) with half of the FBMS dose each time. As a result, proximity effects are eliminated at the grating coupler boundary and junctions as FBMS lines passing through this regions only once with half of the FBMS optimum dose (for PhW). Figure 2.38(b) shows the modified design layout with magnified views of grating coupler and ring resonator as inset. The color of the design components represents the dose for the respective components with red color represents the maximum dose ( $500 \mu\text{C}/\text{cm}^2$ ) and the blue color represents the minimum dose ( $120 \mu\text{C}/\text{cm}^2$ ). It is worth mentioning here that an additional element is placed over the write field boundary region (Figure 2.38(a) and 2.38(b)) to get rid of the stitching error with an elevated dose at the boundary. The dose of the DBR structure near to the taper region is adjusted such that the duty cycle remains uniform throughout the DBR region in presence of the proximity effects due to FBMS lines surrounding the taper. In case of ring resonator, the bus waveguide design is shown (Figure 2.38(b):Inset) in cyan color (half the maximum FBMS dose) as the this region is written twice during

System parameters	Patterning parameters
Acceleration voltage = 20 kV	CP dose (max) = 300 $\mu\text{C}/\text{cm}^2$
Aperture = 10 $\mu\text{m}$	Area step size = 10 nm
Write field = 100 $\mu\text{m} \times 100 \mu\text{m}$	FBMS dose (max) = 500 $\mu\text{C}/\text{cm}^2$
Working distance = 10 mm	Developing time 6 min.

Table 2.2: Optimized electron beam lithography parameters: measured beam current = 40 pA and developer - MF 319.

the patterning. Whereas the ring element is shown in red color (maximum FBMS dose) as it is exposed only once to the electron beam during the patterning. Electron beam lithography dose values are optimized for column parameters 20 kV acceleration voltage, 10  $\mu\text{m}$  aperture size and 10 mm working distance with a measured electron current value of 40 pA. The optimum system and patterning parameters are summarized in the Table 2.2.

Figure 2.39 show the SEM images of the critical regions of the waveguide after modifying the design to achieve stitching error free patterning. Figure 2.39(a) and 2.39(b) show the grating coupler-PhWW junction and the region at which write field boundary passes. Both this regions are defined precisely with the modification of the patterning strategy. Figure 2.39(c) shows the SEM image of the DBR region where the grating element near the taper section is narrowed down in the lateral direction though the grating duty cycle remains same throughout. This is due to the fact that the element is exposed at a lower dose to avoid widening of grating pitch at the middle this element due the proximity effects with the presents of nearby FBMS line. However, while characterizing the device, we did not observe any significant difference in the performance of the grating coupler. Figure 2.39(d) shows the directional coupler region of ring resonator after the electron beam patterning and inductively coupled plasma reactive ion etching (ICPRIE) process. We have used Oxford PlasmaLab 100 ICPRIE system for dry etching of silicon. The dry etching recipe is optimized to have minimum surface roughness and nearly vertical sidewalls. The optimum ICPRIE parameters are: gas flow rate =  $\text{SF}_6:\text{CHF}_3 : : 5 \text{ sccm} : 18 \text{ sccm}$ , Chamber pressure = 15 mT, forward power = 30 W, ICP power = 1500 W, substrate temperature = 20  $^\circ\text{C}$ . The silicon etch rate of the recipe is measured to be 540 nm/minute.

The fabricated submicron waveguides were taken for optical characterization. Fig-

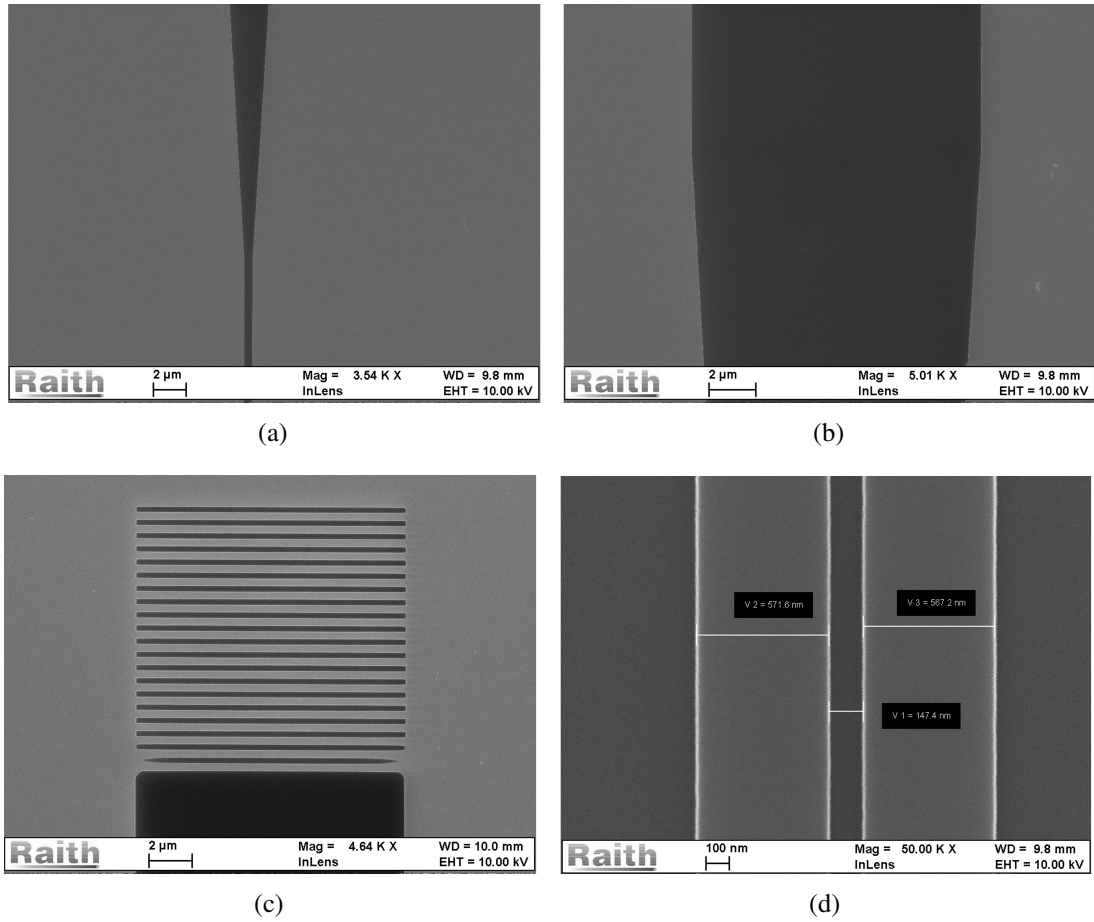
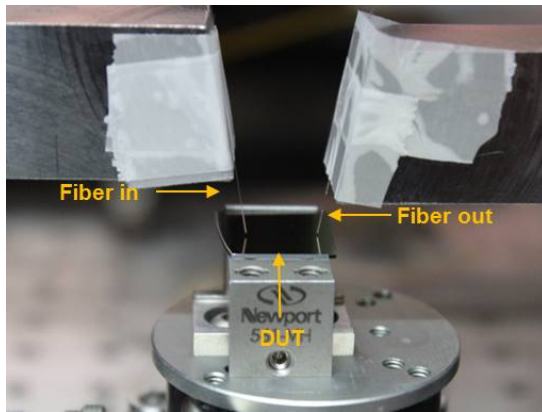


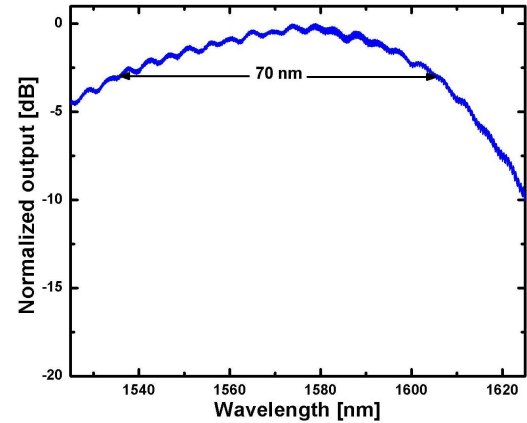
Figure 2.39: SEM images of critical regions of the device: (a) junction region of the grating coupler attached to the waveguide section (b) grating coupler section where the write field boundary passes as shown in Figure 2.37(c), (c) DBR region of grating coupler and (d) directional coupler where the ring and bus waveguides are coupled.

Figure 2.40(a) shows the photographic image of grating coupler setup to couple light from single-mode fiber to submicron silicon PhW ( $W = 560$  nm,  $H = 250$  nm and  $h = 150$  nm). Input and output fibers are fixed at  $10^\circ$  to the waveguide normal. The device has been characterized with the help of an Optical Spectrum Analyzer (OSA) with inbuilt tuneable laser source. According to eq. 2.12, the value of  $\Lambda$  for the grating coupler on a 250 nm SOI substrate for TE polarized light at  $\lambda = 1550$  nm is estimated to be 610 nm. The length of the DBR for the grating coupler is kept to be  $12 \mu\text{m}$  to maximize the overlap fiber mode profile to the grating. The laser is coupled from fiber to waveguide through input grating coupler, at the output, light is again collected back to fiber again through grating coupler and fed to the OSA. The response (for TE polarization) of a straight waveguide integrated with grating coupler at end both ends are shown in Figure





(a)



(b)

Figure 2.40: (a) Grating coupler light coupling setup where input and output fibers angles are fixed  $10^\circ$  normal to the waveguide axis and (b) response of grating coupler integrated with submicron straight waveguide ( $W = 560$  nm,  $H = 250$  nm and  $h = 150$  nm).

2.40(b). The 3 dB bandwidth of the grating coupler with 50% duty cycle and 100 nm etch depth ( $H - h$ ) is measured to be 70 nm. The insertion loss of the grating coupler is measured to be 6 dB/facet. The PhWW propagation loss is estimated by comparing Q-factors (at critical coupling condition) of microring resonators with varying cavity length. This method of loss extraction is discussed in the next chapter. The typical loss of PhWW with  $W = 560$  nm,  $H = 250$  nm and  $h = 150$  nm is measured to be  $\sim 3$  dB/cm.

## 2.4 Summary

Silicon waveguide structures with various waveguide cross-sections have been theoretically analyzed in terms of single-mode guidance, birefringence, dispersion, light coupling, bend induced loss and device fabrication tolerance. These analyses give a broad view on the choice of a suitable silicon waveguide cross-section with respect to the application of interest. It is shown that larger waveguide cross-sections can be preferred for dispersion free, polarization independent operations. In addition to that, they are found to be relatively good for interfacing with SMF/LF. Devices designed on submicron device layers are analyzed to be less fabrication tolerant in comparison with microns thick device layers. However, submicron waveguides are found to be extremely

useful to achieve higher light-matter interaction and compact devices.

To improve the input/output light coupling efficiency and simultaneously to have compact waveguide devices on same substrate, various fabrication techniques are adapted. Isotropic dry etching based waveguide surface trimming is found to be useful to reduce waveguide cross-section from micron to submicron scale without introducing much loss. The propagation loss for untrimmed LCRW ( $W = 5 \mu\text{m}$ ,  $H = 5 \mu\text{m}$  and  $h = 4 \mu\text{m}$ ) and trimmed RCRW ( $W = 2 \mu\text{m}$ ,  $H = 2 \mu\text{m}$  and  $h = 1 \mu\text{m}$ ) is measured to be 0.5 dB/cm and 0.6 dB/cm, respectively. In order to improve the input/output coupling efficiency of the trimmed waveguide, 2D SSC are fabricated using two different techniques: 2D SSC by photolithographic definition and 2D SSC by shadow mask etching. The insertion loss (2.5 dB) of photolithographically defined SSC is measured to be higher due to higher order mode excitation at the transition region. Whereas, SSC defined by shadow mask etching process is found to be adiabatic in terms  $W$ ,  $H$  and  $h$  variation, this results in a lower transition loss of  $\sim 0.25$  dB and remains nearly same for larger wavelength range. These SSCs are designed for only TE polarization to suppress the possibility of polarization rotation.

Certain constrains are identified with the integration 2D SSC s with submicron device components such as directional coupler, DBR, etc. In order to overcome this issue, we have fabricated grating assisted 1D SSCs integrated with submicron waveguide ( $W = 560 \text{ nm}$ ,  $H = 250 \text{ nm}$ ,  $h = 150 \text{ nm}$ ) using optimized electron beam lithography and subsequent ICPRIE process. The typical propagation loss of the fabricated submicron waveguide is estimated to be  $\sim 3$  dB/cm. The bandwidth (3dB) and insertion loss of the grating assisted 1D taper is measured to be 70 nm and 6 dB/facet, respectively. Though, grating assisted 1D SSC is considered mostly for a quick wafer and/or chip level device testing, for a standalone device fabrication one can adapt the advantage of adiabatic 2D spot-size converter based on multiple input multiple output waveguide (MIMOW) platform which is discussed as a future scope of the work in last chapter of this thesis.

# CHAPTER 3

## Ring Resonators: Microns to Submicron Technology

The ring resonators are typically used in integrated optics/optoelectronics to obtain functions like wavelength filters/add-drop multiplexers, modulators/switches, delay lines, lab-on-chip sensors, etc. Its huge success in silicon photonics applications is due to a few important factors: (1) submicron PhWW with tight modal confinement allowing to design compact microring resonators with ring radii as small as  $\sim 3 \mu\text{m}$ , (2) excellent thermo-optic and plasma-dispersion effects facilitating for fast reconfiguration, (3) enabling CMOS technology for the integration of electronics and photonics functions, etc. However, as the CMOS photonics technology is still in its evolving state, a lot more research efforts are required to explore the design aspects and novel technology solutions. This chapter investigates some important design parameters, fabrication and novel application prospects using a critically coupled resonator. The working principle and critical design parameters of microring resonator is briefly given in section 3.1, where we also discuss two different coupling mechanisms between bus and ring waveguides: (i) multi-mode interference coupling and (ii) directional coupling. The optimum design of these couplers for large volume ring resonators as well as compact microring resonator are presented in this section. Experimental demonstration of a large volume ring resonator and subsequently compact critically coupled microring resonators are discussed in section 3.2 and section 3.3, respectively. Finally, a brief summary describing pros and cons of ring resonators with micron and submicron waveguides is given in section 3.4.

### 3.1 Theory and Important Design Parameters

A ring resonator in its simplest form consists of a straight waveguide (bus waveguide) which interacts with a ring through a coupler section. The coupler section is used to

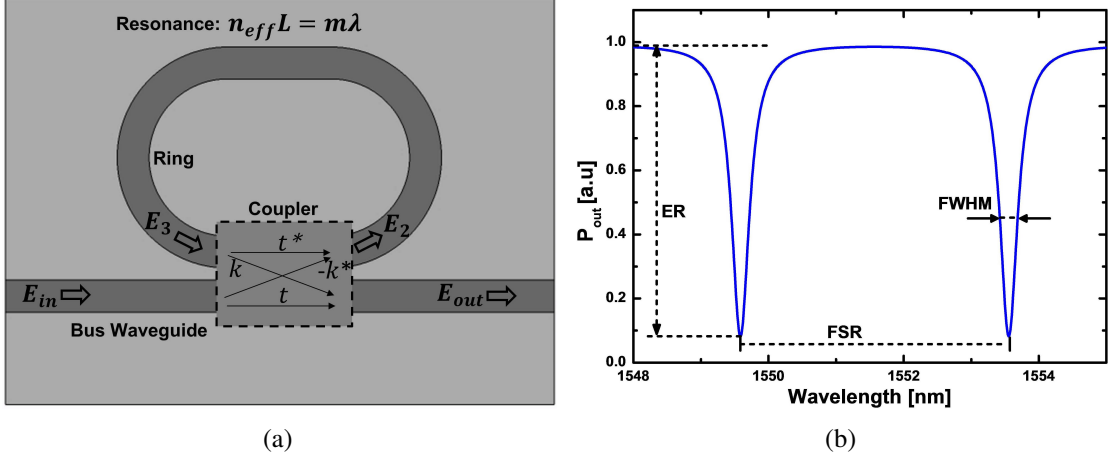


Figure 3.1: (a) Schematic top view of a microring resonator: dashed outline represents coupler section with self coupling coefficient  $t$  and cross-coupling coefficient  $k$ ,  $E_{in}$  and  $E_{out}$  are the input and output electric fields respectively. (b) Typical output characteristics of a photonics wire microring resonator with  $L = 157 \mu\text{m}$ ,  $a = 0.91 \text{ dB/cm}$ ,  $n_{eff} = 2.76$  and  $t = 0.96$  (for  $\lambda \sim 1550 \text{ nm}$ ); where ER - extinction ratio, FSR - free spectral range and FWHM - full width at half maxima.

feed a part of the light from the input waveguide to the ring and simultaneously the circulated light from the ring back again to add into output waveguide. Schematic top view of such a ring resonator (all-pass configuration) is shown in Figure 3.1(a). As indicated,  $E_{in}$  and  $E_{out}$  are the ring resonator input and output electric fields, respectively. In the coupler section,  $t$  is the self coupling coefficient (fraction of input amplitude passed through bus waveguide) and  $k$  is the cross-coupling coefficient (fraction of input amplitude coupled to the ring). Assuming that the unidirectional mode of the resonator is excited, the interaction between bus waveguide and ring can be described by the matrix relation:

$$\begin{bmatrix} E_{out} \\ E_2 \end{bmatrix} = \begin{bmatrix} t & k \\ -k^* & t^* \end{bmatrix} \times \begin{bmatrix} E_{in} \\ E_3 \end{bmatrix} \quad (3.1)$$

where,  $E_3$  is related to  $E_2$  by the following equation:

$$E_3 = a E_2 e^{-j\theta} \quad (3.2)$$

and  $a = e^{-\alpha L}$  is the round trip loss factor with a loss coefficient  $\alpha$ ,  $L$  is the perimeter of the ring,  $\theta = 2\pi n_{eff} L / \lambda$  is the round trip phase factor,  $n_{eff}$  is the effective index of the waveguide and  $\lambda$  is the wavelength of operation. Using eq. 3.1 and 3.2, the transmitted

power at the output can be written as [52]:

$$P_{out} = |E_{out}|^2 = \frac{a^2 - 2 a t \cos(\theta) + t^2}{1 - 2 a t \cos(\theta) + a^2 t^2} \quad (3.3)$$

where, we have assumed loss-less coupling, ie,  $t^2 + k^2 = 1$  and the input power is normalized to 1. Figure 3.1(b) shows a typical transmission characteristics (plotted using eq. 3.3) of PhWW ring resonator with  $L = 167 \mu\text{m}$ ,  $\alpha = 5 \text{ dB/cm}$ ,  $n_{eff} = 2.76$  and  $t = 0.96$  (for  $\lambda \sim 1550 \text{ nm}$ ). It can be observed that the transmitted output power around certain wavelengths are significantly low. The wavelengths with power level minimum are said to be the resonant wavelengths which satisfy the resonance condition  $n_{eff}L = m\lambda$  of the ring resonator, where  $m$  is an integer represents the order of resonance. The throughput power at resonant wavelength is minimum as it is stored in the ring due to constructive interference while circulating inside the ring. The wavelength separation (or corresponding frequency separation) between two consecutive resonant resonances is known as free spectral range (FSR) of the resonator. In terms of wavelength separation, it is defined by:

$$\text{FSR} = \frac{\lambda^2}{n_g L} \quad (3.4)$$

where  $n_g$  is the group index and it is defined as:

$$n_g = n_{eff} - \lambda \frac{dn_{eff}}{d\lambda} \quad (3.5)$$

Extinction ratio (ER) is another figure of merit of a ring resonator which measures the ratio of maximum ( $P_{out}$  at off-resonance) to minimum ( $P_{out}$  at resonance) power levels of the the transmission spectrum and which can be derived from Eq. 3.3:

$$\text{ER} = \frac{(t + a)^2}{(t - a)^2} \times \frac{(1 - t a)^2}{(1 - t a)^2} \quad (3.6)$$

The ER at resonance wavelengths can be made to infinity when  $a = t$ , this condition is known as critically coupled resonance. The full width at half maximum (FWHM) of

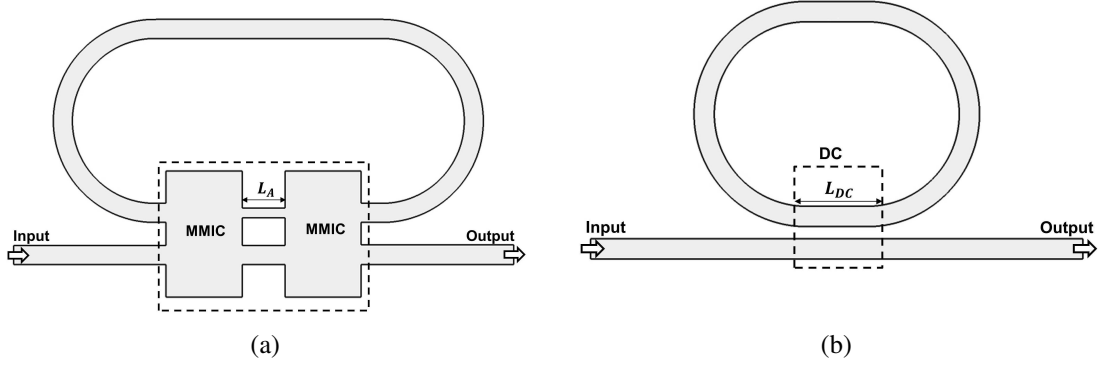


Figure 3.2: Schematic top views of ring resonator with (a) cascaded multi-mode interference coupler (MMIC) or asymmetric Mach-Zehnder interferometer (MZI) and (b) directional coupler (DC). The coupling strengths of (a) and (b) are controlled by the lengths  $L_A$  and  $L_{DC}$ , respectively.

the resonance can be expressed as:

$$\text{FWHM} = \frac{(1 - a t) \lambda_m^2}{\pi n_g L \sqrt{a t}} \quad (3.7)$$

Performance of a ring resonator for any functional application depends on the Q-factor of the resonator and it is expressed as:

$$\text{Q-factor} = \frac{\lambda_m}{\text{FWHM}} = \frac{\pi n_g L \sqrt{t a}}{\lambda_m (1 - t a)} \quad (3.8)$$

Q-factor of a ring resonator decides the amount of energy stored inside the ring at and around a resonance wavelength. In most of the ring resonator applications, high Q-factor is preferred. However, the properties of the ring resonator has to be designed depending on the application. In modulator devices, as it requires higher extinction one should expect very low output power for the resonant wavelength, ie, critically coupled ( $a = t$ ) ring resonator is preferred. However, in delay line applications, higher throughput power and maximum delay are expected for the the resonant wavelengths which requires a different situation than in the case of modulator.

Thus from the above discussion it is evident that the design of coupling region is crucial for a ring resonator performance. Two different types of coupler designs have been considered for present discussion. Figures 3.2(a) and 3.2(b) show the schematic top views of ring resonators based on cascaded multi-mode interference coupler (MMIC)

and directional coupler (DC), respectively. In MMIC based ring resonator, the coupling coefficient is controlled using asymmetric arm length ( $L_A$ ) where as in DC it is controlled using DC length ( $L_{DC}$ ). To achieve fabrication tolerant power splitters, MMICs are preferred [100, 101]. Moreover, as the multi-mode waveguide region width of MMIC is much larger than a single-mode waveguide, it is less dependent to wavelength of operation compared to a DC based power splitter [102]. Also, MMIC power splitters are less sensitive to polarization of operation [103]. DC based power splitters are used wherever compact microring resonator with asymmetric power splitting is required. As we realize that both MMIC and DC based power splitters are attractive for ring resonator in different perspectives, design aspects of both the components are explored in the following sections.

### 3.1.1 Mutlimode Interference Coupler

A simple MMIC consist of input single-mode waveguide(s), a multi-mode waveguide and output single-mode waveguide(s). The multi-mode waveguide section is designed to support higher order modes such that the interference of all the excited modes give rise to localized light spots exactly similar to the excitation profile at the input of the multi-mode waveguide and which can be explained in terms of self imaging principle [104]. The localized spots formed in the multi-mode waveguide region can be tapped through the output single-mode waveguide(s) and thus MMIC can be used as power splitter. The important aspects of MMIC design are:

1. Cross-section geometry of MMIC
2. Input and output waveguide positions
3. Input and output waveguide taper sections

In general, multi-mode waveguide section is defined by increasing the width of the waveguide relative to input/output waveguides and retaining the height of input, output and multi-mode waveguides same. So the number of modes supported by the multi-mode waveguide section depends on the incremental width of MMIC. In addition to MMIC cross-section, input waveguide position also plays a major role as it decides the number and/or selected modes excited in the multi-mode section. For example, though

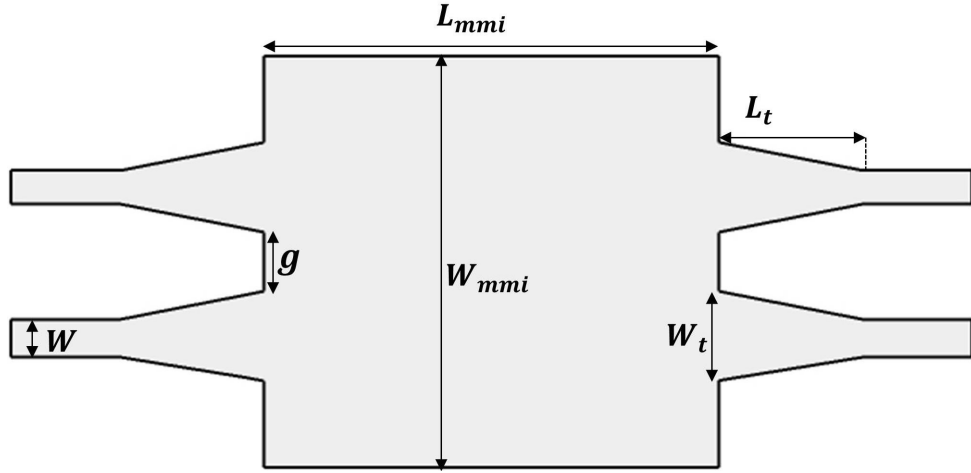


Figure 3.3: Schematic view of a  $2 \times 2$  MMIC

the MMIC width is large enough to support many higher order modes, if the input waveguide is positioned to the center of MMIC, only even order modes are excited, which is explained by symmetric interference condition [104]. Higher the number of modes excited in the multi-mode region, better the resolution and uniformity of the self images formed by interference. As the width of multi-mode waveguide increases, the length at which self images are formed also drastically increased. However, the length of MMIC can be greatly reduced without compromising the image resolution by properly positioning input waveguide(s) and exciting only certain guided modes in the multi-mode waveguide section. This is well explained in paired interference condition discussed in [104]. By utilizing paired interference property of MMIC, one can reduce the length of  $1 \times N$  coupler for  $N$  fold image from  $3L_\pi/N$  to  $L_\pi/N$ ; where,  $L_\pi$  is the beat length of the first two lowest order modes. We have used this property to design  $2 \times 2$  MMIC power splitter. According to paired interference condition, for a  $2 \times 2$  MMIC, the input and output waveguide has to be positioned at  $\frac{W_{mmi}^{eff}}{6}$ , where  $W_{mmi}^{eff}$  is the effective width which accounts the penetration depth of guided modes of the multi-mode section. However, in case of high refractive contrast SOI waveguides, the penetration depth is too small and hence  $W_{mmi}^{eff}$  can be approximated to the physical width of the multi-mode waveguide section ( $W_{mmi}$ ). Figure 3.3 shows the schematic view of a typical  $2 \times 2$  MMIC with input and output interfaced with adiabatically tapered single-mode waveguides. The taper sections are attached to increase the coupling/collection efficiency and to reduce the impedance mismatch. We have compared MMIC designs with SOI device layer thicknesses of  $2 \mu\text{m}$  and  $0.25 \mu\text{m}$ , respectively. It has been also



shown how one can derive a 2  $\mu\text{m}$  design from the 5  $\mu\text{m}$  device layer thickness by surface trimming discussed in previous section. To design the MMIC using surface trimming technique, we have considered the following aspects:

1. Minimum feature size that can be repeatably achieved by i-line (365 nm) photolithography is 2  $\mu\text{m}$
2. Final waveguides are fabricated using surface trimming, as a result photo mask definition of MMIC should be larger than the desired dimension depending on the surface trimming etch rate
3. For compact  $2 \times 2$  MMIC design, input and output waveguides are positioned at  $\frac{W_{mmi}}{6}$  from the centre of MMIC by considering paired interference condition
4. Input and output single-mode waveguide taper length is fixed to be 200  $\mu\text{m}$  for adiabatic transition

Initial device layer thickness of the SOI substrate is assumed to be  $\sim 5 \mu\text{m}$  and it is trimmed to be  $\sim 2 \mu\text{m}$  (height reduction = 3  $\mu\text{m}$ ). As the surface trimming has been optimized for equal width and height reduction rate, the width of the waveguide also reduces by 3  $\mu\text{m}$ . Considering the compactness of MMIC and efficient input excitation/output collection, the taper width ( $W_{it}$ ) of the single-mode waveguide is fixed to be 3  $\mu\text{m}$ . If the desired value of  $W_{it} = 3 \mu\text{m}$  after trimming, the photomask taper width ( $W_{it}^P$ ) should be 6  $\mu\text{m}$ . Also, if we consider minimum feature size ( $g$ ) by optical lithography is 2  $\mu\text{m}$ , the gap between the input/output waveguides should be 2  $\mu\text{m}$ . This results in the minimum center to center separation between input/output waveguides to be  $W_{it}^P + g = 6 + 2 = 8 \mu\text{m}$ . So, from the centre of MMIC, input/output should be at 4  $\mu\text{m}$  and this should be equal to  $\frac{W_{mmi}}{6}$  according to paired interference condition and this fixes the value of  $W_{mmi}$  to 24  $\mu\text{m}$ . In order find optimum MMIC length, we have simulated the designed MMIC using Rsoft Beamprop tool and monitored the Bar and Cross Port power as a function of MMIC length ( $L_{mmi}$ ) keeping all other parameters ( $W_{mmi} = 24 \mu\text{m}$ ,  $L_t = 200 \mu\text{m}$ ,  $W_{it} = 3 \mu\text{m}$  and  $W_{ph} = 1.5 \mu\text{m}$ ) fixed. Figure 3.4(a) shows the power variation of Bar and Cross ports as a function of  $L_{mmi}$ . It is obvious from the plot that at  $L_{mmi} \sim 890 \mu\text{m}$ , the power levels of Bar and Cross ports are same. As a result, we have fixed the optimum  $L_{mmi} = 890 \mu\text{m}$ . Wavelength dependent splitting ratio ( $r$ ) of the MMIC is shown Figure 3.4(b), where  $r$  is defined as:

$$r = \frac{P_{Cross}}{P_{Bar} + P_{Cross}} \quad (3.9)$$

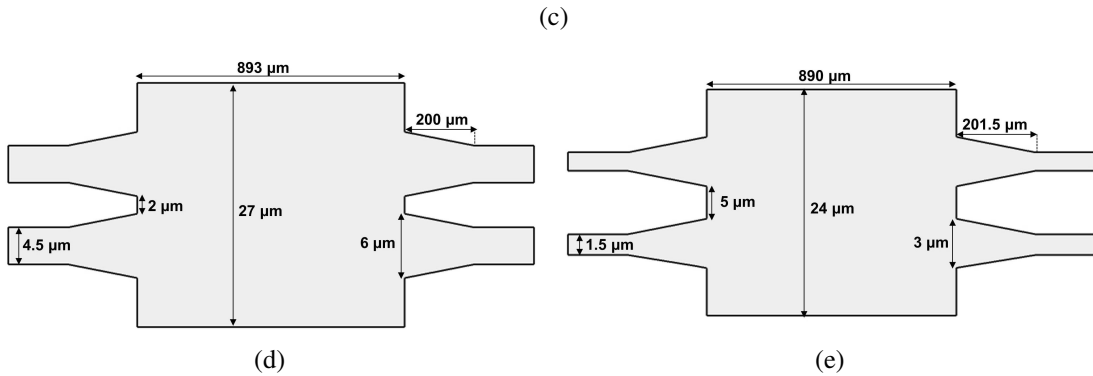
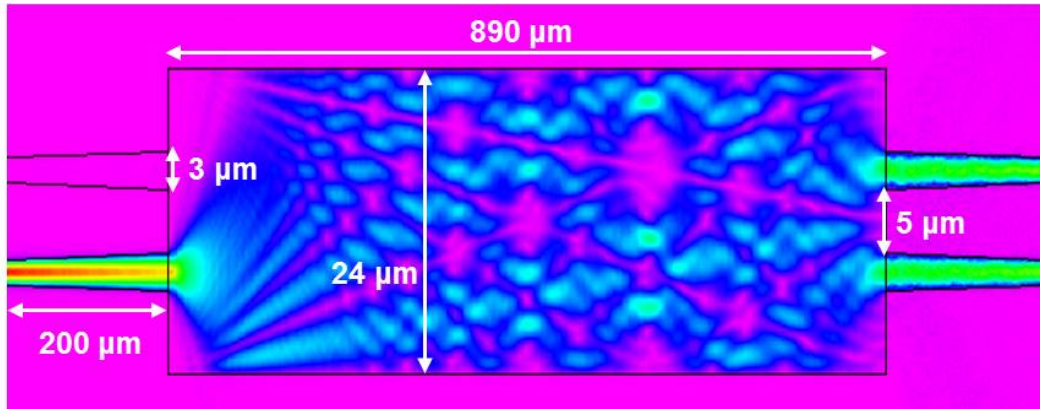
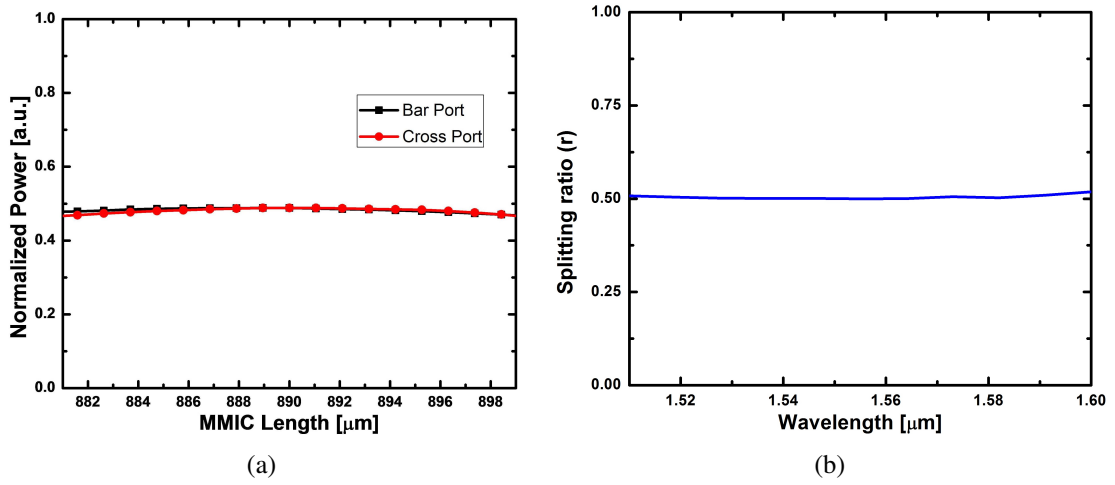


Figure 3.4: (a) MMIC length ( $L_{mmi}$ ) optimization for surface trimmed MMIC by monitoring Bar/Cross port power as function of  $L_{mmi}$ , black and red lines show the variation output power for Bar and Cross ports respectively. (b) Wavelength dependency of  $2 \times 2$  trimmed MMIC designed on 2  $\mu\text{m}$  SOI substrate. (c) Simulated top view of  $2 \times 2$  (3 dB) MMIC with optimum waveguide parameters:  $W_{mmi} = 24 \mu\text{m}$ ,  $L_{mmi} = 890 \mu\text{m}$ ,  $L_t = 200 \mu\text{m}$ ,  $W_{it} = 3 \mu\text{m}$  and  $W_{ph} = 1.5 \mu\text{m}$ . (d) Schematic top views of (d) photo mask layout of MMIC on 5  $\mu\text{m}$  device layer and (e) MMIC layout expected after surface trimming process.

Table 3.1: Optimized MMIC parameters (for TE polarization) on a 2  $\mu\text{m}$  and 0.25  $\mu\text{m}$  device layer SOI substrates.

$H$ [ $\mu\text{m}$ ]	$h$ [ $\mu\text{m}$ ]	$W$ [ $\mu\text{m}$ ]	$W_t$ [ $\mu\text{m}$ ]	$L_t$ [ $\mu\text{m}$ ]	$W_{mmi}$ [ $\mu\text{m}$ ]	$L_{mmi}$ [ $\mu\text{m}$ ]	Simulation Tool
2	1	1.5	3	200	24	890	RSoft - BeamPROP
0.25	0	0.5	1	4	3.6	15.4	Lumerical's - EME

where  $P_{Cross}$  and  $P_{Bar}$  are power obtained at cross and bar port, respectively. The simulation results show that the MMIC performance remains same from 1500 nm to 1600 nm. Simulated top view of  $2 \times 2$  (3 dB) MMIC with optimum waveguide parameters is shown in Figure 3.4(c). The simulated view has been shown for TE polarized light at  $\lambda = 1550$  nm, however the simulation for TM polarization also shows nearly same result. Figure 3.4(d) represents the MMIC layout in the photomask and Figure 3.4(e) represents the expected footprint after surface trimming.

We have also designed MMIC on 250 nm SOI substrate using the similar (paired interference) design protocol as the MMIC on 2  $\mu\text{m}$  SOI substrate. Lumerical's eigen mode expansion (EME) solver is used for designing the MMIC on submicron substrate as the BeamPROP is not suitable for high contrast waveguides. The optimum parameters for  $2 \times 2$  MMICs (3 dB) on 2  $\mu\text{m}$  and 250 nm device layer SOI substrates are summarized in Table 3.1 for TE polarization at  $\lambda = 1550$  nm. Table 3.1 summarizes the MMIC parameters designed on a 2  $\mu\text{m}$  device layer SOI substrate. Conventionally, MMICs are used as  $N \times M$  power splitters where, output power level remain same or a fixed  $r$  for all the output ports. However,  $2 \times 2$  MMIC (3 dB) can be used for achieving variable  $r$  if the two such MMICs are connected back to back with an asymmetric arm in between. Figure 3.5(a) shows the schematic layout of the  $2 \times 2$  coupler based on two 3 dB MMICs. In this configuration,  $r$  can be varied as a function of asymmetric arm length  $L_A$ . The characteristics of this cascaded coupler can be explained using the transfer function of 3 dB MMIC as follows:

$$\begin{pmatrix} E_{Bar} \\ E_{Cross} \end{pmatrix} = \begin{pmatrix} 1/\sqrt{2} & j/\sqrt{2} \\ j/\sqrt{2} & 1/\sqrt{2} \end{pmatrix} \times \begin{pmatrix} 1 & 0 \\ 0 & e^{j\Delta\beta L_A} \end{pmatrix} \times \begin{pmatrix} 1/\sqrt{2} & j/\sqrt{2} \\ j/\sqrt{2} & 1/\sqrt{2} \end{pmatrix} \times \begin{pmatrix} E_{in} \\ 0 \end{pmatrix} \quad (3.10)$$

where,  $E_{in}$ ,  $E_{Bar}$  and  $E_{Cross}$  are the electric field amplitudes at the Input, Bar and Cross

ports, respectively.  $\Delta\beta$  is the differential phase constant induced by the asymmetric arms of the MMICs and it can be defined as:

$$\Delta\beta = \frac{2\pi}{\lambda} (n_{eff}^1 - n_{eff}^2) \quad (3.11)$$

where,  $\lambda$  is the wavelength operation,  $n_{eff}^1$  and  $n_{eff}^2$  are the effective indices of the asymmetric waveguides of width  $W_1$  and  $W_2$ , respectively. Using eqn 3.10 and 3.11, the self coupling ( $t_{mmi}$ ) and cross coupling ( $k_{mmi}$ ) coefficients of the coupler can be defined as:

$$t_{mmi} = e^{j\left(\frac{\Delta\beta L_A + 2\pi}{2}\right)} \sin\left(\frac{\Delta\beta L_A}{2}\right) \quad (3.12)$$

$$k_{mmi} = e^{j\left(\frac{\Delta\beta L_A + \pi}{2}\right)} \cos\left(\frac{\Delta\beta L_A}{2}\right) \quad (3.13)$$

and the normalized power obtained at the bar ( $P_{Bar}$ ) and cross ( $P_{Cross}$ ) ports (assuming zero insertion loss) can be defined in terms of  $L_A$  as:

$$P_{Bar} = \sin^2\left(\frac{\Delta\beta L_A}{2}\right) \quad (3.14)$$

$$P_{Cross} = \cos^2\left(\frac{\Delta\beta L_A}{2}\right) \quad (3.15)$$

Figure 3.5(b) shows the output characteristics of the coupler as a function of  $L_A$  for device designed on a 250 nm device layer SOI. The widths of the asymmetric arms are considered to be  $W_s = 500$  nm and  $W_a = 450$  nm. MMIC parameters are set to be the optimum values of submicron MMIC tabulated in Table 3.1. We have neglected the phase change due to the asymmetric taper sections in coupler. It is found that the  $P_{Bar}$  can be changed from 0 to 1 within the span of  $L_A = 7.3$   $\mu\text{m}$  for a  $\Delta W = W_s - W_a = 50$  nm. The value of  $L_A$  can be reduced further if  $\Delta W$  is increased suitably. Figure 3.5(c) shows the  $r$  (for  $\Delta W = 50$  nm) of the cascaded coupler as a function of wavelength of operation. Here the value of  $L_A$  is fixed to be 3.65  $\mu\text{m}$  to obtain 3 dB splitting. The calculations show that  $r$  remains nearly constant even for a deeply etched submicron waveguide ( $h = 0$ ) for a long wavelength range of  $1500 \text{ nm} \leq \lambda \leq 1600 \text{ nm}$ .

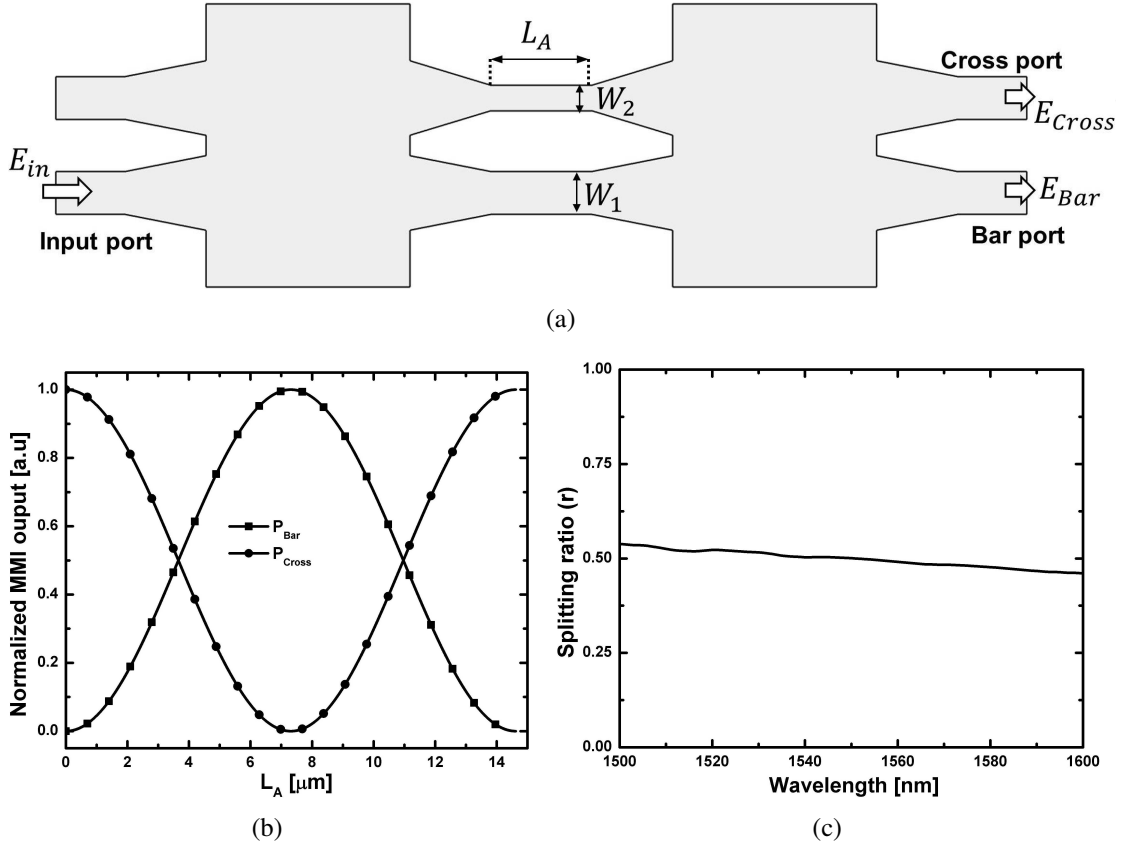


Figure 3.5: (a) Schematic layout of a MMIC based power splitter for variable splitting ratio ( $r$ ):  $L_A$  is the length of the asymmetric arm of width  $W_a$ . (b) Output power variation of the coupler shown in (a) is plotted as a function of  $L_A$ , where asymmetric waveguide cross-section is considered to be  $H = 250$  nm,  $W_1 = 500$  nm  $W_2 = 450$  nm and  $h = 0$  nm. (c) Wavelength dependent  $r$  is shown for the coupler for  $L_A = 3.65$   $\mu\text{m}$ : calculations are shown for the MMIC (on 0.25  $\mu\text{m}$  device layer) parameters given in Table 3.1 for TE polarization.

### 3.1.2 Directional Coupler

DC based power splitters are generally preferred for microring resonator in submicron regime. The reason of choice is mainly because of flexible power splitting ratio (from 0 to 1) by simply scaling the length of DC. As the fraction of power coupled to ring decides certain important characteristics of ring resonator such as Q-factor, ER, etc. it is important to have variable power splitting ratio with compact device footprint.

## Directional Coupler: Theory

Waveguides are said to be coupled when they are exchanging power between them either in co-direction or contra-direction. Co-directional couplers are generally referred as directional couplers (DCs) which consist of two single-mode waveguides in close proximity of each other for a finite length. The schematic top view of a DC is shown in Figure 3.6. When the waveguide separation ( $G$ ) is small enough such that

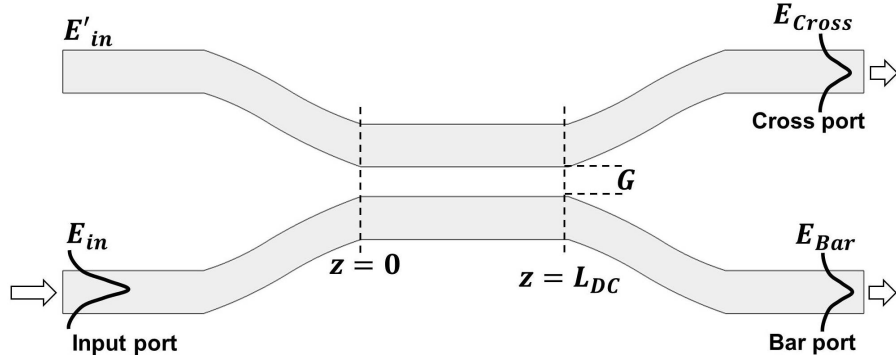


Figure 3.6: Schematic top view of a  $2 \times 2$  DC:  $L_{DC}$  - length of DC,  $G$  - coupled waveguide separation,  $E_{in}$ ,  $E_{Bar}$  and  $E_{Cross}$  are electric field amplitudes at Input, Bar and Cross ports.

the evanescent tails of the guided modes of the waveguides overlap each other causing the exchange of power between waveguides. The efficiency of coupling depends on the strength of evanescent field interaction between the coupled waveguides. The amount coupled power depends on the length ( $L_{DC}$ ) and efficiency of DC. The working principle of a DC can be explained by supermode analysis. The two supermodes of a DC comprised two single-mode waveguides can be represented in terms of symmetric ( $E_s$ ) and anti-symmetric ( $E_a$ ) modes. For the input field amplitudes  $E'_{in}$  and  $E_{in}$  at  $z = 0$  (see Figure 3.6), we can represent the field amplitudes corresponding to symmetric and asymmetric modes as  $E_{s0}$  and  $E_{a0}$  :

$$E_{s0} = \frac{E_{in} + E'_{in}}{2} \quad (3.16)$$

$$E_{a0} = \frac{E_{in} - E'_{in}}{2} \quad (3.17)$$

where,  $E_{in}$  and  $E'_{in}$  are the electric fields at the input ports. Similarly, at  $z = L_{DC}$

$$E_s(z = L_{DC}) = E_{s0}e^{j\beta_s L_{DC}} \quad (3.18)$$

$$E_a(z = L_{DC}) = E_{a0}e^{j\beta_a L_{DC}} \quad (3.19)$$

Where,  $\beta_s = \frac{2\pi n_{eff}^s}{\lambda}$  and  $\beta_a = \frac{2\pi n_{eff}^a}{\lambda}$  are the propagation constants of symmetric and anti-symmetric mode with effective indices  $n_{eff}^s$  and  $n_{eff}^a$  respectively. Then, one can write the electric field at Bar ( $E_{Bar}$ ) port at  $z = L_{DC}$  as:

$$\begin{aligned} E_{Bar} &= E_{s0}e^{j\beta_s L_{DC}} + E_{a0}e^{j\beta_a L_{DC}} \\ &= \frac{E_{in} + E'_{in}}{2}e^{j\beta_s L_{DC}} + \frac{E_{in} - E'_{in}}{2}e^{j\beta_a L_{DC}} \end{aligned} \quad (3.20)$$

If  $E'_{in} = 0$ , one can write,

$$E_{Bar} = E_{in}e^{j\frac{(\beta_s + \beta_a)L_{DC}}{2}} \cos\left(\frac{\Delta\beta L_{DC}}{2}\right) \quad (3.21)$$

where  $\Delta\beta = \beta_s - \beta_a$ . As a result, power obtained at Bar ( $P_{Bar}$ ) and Cross ( $P_{Cross}$ ) ports can be written as:

$$P_{Bar} = |E_{Bar}|^2 = P_{in} \cos^2\left(\frac{\Delta\beta L_{DC}}{2}\right) \quad (3.22)$$

$$P_{Cross} = |E_{Cross}|^2 = P_{in} \sin^2\left(\frac{\Delta\beta L_{DC}}{2}\right) \quad (3.23)$$

where,  $P_{in} = |E_{in}|^2$  is the power at the input port. We have used supermode analysis for the design of DC on 0.25  $\mu\text{m}$  SOI substrate. Lumerical MODE Solutions simulation tool has been used to find effective indices of symmetric and anti-symmetric modes.

### Coupling Efficiency

The coupling efficiency of the DC is defined as the fraction of electric field amplitude coupled per unit length between the waveguides along the propagation direction. Using supermode theory, the coupling efficiency ( $\kappa$ ) can be defined using eq. 3.22 and 3.23

as:

$$\kappa = \frac{\pi \Delta n}{\lambda} \quad (3.24)$$

which is related to the self coupling coefficient ( $t$ ) and cross-coupling coefficient ( $k$ ) as;

$$t = \cos(\kappa L_{DC}) \quad (3.25)$$

$$k = e^{j\pi/2} \sin(\kappa L_{DC}) \quad (3.26)$$

where,  $\Delta n = n_{eff}^s - n_{eff}^a$  is the effective refractive index difference between the symmetric and anti-symmetric modes, respectively. The strength  $\kappa$  depends on the waveguide cross-section ( $W, H, h$ ), separation between the coupled waveguides ( $G$ ) and also the polarization of operation though it is not obvious from eqn. 3.24. So the first step towards the DC design is to find an optimum waveguide cross-section. In a submicron DC based ring resonator, the cavity loss occurs not only due to sidewall roughness and waveguide bending but also because of the non adiabatic tapering of waveguides at the coupling region owing to proximity effects of lithography [105]. A second effect is the lower confinement in the coupling region leading to higher scattering at sidewall roughness (as result higher coupling) [74]. This leads to an unpredictable transmission characteristics especially in the estimation of FWHM [52]. This is predominant in deeply etched waveguides as the guided mode interacts more with the side wall roughness. This results in unpredictable transmission characteristics of ring resonator with deeply etched waveguides. In contrast, in a shallow etched DC, the interaction of the guided mode is through the slab region and thus reduced interaction with the side wall roughness. Figure 3.7(a) and 3.7(b) show the electric field profiles of symmetric and anti-symmetric modes (for TE polarization at  $\lambda \sim 1550$  nm) of a shallow etched DC with waveguide cross-section  $W = 560$  nm,  $H = 250$  nm  $h = 150$  nm and  $G = 150$  nm. From both the mode profiles, it is clear that the interaction with the sidewalls is minimum and major part of the coupling is through the slab region which reduce the additional loss at the DC section. As a result, insignificant loss at the coupling region making the loss-less coupling a reasonable assumption and thus a predictable transmission characteristics of the ring resonator.

It is known that for efficient and broadband grating coupler, shallow etching ( $h \sim$



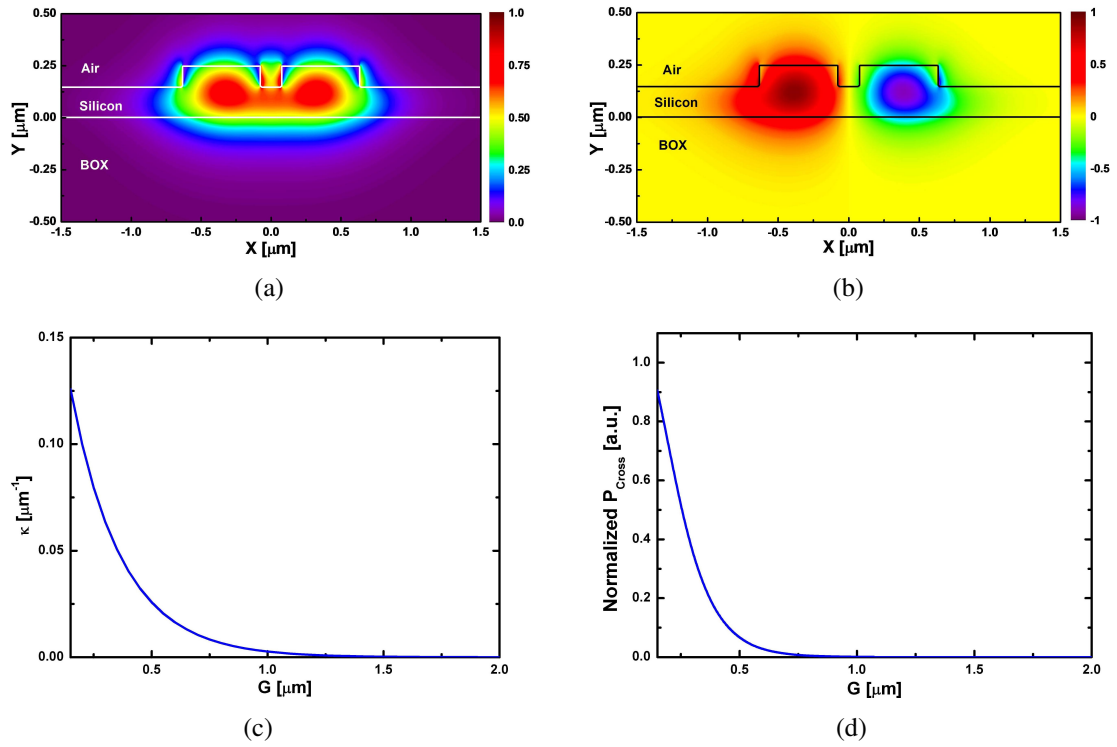


Figure 3.7: Calculated electric field profiles for (a) symmetric and (b) anti-symmetric modes of a DC with  $W = 560$  nm,  $H = 250$  nm,  $h = 150$  nm and  $G = 150$  nm. Calculated (c)  $\kappa$  and corresponding (d)  $P_{\text{Cross}}$  for  $L_{\text{DC}} = 10$   $\mu\text{m}$  plotted as a function of coupled waveguide separation ( $G$ ).

150 nm) is preferred [60]. In addition to that, the resonant devices such as ring resonator should be designed to operate only one polarization. This suppresses spurious resonant peaks due to the excitation of unwanted polarization. Shallow etched waveguides can be designed such that it supports only one polarization (TE). Therefore, we shall confine the etch depth of DCs and waveguides to 100 nm ( $h = 150$  nm), which make the fabrication of ring resonator integrated with broadband grating coupler using a single step lithography and ICPRIE process. Figure 3.7(c) and 3.7(d) shows the calculated  $\kappa$  and  $P_{Cross}$  (for  $L_{DC} = 10$   $\mu\text{m}$ ), respectively as a function of  $G$ . It is expected that the  $\kappa$  reduces exponentially as the function of  $G$  due to the fact that coupling/interaction between the coupled waveguide is through evanescent field. The evanescent field of a guided mode is exponentially reduces beyond the cladding.

Theoretically, DC can be considered as two parallel coupled waveguides separated by a finite distance, whereas in the practical case, the coupling between the waveguides are not only limited in the parallel section of DC but also at the branching region where the coupled waveguides are separated apart. Consequently, while estimating the value of  $L_{DC}$ , one must consider the coupling in branching regions at both ends of the DC. Therefore, the effective length of a DC may be defined by:

$$L_{DC}^{eff} = L_{DC} + 2\Delta L_b \quad (3.27)$$

where  $\Delta L_b$  is the correction term to accommodate coupling in one-side bend region of the DC. This is can be computed numerically by the following expression:

$$\Delta L_b(\lambda) = \frac{1}{\Delta n(G, \lambda)} \int_{z=0}^R \Delta n[\lambda, G'(z)] dz \quad (3.28)$$

where,

$$G'(z) = G + R - \sqrt{R^2 - z^2} \quad (3.29)$$

The function  $G'(z)$  is derived from the geometry shown in Figure 3.8(a). The coupling strength in branching region of DC,  $\kappa_b = \frac{\pi \Delta n[\lambda_0, G'(z)]}{\lambda_0}$  can be calculated as a function of  $G'(z)$  and which will be similar to Figure 3.7(c). Figure 3.8(b) shows the calculated values of  $k_b^2 = P_{Cross}^b$  as a function of interaction length  $z$  for various bend radius ( $R$ ), where  $P_{Cross}^b$  is the power coupled to the cross port due to the bend region. In this

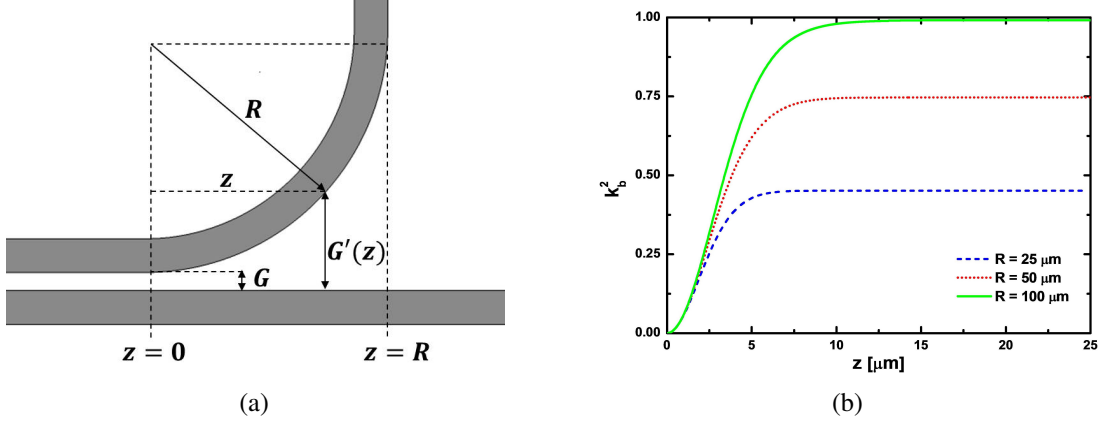


Figure 3.8: (a) Geometrical representation of DC region branching out the ring and the bus waveguides. (b) Cross coupled fraction of input power due to input and output bend regions of DC as a function of interaction length  $z$  in the branching region for  $R = 25 \mu\text{m}$  and  $G = 150 \text{ nm}$ .

calculation we have considered the length of parallel coupled waveguide region  $L_{DC}$  of DC is 0. It is evident from the figure that the cross-coupled power is increased as  $R$  increases. This is expected as the interaction length at the branching is extended due to the smaller variation of  $G'(z)$  for bends with larger radius. However, it must be noted that when we design ring resonator, this effect must be taken care to design  $L_{DC}$  as the coupling co-efficient decides many of the critical characteristics of the ring resonator.

## Dispersion

The waveguide dispersion is directly related to the wavelength dependency of guided mode effective index ( $n_{eff}$ ). Since  $n_{eff}$  is the characteristics of the guided mode size, wavelength dependent  $n_{eff}$  makes the interaction between the coupled waveguide wavelength dependent and thus  $\kappa$  is wavelength dependent which makes DC is dispersive. In this perspective, shallow etched waveguides  $n_{eff}$  is less dependent to the wavelength compared to deeply etched waveguides. Consequently, one may tend to think that the shallow etched waveguides are less dispersive. However, from eq. 3.24 - 3.26, one can clearly understand that the coupling can be made wavelength dependent if the  $L_{DC}$  is large enough though  $\Delta n$  is wavelength independent. In calculation, we found that the value  $\Delta n$  is higher for shallow etched waveguide ( $W = 560 \text{ nm}$ ,  $H = 250 \text{ nm}$  and  $h = 150 \text{ nm}$ ) compared to deeply etched waveguide ( $W = 500 \text{ nm}$ ,  $H = 250 \text{ nm}$  and  $h = 0 \text{ nm}$ ). So, shallow etched waveguides turns out to be highly dis-

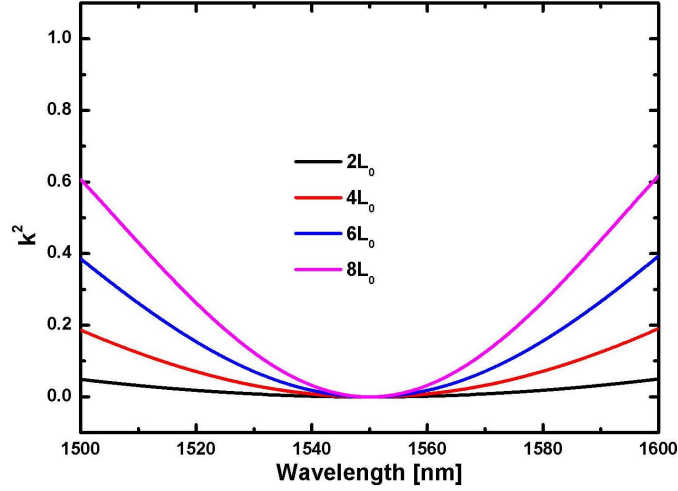


Figure 3.9: Dispersion characteristics of cross-coupling ( $k^2$ ) for shallow etched waveguide ( $W = 560$  nm,  $H = 250$  nm and  $h = 150$  nm) at various lengths ( $2L_0$ ,  $4L_0$ ,  $6L_0$  and  $8L_0$ ).  $L_0$  represents the cross-coupling length of the DCs at a reference operating wavelength  $\lambda_0 = 1550$  nm.

persive than deeply etched waveguides for fixed  $L_{DC}$ . Figure 3.9 shows the dispersion characteristics of a shallow etch waveguide ( $W = 560$  nm,  $H = 250$  nm and  $h = 150$  nm) for various DC cross-coupling lengths ( $L_0$ ).  $L_0$  is defined as the DC length at which power is completely transferred from the bar port to cross port and which is expressed as:

$$L_0 = \frac{\lambda_0}{2\Delta n} \quad (3.30)$$

Though the DC coupling coefficient is periodic as function of  $L_{DC}$ , it is important to choose appropriate  $L_{DC}$  while designing ring resonator to control the dispersion.

### Asymmetric Directional Coupler

So far, for the numerical simulations, we have considered the DC is geometrically symmetric, ie, the coupled waveguides have identical size and shape. However, practically, the fabrication of symmetric DC in submicron regime is really challenging due fabrication induced errors/proximity effects especially in the case of electron beam lithography. In order to calculate the exact characteristics of asymmetric DC, one should use coupled mode theory [106]. Using coupled mode theory, Bar and Cross port electric

field amplitudes propagating along  $z$  direction can be defined as:

$$E_{Bar}(z) = E_0 e^{i\delta z} \left( \cos(\sqrt{\kappa^2 + \delta^2} z) - i \frac{\delta}{\sqrt{\kappa^2 + \delta^2}} \sin(\sqrt{\kappa^2 + \delta^2} z) \right) \quad (3.31)$$

$$E_{Cross}(z) = -i E_0 e^{i\delta z} \frac{\kappa}{\sqrt{\kappa^2 + \delta^2}} \sin(\sqrt{\kappa^2 + \delta^2} z) \quad (3.32)$$

where,  $2\delta$  is the phase mismatch and is given by

$$2\delta = (\beta_{Bar} + \kappa_{Bar}) - (\beta_{Cross} + \kappa_{Cross}) \quad (3.33)$$

where,  $\beta_{Bar}$ , and  $\beta_{Cross}$  are the propagation constants of bar and cross ports when they are isolated (not coupled).  $\kappa_{Bar}$  and  $\kappa_{Cross}$  are the correction to the propagation constant when Bar and Cross ports are coupled. The  $\kappa$  for an asymmetric coupler can still be calculated using supermode theory. However, to calculate the correction factors ( $\kappa_{Bar}$  and  $\kappa_{Cross}$ ) one should use coupled mode theory [106]. We have used Lumerical ModeSolutions tool for the calculation of individual mode profiles of the Bar and Cross ports and the numerical values of asymmetric DC parameters are obtained using Matlab. Figure 3.10(a) shows the power distribution of bar (black line) and cross (red line) ports of an asymmetric DC as function of  $L_{DC}$ . Here, we have considered bar port width ( $W_{Bar}$ ) to be 560 nm and cross port width ( $W_{Cross}$ ) to be 480 nm with  $H = 250$  nm and  $h = 150$  nm. It can be noticed that the power is not transferred 100 % to the Cross port due to the phase mismatch of the Bar and Cross ports. As a consequence of this, there would be the presence of resonance peaks in the throughput characteristics of the ring resonator though it is operated at cross-coupling point ( $L_{DC} = L_0$ ). Figure 3.10(b) and 3.10(c) show the coupling induced delay ( $\tau_{dc}$ ) and corresponding effective group index ( $n_g^{eff}$ ), respectively for various values of Cross port width ( $W_{Cross}$ ) by keeping a fixed Bar port width ( $W_{Bar}$ ). Here the  $\tau_{dc}$  and  $n_g^{eff}$  can be calculated using the following eqns.:

$$\tau_{DC} = \frac{d\phi}{d\omega} \quad (3.34)$$

$$n_g^{eff} = \frac{\tau_{DC} c}{L_{DC}} \quad (3.35)$$

where,  $\phi = \angle E_{Bar}$  is the coupling induced phase. It is interesting to notice from the Figure 3.10(b) that the value of  $n_g^{eff}$  can be higher or lower than the straight waveguide

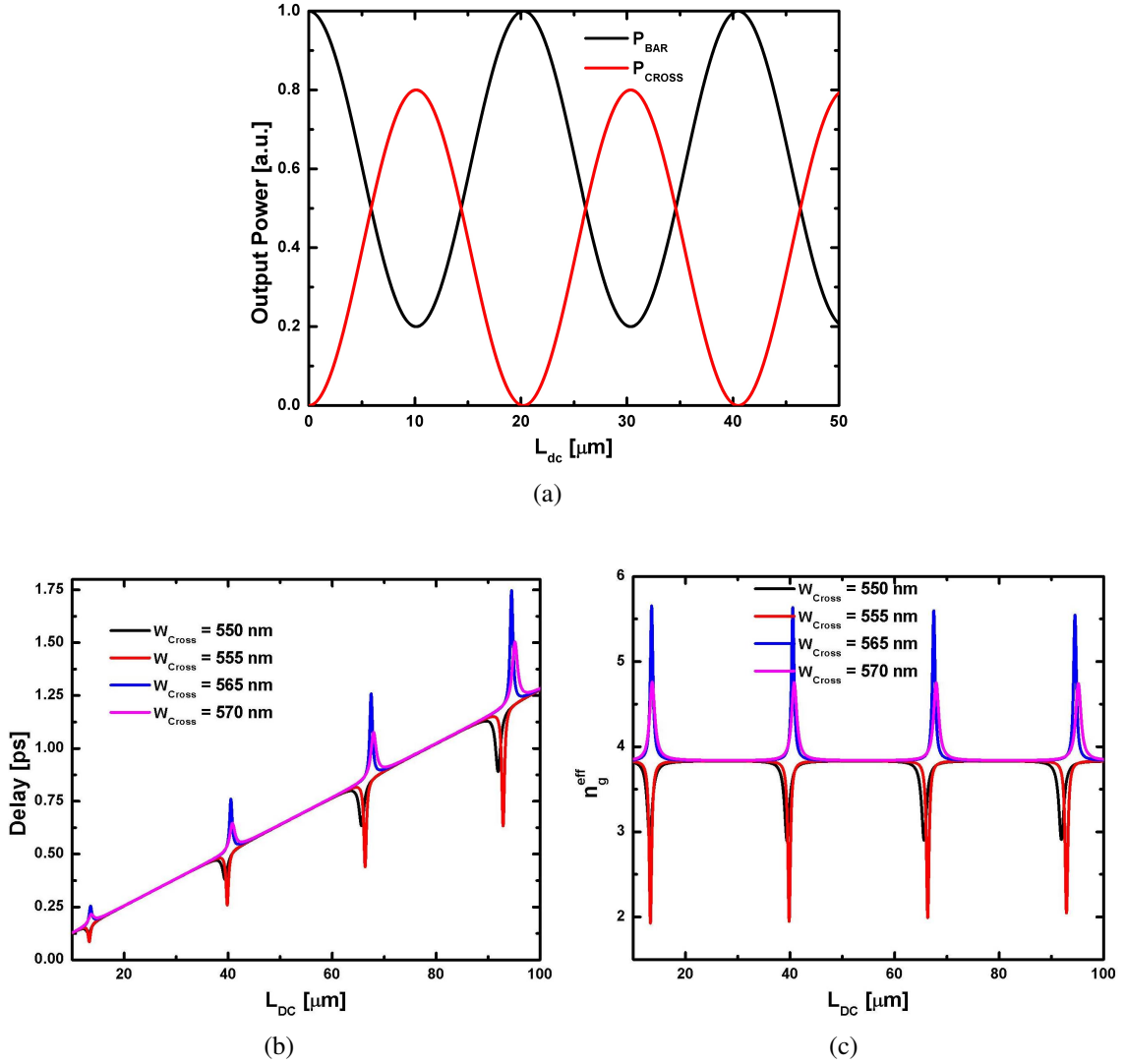


Figure 3.10: (a) Typical power distribution of bar and cross ports of an asymmetric DC as function of  $L_{DC}$ : where,  $W_{Bar} = 560$  nm for  $W_{Cross} = 480$  nm. (b) Coupling induced delay and (c) corresponding effective group index of asymmetric DC is plotted as function of  $L_{DC}$  for various values of cross port waveguide widths ( $W_{Cross}$ ) for a fixed bar port width ( $W_{Bar}$ ) of 560 nm. All calculations are shown for  $H = 250$  nm,  $h = 150$  nm and  $\lambda = 1550$  nm.

group index at every  $L_{DC} = mL_0$  depending on the value of  $\Delta W = W_{Bar} - W_{Cross}$ , where  $m = 1, 3, 5, \dots$ . Depending on the value of  $\Delta W$  (positive or negative),  $n_g^{eff}$  is calculated to be less or more than the  $n_g$  of straight waveguide giving a delay less or more than the straight waveguide. This property of DC may find many applications in the field of delay lines as discussed in [107]. From Figure 3.10(b) and 3.10(c) it can be observed that the the peak points of the delay or  $n_g^{eff}$  is being separated for various  $W_{Cross}$  values as the  $L_{DC}$  is increased. This is happening because the differential change in  $L_0$  with respect to  $W_{Cross}$  is amplified as the value of  $m$  increased.

### 3.1.3 Design of Ring Resonator Cavity

The ring resonator cavity has to be designed based on many parameters such as bend induced loss, FSR, Q-factor, propagation loss of the waveguide, critical coupling, etc. We have seen from chapter 2 that the minimum bend radius ( $R_{min}$ ) for a bend waveguide designed on 2  $\mu\text{m}$  device layer SOI is limited to 500  $\mu\text{m}$ . From section 3.1.1, it is clear that the splitting ratio of a  $2 \times 2$  MMIC remain almost constant (0.5) throughout the wavelength of interest. It is also known that that the MMIC is a fabrication tolerant structure. Thus, we set the cavity length of large volume ring resonator to  $2\pi R_{min} + 2(L_{mmi} + L_t) = 5320 \mu\text{m}$  for experimental demonstration.

In contrast, the DC designed on submicron device layer is found to be less fabrication tolerant and highly dispersive. Also, it is observed that bend induced coupling is significant in DCs with shallow etched submicron waveguides. So, the cavity design of micro-ring resonators with submicron waveguide cross-section has to be analyzed carefully. Since our discussion is confined in the shallow etched waveguide, the minimum bend radius is the limiting factor of maximum FSR that can be achieved. Figure 3.11 shows the bend induced loss of a shallow etched waveguide as a function  $R$ . From the figure it is clear that, theoretically, the bend induced loss can be neglected if the minimum radius of the ring kept to be  $\sim 25 \mu\text{m}$ . If we assume that  $R = 25 \mu\text{m}$ , the loss factor  $a$  can be calculated to be  $\sim 0.991$  for a ring resonator (with  $L_{DC} = 0$ ) made of photonic wire waveguide with a propagation loss of  $\alpha \sim 5 \text{ dB/cm}$ . From Figure 3.8(b) we have seen that  $t$  due to bend induced coupling is  $\sim 0.6716$ . Using eq. 3.6, one can

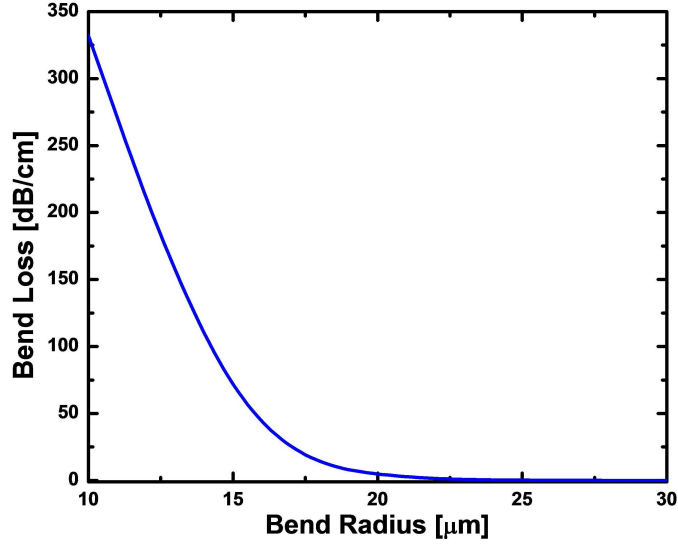


Figure 3.11: Bend induced loss of a shallow etched waveguide ( $W = 560$  nm,  $H = 250$  nm and  $h = 150$  nm) as function of bend radius  $R$ .

calculate the extinction ratio (ER) corresponds to the above mentioned configuration to be  $\sim 1.09$  (0.4 dB). So, to have higher ER, the  $L_{DC}$  has to be increased such that the critical condition has to be satisfied. Figure 3.12(a) shows the ER variation of ring resonator as function of  $L_{DC}$  for various  $R$ . In the calculation, we have included the coupling due to bends at the branching region of DC. The propagation loss assumed for the calculation of ER is 5 dB/cm. From the figure it can be noticed that a larger  $L_{DC}$  required for critical coupling of microring resonator with radius 25  $\mu\text{m}$  in comparison with 50  $\mu\text{m}$  ring radius. This is expected because bend induced coupling is larger for ring resonator with  $R = 50$   $\mu\text{m}$ . Similarly, Figure 3.12(b) shows the calculated Q-factor variation of the ring resonator as a function of  $L_{DC}$  near to the resonance at  $\lambda = 1550$  nm. Here we have used the calculated value of  $n_g = 3.86$  for Q-value calculation. The Q-value reaches maximum ( $1.37 \times 10^5$ ) for both ring resonators with  $R = 25$   $\mu\text{m}$  and 50  $\mu\text{m}$  as  $t \rightarrow 0$ . Though we have seen from eq. 3.6 that the Q-factor is directly proportional to perimeter of the ring  $L$ , the difference has not been observed in Figure. 3.12(b). This is due to the trade-off between the total loss of the cavity and ring perimeter. The cavity loss increases as the perimeter of the ring resonator increases this reduces Q-factor. Figures 3.12(c) and 3.12(d) show the calculated transmission characteristics and corresponding  $k^2$  of microring resonators ( $R = 25$   $\mu\text{m}$ ) with  $L_{DC} = 18.5$   $\mu\text{m}$  and 96  $\mu\text{m}$ , respectively. The  $L_{DC}$  of the ring resonator such that the ER is maximum near to  $\lambda \sim 1550$  nm. To show the dispersion characteristics of the DC, we have used



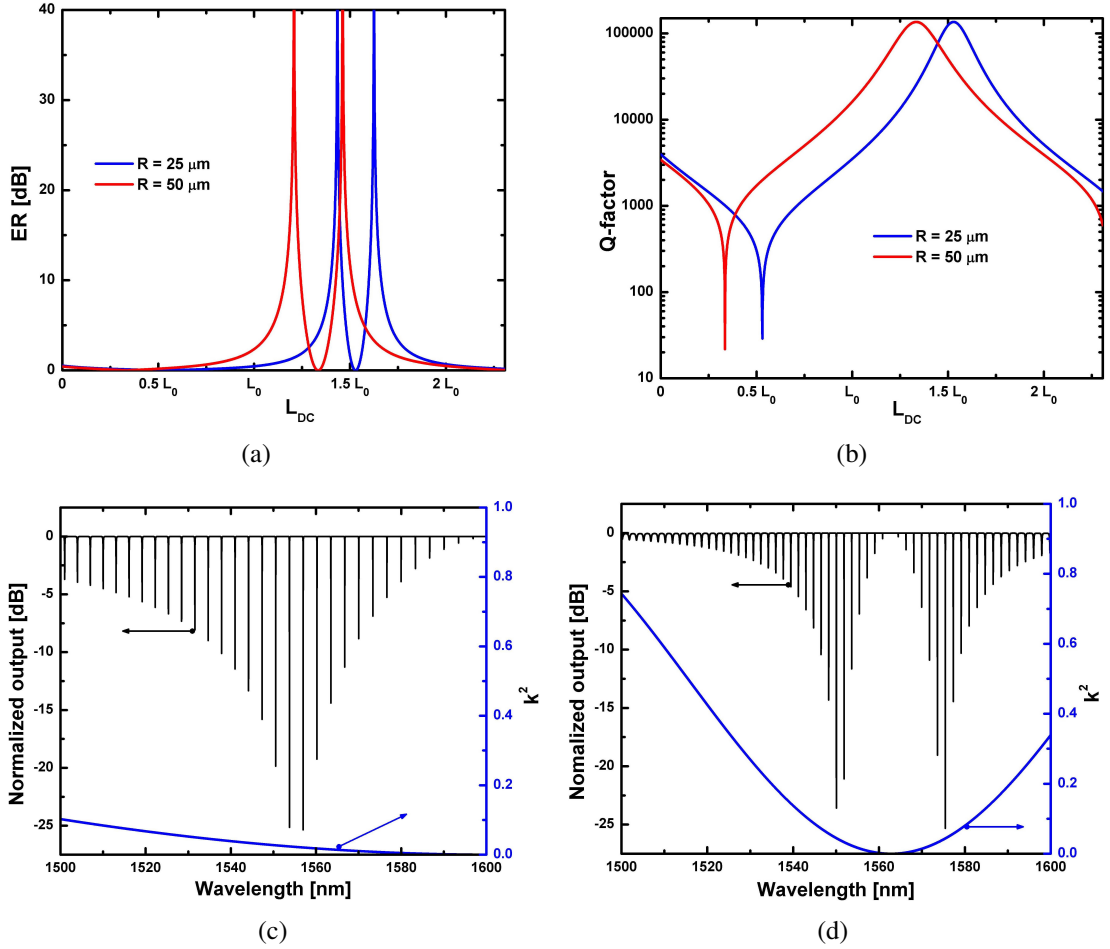


Figure 3.12: Calculated values of (a) ER and (b) Q-factor of shallow etched photonic wire ring resonator as function of  $L_{DC}$ : where  $L_0 = 13 \mu\text{m}$ . Calculations are done by including the bend induced coupling at the branching region of DC. Calculated output characteristics and corresponding  $k^2$  (right axis) of ring resonator with (c)  $L_{DC} = 18.5 \mu\text{m}$  and (d)  $L_{DC} = 96 \mu\text{m}$ . Parameters used for calculation are :  $\alpha = 5 \text{ dB/cm}$ ,  $W = 560 \text{ nm}$ ,  $H = 250 \text{ nm}$ ,  $h = 150 \text{ nm}$ ,  $G = 150 \text{ nm}$  and  $R = 25 \mu\text{m}$ .

wavelength dependent effective index  $n_{eff}(\lambda)$ . It is interesting to notice from Figures 3.12(c) and 3.12(d) that the ER variation as function of wavelength. Though all the cross-sectional parameters are same for both the ring resonators, Figure 3.12(d) looks highly dispersive as the  $L_{DC}$  ( $96 \mu\text{m}$ ) of this ring resonator is significantly higher than the ring resonator  $L_{DC}$  ( $18.5 \mu\text{m}$ ) shown in Figure 3.12(c). This in fact justifies the discussion of DC dispersion that we made in section 3.1.2.

## 3.2 Demonstration of Large Volume Ring Resonator

For experimental demonstration of large volume ring resonator, we have preferred MMIC based design on 2  $\mu\text{m}$  device layer substrates. We prepared two ring resonator samples on 5  $\mu\text{m}$  and 2  $\mu\text{m}$  device layer substrates separately. Both the samples are prepared using i-line photolithography and conventional RIE process. Ring resonator fabrication on 5  $\mu\text{m}$  device layer was meant to test the feasibility of device fabrication using the proposed surface trimming technique. Whereas, the ring resonator fabricated on 2  $\mu\text{m}$  device layer is used as the reference sample for performance comparison of surface trimmed ring resonator. To fabricate surface trimmed ring resonator, initially, ring resonators along with reference waveguides and MMICs are patterned with larger cross-section waveguides on an optical grade SOI substrate (device layer thickness = 5  $\mu\text{m}$ , BOX thickness = 1  $\mu\text{m}$  and handle wafer thickness = 500  $\mu\text{m}$ ) using photolithography and subsequent first RIE process ( $\text{SF}_6$  : Ar :: 20 sccm : 20 sccm, power = 150 W, chamber pressure = 200 mT, duration = 3 min. 15 sec.). Initial single-mode waveguide parameters are measured to be  $W_0 = 5 \mu\text{m}$ ,  $H_0 = 5 \mu\text{m}$  and  $h_0 = 4 \mu\text{m}$ . The MMIC parameters ( $W_{mmi}$ ,  $L_{mmi}$ ,  $W_t$ ,  $W_{ph}$  and  $L_t$ ) after lithography and first RIE are measured to be nearly same as photomask specification shown in Figure 3.4(d). During the second RIE process ( $\text{SF}_6$  : Ar :: 25 : 25 sccm, Power = 150 W, Pressure = 250 mT, duration = 7 min. 20 sec.), the 5  $\mu\text{m}$  waveguides are trimmed to a 2  $\mu\text{m}$  waveguide with cross-sectional parameters  $W = 1.8 \mu\text{m}$ ,  $H = 2 \mu\text{m}$  and  $h = 1 \mu\text{m}$ . After trimming the waveguide, end-facets of samples were polished carefully perpendicular to the waveguide axes before they were taken for optical characterizations. Optical microscopic images of a polished end facets of typical 5  $\mu\text{m}$  and 2  $\mu\text{m}$  are shown in Figure 3.13(a) and 3.13(b), respectively. Similarly, the reference sample is prepared on 2  $\mu\text{m}$  device layer SOI substrate using a single step photolithography and anisotropic (first) RIE process ( $\text{SF}_6$  : Ar :: 20 sccm : 20 sccm, power = 150 W, chamber pressure = 200 mT, duration = 3 min. 15 sec.). The waveguide dimensions of the reference (untrimmed) sample was nearly matching with the trimmed waveguide except the slanted sidewalls. The mode profile measurements of the waveguides are carried out by free-space light coupling set-up where laser light is launched at the input using a 20X lens and imaging the near-field profile at the output IR camera (LBP2-HR-IR) using a 60X lens. The mode-size

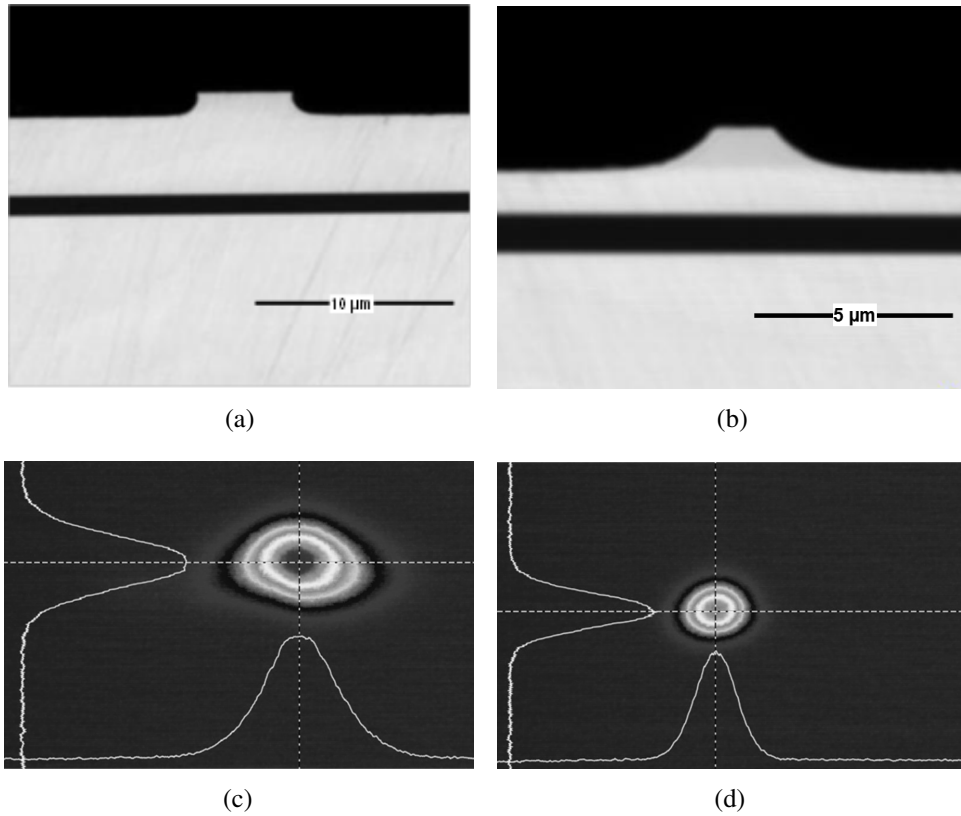


Figure 3.13: Optical microscopic images of polished end-facets for 5  $\mu\text{m}$  waveguide (a) and trimmed 2  $\mu\text{m}$  waveguide (b); and guided fundamental mode intensity distributions for 5  $\mu\text{m}$  (c) and 2  $\mu\text{m}$  (d), for TE polarized light at  $\lambda = 1550$  nm.

(full width at  $1/e^2$  intensity) of the fundamental guided mode for LCRW and trimmed waveguides have been found to be nearly polarization independent and estimated to be  $8.2 \mu\text{m} \times 4.4 \mu\text{m}$  and  $3.5 \mu\text{m} \times 2.5 \mu\text{m}$ , respectively (see Figures. 3.13(c) and 3.13(d)), which are closely matched to the theoretical values. The waveguide loss is estimated using reference waveguides by recording the transmitted Fabry-Perot resonance contrast obtained by tuning the wavelength of input laser light (with a tuning step of 1 pm). Average waveguide loss for 5  $\mu\text{m}$  is  $\sim 0.5$  dB/cm and is found to be polarization independent; whereas for surface trimmed 2  $\mu\text{m}$  waveguide, it is measured to be 0.6 dB/cm and 0.6 dB/cm for TE and TM polarization, respectively). Whereas, the propagation loss of the untrimmed 2  $\mu\text{m}$  waveguide is measured to be slightly higher  $\sim 2.3$  dB/cm and 2 dB/cm for TE and TM polarization, respectively. This is expected in untrimmed waveguide (vertical sidewalls) as major part of the guided mode profile is confined in the rib region which leads to enhanced light interaction with the sidewall roughness.

Table 3.2: Characterization summary of large volume MMICs based ring resonators (Untrimmed and trimmed) with 500  $\mu\text{m}$  ring radius.

Property	Untrimmed		Trimmed	
	TE	TM	TE	TM
ER [dB]	6.2	10	5.7	4
loss [dB/cm]	2.3	2	0.6	0.8
FSR [pm]	115	123	110	110
Q-factor	51,670	96,884	33,698	25,412

Also, first RIE is optimized for anisotropic etch profile which in turn increases the surface roughness leading to a higher propagation loss. In the case of trimmed waveguide, since the sidewalls are slanted (see Figure 3.13(b)) mode is pushed toward the slab and which reduces guided mode interaction with sidewall roughness. The estimated propagation loss values have to be considered as the maximum possible loss as we have assumed the polished end-facets are ideal and offers a Fresnel reflectivity for the guided mode as  $R_F = 0.31$ . The actual reflectivity has to be lower than this as there are additional losses due to end-facet imperfections. Importantly, we do not observe much difference in waveguide losses in spite of reducing the waveguide cross-section from 5  $\mu\text{m}$  to 2  $\mu\text{m}$ . This is mainly attributed to the relatively smoother side-walls of the trimmed waveguide; the second RIE process is dominated by chemical reactions. Optical microscopic image of a surface trimmed ring resonator ( $R = 500 \mu\text{m}$ ) is shown in Figure 3.14(a) with the reference  $2 \times 2$  MMIC and straight waveguides. Magnified SEM image of surface trimmed  $2 \times 2$  MMIC is shown Figure 3.14(b). The fabricated ring resonators were characterized by measuring wavelength dependent throughput - a tunable laser source ( $P = 10 \text{ mW}$ ,  $1520 \text{ nm} \leq \lambda \leq 1600 \text{ nm}$ , tunable resolution 1 pm) is used in the characterization setup. Figure 3.14(c) and Figure 3.14(d) show a portion of transmission characteristics of untrimmed (reference) and trimmed ring resonators, respectively. Blue and red lines represent the characteristics for TE and TM polarization, respectively. The measured characteristics for the large volume ring resonators are summarized in Table 3.2. The ER for trimmed and untrimmed ring resonators are measured to be nearly same for TE polarization, however, the ER difference (trimmed and untrimmed) is significant in case of TM polarization. An optimum MMIC is expected to give 3 dB splitting, in that case the ER variation is only due to the variation in loss factor ( $a$ ) of ring. we can expect a reasonable change in  $a$  due large ring perimeter and

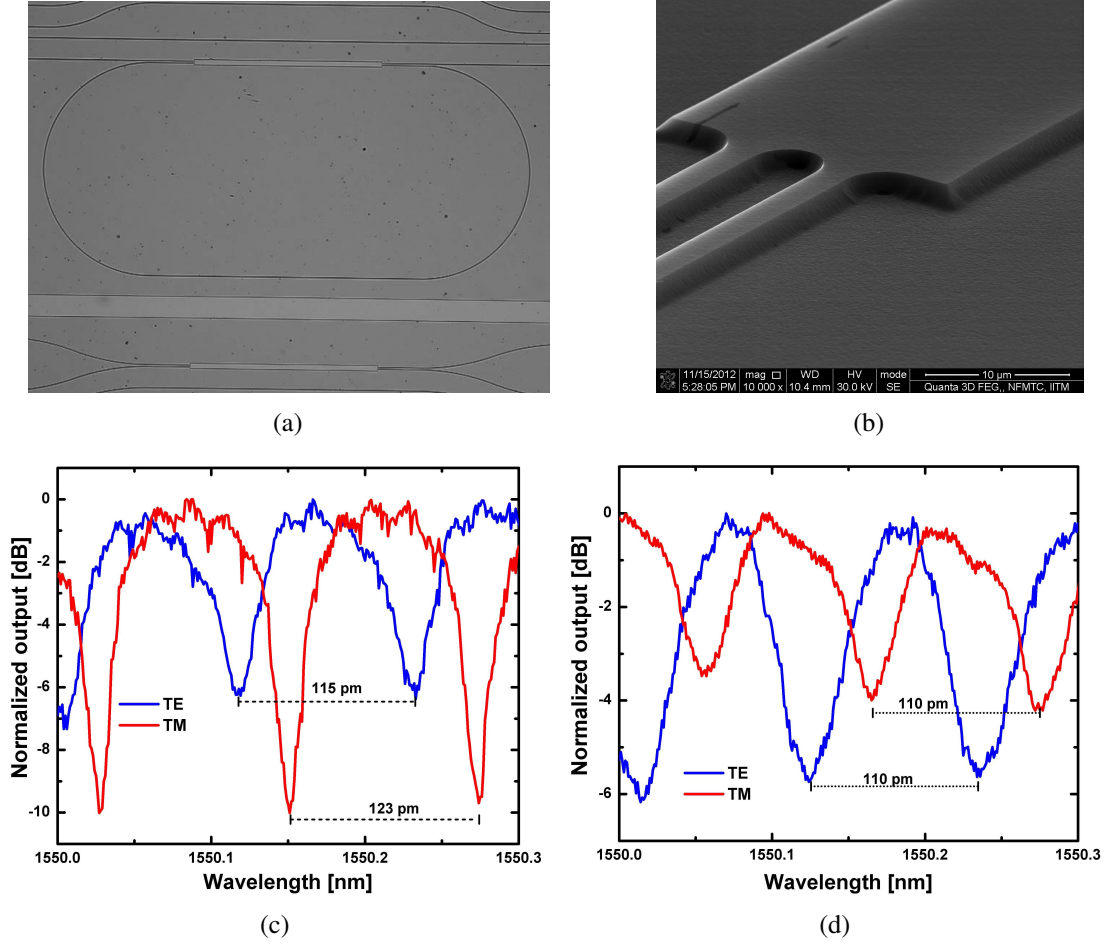


Figure 3.14: (a) Optical microscopic image of MMIC based ring resonator (ring radius  $\sim 500 \mu\text{m}$ ) with reference MMIC and straight waveguides. (b) SEM image of a surface trimmed MMIC. Measured transmission characteristics of ring resonators: (c) fabricated directly on  $2 \mu\text{m}$  device layer and (d) fabricated on  $5 \mu\text{m}$  device layer and surface trimming process is carried out to reduce waveguide cross-section.

propagation loss difference between trimmed and untrimmed waveguides. However, the Q-factor of trimmed ring resonator is measured to be much less than untrimmed resonator though the propagation loss is better for trimmed waveguide. This suggests that coupling induced loss of trimmed MMIC is large or the MMI is not splitting power equally. Interestingly, the FSR of the trimmed ring resonator is found to be equal for both TE and TM polarization, suggesting that the trimmed waveguide is polarization independent in terms of group index ( $n_g$ ).

### 3.3 Demonstration of Compact Microring Resonator

It is observed that the major challenges of microring resonator made out of trimmed waveguides (2  $\mu\text{m}$  device layer height) are the bend induced loss due to smaller core-cladding index contrast and the variation MMIC splitting conditions. As the bend induced loss is significant, large resonator volume limits the maximum achievable FSR (up to a few hundreds of picometer) of ring resonator with micron-sized waveguides. So, to have a single-mode silicon waveguide with higher guided mode optical confinement, one should choose submicron waveguide geometry. This ensure compact bend radius and thus higher ring resonator FSR which is necessary for many applications. In the following section, fabrication and characterization of DC based microring resonator with submicron waveguide cross-section is discussed.

#### 3.3.1 Microring Resonator: Fabrication and Characterization

Ring resonator devices with grating coupler at the input and output ends are fabricated on submicron device layer SOI substrate (device layer - 250 nm, BOX - 3  $\mu\text{m}$  and handle layer -  $\sim$  500  $\mu\text{m}$ ) using electron beam lithography and ICPRIE process with the optimized recipe discussed in section 2.3.3. The characterization of the devices is carried out using an optical spectrum analyzer (Apex-AP2043B) with an inbuilt laser source. Figure 3.15(a) shows the SEM image of a fabricated ring resonator with  $L_{DC} = 10 \mu\text{m}$  and  $R = 50 \mu\text{m}$ . The waveguide geometrical parameter are measured to be  $W \sim 564 \text{ nm}$ ,  $H \sim 250 \text{ nm}$ .  $h \sim 150 \text{ nm}$  and  $G \sim 132 \text{ nm}$ . From SEM image, it can be noticed that the coupled waveguides at branching region of the DC is separated apart due to bend regions of both bus and ring waveguides. As a result, the effect of the bend induced coupling would be less compared to the structure where the bus waveguide is straight. Figure 3.15(b) shows the measured transmission characteristics of the ring resonator shown in Figure 3.16(d). The ring resonator transmission spectrum is normalized to reference straight waveguide fabricated on the same chip to get rid of the wavelength dependent grating response. Since we have designed the submicron waveguide and grating coupler to support only TE polarized light, all the measurements are shown for TE polarization until and otherwise mentioned. The ER variation of

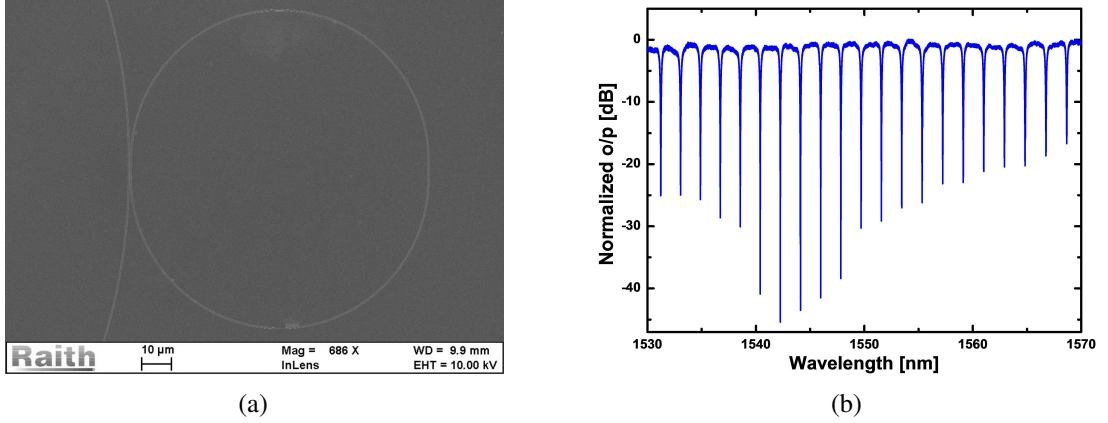
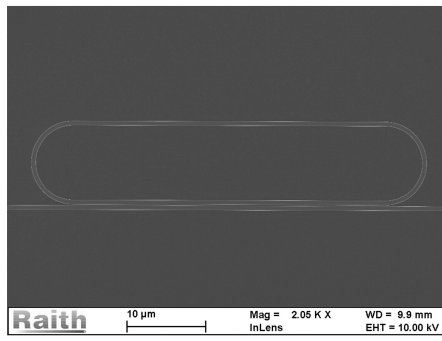


Figure 3.15: (a) SEM image of the fabricated ring resonator with  $L_{DC} = 10 \mu\text{m}$  and  $R = 50 \mu\text{m}$ , where magnified view of the DC region is shown as the inset. (b) Measured transmission (normalized to straight waveguide) characteristics of the device shown in (a).

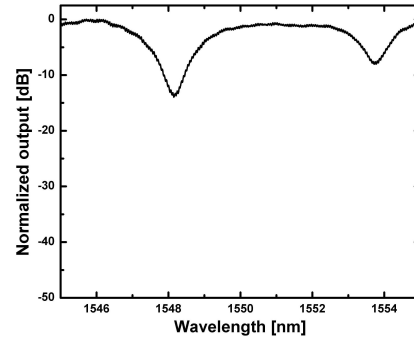
the transmission spectrum conveys that the ring resonator is slightly dispersive and the critical coupling condition ( $t = a$ ) is satisfied near to  $\lambda = 1542 \text{ nm}$ .

### 3.3.2 Spectral Characteristics

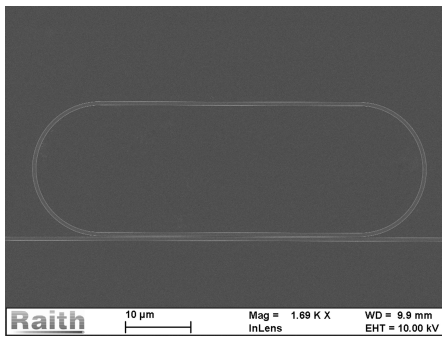
In order to study the bend induced spectral characteristics, we have fabricated microring resonators with various bend radius (from  $5 \mu\text{m}$  to  $100 \mu\text{m}$ ). Figure 3.16(a), 3.16(b), 3.16(c) and 3.16(d) show the SEM images of fabricated race track ring resonators ( $L_{DC} = 40 \mu\text{m}$ ) with  $R = 5 \mu\text{m}$ ,  $R = 10 \mu\text{m}$ ,  $R = 25 \mu\text{m}$  and  $R = 50 \mu\text{m}$ , respectively. Transmission characteristics of devices shown in Figure 3.16(a), 3.16(b), 3.16(c) and 3.16(d) are given in Figure 3.16(e), 3.16(f), 3.16(g) and 3.16(h), respectively. Notice that in this case bend induced coupling of the DC is significant as the coupled waveguides are separated only due to the ring waveguide bend. Though  $L_{DC}$  of all the devices are same, the ER and Q-factor are found to be varying significantly. This is due to the variation of bend induced coupling and loss factor of ring resonators as a function of  $R$ . The sinusoidal variation of off-resonant power level of the ring resonator with  $R = 50 \mu\text{m}$  is indicating that an addition resonance due to fabrication error. The FWHM of ring resonator with  $R = 5 \mu\text{m}$  is measured to be  $\sim 2.1 \text{ nm}$ , much higher than other devices, indicating that this device has the highest bend induced loss, as expected. Figure 3.17(a) shows the transmission characteristics (black line) of a high



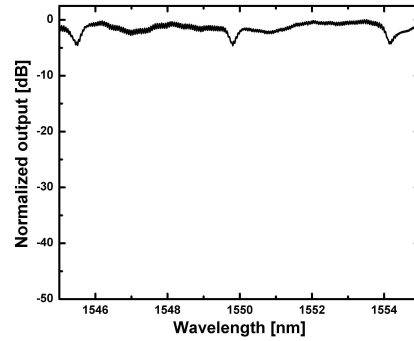
(a)



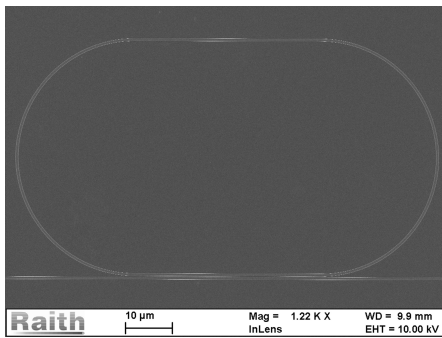
(e)



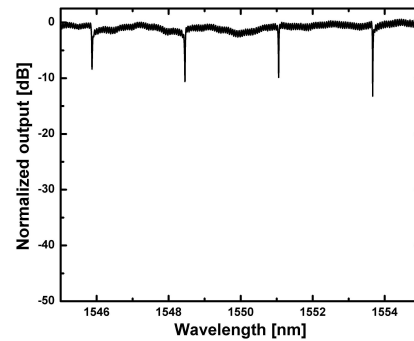
(b)



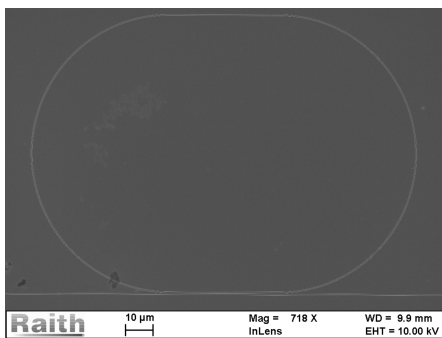
(f)



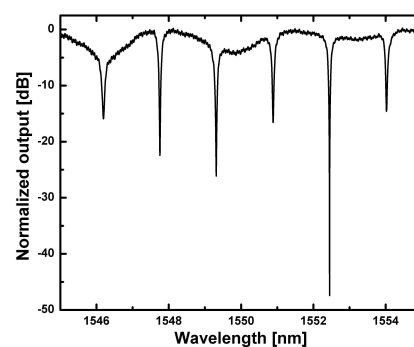
(c)



(g)



(d)



(h)

Figure 3.16: SEM images of fabricated race track ring resonators with (a)  $R = 5 \mu\text{m}$  and (b)  $R = 10 \mu\text{m}$  (b)  $R = 25 \mu\text{m}$  (b)  $R = 50 \mu\text{m}$  and their corresponding transmission characteristics are shown in (e), (f), (g), (h), (i) respectively. The waveguide parameters ( $W = 560 \text{ nm}$ ,  $H = 250 \text{ nm}$ ,  $h = 150 \text{ nm}$  and  $G = 150 \mu\text{m}$ ) and  $L_{DC} = 40 \mu\text{m}$  are same for all the devices.



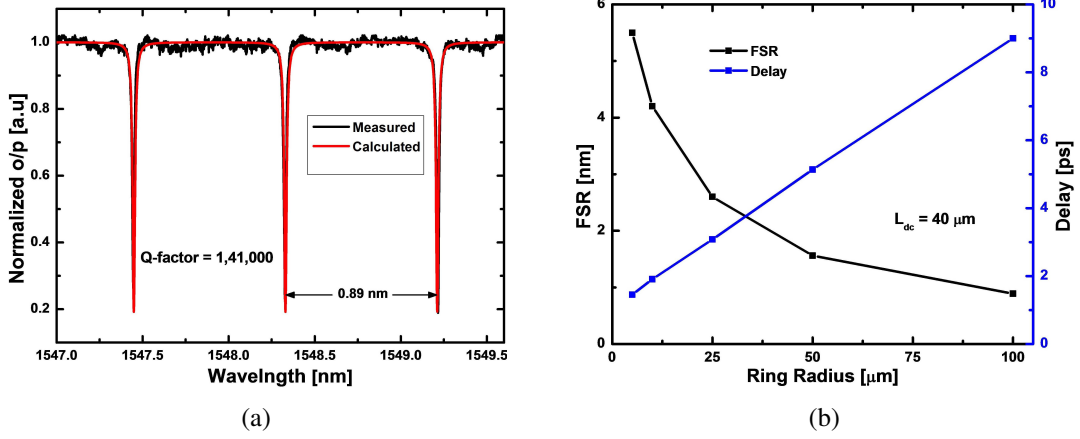


Figure 3.17: (a) Measured and fitted transmission spectrum of a high Q-factor ring resonator with  $R = 100 \mu\text{m}$ . (b) FSR (left axis) and resonant delay (right axis) variation are shown as a function  $R$  for devices with  $W = 560 \text{ nm}$ ,  $H = 250 \text{ nm}$ ,  $h = 150 \text{ nm}$ ,  $G = 150 \text{ nm}$  and  $L_{DC} = 40 \mu\text{m}$ .

Q-factor ring resonator with  $R = 100 \mu\text{m}$  and  $L_{DC} = 40 \mu\text{m}$ . The Q-value of this ring resonator is estimated to be  $\sim 1,41,000$ . The red line represents the theoretical fitting to extract the  $\alpha$  and  $n_g$ . The values of  $\alpha$  and  $n_g$  are estimated to  $\sim 2 \text{ dB/cm}$  and  $3.8$ , respectively. Figure 3.17(b) shows the measured FSR variation at  $\lambda \sim 1550 \text{ nm}$  as a function of  $R$  of the ring resonator. The maximum FSR is measured to be  $\sim 5.5 \text{ nm}$  for the ring resonator with  $R = 5 \mu\text{m}$  and the minimum value is found to be  $\sim 0.89 \text{ nm}$  for the resonator with  $R = 100 \mu\text{m}$ . The delay ( $\tau_{res}$ ) corresponds to ring resonator FSR is shown in the right axis of Figure. 3.17(b) and it is defined as:

$$\tau_{res} = \frac{\lambda^2}{c \times \text{FSR}} \quad (3.36)$$

where,  $c$  is the light velocity in free space. The linear dependence of  $\tau_{res}$  on the  $R$  indicating that the group index ( $n_g$ ) of the waveguide is constant as function of ring radius. Here,  $n_g$  can be calculated using eqs. 3.4 and 3.36;

$$n_g = \frac{d\tau_{res}}{dR} \times \frac{c}{2\pi} \quad (3.37)$$

The value of  $n_g$  estimated from Figure 3.17(b) and it is found to be  $\sim 3.8$  and which is closely matching with the theoretically obtained value (3.83).

### 3.3.3 Propagation Loss Extraction

In order to estimate the propagation loss of the waveguide, we have fabricated ring resonators with varying perimeter just by increasing the straight section of the ring keeping all other parameters same. The  $L_{DC}$  of this device is made large ( $\sim 100 \mu\text{m}$ ) such that the ring resonator critical coupling is obtained within the wavelength region ( $1525 \text{ nm} \leq \lambda \leq 1625 \text{ nm}$ ) of interest. At critical coupling, Eqn. 3.8 can be modified as:

$$Q_C = \frac{\pi n_g L a}{\lambda_{res}(1 - a^2)} \quad (3.38)$$

where,  $Q_C$ ,  $n_g$  and  $\lambda_{res}$  can be directly measured from the ring resonator transmission spectrum and  $L$  is a known parameter from the design. Then, one can easily calculate  $t$  or  $a$  using Eqn. 3.38 for various  $L$ . Since all other ring resonator parameters except  $L$  remain same, the difference in the  $a$  is only due to the difference in  $L$ . We have estimated the propagation loss of the waveguide  $\alpha \sim 2 - 3 \text{ dB/cm}$  using this technique. The only assumption that we have made in estimating the  $\alpha$  is that it remains same for the shift of  $\lambda_{res}$  for various  $L$ . However, this assumption is valid as the waveguides are shallow etched,  $\alpha$  variation within 20 nm variation of  $\lambda$  can be neglected.

### 3.3.4 Dispersion Characteristics

To study the dispersion characteristics of the ring resonator experimentally, we have fabricated ring resonator devices with varying DC lengths with a fixed  $R = 25 \mu\text{m}$ . In these ring resonators, we have increased the perimeter of the ring just by adding an extra straight section of length  $L_x$  to the ring. This in fact helps to reduce the FSR of the resonance spectrum such that the ER variation of the transmission can be identified clearly. Figure 3.18(a) and 3.18(b) show the measured transmission characteristics of ring resonators with  $L_{DC} = 40 \mu\text{m}$  and  $100 \mu\text{m}$  respectively.  $L_x$  for both resonators fixed to be  $400 \mu\text{m}$  to reduce the FSR. As we have discussed in the section 3.1.2, the ER variation is higher for ring resonator with  $L_{DC} = 100 \mu\text{m}$  due to the enhanced DC dispersion. The wavelength with lowest throughput transmission corresponds to the critically coupled wavelength. In transmission spectrum, both sides of the critically coupled wavelength, the ER is reduced. Referring to the Figure 3.12(a), it can be easily

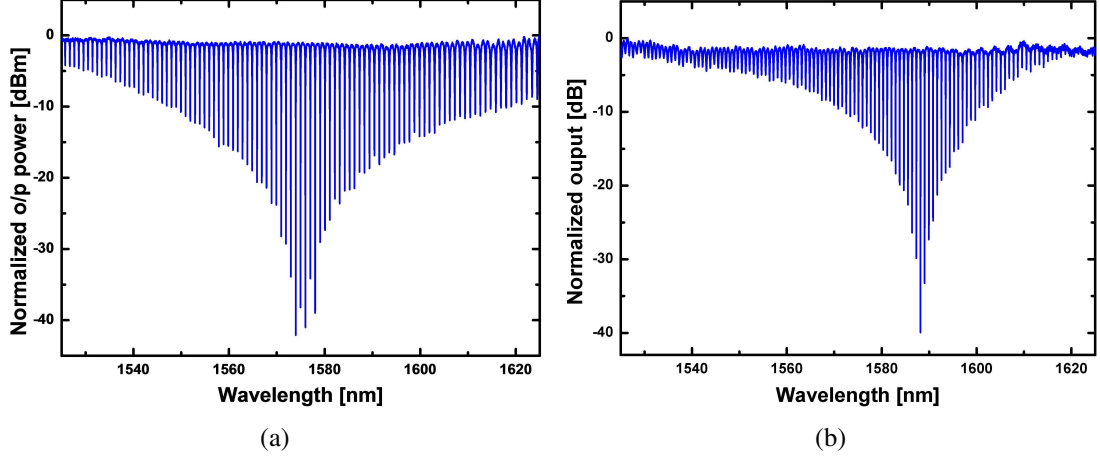


Figure 3.18: Measured transmission spectrum of ring resonators with (a)  $L_{DC} = 40 \mu\text{m}$  and (b)  $L_{DC} = 100 \mu\text{m}$ :  $L_x$  is fixed to be  $400 \mu\text{m}$  for the ring resonators.

understood that the ER is sharply varying towards the through coupling region ( $t = 1$ ) compared to the cross coupling region ( $t = 0$ ). This suggests that in Figure 3.18(b), right side of critical coupling corresponds to the through coupling region. In a ring resonator with symmetric DC, the ER has to be 0 at both the through and cross coupling regions (see Figure 3.12(a)). However, in the measured ring resonator transmission spectrum (Figure 3.18(b)), the ER becomes 0 at the through coupling region, but, in the cross-coupling region ER is higher than 0 indicating the DC is asymmetric.

In order to confirm the asymmetric nature of DC, we have fabricated and characterized a microring resonator with  $L_{DC} = 70 \mu\text{m}$  so that cross coupling region appears near the center of the operating wavelength of OSA. Though, the mask design of the ring resonator is done for symmetric DC, a small asymmetry ( $\sim \pm 10 \text{ nm}$ ) in the waveguide width is observed at DC region and this may be attributed to the proximity effects of the electron beam patterning. Figure 3.19(a) shows the transmission characteristics of a ring resonator with asymmetric DC ( $L_{DC} = 70 \mu\text{m}$  and  $L_x = 400 \mu\text{m}$ ). In an asymmetrical DC, at the cross-coupling region, total power is not coupled to cross port as it is evident from Figure 3.10(a). As a result, the ER of the ring resonator can have a finite value at the cross-coupling regime. Since, the DC is found to be asymmetric, it is also important to analyze the coupling induced phase delay. The total delay ( $\tau_{total}$ ) which includes the delay due to the resonance ( $\tau_{res}$  and the contribution from the asymmetric coupling induced delay  $\tau_{DC}$ ). In order to separate the delay components, we have fabricated ring resonators with various  $L_{DC}$ s and  $L_x$ . The total delay ( $\tau_{total}$ ) of the

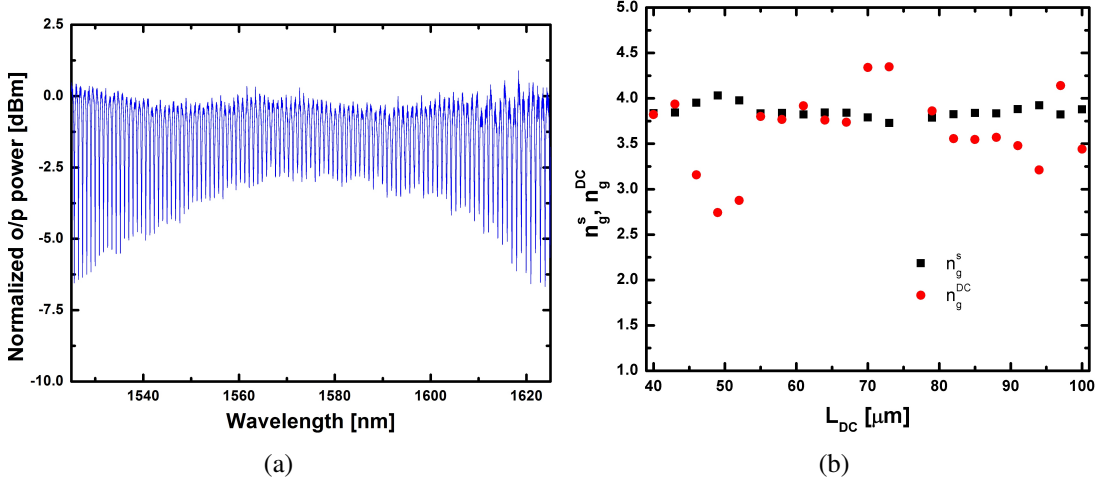


Figure 3.19: Transmission spectrum of ring resonator with asymmetric DC ( $L_{DC} = 70 \mu\text{m}$ ) showing full cross-coupling at  $\lambda \sim 1550 \text{ nm}$ . (b) Extracted values of waveguide group index  $n_g^s$  and effective group index of the DC ( $n_g^{DC}$ ) at  $\lambda \sim 1550 \text{ nm}$  are shown as a function of  $L_{DC}$ .

ring resonator can be related to the group index of the straight section ( $n_g^s$ ) and effective group index of DC ( $n_g^{DC}$ ) by:

$$\tau_{total} = \frac{\lambda^2}{FSR \times c} = \frac{n_g^s \times L_p + n_g^{DC} \times L_{DC}}{c} \quad (3.39)$$

where,  $L_p = 2\pi R + L_x + L_{DC}$  with  $L_x$  is the length of the straight section included to increase the ring perimeter. Now the group index of the waveguide ( $n_g^s$ ) alone can be derived from Eq. 3.39 as:

$$n_g^s = c \times \frac{d\tau_{total}}{dL_p} \quad (3.40)$$

Once we know  $n_g^s$  from eqn. 3.40, we can easily calculate back the  $n_g^{DC}$  using the following relation:

$$n_g^{DC} = \frac{\tau_{total} \times c - n_g^s \times L_p}{L_{DC}} \quad (3.41)$$

Figure 3.19(b) shows the estimated (from experimental results) values  $n_g^s$  and  $n_g^{DC}$  at  $\lambda \sim 1550 \text{ nm}$  as a function of  $L_{DC}$ . It can be noticed from the plot that  $n_g^s$  remains nearly constant for all values of  $L_{DC}$ . However,  $n_g^{DC}$  values are shifted from  $n_g^s$  at certain  $L_{DC}$ s with a period which is nearly equivalent to  $2L_0$  of the DC. This is expected due to the fact that the coupling induced phase delay is prominent at the cross-coupling regions. Slight variation of the periodicity is expected due to the fabrication error in

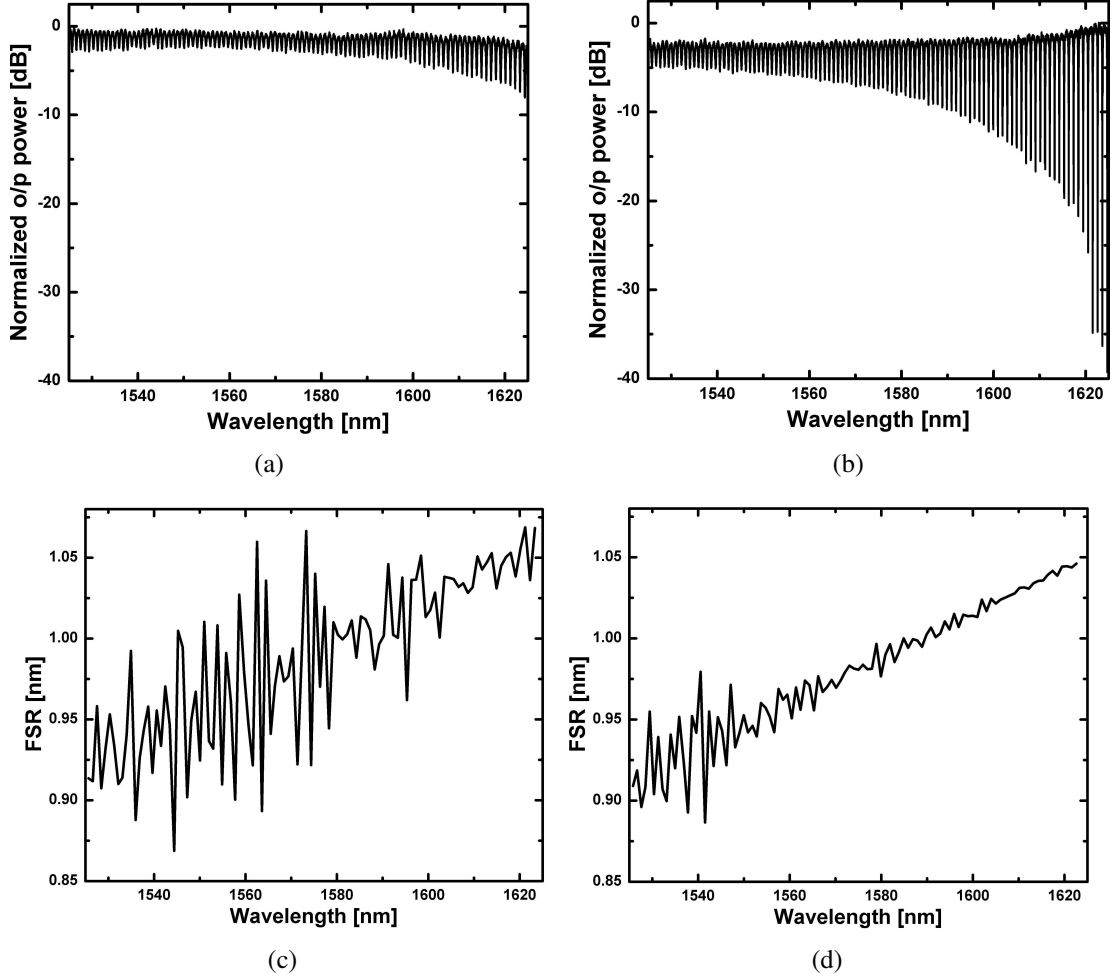


Figure 3.20: Measured transmission characteristics of microring resonators with asymmetric DCs of (a)  $L_{DC} = 49 \mu\text{m}$  and (b)  $L_{DC} = 52 \mu\text{m}$ . Measured FSR for (a) and (b) are shown in (c) and (d), respectively.

DC region and bend induced coupling at the branching regions of the DC. Referring to Figure 3.10(c), it can be justified that the  $n_g^{DC}$  values above and below  $n_g^s$  corresponds to the cross port width higher and lower than the bar port width respectively. Also, a slight variation of  $n_g^{DC}$  is observed for  $L_{DC}$ s away from  $L_0$ s, this may be attributed to the variation of DC structures due to fabrication induced error. Figure 3.20(a) and 3.20(b) show the measured transmission characteristics of microring resonators with asymmetric DC length of  $49 \mu\text{m}$  and  $52 \mu\text{m}$ , respectively. FSR corresponding to Figure 3.20(a) and 3.20(b) are shown in Figure 3.20(c) and 3.20(d). It is interesting to note that the FSR spectrum for ring with  $L_{DC} = 49 \mu\text{m}$  is fluctuating over the entire (100 nm) wavelength region. At the same time, by looking at Figure 3.20(a), it can be observed that this ring resonator is being operated at cross-coupling region over the wavelength

range of interest. Again, FSR spectrum of ring resonator with  $L_{DC} = 52 \mu\text{m}$  is fluctuating towards the lower wavelength ( $\sim 1540 \text{ nm}$ ) region and remains nearly linear as the wavelength increases. The transmission spectrum of this ring resonator device shows that the device is operated at cross coupling region towards the lower wavelength side and as the wavelength increases it moves away from the cross coupling region and thus higher ER. This proves that the ring resonator (with asymmetric DC) performance can be unpredictable due to the coupling induced phase delay when it is operated at cross coupling region. As a result, care must be taken when ring resonators are designed to operate at cross-coupling regimes for applications such as delay lines.

### 3.4 Summary

Ring resonator theory and working principle are discussed to introduce the key parameters of micro ring resonator. We have explored the design and fabrication of microring resonators on microns ( $5 \mu\text{m}$ ) as well as submicron ( $250 \text{ nm}$ ) thick device layer SOI substrates. MMICs are found to be better choice for microring resonator fabrication using photolithography and surface trimming technique. Large volume MMIC based ring resonators are fabricated on  $5 \mu\text{m}$  device layer and waveguide cross-sections are scaled down using surface trimming process to reduce the bend induced loss. The Q-factor of a trimmed waveguide ring resonators is measured to be  $\sim 33698$  ( $25412$ ) for TE (TM) polarization. The extinction ratio is found to be  $5.7 \text{ dB}$  and  $4 \text{ dB}$  for TE and TM polarizations, respectively. The free spectral range of the resonator is measured to be  $110 \text{ pm}$  both TE and TM polarizations. The surface trimmed ring resonator characteristics are compared with an untrimmed large volume ring resonator fabricated directly on  $2 \mu\text{m}$  device layer SOI substrate. The comparison shows that surface trimmed MMIC splitting characteristics are slightly changed from untrimmed MMIC.

The DC based microring resonators are demonstrated using photonic wire waveguide in SOI substrate with  $250 \text{ nm}$  device layer thickness. As the submicron DC is highly fabrication stringent, various critical aspects such as dispersion and asymmetry of DC, bend induced coupling, bend induced loss, etc. of submicron waveguide ring resonator has been theoretically analyzed. It is found that the bend induced coupling of

shallow etched DC is an important parameter in designing DC based ring resonators. Also, it has been theoretically analyzed that there can be a significant coupling induced delay when the DC are operated at cross-coupling regime. PhWW microring resonator in all pass configuration has been fabricated using electron beam lithography and IC-PRIE. Grating assisted 1D SSCs are integrated with microring resonator for chip level testing of the device. The highest Q-factor of a fabricated ring resonator is measured to be  $\sim 1,41,000$  for a shallow etched waveguide ( $W = 560$  nm,  $H = 250$  nm and  $h = 150$  nm) with ring radius  $100$   $\mu\text{m}$  and  $L_{DC} = 40$   $\mu\text{m}$ . The maximum ER of  $\sim 45$  dB is measured for a ring resonator with  $L_{DC} = 10$   $\mu\text{m}$  and ring radius  $50$   $\mu\text{m}$ . It is experimentally observed that the  $L_{DC}$  is playing an important role in the dispersion characteristics of microring resonator. For longer  $L_{DC}$ , the ER of the ring resonator transmission varies very sharply. Critically coupled resonance has been utilized to estimate the propagation loss of the waveguide. The experimental studies on ring resonator with asymmetric DC show that the device performance can be unpredictable when the devices are operated in cross-coupling regime.

# CHAPTER 4

## Refractive Index Sensor: Design, Fabrication and Testing

Various ring resonator configurations used for refractive index sensing are discussed in chapter 1. Basic sensing principle of all of those devices was based on the change of microring resonator characteristics in response to the top cladding (analyte) refractive index variation. Also, we have seen that to improve the  $S$  of the device, relatively complex designs such as ring resonator based on Vernier effect has been proposed and demonstrated. In this chapter, we present a refractive index sensor which is designed to track critically coupled wavelength of the ring resonator in all-pass configuration. The dispersion enhanced coupling in the DC without compromising much on loss factor, is the key of this design. The device is shown to be very efficient in detecting wide-range refractive index as the light is confined as a dielectric mode in low-loss silicon strip waveguide. The device design principle is discussed in Section 4.1 and the experimental demonstration is given in Section 4.2. Finally, the conclusions and future scopes for improvements of the sensor have been briefly outlined in Section 4.3.

### 4.1 Device Design

As an integrated optical sensor device, the microring resonator in SOI platform is primarily used to detect the refractive index of a cladding analyte. We present here a new design rule of ring resonator for an efficient and wide range refractive index sensing. A generic 3D schematic view of a microring resonator based refractive index sensor is shown in Figure 4.1(a); partially transparent region on top of ring represents the analyte material with refractive index  $n_c$ ,  $L_{DC}$  is the length of directional coupler (DC) and  $L_x$  is extra length added to the ring, mainly to control free spectral range (FSR) of the resonance spectrum. The transmission characteristics of a ring resonator in all-pass



configuration can be expressed by eq. 4.3. By the observation of resonance shift in an all-pass filter configuration, one can estimate the refractive index of any analyte/fluid introduced as a surface cladding of the microring resonator. The resonance condition without cladding analyte ( $n_c = n_{air} = 1$ ) is given by:

$$n_{eff}L = m\lambda_m \quad (4.1)$$

where,  $m$  is an integer representing the order of resonance at  $\lambda_m$ .

In the presence of cladding analyte with refractive index  $n_c$ , the  $m^{th}$  order resonance shift is given by:

$$\Delta\lambda_m = \frac{\lambda_m}{n_g} \left( \frac{dn_{eff}}{dn_c} \right)_{\lambda=\lambda_m} \Delta n_c \quad (4.2)$$

where,  $\Delta n_c = n_c - n_{air}$  and  $n_g = n_{neff} - \lambda \frac{dn_{eff}}{d\lambda}$ . Thus the refractive index of the analyte is usually determined by tracking a given order of resonance wavelength. In this method, the role of DC is merely to feed the ring resonator at an optimum level so that one can achieve ring resonator response with a reasonable Q-value and extinction at the resonance wavelength. However, the dispersion characteristics of a DC (wavelength dependent coupling) has not been explored so far for the ring resonator based refractive index sensing. By introducing a highly dispersive DC, one can easily single-out resonance wavelength near critical coupling condition ( $a = t$ ). Thus the critically coupled resonance wavelength ( $\lambda_c$ ) may be tracked as an alternative approach for refractive index sensing instead of tracking the  $m^{th}$  order resonance wavelength.

Before going into the details of transmission characteristics of above mentioned critically coupled ring resonator, we need to discuss first how one can achieve highly dispersive coupling in a conventional DC at a desired cross-coupling coefficient  $k(\lambda_c) = k_c$ . The cross-sectional view of a typical DC comprised of two single-mode SOI waveguides as shown in Figure 4.1(b) has been considered for theoretical analysis. The important design parameters are waveguide width  $W$ , rib height  $H$ , slab height  $h$ , and gap  $G$ . For a given set of these design parameters, one can easily estimate the length of DC for a desired cross-coupling coefficient by analyzing symmetric and anti-symmetric super-modes [106]:

$$k(\lambda) = \sin \left[ \frac{\pi \Delta n(\lambda) L_{DC}}{\lambda} \right] \quad (4.3)$$

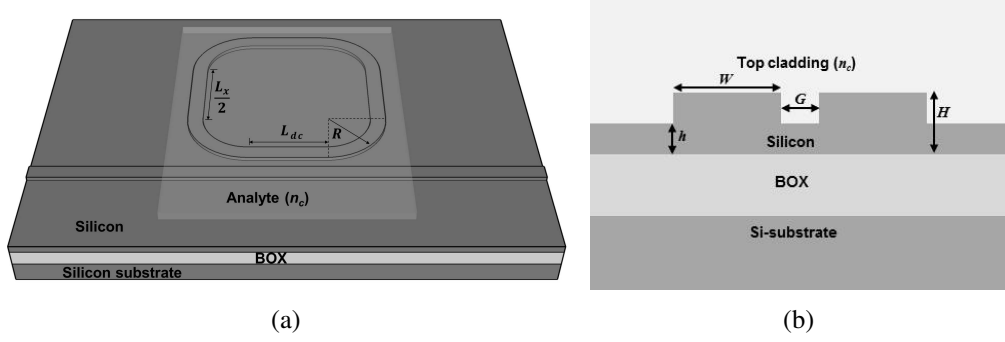


Figure 4.1: (a) Schematic view of a ring resonator refractive index sensor in SOI substrate. Partially transparent material above the ring and DC represents the analyte with refractive index ( $n_c$ ). (b) Schematic cross-sectional view of the DC:  $W$  - width of the waveguide,  $H$  - rib height,  $h$  - slab height and  $G$  - separation between the coupled waveguides.

In this equation, we have used  $\Delta n(\lambda) = n_{eff}^s(\lambda) - n_{eff}^{as}(\lambda)$  with  $n_{eff}^s(\lambda)$  and  $n_{eff}^{as}(\lambda)$  are effective indices of symmetric and anti-symmetric modes of DC, respectively. If the optical losses in the waveguide ring and DC remain constant within the wavelength range of detection, the critically coupled resonant wavelength is given by:

$$\lambda_c = \frac{\pi L_{DC} \Delta n(\lambda_c)}{\sin^{-1}(k_c)} \quad (4.4)$$

Again for a conventional ring resonator with strip waveguide, the deviation in cladding refractive index hardly alters wavelength dependent loss figures (unlike slot waveguide). Therefore, shift in critically coupled resonance wavelength because of differential change in cladding refractive index can be derived as:

$$\Delta \lambda_c = -\frac{\lambda_c}{\Delta n_g(\lambda_c)} \left( \frac{d\Delta n}{dn_c} \right)_{\lambda=\lambda_c} \Delta n_c \quad (4.5)$$

where

$$\Delta n_g = \lambda \frac{d\Delta n(\lambda)}{d\lambda} - \Delta n(\lambda) \quad (4.6)$$

Now, the shift of  $\lambda_m$  and  $\lambda_c$  (and hence the sensitivity) can be compared using Eqns. 4.2 and 4.5. By calculating numerical values of effective indices ( $n_{eff}$ ,  $n_{eff}^s$ , and  $n_{eff}^{as}$ ) and their slopes w.r.t. cladding refractive index  $n_c$ , we observed that shift in  $\lambda_c$  is at least one order higher than that of  $\lambda_m$ .

The accuracy in detecting/tracking  $\lambda_c$  relies on higher Q-value, lower FSR, and highly dispersive coupling coefficient near critical coupling condition of the ring resonator. Since Q-value of a strip waveguide based microring resonator can be very large ( $\gg 10^4$ ), the FSR can be reduced to a desired limit by increasing the perimeter  $L$  of the resonator. The question remains how to achieve highly dispersive coupling coefficient without compromising much with the quality factor and/or loss factor  $a$ . In this context, we can further look into Eqn 4.3 for the slope of wavelength dependent cross-coupling co-efficient:

$$\frac{dk}{d\lambda} = \frac{\pi L_{DC} \Delta n_g}{\lambda^2} \cos \left[ \frac{\pi L_{DC} \Delta n(\lambda)}{\lambda} \right] \quad (4.7)$$

Thus Eqn 4.7 may be re-arranged to quantify the dispersion near the critically coupled resonance wavelength:

$$\left. \frac{dk}{d\lambda} \right|_{\lambda=\lambda_c} = \frac{\pi L_{DC} \Delta n_g}{\lambda_c^2} \sqrt{1 - k_c^2} \quad (4.8)$$

It is worth mentioning here that the change in  $L_{DC}$  may result into variations in  $k_c$  and  $\lambda_c$ , but the slope is mostly dominated by the value of  $L_{DC}$  in case of low-loss directional couplers. Again, it is evident from Eqn 4.3 that a desired value of  $|k|$  for a reference wavelength  $\lambda$  can be repeated if the DC length increases in steps of cross-coupling length  $L_0(\lambda) = \frac{\lambda}{2\Delta n(\lambda)}$ . Since typical microring resonators with low-loss strip waveguide in SOI platform exhibit  $a \rightarrow 1^-$  and  $k_c = \sqrt{1 - a^2} \rightarrow 0^+$ , we have studied the dispersion characteristics of coupling efficiency ( $k^2$  vs.  $\lambda$ ) considering DC length as parameter in steps of  $2L_0$  (calculated for  $\lambda_0 = 1550$  nm). From these dispersion characteristics and the knowledge of  $k_c$ , one can easily estimate a value of  $\lambda_c$  (closest to the value of  $\lambda_0$ ) and hence the slope as defined in Eqn. 4.8, for DC lengths given by:

$$L_{DC}^q = \left[ \frac{\lambda_c}{\pi \Delta n(\lambda_c)} \right] \sin^{-1} |k_c| + 2qL_0 \quad (4.9)$$

where,  $q = 0, 1, 2, 3, \dots$

It must be noted that the performance of DCs and ring resonators depend on the polarization of guided mode. In following discussions, our focus is kept only on TE-like guided mode, as the DC is found to be more sensitive to cladding refractive index change, in comparison to that of TM-like guided mode. For numerical simulations,

Table 4.1: Parameters used for studying dispersion characteristics of two types DCs designed with deeply-etched (DE) and shallow-etched (SE) waveguides.

Type	$H$ [nm]	$W$ [nm]	$h$ [nm]	$G$ [nm]	$L_0$ [ $\mu\text{m}$ ]
DEDC	250	500	0	150	52
SEDC	250	560	150	150	13

two different types of cross-sectional geometries namely, deeply etched DC (DEDC) and shallow etched DC (SEDC) have been considered to study the dispersion characteristics. The design parameters for DEDC and SEDC (also see Figure 4.1(b)) are given in Table 4.1. They are carefully chosen to ensure single-mode guidance ( $1500 \text{ nm} < \lambda < 1650 \text{ nm}$ ), if the waveguides are not coupled. In practice, the DE waveguides are used to achieve very compact circuits (sharp bendings), whereas, SE waveguides are preferred for low-loss and less dispersive operations [108, 17]. Our calculations show that the value of  $L_0$  for SEDC ( $L_0^{SE} = 13 \mu\text{m}$ ) is four-times smaller than that of DEDC ( $L_0^{DE} = 52 \mu\text{m}$ ). This is due to stronger mode overlap between individual guided modes in case of SEDC in comparison to that of DEDC (for the given design parameters). Lumerical Mode Solver was used for numerical simulations, which includes the material dispersion model for silicon as presented by Salzberg and Villa [84].

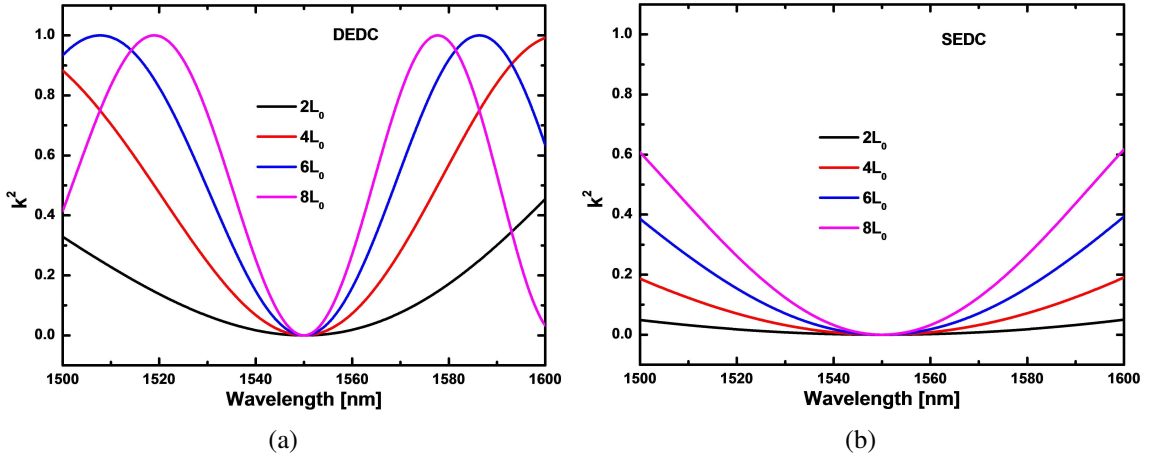


Figure 4.2: Dispersion characteristics of cross-coupling efficiency ( $k^2$ ) for DEDC (a) and SEDC (b) at various lengths ( $2L_0$ ,  $4L_0$ ,  $6L_0$  and  $8L_0$ ).  $L_0$  represents the cross-coupling length of the DCs at a reference operating wavelength  $\lambda_0 = 1550 \text{ nm}$ . Calculations were carried out for TE-like guided mode

The cross-coupling efficiencies as a function of wavelength ( $k^2$  vs.  $\lambda$ ) for both DEDC and SEDC of various lengths ( $2L_0$ ,  $4L_0$ ,  $6L_0$  and  $8L_0$ ) have been shown in Fig-

ures. 4.2(a) and 4.2(b), respectively. It is evident that as the length of a DC increases the critically coupled wavelength  $\lambda_c$  (solved for a given  $|k_c|$ ) moves closure and closure to  $\lambda_0 = 1550$  nm. This is because of the enhanced dispersion. Moreover, the rate of change of  $|k_c|$  w.r.t.  $\lambda$  at  $\lambda_c$  becomes faster and faster as the length of a DC increases. It appears from the plots that the DEDC is more dispersive compare to SEDC in the scales of their respective values of  $L_0$ . However, one can carefully note that the SEDC is in fact more dispersive than the DEDC when they are compared for a same length of  $L_{DC}$ . As an example, we have had the opportunity to compare dispersion characteristics directly for  $L_{DC} = 2L_0^{DE} = 8L_0^{SE} = 104 \mu\text{m}$ ; thanks for this rare coincidence in our calculations for the given waveguide design parameters. For this length, we observe that  $k^2$  varies from 0 to 0.475 (0.6) for DEDC (SEDC) within the wavelength span from 1550 nm to 1600 nm.

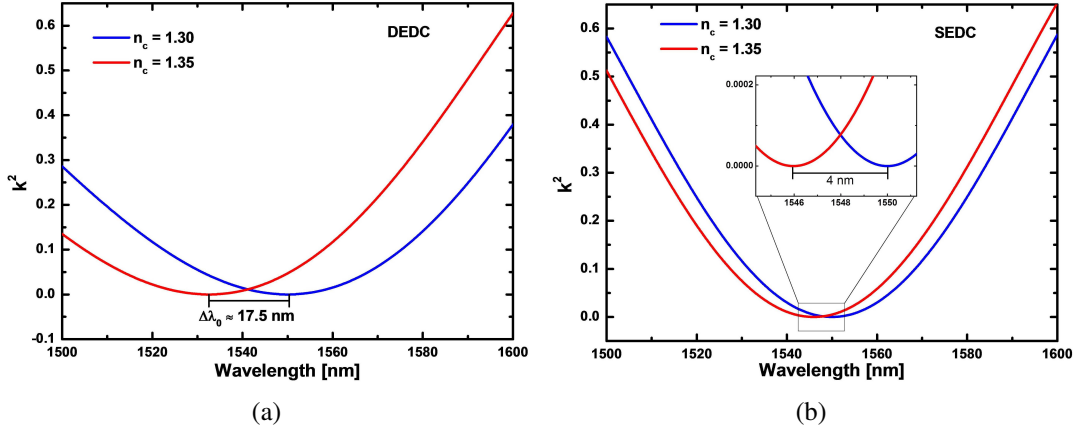


Figure 4.3: Dispersion characteristics of cross-coupling efficiency of DCs for two different cladding indices ( $n_c = 1.30$  and  $1.35$ ): (a) DEDC with  $L_{DC} = 104 \mu\text{m}$  and (b) SEDC with  $L_{DC} = 104 \mu\text{m}$ .

The tuning rate of a dispersion characteristics w.r.t. cladding refractive index or  $\frac{d\lambda_0}{dn_c}$  may be considered as the actual figure merit of a DC for sensing applications. To compare the figure merits, we have simulated dispersion characteristics for both DEDC and SEDC of same lengths ( $L_{DC} = 104 \mu\text{m}$ ) by varying the cladding refractive index. Figures. 4.3(a) and 4.3(b) are showing the dispersion characteristics of DEDC and SEDC, respectively; each for  $n_c = 1.3$  (blue curves) and  $n_c = 1.35$  (red curves). From these plots one can estimate the sensitivity:

$$S = \frac{d\lambda_c}{dn_c} \simeq \frac{d\lambda_0}{dn_c} \quad (4.10)$$

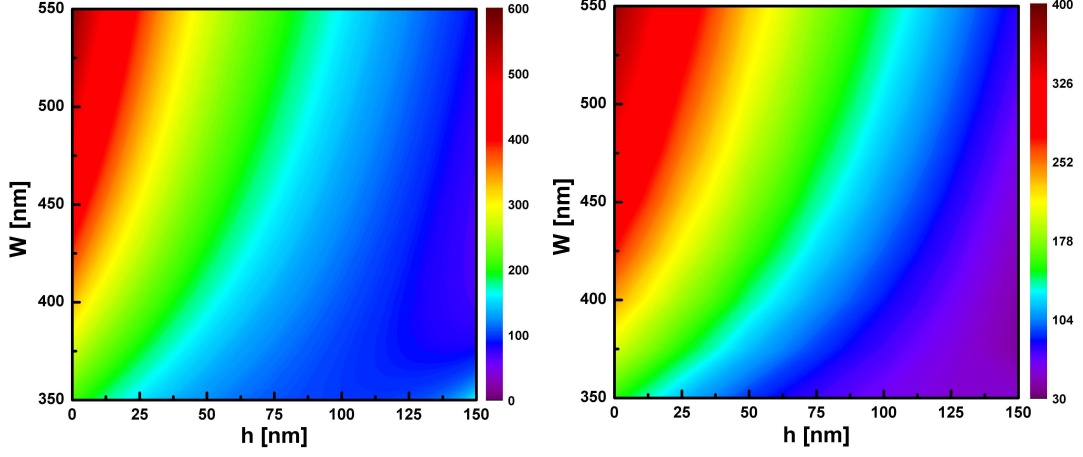


Figure 4.4: Calculated sensitivity ( $S$ ) is shown as function of  $W$  and  $h$  for (a)  $G = 100$  nm and (b)  $G = 150$  nm.

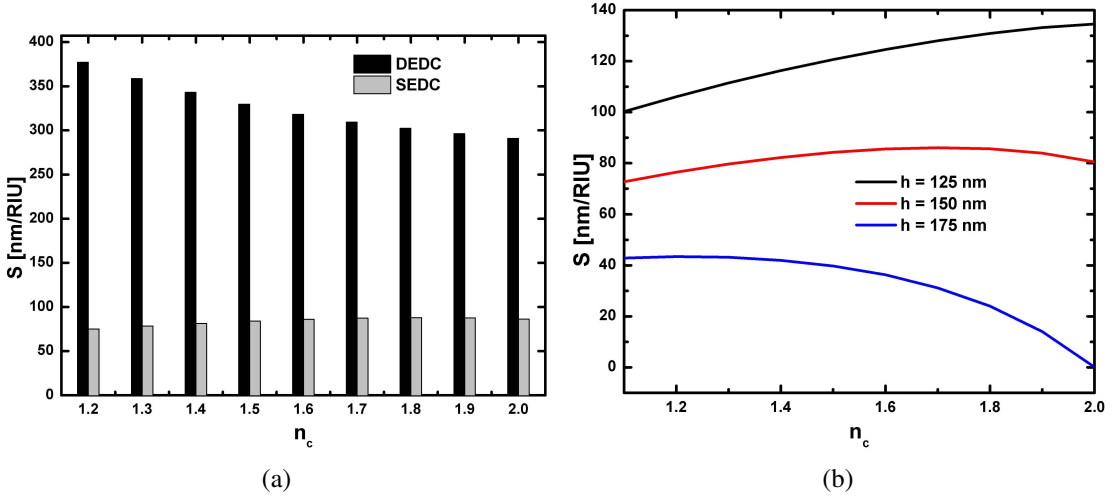


Figure 4.5: (a) Calculated sensitivity ( $S$ ) for a wide-range of cladding refractive index ( $1.2 \leq n_c \leq 2.0$ ) in steps of 0.1: black bars for DEDC and gray bars for SEDC, (b) Calculated  $S$  as a function of  $n_c$  for SEDCs with three different slab heights satisfying single-mode guidance in TE-polarization.

In fact, one can estimate the sensitivity of a DC dominated ring resonator directly from Eqn. 4.5, by computing  $\Delta n$  and the slope  $\frac{d\Delta n}{dn_c}$  for a given value of critically coupled wavelength  $\lambda_c$ . However, to know the value of  $\lambda_c$ , one needs to depend on dispersion characteristics of the DC and the loss factor  $a$  (and hence  $k_c = \sqrt{1 - a^2}$ ) of the ring resonator. Figure 4.4(a) and 4.4(b) show the calculated  $S$  (at  $n_c \sim 1.3$ ) variation of DC dominated sensor as a function of  $W$  and  $h$  for DC with  $G = 100$  nm and  $G = 150$  nm, respectively. Comparing Figures 4.4(a) and 4.4(b), it is clear that the  $S$  is higher for smaller  $G$  for identical  $W$  and  $h$ . This is expected due to reason that the

evanescent field strength is increased as DC gap is reduced. The  $S$  of the device can be much above 500 nm/RIU for a cladding sensitive waveguide cross-section. However, to have practically feasible design, one should consider fabrication reproducible of sub-micron features. To study the uniformity of  $S$  as a function of  $n_c$ , we compared the sensitivity of DEDC and SEDC. Figure 4.5(a) shows a bar chart comparison of  $S$  for DEDC (black bars) and SEDC (gray bars) for a wide-range of cladding refractive index ( $1.2 \leq n_c \leq 2.0$ ) in steps of 0.1, using the assumption given by Eqn. 4.10. It can be clearly observed from the chart that  $S$  of DEDC is larger ( $\sim 380$  RIU/nm @  $n_c = 1.2$ ) but reduces monotonously as the value of  $n_c$  increases, whereas the sensitivity of SEDC is somewhat lower but remains nearly constant ( $\sim 80$  RIU/nm) for the entire range of  $n_c$  (1.2 to 2.0). It is needless to point out that this figure of merit does not depend on the length ( $L_{DC}$ ) of DC for a given gap  $G$  between the waveguides and the slab height  $h$ . For an example, we have calculated the values of  $S$  as a function of  $n_c$  for three different slab heights (125 nm, 150 nm, and 175 nm) satisfying single-mode guidance in TE-polarization and they are presented in Figure 4.5(b) for comparisons. We see that the variation of  $S$  remains relatively flat for  $h = 150$  nm, in comparison to those for  $h = 125$  nm and 175 nm.

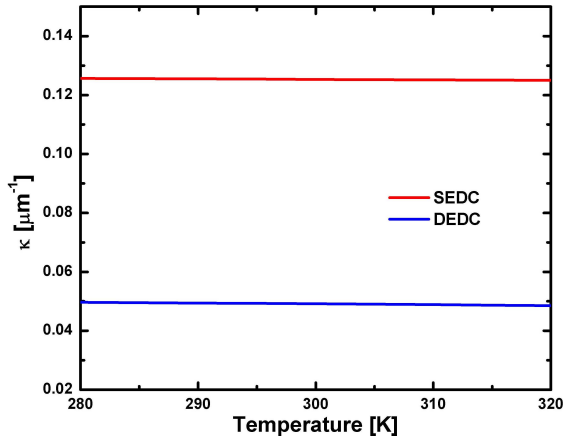


Figure 4.6: The cross-coupling strength ( $\kappa$ ) as function of operating temperature for the SEDC (red line) and DEDC (blue line) with DI water as cladding material. The corresponding slopes are  $-1.6 \times 10^{-5}/\mu\text{m-K}$  and  $-2.8 \times 10^{-5}/\mu\text{m-K}$ , respectively.

The thermal stability is an important factor for a refractive index sensor device. However, the effective indices of symmetric and anti-symmetric modes of a DC with SOI waveguides vary with positive slopes but with slightly different rates resulting into

temperature dependent fluctuations in coupling strength  $\kappa$  ( $= \pi\Delta n/\lambda$ ) at  $\lambda = 1550$  nm. We have calculated the values of  $\kappa$  around room temperatures ( $280 \text{ K} \leq T \leq 320 \text{ K}$ ) for both DEDC and SEDC (see Figure 4.6) with DI water as a cladding material. The thermo-optic coefficients of silicon dioxide, silicon and DI water are considered as  $+1.2 \times 10^{-5}/\text{K}$ ,  $+1.86 \times 10^{-4}/\text{K}$  and  $-1.1 \times 10^{-4}/\text{K}$ , respectively [109]. As expected, the SEDC is found to be more thermally stable than that of a DEDC. The  $\kappa$  variation for the SEDC (DEDC) is estimated to be  $-1.6 \times 10^{-5}/\mu\text{m-K}$  ( $-2.8 \times 10^{-5}$ ). This results into a  $\lambda_c$  variation of  $\sim 0.095 \text{ nm/K}$  ( $\sim 0.146 \text{ nm/K}$ ) for the corresponding ring resonators.

Nonetheless, as mentioned earlier  $L_{DC}$  plays a vital role to detect the nearly accurate value of critically coupled wavelength  $\lambda_c$ . The accuracy also depends on FSR of the ring resonator. Thus higher dispersion characteristics of the DC (achieved via increasing the value of  $L_{DC}$ ) and smaller FSR (achieved via increasing the ring perimeter length  $L$ ) are the crucial factors for the accuracy in detection. For a given value of  $L_{DC}$ , one can increase perimeter length by increasing the value of  $L_x$  in race-track configuration (see Figure 4.1(a)). While estimating the value of  $L_{DC}$ , one must consider the coupling in branching regions at both ends of the DC as shown in eq. 3.27. The value of  $\Delta L_b$  for SEDC (DEDC) with  $R = 25 \mu\text{m}$  is calculated to be  $\sim 3.32 \mu\text{m}$  ( $3.05 \mu\text{m}$ ). This  $\Delta L_b$  values corresponds the to a total power coupled to the cross port is estimated to be  $\sim 45\%$  and  $\sim 5 \%$  for SEDC and DEDC.

Thus, due to significant bend induced coupling, the critical coupling is impossible for an all-pass ring resonator with  $L_{DC} \sim 0$ , if the value of  $k_c^2$  is small especially in the case of ring resonator with SEDC. In such situations (e.g., ring resonators with low-loss waveguides), one needs to find a critical coupling condition with  $L_{DC} \sim 2qL_0$  (as given by Eqn. 4.9) but for  $q \neq 0$ .

Though it has been shown that the DE device structure is superior in terms of sensitivity, lower bend-induced losses, etc., SE device structure is found to be more appropriate because of following practical reasons:

1. Since, the variation of  $k^2$  as a function of wavelength is faster in SEDC (see Figures. 4.2(a) and 4.2(b)), resonance near critically coupled wavelength stands out from the rest of resonance wavelengths in the ring resonator response. This in turn helps for a precise tracking of envelop shift and hence the value of  $\lambda_c$ .



2. Propagation loss of a SE waveguide is lower than that of DE waveguides. This allows to increase the perimeter of the ring so as to increase the ring Q-value and reduce FSR to improve the LOD of the refractive index sensor.
3. The SE device structure shows nearly no increase in loss budget because of differential change in cladding refractive index  $n_c$ .
4. SE waveguides can be fabricated along with input/output grating couplers in a single-step lithography and reactive ion etching process. Shallow etched grating coupler is generally preferred for efficient and broadband light coupling.
5. SE waveguides can be easily designed for single-mode guidance for a wide-range of operating wavelengths in TE-like mode, maintaining cut-off for TM-like mode. This in fact suppress the possibility of spurious peaks that may occur in the resonance spectrum which is undesirable for devices such as sensors.

Two different ring resonators with single mode SE waveguides and DC (see Table 4.1 for design parameters) for  $L_{DC}^{eff} = 4L_0$  and  $8L_0$ , respectively, are investigated and compared. The  $90^\circ$  waveguide bends with radius  $R = 25 \mu\text{m}$  is considered for acceptable bend-induced losses and to accommodate  $L_x = 400 \mu\text{m}$  in race-track configuration for both the ring resonators. The average waveguide loss is assumed to be 5 dB/cm (higher than our typical experimental value of 3 dB/cm for straight SE waveguides), which gives the value of loss factor  $a \sim 0.98$ . Wavelength dependent transmission characteristics in all-pass configuration for both the devices are obtained by computing the numerical values of  $n_{eff}(\lambda)$ ,  $t(\lambda) = \sqrt{1 - k^2(\lambda)}$  and inserting them in Eqn. ???. The simulation results are shown in Figures. 4.7(a) and 4.7(b), respectively, for two different cladding refractive indices ( $n_c = 1.30$  and  $1.35$ ), with maximum transmission normalized to 1 mW or 0 dBm. Calculations were carried out with a wavelength resolution bandwidth of 0.1 pm. As expected, the transmitted comb spectra correspond to  $L_{DC}^{eff} = 8L_0$  are narrower than those of  $L_{DC}^{eff} = 4L_0$ . It may be also noted that near critically coupled wavelength of  $\lambda_c$ , there are about three resonances at a level of -30 dB detection limit for  $L_{DC}^{eff} = 4L_0$ , whereas it is only one for  $L_{DC}^{eff} = 8L_0$ . Thus longer length of DC ensures better accuracy in detecting the value of  $\lambda_c$ . The observed shift in  $\lambda_c$  ( $\Delta\lambda_c \sim 4 \text{ nm}$ ) for a differential cladding refractive index change of  $\Delta n_c = 0.05$  is comparable to the shift in  $\lambda_0$  as described in Figure 4.3(b). However, as mentioned earlier the accuracy in detecting  $\lambda_c$  (and LOD) improves by lowering FSR (e.g., by increasing the value of  $L_x$ ) and/or increasing the Q-value (e.g., by reducing the waveguide losses).

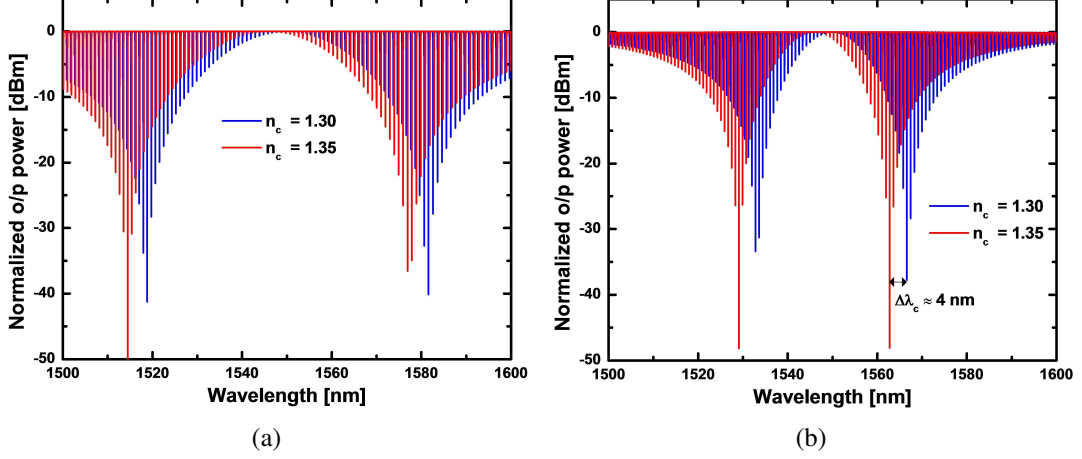


Figure 4.7: Transmitted V-shaped comb spectra of ring resonators with SE waveguides (see Table 4.1 for design parameters) for two different cladding indices (1.30 and 1.35): (a)  $L_{DC}^{eff} = 4L_0$ , and (b)  $L_{DC}^{eff} = 8L_0$ . The calculations were carried out assuming waveguide loss of 5 dB/cm.

## 4.2 Experimental Demonstration

Ring resonators with dispersion enhanced couplers were demonstrated with optical grade SOI substrate (Device layer  $\sim 250$  nm, BOX layer  $\sim 3$   $\mu\text{m}$  and handle wafer  $\sim 500$   $\mu\text{m}$ ) for wide range refractive index sensing. Devices were fabricated by selective dry etching of Si using e-beam written negative-tone resist (HSQ - XR1541) mask. We used fixed beam moving stage (FBMS) patterning technique for stitch-free electron beam writing (Raith 150 TWO system). An inductively coupled plasma reactive ion etching system (Oxford Plasmalab System 100) was used for Si etching with an optimized recipe (gas flow rate -  $SF_6 : CHF_3 :: 5$  sccm:18 sccm, chamber pressure - 15 mT, ICP power - 1000 W, forward power - 30 W and operating temperature - 20  $^\circ\text{C}$ ) to obtain nearly vertical side-walls and an acceptable surface roughness.

Based on design principle and comfort factors discussed in previous section, the ring resonator devices were defined with shallow etched rib waveguides and DCs ( $W \sim 560$  nm,  $G \sim 150$  nm,  $h \sim 150$  nm). The race-track type waveguide ring resonators with  $L_x = 400$   $\mu\text{m}$ ,  $90^\circ$  bends with  $R = 25$   $\mu\text{m}$  were mainly studied to investigate dispersion with varying  $L_{DC}$  from 40  $\mu\text{m}$  to 100  $\mu\text{m}$ , in steps of 3  $\mu\text{m}$ . This is to ensure possible hitting of desired DC lengths near  $4L_0$ ,  $6L_0$  and  $8L_0$  corresponding to any value of  $\lambda_0$  falling within the available wavelength range (1520 nm to 1630 nm) of the tunable laser

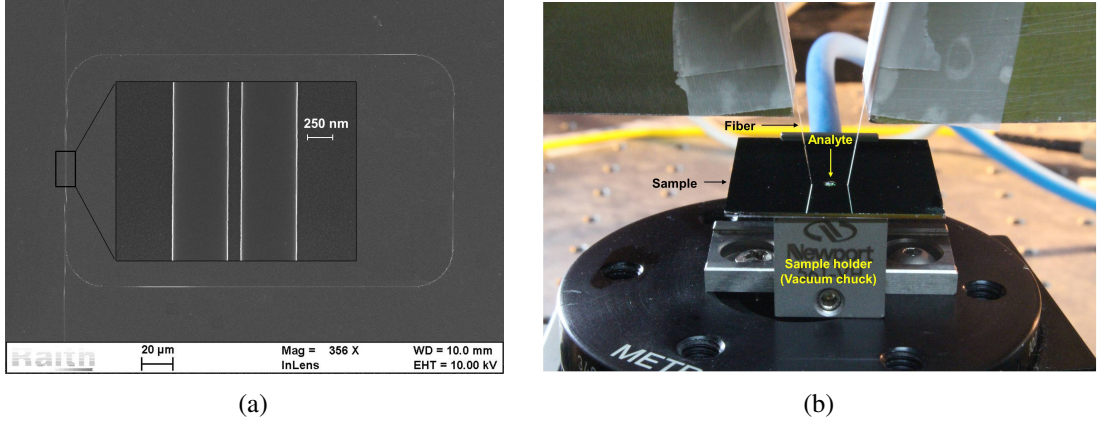


Figure 4.8: (a) SEM image of a fabricated ring resonator with  $L_{DC} = 100 \mu\text{m}$ . Inset: Zoomed image of the DC region. (b) Photograph of the experimental setup highlighting devices under test (sample mounted on a vacuum chuck), drop of an analyte on top of a device (F-IMF-150), and the input/output fiber probes. Both input and output fibers are connected to a high resolution optical spectrum analyzer (OSA) with internal light source (Apex - AP2043B).

source in our labs for experimental measurements. We expected some deviations in DC characteristics (from the design) because of some unavoidable fabrication related errors (e.g. slanted waveguide side-walls, variations in waveguide width  $W$ , gap  $G$  because of proximity effects, etc.). The input/output grating couplers were defined on the surface of adiabatically expanded (over a length of  $100 \mu\text{m}$ ) waveguide terminal block of area  $12 \mu\text{m} \times 12 \mu\text{m}$ , with same etching depth of  $100 \text{ nm}$  ( $= H - h$ ) and with 50% duty of its period  $\Lambda = 610 \text{ nm}$ . The design parameters for input/output gratings were optimized to couple light using standard single-mode fibers aligned at  $10^\circ$  angle with the normal on the sample surface (and input/output waveguide axis). Reference waveguides with input/output grating couplers were fabricated to extract the wavelength dependent response of a ring resonator alone.

Figure 4.8(a) shows the SEM image of a fabricated ring resonator structure with  $L_{DC} = 100 \mu\text{m}$ ; magnified view of the DC region is shown in the inset. The fabricated devices were characterized using an optical spectrum analyzer (OSA) with internal light source ( $1520 \text{ nm} < \lambda < 1630 \text{ nm}$ , Power -  $250 \mu\text{W}$ ). The OSA (Apex - AP2043B) has the capability of detecting wavelengths within  $0.04 \text{ pm}$  resolution bandwidth. A photograph highlighting devices under test (sample mounted on a vacuum chuck), drop of an analyte (F-IMF-150) on top of a device, and the input/output fiber probe has been shown in Figure 4.8(b). In this setup, average power available at the input fiber was

measured to be  $\sim 125 \mu\text{W}$ .

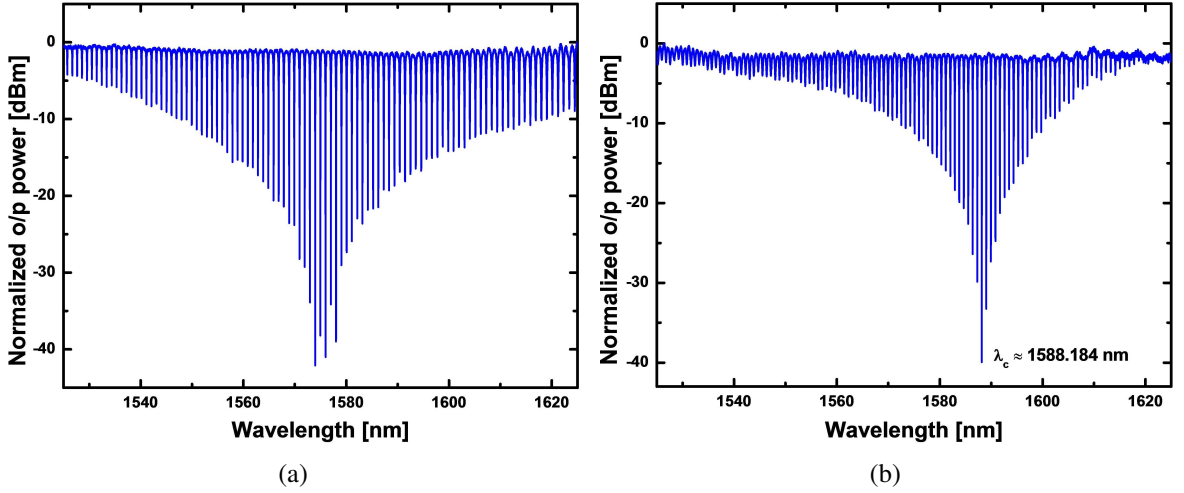


Figure 4.9: Measured transmission characteristics of fabricated ring resonators for  $n_c = 1$  (air cladding): (a)  $L_{DC} = 40 \mu\text{m}$ , and (b)  $L_{DC} = 100 \mu\text{m}$ .

The transmission characteristics (normalized to 0 dBm) of ring resonators with  $L_{DC} = 40 \mu\text{m}$  and  $100 \mu\text{m}$  are shown in Figures. 4.9(a) and 4.9(b), respectively, for  $n_c = 1$  (air cladding). According to our theoretical prediction, the observed comb envelope for  $L_{DC} = 100 \mu\text{m}$  is much narrower and the resonance wavelength @ $\lambda = 1588.184 \text{ nm}$ , near critically coupled wavelength  $\lambda_c$  stands out from the rests. We have noted a clear trend of narrowing envelope function and reducing the value of FSR as the value of  $L_{DC}$  increases. Figure 4.10 shows the 30 dB envelope bandwidths ( $\Delta f_{env.}$ ) and the values of FSR for six different devices having  $L_{DC}$ s of  $40 \mu\text{m}$ ,  $61 \mu\text{m}$ ,  $82 \mu\text{m}$ ,  $88 \mu\text{m}$ ,  $97 \mu\text{m}$ , and  $100 \mu\text{m}$ , respectively, exhibiting critically coupled wavelengths within the measurement range of our characterization setup ( $1520 \text{ nm} \leq \lambda_c \leq 1630 \text{ nm}$ ). It is evident that for the device with  $L_{DC} = 100 \mu\text{m}$ , the value of  $\Delta f_{env.}$  (150 GHz) is smaller than the corresponding value of two times FSR (210 GHz). Thus we could ensure the detection of  $\lambda_c$  within the limit of FSR value by selecting the device with  $L_{DC} = 100 \mu\text{m}$  and  $L_x = 400 \mu\text{m}$ , if the extinction ratio of  $\geq 30 \text{ dB}$  is considered to be the reference level in actual measurements.

Besides air cladding, the above mentioned device was also characterized for two other cladding materials: (i) DI water with known refractive index of 1.318 @ $\lambda = 1550 \text{ nm}$ , (ii) Newport index matching fluid (F-IMF-150) with known refractive index of 1.52 @ $\lambda = 589 \text{ nm}$  (refractive index at  $\lambda \sim 1550 \text{ nm}$  was not supplied by the manufacturer).

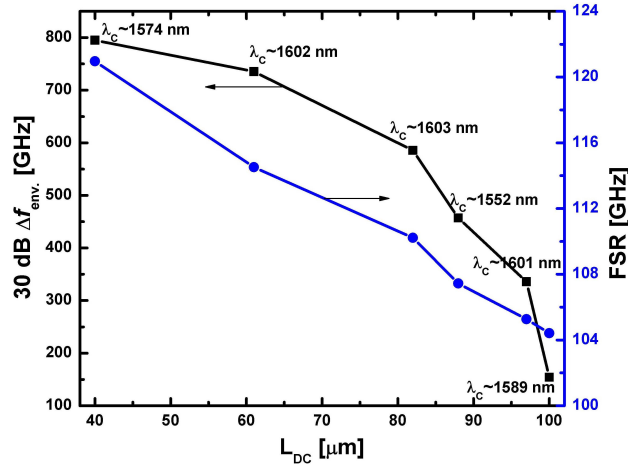


Figure 4.10: Comparisons of 30 dB envelope bandwidth ( $\Delta f_{env}$ ) and FSR for six ring resonator devices with increasing values of  $L_{DC}$ . The critically coupled wavelengths extracted from the resonance envelopes are shown in the inset.

All the three transmission characteristics are shown together in Figure 4.11 for comparisons. The estimated critical wavelengths corresponding to DI water and Newport IMF are  $\sim 1570.288$  nm and  $\sim 1561.682$  nm, respectively. Comparing the results for air and DI water, we estimate the sensitivity of  $\sim 57$  nm/RIU which is somewhat lower than the theoretical prediction of  $\sim 80$  nm/RIU. This may be attributed to the fabrication process related deviations in waveguide width and geometry, gap between the coupled waveguides, etc from the actual design parameters. Nevertheless, using this sensitivity figure of merit, we could evaluate the refractive index of the Newport IMF to be  $\sim 1.477$ . This value is well justified as an index matching fluid used at the junction point of two glass fibers for the operating wavelength window of  $\lambda \sim 1550$  nm.

To validate the response of the sensor for a wide range of refractive indices, we have used commercial Cargille refractive index liquids [55]. Figure 4.12(a) shows the measured transmission characteristics of the refractive index sensor for various cladding refractive indices. Figure 4.12(b) shows the  $\lambda_c$  as function of cladding refractive indices (Cargille liquids) those are extracted from Figure 4.12(a). Rectangular symbols represent the measured data and the solid line represents the linear fit to the measurement. It is clear from the figure that all the measurements are almost falling to the straight line fit. This justifies that  $S$  remains almost constant same throughout the cladding refractive range of 0.7 RIU (1 to 1.7). The error bar shown in plot indicates the maximum uncer-

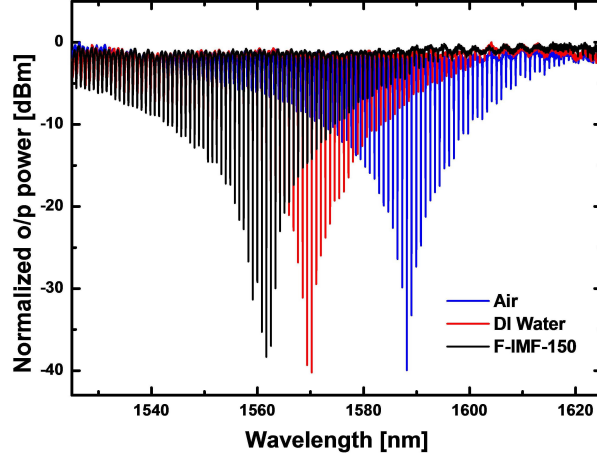


Figure 4.11: Transmission spectra of a dispersion enhanced ring resonator fabricated with SE waveguides ( $R = 25 \mu\text{m}$ ,  $L_x = 400 \mu\text{m}$ ,  $L_{DC} = 100 \mu\text{m}$ ) corresponding to the surface cladding of air (blue), DI water (red) and F-IMF-150 (black).

tainty ( $\pm\text{FSR}/2$ ) in locating the  $\lambda_c$  due to a finite FSR. The  $S$  is estimated to  $\sim 54.1$  from the slope of  $\lambda_c - n_c$  plot.

To verify the LOD of the device, we tested the sensor with cladding refractive indices of 1.3 and 1.31. Figure 4.13(a) shows the transmission characteristics for  $n_c = 1.3$  (red line) and 1.31 (blue line). The  $\Delta\lambda_c$  is measured to be 0.64 nm for  $\Delta n_c$  of 0.02 RIU, though the expected value is  $\sim 0.541$  nm with estimated  $S$  (54.1 nm/RIU). It can be observed from the Figure 4.13(a) that highest ER of resonance for  $n_c = 1.31$  indicates that this wavelength is near to  $\lambda_c$ , whereas for  $n_c = 1.30$  the minimum ER is relatively less suggests that this resonance is slightly away from  $\lambda_c$ . This in fact adds error in the cladding refractive index detection due to the finite value of FSR. The LOD of the device is  $\sim 1.67 \times 10^{-2}$  RIU, estimated by taking the ratio of measured values of FSR ( $\sim 0.95$  nm) and  $S$  ( $\sim 54.1$  nm/RIU). It is now evident from our experimental results that the LOD is limited by FSR of the device. Smaller FSR can be easily obtained by increasing perimeter of the ring. However one must be careful to keep the overall loss budget as small as possible for maintaining a reasonable Q-value. It would be extremely difficult to resolve the individual resonances in the comb envelope, if the Q-value is poor. Nevertheless, the numerical value of  $Q$  depends on the absolute value of resonant wavelengths  $\lambda_m$ , the coupling efficiency  $k^2(\lambda_m)$ , and the loss factor  $a(\lambda_m)$ . Since transmission maxima remain nearly constant as a function of wavelength (see Figures. 4.9 and 4.11), we can conclude that  $a$  is nearly independent of  $\lambda_m$  (unlike slot

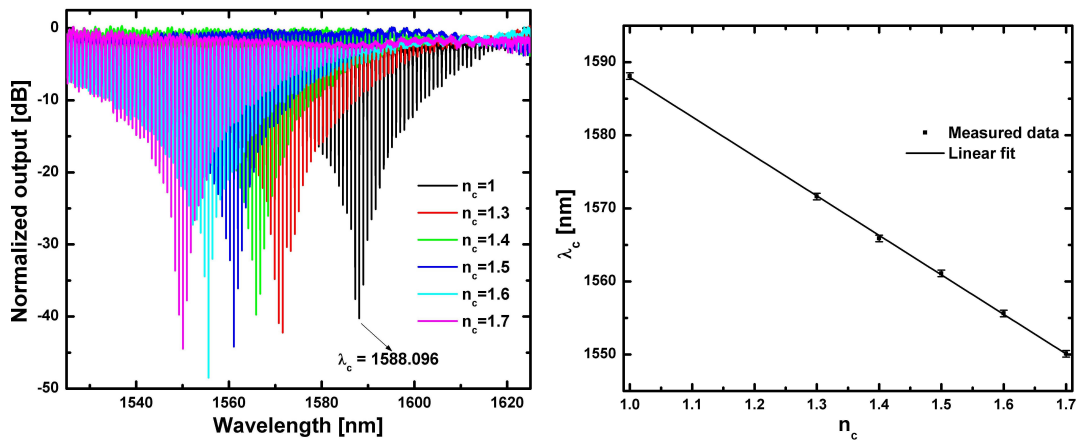


Figure 4.12: Measured transmission (normalized) characteristics of the sensor for air and various refractive index liquid claddings. (b) Critically coupled wavelength ( $\lambda_c$ ) as a function of  $n_c$  for refractive index liquids shown in (a): error bar indicates maximum uncertainty ( $\pm$  FSR/2) of locating  $\lambda_c$  due to finite FSR value.

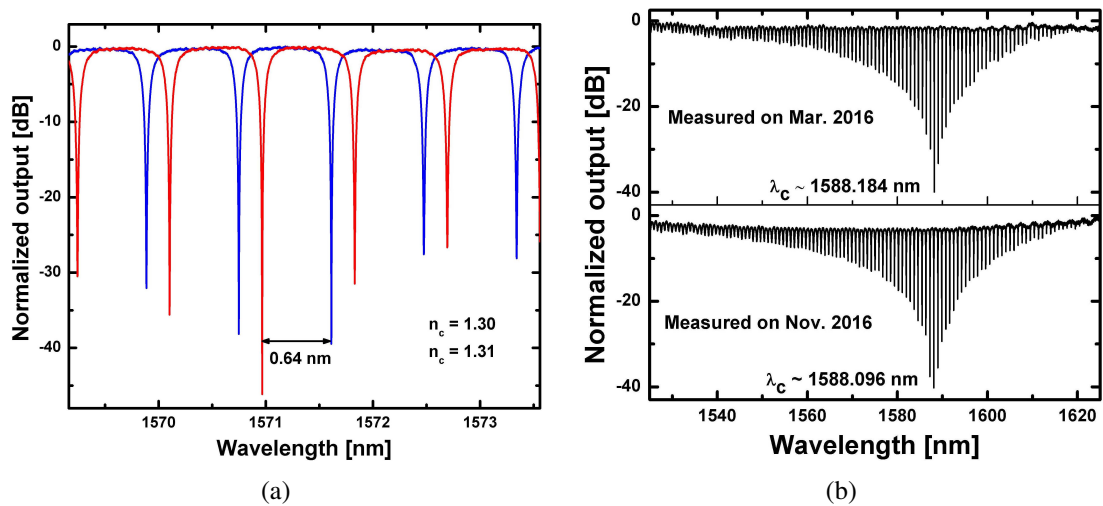


Figure 4.13: Measured transmission characteristics of the sensor for cladding refractive indices of 1.3 (red line) and 1.32 (blue line). (b) Transmission characteristics of the device for air cladding measured on March 2016 and November 2016 to test the spectral stability.

waveguide based ring resonators). The observed Q-values near critically coupled wavelengths corresponding to claddings of air, DI water, and F-IMF-150 are estimated as 18500, 15400 and 13000, respectively. Since they are not exactly following the ratio of respective critically coupled wavelengths of 1588.184 nm, 1570.228 nm, and 1561.682 nm; we can assume that the waveguide loss increases a bit as the cladding refractive index increases. However, increase of this loss hardly affects the error in detection. The FSR of this ring resonator based sensing devices can be reduced to the limit of  $\lambda_c/Q \approx 0.1$  nm, resulting into a LOD value of  $\sim 10^{-3}$  RIU, for  $Q = 15000$ . Thus higher Q-value, lower FSR, and lower waveguide losses of the ring resonator promise for a better accuracy in detecting  $\lambda_c$  and hence achievable LOD can be  $\ll 10^{-3}$  RIU. It is interesting to note from Figure 4.13(b) that the values of  $\lambda_c$  for air cladding at repeated measurements. Though, these two measurements are taken with an interval of 8 months, the difference is measured to be  $\sim 1$  pm which much less than the FSR of the microring resonator. This in fact justifies that the device is very stable over the time.

### 4.3 Summary

In this chapter, we have described how the length of a DC can be used as an important design parameter for ring resonator based refractive index sensor. Two different types of waveguide geometries representing as "shallow-etched" and "deeply-etched" are considered to investigate device performances with numerical simulations. Merits and demerits of devices with both types waveguide geometries are discussed in detail. It is shown theoretically that the sensitivity of a ring resonator with DEDC ( $S \sim 380$  nm/RIU) is nearly five times higher than that of SEDC based ring resonator ( $S \sim 80$  nm/RIU). However, it has been also argued that the fabrication and characterization of a ring resonator with SEDC is relatively easier. The proposed devices are shown to be capable of wider-range of refractive index sensing ( $\Delta n_c > 0.8$ ).

The fabricated devices with shallow-etched waveguides are characterized with an average sensitivity of  $\sim 54$  nm/RIU, LOD of  $\sim 1.7 \times 10^{-2}$  RIU, and tested for a cladding refractive index variation of  $\Delta n_c \sim 0.5$ . The error in refractive index sensing can be reduced significantly to  $\ll 10^{-3}$  RIU by increasing perimeter length of the ring



and of course by reducing waveguide losses. The superiority of the proposed integrated optical sensor device lies in its simpler design, easier operation, wider-range and nearly accurate detection mechanism. It is now evident from our experimental results that the LOD is limited by FSR of the device. Smaller FSR can be easily obtained by increasing perimeter of the ring. However one must be careful to keep the overall loss budget as small as possible for maintaining a reasonable Q-value. It would be extremely difficult to resolve the individual resonances in the comb envelope, if the Q-value is poor. Nevertheless, the numerical value of  $Q$  depends on the absolute value of resonant wavelengths  $\lambda_m$ , the coupling efficiency  $k^2(\lambda_m)$ , and the loss factor  $a(\lambda_m)$ . Since transmission maxima remain nearly constant as a function of wavelength (see Figures. 4.9 and 4.11), we can conclude that  $a$  is nearly independent of  $\lambda_m$  (unlike slot waveguide based ring resonators). The observed Q-values near critically coupled wavelengths corresponding to claddings of air, DI water, and F-IMF-150 are estimated as 18500, 15400 and 13000, respectively. Since they are not exactly following the ratio of respective critically coupled wavelengths of 1588.184 nm, 1570.228 nm, and 1561.682 nm; we can assume that the waveguide loss increases a bit as the cladding refractive index increases. However, increase of this loss hardly affects the error in detection. In summary, the FSR of this ring resonator based sensing devices can be reduced to the limit of  $\lambda_c/Q \approx 0.1$  nm, resulting into a LOD value of  $\sim 10^{-3}$  RIU, for  $Q = 15000$ . Thus higher Q-value, lower FSR, and lower waveguide losses of the ring resonator promise for a better accuracy in detecting  $\lambda_c$  and hence achievable LOD can be  $\ll 10^{-3}$  RIU.

# CHAPTER 5

## Conclusions

The major research outcome of this thesis work is a novel design and demonstration of critically coupled ring resonator in SOI platform for wide range refractive index sensing of cladding analytes. However, because of the technological limitations, it was started with the design and fabrication optimizations of microns to submicron single-mode waveguides, spot-size converters and thus to demonstrate a large volume ring resonator. Nevertheless, the initial technological limitations helped us to develop a novel surface trimming method of pre-defined waveguides and hence facilitating monolithic integration of varying waveguide cross-sections via low-loss 2D spot-size converters. The research work is then progressed towards the demonstration of a microring resonator based compact design of refractive index sensor with the availability of e-beam lithography and ICPRIE systems. The actual contribution of this work has been described in previous four chapters. In this chapter, we would like to present a brief summary of the entire thesis works and possible future scopes.

### 5.1 Research Summary

The major difficulty associated with the submicron silicon waveguide devices is the effective light coupling mechanism. We have investigated various aspects to improve the light coupling efficiency to silicon waveguides. Initially, a theoretical analysis has been carried out to study the cross-section dependent waveguide characteristics/properties. The analysis shows that larger waveguide cross-sections are preferred for dispersion free, less birefringent and highly fabrication tolerant waveguide structures. It is also observed that higher waveguide cross-section is efficient for coupling light from standard single-mode fibers. Whereas, smaller silicon waveguide cross-sections (with high index contrast) are preferred for achieving compact structures such as ring resonators. Due to tight guided mode confinement in silicon, smaller waveguide cross-section facilitate an

improved light matter interaction and thus the realization of cladding sensitive refractive index sensors. In order to take the advantages both large and smaller waveguide cross-sections, we have adopted multiple approaches for monolithic integration of various waveguide cross-sections on a single SOI substrate platform. Two different surface trimming techniques - (i) repeated oxidation and removal and (ii) isotropic dry etching are developed for the monolithic integration of microns to submicron waveguides. Isotropic dry etching technique is found to be more attractive for surface trimming as this process is much faster than the oxide growth and removal.

To improve the coupling efficiency between fiber and smaller silicon waveguides, we have developed various spot-size converter fabrication techniques. Naturally tapered 2D SSCs are found to be simpler in fabrication point of view, however the insertion loss associated with SSC are high ( $> 5$  dB). Photolithographically defined SSCs with an average insertion loss of  $\sim 2.5$  dB are shown to be better than naturally tapered SSCs. However, higher order mode excitation at the transition region (where the slab height of rib waveguide changes abruptly) of the photolithographically defined SSC makes the performance unpredictable due to fabrication induced errors. A shadow mask etching technique has been developed to improve the coupling efficiency between the micron and submicron sized waveguides. In SSCs fabricated using shadow mask etching technique, slab and rib heights of the waveguide are adiabatically tapered to form an efficient SSC with an insertion loss of 0.25 dB. We have also fabricated gating assisted 1D SSCs on submicron thick (250 nm) device layer SOI using electron beam lithography and inductively coupled plasma reactive ion etching. To fabricate longer ( $> 5$  mm) PhWWs integrated with grating coupler, we have developed and optimized a mixed writing technique for stitch-error free patterning. In mixed patterning technique conventional write field stitching is adopted to expose the SSC region and fixed beam moving stage exposure is used to pattern longer waveguides. The insertion loss and 3 dB bandwidth of the grating coupler are measured to be 6 dB/facet and 70 nm respectively.

Large volume MMIC based ring resonators with bend radius of  $500 \mu$  are fabricated on  $5 \mu$ m device layer and trimmed down to  $2 \mu$ m using the proposed surface trimming technique. Here, the FSR is measured to be  $\sim 110$  pm for both TE and TM polarization. The estimated Q-factor of trimmed waveguide ring resonator is measured to be 33698

(25412) for TE (TM) polarization. As the cladding refractive index sensitivity of the ring resonator with micron sized cross-section is not sufficient enough, we have fabricated microring resonators in submicron SOI integrated with grating assisted 1D SSC. Shallow etched waveguides ( $W = 560$  nm,  $H = 250$  nm and  $h = 150$  nm) are used for microring resonator fabrication as this waveguides supports only TE polarization. In addition to that, shallow etched waveguides can be fabricated with grating coupler in a single step lithography and subsequent dry etching. Various aspects of the microring resonators such as FSR, group index, Q-factor, dispersion, DC asymmetry etc. are studied theoretically and experimentally. The highest Q-factor of  $\sim 1,41,000$  has been measured for ring resonator with bend radius of  $100$   $\mu\text{m}$  and DC length  $40$   $\mu\text{m}$ . DC dispersion is identified to be an important characteristics which can be utilized for wide range refractive index sensing based on tracking the critically coupled wavelength of ring resonator transmission. Two different types of waveguide geometries representing as "shallow-etched" and "deeply-etched" are considered to investigate device performances with numerical simulations. Merits and demerits of devices with both types waveguide geometries are discussed in detail. It is shown theoretically that the sensitivity of a ring resonator with DEDC ( $S \sim 380$  nm/RIU) is nearly five times higher than that of SEDC based ring resonator ( $S \sim 80$  nm/RIU). However, it has been also argued that the fabrication and characterization of a ring resonator with SEDC is relatively easier. The proposed devices are shown to be capable of wider-range of refractive index sensing ( $\Delta n_c > 0.8$ ).

The fabricated devices (with shallow-etched waveguides) are characterized with an average sensitivity of  $\sim 54$  nm/RIU and LOD of  $\sim 1.6 \times 10^{-2}$  RIU. The sensor device has been tested for a cladding refractive index variation of  $\Delta n_c \sim 0.7$  and verified that the sensitivity remains almost same. The error in refractive index sensing can be reduced significantly to  $\ll 10^{-3}$  RIU by increasing perimeter length of the ring and of course by reducing waveguide losses. The superiority of the proposed integrated optical sensor device lies in its simpler design, easier operation, wider-range and nearly accurate detection mechanism.

## 5.2 Research Outlook

We have seen from section 2.3.3 that the grating coupler based SSC response is highly dependent on the wavelength of operation. Consequently, to extract the response of a ring resonator sensor, it need to be normalized with a reference straight waveguide and which is not desirable for a stand alone device. In contrast, the adiabatic SSC developed using shadow mask is found to be nearly independent to the wavelength of operation (see section 2.3.2). So the integration of this adiabatic SSC with ring resonator refractive index sensor would offer efficient and accurate sensing mechanism. The schematic representation of the fabrication process flow for integrating photonic wire microring resonator refractive index sensor (on submicron device layer) to larger input/output waveguide through an adiabatic SSC is shown in Figure 5.1. The schematic represen-

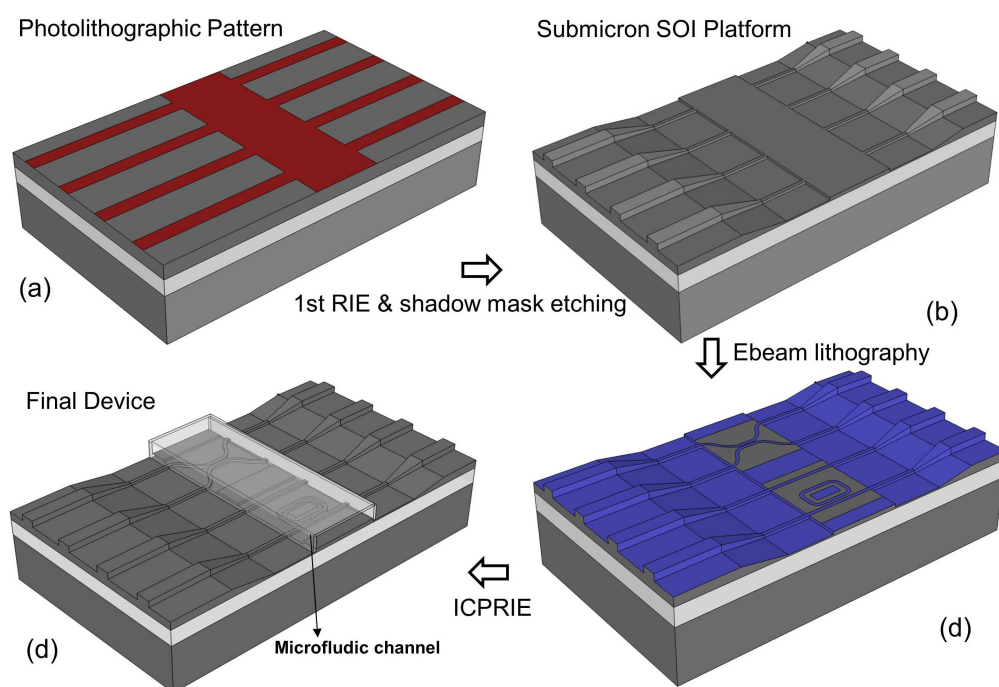


Figure 5.1: Schematic view of fabrication process flow for achieving DC based microring resonator sensor on submicron platform is integrated with large cross-section waveguide. (a) Photolithographically defined photoresist pattern of multiple input multiple output (MIMOW) platform, (b) MIMOW platform is transferred to silicon by RIE, (c) submicron device patterning using electron beam lithography and (d) final device on the submicron platform with microfluidic channel to supply analyte.

tation of the fabrication process flow for integrating photonic wire microring resonator refractive index sensor (on submicron device layer) to larger input/output waveguide

through an adiabatic SSC is shown in Figure 5.1. In the first step, multiple input and multiple output waveguides (MIMOWs) along with a center platform are defined using photolithography (see Figure 5.1(a)). This MIMOW platform is transferred to silicon by means of an anisotropic RIE process. After removing the photo/electron beam resist, an isotropic RIE has been carried out on the sample, where input and output waveguide sections are covered with a shadow mask. This helps in forming adiabatic 2D taper from input/output waveguide to the center platform whose height has been reduced to sub-micron (see Figure 5.1(b)). In the next step, photonic wire ring resonator devices and reference structures are patterned on the platform region using electron beam lithography (see Figure 5.1(c)). Here positive tone electron beam resist (PMMA) is preferred as the selected regions of the platform can be utilized to define circuit and remaining platform area can be preserved for later use. ICPRIE process is carried out to transfer the electron beam lithography pattern to the submicron silicon device layer. Finally, the device has been provided with a microfluidic channel to supply the analyte to the active area of the sensor. The process flow allows us to integrate/interface micron and sub-micron sized waveguides on a single substrate platform and that would enable the fiber pigtailling and packaging. The MIMOW platform also facilitates the usage of substrate repeatedly for device fabrication multiple times without end-facet preparation. Input and output waveguides can be used for optical access to any integrated optical device defined on the platform.

The dispersion enhanced critically coupled ring resonators are found to be useful for wide range refractive index sensing. However, the LOD of the demonstrated refractive index sensor is limited by the FSR of the microring resonator in the present configuration. LOD of the device can be significantly improved by incorporating the a heater element for active tuning of phase of the guided mode in the ring. Figure 5.2(a) shows the schematic view of a ring refractive index sensor with a heater for active phase tuning of the guided mode. The advantage of this configuration is that the resonance wavelength near to  $\lambda_c$  can be made exactly equal to the critically coupled wavelength by slightly changing phase of the guided mode by tuning the heater temperature without affecting the sensing region. The resolution of temperature/phase tuning can be improved by optimizing separation between the heater and the waveguide. Similar configuration can be used for realizing a refracting index sensor with electronic interrogation by the

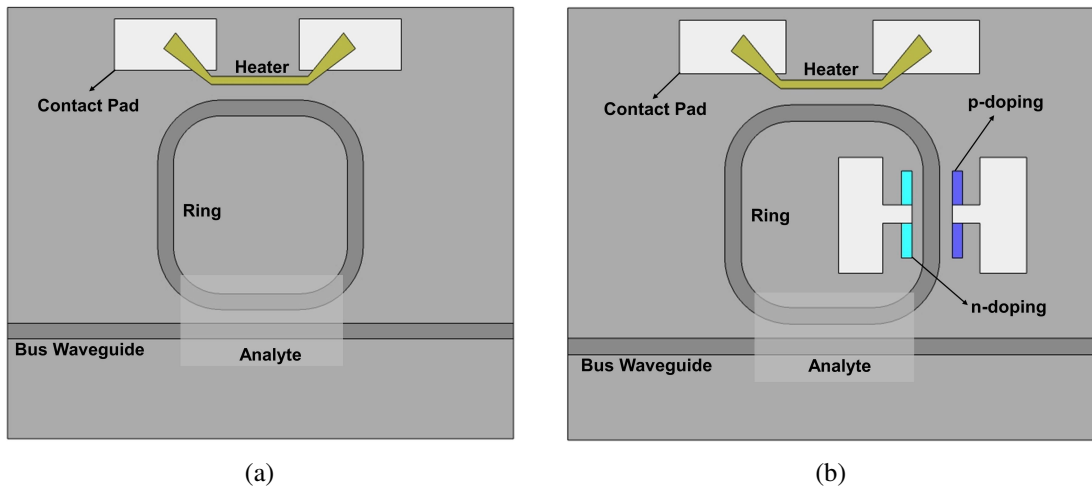


Figure 5.2: Schematic view of ring resonator refractive sensor with (a) heater for active phase tuning and (b) pin diode for electronic interrogation.

addition of pin diode across the ring waveguide. Figure 5.2(b) shows the schematic representation of refractive sensor with electronic interrogation using pin diode. It is known that the  $\lambda_c$  of microring resonator can be tuned either by controlling  $t$  or  $a$ . The analyte on the sensor region shift the  $t$  of DC and thus shift in  $\lambda_c$ , so it possible to shift back the  $\lambda_c$  by tuning  $a$ . The sensor with a pin diode across ring waveguide can be efficiently used for tuning  $a$  ring just controlling the driving voltage of the diode. This in fact, helps to get rid of the sensing based on spectroscopic measurements where generally, expensive optical spectrum analyzers are used.

## REFERENCES

- [1] R. Soref and J. Lorenzo, "Single-crystal silicon: a new material for 1? 3 and 1? 6  $\mu\text{m}$  integrated-optical components," *Electronics Letters*, vol. 21, no. 21, pp. 953–954, 1985.
- [2] R. R. Schaller, "Moore's law: past, present and future," *IEEE spectrum*, vol. 34, no. 6, pp. 52–59, 1997.
- [3] A. C. Cangellaris, "The interconnect bottleneck in multi-ghz processors; new opportunities for hybrid electrical/optical solutions," in *Massively Parallel Processing, 1998. Proceedings. Fifth International Conference on.* IEEE, 1998, pp. 96–103.
- [4] R. Kirchain and L. Kimerling, "A roadmap for nanophotonics," *Nature Photonics*, vol. 1, no. 6, pp. 303–305, 2007.
- [5] D. Miller, "Device requirements for optical interconnects to silicon chips," *Proceedings of the IEEE*, vol. 7, no. 97, pp. 1166–1185, 2009.
- [6] ———, "Device requirements for optical interconnects to cmos silicon chips," in *Photonics in Switching.* Optical Society of America, 2010, p. PMB3.
- [7] J. Foresi, P. R. Villeneuve, J. Ferrera, E. Thoen, G. Steinmeyer, S. Fan, J. Joannopoulos, L. Kimerling, H. I. Smith, and E. Ippen, "Photonic-bandgap microcavities in optical waveguides," *nature*, vol. 390, no. 6656, pp. 143–145, 1997.
- [8] A. Sakai, G. Hara, and T. Baba, "Propagation characteristics of ultrahigh- $\delta$  optical waveguide on silicon-on-insulator substrate," *Japanese Journal of Applied Physics*, vol. 40, no. 4B, p. L383, 2001.
- [9] Z. Fang and C. Z. Zhao, "Recent progress in silicon photonics: a review," *ISRN Optics*, vol. 2012, 2012.
- [10] J.-i. Takahashi, T. Tsuchizawa, T. Watanabe, and S.-i. Itabashi, "Oxidation-induced improvement in the sidewall morphology and cross-sectional profile of silicon wire waveguides," *Journal of Vacuum Science & Technology B*, vol. 22, no. 5, pp. 2522–2525, 2004.
- [11] F. Gao, Y. Wang, G. Cao, X. Jia, and F. Zhang, "Improvement of sidewall surface roughness in silicon-on-insulator rib waveguides," *Applied Physics B*, vol. 81, no. 5, pp. 691–694, 2005.
- [12] M.-C. M. Lee and M. C. Wu, "Thermal annealing in hydrogen for 3-d profile transformation on silicon-on-insulator and sidewall roughness reduction," *Microelectromechanical Systems, Journal of*, vol. 15, no. 2, pp. 338–343, 2006.



- [13] M. Borselli, T. Johnson, C. Michael, M. Henry, and O. Painter, "Surface encapsulation for low-loss silicon photonics," *arXiv preprint arXiv:0707.0415*, 2007.
- [14] F. Gao, Y. Wang, G. Cao, X. Jia, and F. Zhang, "Reduction of sidewall roughness in silicon-on-insulator rib waveguides," *Applied surface science*, vol. 252, no. 14, pp. 5071–5075, 2006.
- [15] Q. Xia, P. F. Murphy, H. Gao, and S. Y. Chou, "Ultrafast and selective reduction of sidewall roughness in silicon waveguides using self-perfection by liquefaction," *Nanotechnology*, vol. 20, no. 34, p. 345302, 2009.
- [16] P. Dong, W. Qian, S. Liao, H. Liang, C.-C. Kung, N.-N. Feng, R. Shafiha, J. Fong, D. Feng, A. V. Krishnamoorthy *et al.*, "Low loss shallow-ridge silicon waveguides," *Optics express*, vol. 18, no. 14, pp. 14 474–14 479, 2010.
- [17] G. Li, J. Yao, H. Thacker, A. Mekis, X. Zheng, I. Shubin, Y. Luo, J.-H. Lee, K. Raj, J. E. Cunningham *et al.*, "Ultralow-loss, high-density soi optical waveguide routing for macrochip interconnects," *Optics express*, vol. 20, no. 11, pp. 12 035–12 039, 2012.
- [18] A. Sakai, T. Fukazawa, and T. Baba, "Micro-branch in silicon photonic wire waveguides," in *Integrated Photonics Research*. Optical Society of America, 2002, p. IThI12.
- [19] W. Bogaerts, R. Baets, P. Dumon, V. Wiaux, S. Beckx, D. Taillaert, B. Luyssaert, J. Van Campenhout, P. Bienstman, and D. Van Thourhout, "Nanophotonic waveguides in silicon-on-insulator fabricated with cmos technology," *Journal of Lightwave Technology*, vol. 23, no. 1, pp. 401–412, 2005.
- [20] M. Asghari and A. V. Krishnamoorthy, "Silicon photonics: Energy-efficient communication," *Nature photonics*, vol. 5, no. 5, pp. 268–270, 2011.
- [21] A. Narasimha, B. Analui, Y. Liang, T. J. Sleboda, S. Abdalla, E. Balmater, S. Gloeckner, D. Guckenberger, M. Harrison, R. G. Koumans *et al.*, "A fully integrated  $4 \times 10$ -gb/s dwdm optoelectronic transceiver implemented in a standard  $0.13 \mu\text{m}$  cmos soi technology," *IEEE Journal of Solid-state circuits*, vol. 42, no. 12, pp. 2736–2744, 2007.
- [22] Y. Ma, Y. Zhang, S. Yang, A. Novack, R. Ding, A. E.-J. Lim, G.-Q. Lo, T. Baehr-Jones, and M. Hochberg, "Ultralow loss single layer submicron silicon waveguide crossing for soi optical interconnect," *Optics express*, vol. 21, no. 24, pp. 29 374–29 382, 2013.
- [23] S. Assefa, S. Shank, W. Green, M. Khater, E. Kiewra, C. Reinholm, S. Kamalapurkar, A. Rylyakov, C. Schow, F. Horst *et al.*, "A 90 nm cmos integrated nanophotonics technology for 25 gbps wdm optical communications applications," in *IEEE International Electron Devices Meeting (IEDM)*, vol. 33, 2012, pp. 8–33.
- [24] Y. Vlasov, W. M. Green, and F. Xia, "High-throughput silicon nanophotonic wavelength-insensitive switch for on-chip optical networks," *nature photonics*, vol. 2, no. 4, pp. 242–246, 2008.

- [25] B. G. Lee, A. Biberman, J. Chan, and K. Bergman, "High-performance modulators and switches for silicon photonic networks-on-chip," *IEEE Journal of Selected Topics in Quantum Electronics*, vol. 16, no. 1, pp. 6–22, 2010.
- [26] V. R. Almeida, C. A. Barrios, R. R. Panepucci, and M. Lipson, "All-optical control of light on a silicon chip," *Nature*, vol. 431, no. 7012, pp. 1081–1084, 2004.
- [27] F. Xia, L. Sekaric, and Y. Vlasov, "Ultracompact optical buffers on a silicon chip," *Nature photonics*, vol. 1, no. 1, pp. 65–71, 2007.
- [28] A. Canciamilla, M. Torregiani, C. Ferrari, F. Morichetti, R. De La Rue, A. Samarelli, M. Sorel, and A. Melloni, "Silicon coupled-ring resonator structures for slow light applications: potential, impairments and ultimate limits," *Journal of Optics*, vol. 12, no. 10, p. 104008, 2010.
- [29] Y. Su, F. Liu, Q. Li, Z. Zhang, and M. Qiu, "System performance of slow-light buffering and storage in silicon nano-waveguide," in *Asia-Pacific Optical Communications*. International Society for Optics and Photonics, 2007, pp. 67 832P–67 832P.
- [30] Q. Xu, S. Manipatruni, B. Schmidt, J. Shakya, and M. Lipson, "12.5 gbit/s carrier-injection-based silicon micro-ring silicon modulators," *Optics express*, vol. 15, no. 2, pp. 430–436, 2007.
- [31] C. Li, L. Zhou, and A. W. Poon, "Silicon microring carrier-injection-based modulators/switches with tunable extinction ratios and or-logic switching by using waveguide cross-coupling," *Optics express*, vol. 15, no. 8, pp. 5069–5076, 2007.
- [32] L. Zhang, J. Ding, Y. Tian, R. Ji, L. Yang, H. Chen, P. Zhou, Y. Lu, W. Zhu, and R. Min, "Electro-optic directed logic circuit based on microring resonators for xor/xnor operations," *Optics express*, vol. 20, no. 11, pp. 11 605–11 614, 2012.
- [33] A. Nitkowski, L. Chen, and M. Lipson, "Cavity-enhanced on-chip absorption spectroscopy using microring resonators," *Optics express*, vol. 16, no. 16, pp. 11 930–11 936, 2008.
- [34] Z. Xia, A. A. Eftekhari, M. Soltani, B. Momeni, Q. Li, M. Chamanzar, S. Yegnanarayanan, and A. Adibi, "High resolution on-chip spectroscopy based on miniaturized microdonut resonators," *Optics express*, vol. 19, no. 13, pp. 12 356–12 364, 2011.
- [35] A. L. Washburn, L. C. Gunn, and R. C. Bailey, "Label-free quantitation of a cancer biomarker in complex media using silicon photonic microring resonators," *Analytical chemistry*, vol. 81, no. 22, pp. 9499–9506, 2009.
- [36] A. L. Washburn, M. S. Luchansky, A. L. Bowman, and R. C. Bailey, "Quantitative, label-free detection of five protein biomarkers using multiplexed arrays of silicon photonic microring resonators," *Analytical chemistry*, vol. 82, no. 1, pp. 69–72, 2009.

- [37] M. K. Park, J. S. Kee, J. Y. Quah, V. Netto, J. Song, Q. Fang, E. M. La Fosse, and G.-Q. Lo, "Label-free aptamer sensor based on silicon microring resonators," *Sensors and Actuators B: Chemical*, vol. 176, pp. 552–559, 2013.
- [38] J. T. Robinson, L. Chen, and M. Lipson, "On-chip gas detection in silicon optical microcavities," *Optics Express*, vol. 16, no. 6, pp. 4296–4301, 2008.
- [39] M.-S. Kwon and W. H. Steier, "Microring-resonator-based sensor measuring both the concentration and temperature of a solution," *Optics Express*, vol. 16, no. 13, pp. 9372–9377, 2008.
- [40] V. Passaro, C. d. Tullio, B. Troia, M. L. Notte, G. Giannoccaro, and F. D. Leonardis, "Recent advances in integrated photonic sensors," *Sensors*, vol. 12, no. 11, pp. 15 558–15 598, 2012.
- [41] G. Mi, C. Horvath, M. Aktary, and V. Van, "Silicon microring refractometric sensor for atmospheric CO<sub>2</sub> gas monitoring," *Optics Express*, vol. 24, no. 2, pp. 1773–1780, 2016.
- [42] A. Fernández Gavela, D. Grajales García, J. C. Ramirez, and L. M. Lechuga, "Last advances in silicon-based optical biosensors," *Sensors*, vol. 16, no. 3, p. 285, 2016.
- [43] K. De Vos, I. Bartolozzi, E. Schacht, P. Bienstman, and R. Baets, "Silicon-on-insulator microring resonator for sensitive and label-free biosensing," *Optics Express*, vol. 15, no. 12, pp. 7610–7615, 2007.
- [44] D. Xu, A. Densmore, A. DelÔge, P. Waldron, R. McKinnon, S. Janz, J. Lapointe, G. Lopinski, T. Mischki, E. Post *et al.*, "Folded cavity SOI microring sensors for high sensitivity and real time measurement of biomolecular binding," *Optics Express*, vol. 16, no. 19, pp. 15 137–15 148, 2008.
- [45] N. A. Yebo, D. Taillaert, J. Roels, D. Lahem, M. Debliquy, D. Van Thourhout, and R. Baets, "Silicon-on-insulator (SOI) ring resonator-based integrated optical hydrogen sensor," *IEEE Photonics Technology Letters*, vol. 21, no. 14, pp. 960–962, 2009.
- [46] C. Kang, C. T. Phare, Y. A. Vlasov, S. Assefa, and S. M. Weiss, "Photonic crystal slab sensor with enhanced surface area," *Optics Express*, vol. 18, no. 26, pp. 27 930–27 937, 2010.
- [47] S. Chakravarty, W.-C. Lai, Y. Zou, H. A. Drabkin, R. M. Gemmill, G. R. Simon, S. H. Chin, and R. T. Chen, "Multiplexed specific label-free detection of NCI-H358 lung cancer cell line lysates with silicon based photonic crystal microcavity biosensors," *Biosensors and Bioelectronics*, vol. 43, pp. 50–55, 2013.
- [48] Q. Liu, J. S. Kee, and M. K. Park, "A refractive index sensor design based on grating-assisted coupling between a strip waveguide and a slot waveguide," *Optics Express*, vol. 21, no. 5, pp. 5897–5909, 2013.

- [49] F. Prieto, B. Sepulveda, A. Calle, A. Llobera, C. Dominguez, and L. M. Lechuga, "Integrated Mach-Zehnder interferometer based on arrow structures for biosensor applications," *Sensors and Actuators B: Chemical*, vol. 92, no. 1, pp. 151–158, 2003.
- [50] F. Prieto, L. M. Lechuga, A. Calle, A. Llobera, and C. Domínguez, "Optimized silicon antiresonant reflecting optical waveguides for sensing applications," *Journal of Lightwave Technology*, vol. 19, no. 1, pp. 75–83, 2001.
- [51] A. Brandenburg, R. Krauter, C. Künzel, M. Stefan, and H. Schulte, "Interferometric sensor for detection of surface-bound bioreactions," *Applied Optics*, vol. 39, no. 34, pp. 6396–6405, 2000.
- [52] W. Bogaerts, P. De Heyn, T. Van Vaerenbergh, K. De Vos, S. Kumar Selvaraja, T. Claes, P. Dumon, P. Bienstman, D. Van Thourhout, and R. Baets, "Silicon microring resonators," *Laser & Photonics Reviews*, vol. 6, no. 1, pp. 47–73, 2012.
- [53] M.-C. Estevez, M. Alvarez, and L. M. Lechuga, "Integrated optical devices for lab-on-a-chip biosensing applications," *Laser & Photonics Reviews*, vol. 6, no. 4, pp. 463–487, 2012.
- [54] R. Guider, D. Gandolfi, T. Chalyan, L. Pasquardini, A. Samusenko, C. Pederzoli, G. Pucker, and L. Pavesi, "Sensitivity and limit of detection of biosensors based on ring resonators," *Sensing and Bio-Sensing Research*, vol. 6, pp. 99–102, 2015.
- [55] W. Zhang, S. Serna, X. Le Roux, L. Vivien, and E. Cassan, "Highly sensitive refractive index sensing by fast detuning the critical coupling condition of slot waveguide ring resonators," *Optics Letters*, vol. 41, no. 3, pp. 532–535, 2016.
- [56] G. A. Rodriguez, S. Hu, and S. M. Weiss, "Porous silicon ring resonator for compact, high sensitivity biosensing applications," *Optics Express*, vol. 23, no. 6, pp. 7111–7119, 2015.
- [57] D. Dai, "Highly sensitive digital optical sensor based on cascaded high-q ring-resonators," *Optics Express*, vol. 17, no. 26, pp. 23 817–23 822, 2009.
- [58] T. Claes, W. Bogaerts, and P. Bienstman, "Experimental characterization of a silicon photonic biosensor consisting of two cascaded ring resonators based on the vernier-effect and introduction of a curve fitting method for an improved detection limit," *Optics Express*, vol. 18, no. 22, pp. 22 747–22 761, 2010.
- [59] T. Claes, J. G. Molera, K. De Vos, E. Schacht, R. Baets, and P. Bienstman, "Label-free biosensing with a slot-waveguide-based ring resonator in silicon on insulator," *IEEE Photonics Journal*, vol. 1, no. 3, pp. 197–204, 2009.
- [60] D. Taillaert, W. Bogaerts, P. Bienstman, T. F. Krauss, P. Van Daele, I. Moerman, S. Verstuyft, K. De Mesel, and R. Baets, "An out-of-plane grating coupler for efficient butt-coupling between compact planar waveguides and single-mode fibers," *Quantum Electronics, IEEE Journal of*, vol. 38, no. 7, pp. 949–955, 2002.

- [61] F. Van Laere, G. Roelkens, M. Ayre, J. Schrauwen, D. Taillaert, D. Van Thourhout, T. F. Krauss, and R. Baets, "Compact and highly efficient grating couplers between optical fiber and nanophotonic waveguides," *Journal of Lightwave Technology*, vol. 25, no. 1, pp. 151–156, 2007.
- [62] A. Mekis, S. Gloeckner, G. Masini, A. Narasimha, T. Pinguet, S. Sahni, and P. De Dobbelaere, "A grating-coupler-enabled cmos photonics platform," *IEEE Journal of Selected Topics in Quantum Electronics*, vol. 17, no. 3, pp. 597–608, 2011.
- [63] X. Chen, C. Li, and H. K. Tsang, "Fabrication-tolerant waveguide chirped grating coupler for coupling to a perfectly vertical optical fiber," *IEEE Photonics Technology Letters*, vol. 20, no. 23, pp. 1914–1916, 2008.
- [64] T. Shoji, T. Tsuchizawa, T. Watanabe, K. Yamada, and H. Morita, "Low loss mode size converter from 0.3  $\mu\text{m}$  square si wire waveguides to singlemode fibres," *Electronics Letters*, vol. 38, no. 25, pp. 1669–1670, 2002.
- [65] R. Takei, M. Suzuki, E. Omoda, S. Manako, T. Kamei, M. Mori, and Y. Sakakibara, "Silicon knife-edge taper waveguide for ultralow-loss spot-size converter fabricated by photolithography," *Applied Physics Letters*, vol. 102, no. 10, p. 101108, 2013.
- [66] V. R. Almeida, R. R. Panepucci, and M. Lipson, "Nanotaper for compact mode conversion," *Optics letters*, vol. 28, no. 15, pp. 1302–1304, 2003.
- [67] K. K. Lee, D. R. Lim, D. Pan, C. Hoepfner, W.-Y. Oh, K. Wada, L. C. Kimerling, K. P. Yap *et al.*, "Mode transformer for miniaturized optical circuits," *Optics letters*, vol. 30, no. 5, pp. 498–500, 2005.
- [68] W. S. Zaoui, A. Kunze, W. Vogel, M. Berroth, J. Butschke, F. Letzkus, and J. Burghartz, "Bridging the gap between optical fibers and silicon photonic integrated circuits," *Optics express*, vol. 22, no. 2, pp. 1277–1286, 2014.
- [69] T. Tsuchizawa, K. Yamada, H. Fukuda, T. Watanabe, J.-i. Takahashi, J.-i. Takahashi, T. Shoji, E. Tamechika, S.-i. Itabashi, and H. Morita, "Microphotonics devices based on silicon microfabrication technology," *Selected Topics in Quantum Electronics, IEEE Journal of*, vol. 11, no. 1, pp. 232–240, 2005.
- [70] P. O'Brien, L. Carrol, C. Eason, and J. S. Lee, "Packaging of silicon photonic devices," in *Silicon Photonics III*. Springer, 2016, pp. 217–236.
- [71] S.-H. Hsu, S.-C. Tseng, and H.-Z. You, "Birefringence characterization on soi waveguide using optical low coherence interferometry," in *7th IEEE International Conference on Group IV Photonics*, 2010.
- [72] G. R. Bhatt, R. Sharma, U. Karthik, and B. K. Das, "Dispersion-free soi interleaver for dwdm applications," *Lightwave Technology, Journal of*, vol. 30, no. 1, pp. 140–146, 2012.

- [73] A. Khilo, M. A. Popović, M. Araghchini, and F. X. Kärtner, “Efficient planar fiber-to-chip coupler based on two-stage adiabatic evolution,” *Optics express*, vol. 18, no. 15, pp. 15 790–15 806, 2010.
- [74] P. Dumon, W. Bogaerts, V. Wiaux, J. Wouters, S. Beckx, J. Van Campenhout, D. Taillaert, B. Luyssaert, P. Bienstman, D. Van Thourhout *et al.*, “Low-loss soi photonic wires and ring resonators fabricated with deep uv lithography,” *IEEE Photonics Technology Letters*, vol. 16, no. 5, pp. 1328–1330, 2004.
- [75] F. Xia, M. Rooks, L. Sekaric, and Y. Vlasov, “Ultra-compact high order ring resonator filters using submicron silicon photonic wires for on-chip optical interconnects,” *Optics express*, vol. 15, no. 19, pp. 11 934–11 941, 2007.
- [76] A. Vörckel, M. Mönster, W. Henschel, P. H. Bolivar, and H. Kurz, “Asymmetrically coupled silicon-on-insulator microring resonators for compact add-drop multiplexers,” *Photonics Technology Letters, IEEE*, vol. 15, no. 7, pp. 921–923, 2003.
- [77] W. Bogaerts, P. Dumon, D. Van Thourhout, D. Taillaert, P. Jaenen, J. Wouters, S. Beckx, V. Wiaux, and R. G. Baets, “Compact wavelength-selective functions in silicon-on-insulator photonic wires,” *Selected Topics in Quantum Electronics, IEEE Journal of*, vol. 12, no. 6, pp. 1394–1401, 2006.
- [78] A. Liu, R. Jones, L. Liao, D. Samara-Rubio, D. Rubin, O. Cohen, R. Nicolaescu, and M. Paniccia, “A high-speed silicon optical modulator based on a metal–oxide–semiconductor capacitor,” *Nature*, vol. 427, no. 6975, pp. 615–618, 2004.
- [79] D.-X. Xu, P. Cheben, D. Dalacu, A. Delâge, S. Janz, B. Lamontagne, M.-J. Picard, and W. Ye, “Eliminating the birefringence in silicon-on-insulator ridge waveguides by use of cladding stress,” *Optics letters*, vol. 29, no. 20, pp. 2384–2386, 2004.
- [80] N. Y. Winnie, D.-X. Xu, S. Janz, P. Cheben, A. Delage, M.-J. Picard, B. Lamontagne, and N. G. Tarr, “Stress-induced birefringence in silicon-on-insulator (soi) waveguides,” in *Integrated Optoelectronic Devices 2004*. International Society for Optics and Photonics, 2004, pp. 57–66.
- [81] N. Y. Winnie, D.-X. Xu, S. Janz, P. Cheben, M.-J. Picard, B. Lamontagne, and N. G. Tarr, “Birefringence control using stress engineering in silicon-on-insulator (soi) waveguides,” *Journal of lightwave technology*, vol. 23, no. 3, p. 1308, 2005.
- [82] D.-X. Xu, P. Cheben, D. Dalacu, S. Janz, M.-J. Picard, N. Tarr, and W. Ye, “Control and compensation of birefringence in soi waveguides,” in *Lasers and Electro-Optics Society, 2003. LEOS 2003. The 16th Annual Meeting of the IEEE*, vol. 2. IEEE, 2003, pp. 590–591.
- [83] L. Vivien, S. Laval, B. Dumont, S. Lardenois, A. Koster, and E. Cassan, “Polarization-independent single-mode rib waveguides on silicon-on-insulator for telecommunication wavelengths,” *Optics communications*, vol. 210, no. 1, pp. 43–49, 2002.

- [84] C. D. Salzberg and J. J. Villa, “Infrared refractive indexes of silicon germanium and modified selenium glass\*,” *JOSA*, vol. 47, no. 3, pp. 244–246, 1957.
- [85] W. R. Headley, G. T. Reed, S. Howe, A. Liu, and M. Paniccia, “Polarization-independent optical racetrack resonators using rib waveguides on silicon-on-insulator,” *Applied physics letters*, vol. 85, no. 23, pp. 5523–5525, 2004.
- [86] K. Shiraishi, H. Yoda, A. Ohshima, H. Ikedo, and C. S. Tsai, “A silicon-based spot-size converter between single-mode fibers and si-wire waveguides using cascaded tapers,” *Applied Physics Letters*, vol. 91, no. 14, p. 141120, 2007.
- [87] T. Aalto, K. Solehmainen, M. Harjanne, M. Kapulainen, and P. Heimala, “Low-loss converters between optical silicon waveguides of different sizes and types,” *Photonics Technology Letters, IEEE*, vol. 18, no. 5, pp. 709–711, 2006.
- [88] A. Barkai, A. Liu, D. Kim, R. Cohen, N. Elek, H.-H. Chang, B. H. Malik, R. Gabay, R. Jones, M. Paniccia *et al.*, “Double-stage taper for coupling between soi waveguides and single-mode fiber,” *Journal of Lightwave Technology*, vol. 26, no. 24, pp. 3860–3865, 2008.
- [89] A. Sure, T. Dillon, J. Murakowski, C. Lin, D. Pustai, and D. W. Prather, “Fabrication and characterization of three-dimensional silicon tapers,” *Optics express*, vol. 11, no. 26, pp. 3555–3561, 2003.
- [90] M. Fritze, J. Knecht, C. Bozler, C. Keast, J. Fijol, S. Jacobson, P. Keating, J. LeBlanc, E. Fike, B. Kessler *et al.*, “Fabrication of three-dimensional mode converters for silicon-based integrated optics,” *Journal of Vacuum Science & Technology B*, vol. 21, no. 6, pp. 2897–2902, 2003.
- [91] A. Prinzen, M. Waldow, and H. Kurz, “Fabrication tolerances of soi based directional couplers and ring resonators,” *Optics express*, vol. 21, no. 14, pp. 17 212–17 220, 2013.
- [92] J. Schrauwen, D. Van Thourhout, and R. Baets, “Trimming of silicon ring resonator by electron beam induced compaction and strain,” *Optics express*, vol. 16, no. 6, pp. 3738–3743, 2008.
- [93] A. Canciamilla, F. Morichetti, S. Grillanda, P. Velha, M. Sorel, V. Singh, A. Agarwal, L. C. Kimerling, and A. Melloni, “Photo-induced trimming of chalcogenide-assisted silicon waveguides,” *Optics express*, vol. 20, no. 14, pp. 15 807–15 817, 2012.
- [94] S. Grillanda, V. Raghunathan, V. Singh, F. Morichetti, J. Michel, L. Kimerling, A. Melloni, and A. Agarwal, “Post-fabrication trimming of athermal silicon waveguides,” *Optics letters*, vol. 38, no. 24, pp. 5450–5453, 2013.
- [95] T. Lipka, M. Kiepsch, H. K. Trieu, and J. Müller, “Hydrogenated amorphous silicon photonic device trimming by uv-irradiation,” *Opt. Express*, vol. 22, pp. 12 122–12 132, 2014.

- [96] L. Zhou, K. Okamoto, and S. Yoo, "Athermalizing and trimming of slotted silicon microring resonators with uv-sensitive pmma upper-cladding," *Photonics Technology Letters, IEEE*, vol. 21, no. 17, pp. 1175–1177, 2009.
- [97] S. Chandran and B. Das, "Surface trimming of silicon photonics devices using controlled reactive ion etching chemistry," *Photonics and Nanostructures-Fundamentals and Applications*, vol. 15, pp. 32–40, 2015.
- [98] S. Obayya, B. Rahman, K. Grattan, and H. El-Mikati, "Beam propagation modeling of polarization rotation in deeply etched semiconductor bent waveguides," *Photonics Technology Letters, IEEE*, vol. 13, no. 7, pp. 681–683, 2001.
- [99] V. P. Tzolov and M. Fontaine, "A passive polarization converter free of longitudinally-periodic structure," *Optics Communications*, vol. 127, no. 1, pp. 7–13, 1996.
- [100] D. Thomson, Y. Hu, G. Reed, and J.-M. Fedeli, "Low loss mmi couplers for high performance mzi modulators," *Photonics Technology Letters, IEEE*, vol. 22, no. 20, pp. 1485–1487, 2010.
- [101] J. Xia, J. Yu, Z. Wang, Z. Fan, and S. Chen, "Low power  $2 \times 2$  thermo-optic soi waveguide switch fabricated by anisotropy chemical etching," *Optics communications*, vol. 232, no. 1, pp. 223–228, 2004.
- [102] D.-X. Xu, A. Densmore, P. Waldron, J. Lapointe, E. Post, A. DelÔge, S. Janz, P. Cheben, J. H. Schmid, and B. Lamontagne, "High bandwidth soi photonic wire ring resonators using mmi couplers," *Optics Express*, vol. 15, no. 6, pp. 3149–3155, 2007.
- [103] D.-X. Xu, S. Janz, and P. Cheben, "Design of polarization-insensitive ring resonators in silicon-on-insulator using mmi couplers and cladding stress engineering," *Photonics Technology Letters, IEEE*, vol. 18, no. 2, pp. 343–345, 2006.
- [104] L. B. Soldano and E. Pennings, "Optical multi-mode interference devices based on self-imaging: principles and applications," *Lightwave Technology, Journal of*, vol. 13, no. 4, pp. 615–627, 1995.
- [105] W. Bogaerts, P. Bienstman, and R. Baets, "Scattering at sidewall roughness in photonic crystal slabs," *Optics letters*, vol. 28, no. 9, pp. 689–691, 2003.
- [106] A. Yariv and P. Yeh, *Photonics: optical electronics in modern communications (the oxford series in electrical and computer engineering)*. Oxford University Press, Inc., 2006.
- [107] W. J. Westerveld, J. Pozo, S. M. Leinders, M. Yousefi, and H. P. Urbach, "Demonstration of large coupling-induced phase delay in silicon directional cross-couplers," *IEEE Journal of Selected Topics in Quantum Electronics*, vol. 20, no. 4, pp. 1–6, 2014.
- [108] W. Bogaerts, S. K. Selvaraja, P. Dumon, J. Brouckaert, K. De Vos, D. Van Thourhout, and R. Baets, "Silicon-on-insulator spectral filters fabricated with CMOS technology," *IEEE journal of Selected Topics in Quantum Electronics*, vol. 16, no. 1, pp. 33–44, 2010.



- [109] Y. H. Kim, S. J. Park, S.-W. Jeon, S. Ju, C.-S. Park, W.-T. Han, and B. H. Lee, “Thermo-optic coefficient measurement of liquids based on simultaneous temperature and refractive index sensing capability of a two-mode fiber interferometric probe,” *Optics express*, vol. 20, no. 21, pp. 23 744–23 754, 2012.

# APPENDIX A

## List of Publications Based on Thesis

### Patent

1. **S. Chandran**, S. M. Sundaram and B. K. Das, "Method and apparatus for modifying dimensions of a waveguide", US Patent App. 15/218,300.

### Journal

1. B. K. Das, N. DasGupta, **S. Chandran**, et al., "Silicon Photonics Technology: Ten Years of Research at IIT Madras," *Asian Journal of Physics*, vol. 25, no. 7, 2016 (21 pages).
2. **S. Chandran**, R. K. Gupta and B. K. Das, "Dispersion enhanced critically coupled ring resonator for wide range refractive index sensing," *IEEE Journal of Selected Topics in Quantum Electronics*, vol. 23, no. 2, March/April 2017 (9 pages).
3. **S. Chandran** and B. K. Das, "Surface trimming of silicon photonics devices using controlled reactive ion etching chemistry," *Photonics and Nanostructures Fundamentals and Applications (Elsevier)*, vol. 15, pp. 32-40, 2015 (9 pages).

### Conference (Presentations / Proceedings)

1. B.K. Das, **S. Chandran**, R. Sidharth, S. Kaushal, and P. Sah, "Nanoscale tolerance for silicon optical interconnect devices," NS & NT 2014, University of Calcutta, India, Sept. 18-19 2014 (Invited).
2. B.K Das, **S. Chandran** and S. Kaushal, "Optical interconnect devices with scalable device cross-sections in SOI platform," ICOL-2014, Dehradun, India, March 05-08 2014 (Invited).
3. **S. Chandran**, S. Kaushal and B. K. Das, "Monolithic integration of micron to sub-micron waveguides with 2D mode-size converters in SOI platform," SPIE Photonic West, San Francisco, USA, February 02-07, 2014 (Invited).
4. **S. Chandran**, B.K. Das, "Tapering and size reduction of single-mode silicon waveguides by maskless RIE," 17th Opto-Electronics and Communications Conference (OECC/IEEE), Busan, South Korea, Proc. OECC, pp. 655 - 656, 2012.

5. B.K. Das, **S. Chandran** and U. Karthik, "Silicon photonics and optical interconnect Technology," ICOE - International Conference on Optical Engineering 2012, VTU, Belgaum, India, July 26-28,2012 (Invited).
6. B.K. Das, **S. Chandran** and U. Karthik, "Research advances in SOI based waveguide sensors," IConTOP - Trends in Optics and Photonics II, Kolkata, India, 7-9 Dec, 2011 (Invited).
7. B.K. Das, **S. Chandran**, G.R. Bhatt, U. Karthik and R. Sharma, "Silicon photonics in SOI platform: problems with waveguide dispersion and birefringence Effects" FOP 11 - Frontiers in Optics and Photonics, XXXVI OSI Symposium, New Delhi, India, 3-5 Dec, 2011 (Invited).

# APPENDIX B

## Curriculum Vitae

Name : Sujith C  
Date of Birth : 30-May-1983  
Educational Qualification : M. Tech

### **2005 Master of Science (M. Sc)**

Institution : M G University, Kottayam  
Specialization : Physics

### **2008 Master of Technology (M. Tech)**

Institution : University of Kerala  
Specialization : Optoelectronics and Optical Communication

# APPENDIX C

## DOCTORAL COMMITTEE

- CHAIR PERSON** : Dr. Anil Prabhakar  
Professor  
Department of Electrical Engineering  
Indian Institute of Technology Madras
- GUIDE** : Dr. Bijoy Krisha Das  
Associate Professor  
Department of Electrical Engineering  
Indian Institute of Technology Madras
- MEMBERS** : Dr. Nandita DasGupta  
Professor  
Department of Electrical Engineering  
Indian Institute of Technology Madras
- : Dr. Balaji Srinivasan  
Associate Professor  
Department of Electrical Engineering  
Indian Institute of Technology Madras
- : Dr. C. Vijayan  
Professor  
Department of Physics  
Indian Institute of Technology Madras
- : Dr. Nilesh J. Vijayan  
Professor  
Department of Engineering Design  
Indian Institute of Technology Madras